The environments giving birth to long Gamma Ray Bursts : preparing the SVOM science

Benjamin Schneider

université PARIS-SACLAY

The environments giving birth to Long Gamma-Ray Bursts: preparing the SVOM science

Les environnements à l'origine des sursauts gamma longs: préparation à la mission SVOM

Thèse de doctorat de l'université Paris-Saclay

École doctorale n°127 : Astronomie et Astrophysique d'Île-de-France (AAIF)
Spécialité de doctorat: Astronomie et Astrophysique
Graduate School : Physique, Référent : Faculté des sciences d'Orsay

Thèse préparée au CEA, dans l'unité de recherche Astrophysique, Instrumentation et Modélisation de Paris-Saclay (Université Paris-Saclay, CNRS, CEA), sous la direction de Emeric Le Floc'h, Ingénieur-chercheur

Thèse soutenue à Paris-Saclay, le 17 Novembre 2022, par

Benjamin SCHNEIDER

Composition du jury

Laurent Verstraete Professeur Institut d'Astrophysique Spatiale (IAS)	Président
Johan Richard Astronome Centre de Recherche Astrophysique de Lyon (CRAL)	Rapporteur & Examinateur
Etienne Pointecouteau Directeur de recherche Institut de Recherche en Astrophysique et Planétologie (IRAP)	Rapporteur & Examinateur
Samuel Boissier Directeur de recherche Laboratoire d'Astrophysique de Marseille (LAM)	Examinateur
Françoise Combes Professeure Collège de France & Observatoire de Paris (LERMA)	Examinatrice
Pierre-Alain Duc Directeur de recherche Observatoire Astronomique de Strasbourg (ObAS)	Examinateur
Aline Meuris Ingénieure-chercheuse CEA Paris-Saclay, Département d'Astrophysique (DAp)	Invitée
Emeric Le Floc'h Ingénieur-chercheur (HDR) CEA Paris-Saclay, Département d'Astrophysique (DAp)	Directeur de thèse

THESE DE DOCTORAT
NNT : 2022UPASP123

Doctoral School Astronomy and Astrophysics for Paris Area
University of Paris-Saclay

DOCTORATE THESIS

Presented and defended in Saclay
November 17th 2022

by

Benjamin Schneider

The environments giving birth to Long Gamma-Ray Bursts: preparing the SVOM science

Thesis advisor: Emeric Le Floc'h

Prepared at the Astrophysics Division of CEA Paris-Saclay
DAp - UMR AIM

NNT: 2022UPASP123

For Laurie, Dad, Mom and Sarah,
with love

"All men have stars, but they are not the same things for different people. For some, who are travelers, the stars are guides. For others they are no more than little lights in the sky. For others, who are scholars, they are problems... But all these stars are silent. You-You alone will have stars as no one else has them."

The Little Prince
Antoine de Saint-Exupéry

université PARIS-SACLAY

ÉCOLE DOCTORALE
Astronomie
et Astrophysique
d'Île-de-France (AAIF)

Title: The environments giving birth to Long Gamma-Ray Bursts: preparing the SVOM science

Keywords: Gamma-ray bursts, Galaxies structure, Star formation, Follow-up, SVOM, MXT

Abstract: Gamma-Ray Bursts (GRBs) are brief flashes of gamma-ray photons produced by ultra-relativistic jets after a newly born stellar black hole, and represent the most energetic phenomena known in the Universe. The forthcoming Sino-French mission SVOM will be dedicated to the observation of GRBs and will open a new era in the time-domain and multi-messenger astrophysics. With a better synergy between the detection of GRBs by instruments on board the satellite and their follow-up with ground telescopes, SVOM will offer a new insight on these extreme phenomena. In this thesis, I focused on the preparation and the scientific exploitation of the mission on long, medium and short term.
Long-term: among the GRB population, a subpopulation known as Long Gamma-Ray Bursts (LGRBs) is believed to be associated with the death of massive stars, which makes them promising tracers of the cosmic star formation history up to very high redshift ($z > 8$). However, previous work suggested that some conditions seem to be required to form an LGRB, related for instance to the low metallicity of the progenitor or its surrounding environment. Through my work, I studied the influence of the stellar density on the efficiency of LGRB formation. Given that these phenomena are extragalactic, the analysis can only be performed through the global properties of the host galaxy. By comparing a sample of LGRB host galaxies to a sample of star-forming galaxies obtained from a deep survey, I showed that LGRBs tend to be observed more frequently in compact galaxies with a density of star formation and stellar mass higher than found in galaxies of the field.
Mid-term: the build-up of the new sample of well-characterized GRBs identified with SVOM will require an efficient follow-up by the SVOM science community. In this goal, I actively contributed to the program led with the Very Large Telescope by the Stargate consortium to follow-up the GRBs currently detected by the Swift satellite. I also played a key role in setting up the recent follow-up of these alerts with the MISTRAL spectro-imager mounted on the T193 at the Observatoire de Haute-Provence.
Short-term: SVOM will perform a systematic X-ray follow-up of GRBs using the X-ray telescope on board the satellite (MXT). In this context, I actively participated in the energy calibration of the MXT flight model and in the development of an optimized data processing. This demonstrated the excellent spectral performance of MXT before its launch. Once in flight, this processing will ensure high quality reduced products for scientific analysis.

université PARIS-SACLAY

ÉCOLE DOCTORALE
Astronomie
et Astrophysique
d'Île-de-France (AAIF)

Titre: Les environnements à l'origine des sursauts gamma longs : préparation à la mission SVOM

Mots clés: Sursauts gamma, Structure des galaxies, Formation stellaire, Suivi des alertes, SVOM, MXT

Résumé: Les sursauts gamma (GRBs) sont de brefs flashs de rayons gamma causés par des jets ultra-relativistes après la formation d'un trou noir stellaire et représentent les phénomènes les plus énergétiques connus dans l'Univers. La future mission franco-chinoise SVOM sera dédiée à l'observation des GRBs et ouvrira une nouvelle ère dans le domaine du ciel transitoire et multi-messager. Grâce à une meilleure synergie entre la détection des GRBs par les instruments à bord du satellite et leur suivi par les télescopes au sol, SVOM promet d'apporter un nouveau regard sur ces phénomènes extrêmes. Dans cette thèse, je me suis intéressé à la préparation et à l'exploitation scientifique de la mission à long, moyen et court terme.
À long terme : parmi la population des GRBs, une sous-population constituée des sursauts gamma longs (LGRB) s'est révélée être associée à la fin de vie des étoiles massives, ce qui en fait des traceurs prometteurs de la formation stellaire cosmique jusqu'à de très grands décalages spectraux ($z > 8$). Cependant, des études ont suggéré que certaines conditions semblent être requises pour former un LGRB, liées par exemple à la faible métallicité du progéniteur ou de son environnement proche. À travers mon travail, j'ai étudié l'influence de la densité stellaire sur l'efficacité de formation des LGRBs. Puisque ces phénomènes sont extragalactiques, ce type d'étude ne peut se faire qu'à travers les propriétés globales de la galaxie hôte. En comparant un échantillon de galaxies hôtes de LGRBs à un échantillon de galaxies à formation d'étoiles obtenu à partir d'un sondage profond de l'Univers, j'ai montré que les LGRBs ont tendance à être observés plus fréquemment dans des galaxies compactes ayant une densité de formation d'étoiles et de masse stellaire plus élevées que la normale.
À moyen terme : la constitution du nouvel échantillon de GRBs proprement caractérisés et identifiés par la mission SVOM nécessitera un suivi efficace des alertes par la communauté scientifique de SVOM. Dans ce but, j'ai pris part de manière active au programme mené par le consortium Stargate à l'aide du Very Large Telescope pour conduire le suivi des GRBs actuellement détectés par la mission Swift. J'ai également joué un rôle important dans la récente mise en place du suivi de ces alertes avec le spectro-imageur MISTRAL installé sur le T193 de l'Observatoire de Haute-Provence.
À court terme : SVOM effectuera un suivi systématique des GRBs dans le domaine des rayons X en utilisant un télescope X à bord du satellite (MXT). Dans ce contexte, j'ai participé activement à la calibration en énergie du modèle de vol de MXT et à la mise en place d'un traitement optimisé des données. Ceci a permis de démontrer l'excellente performance spectrale de MXT avant son lancement. Une fois en vol, ces traitements permettront de tirer le meilleur parti des données pour leur exploitation scientifique.

Remerciement

Une thèse est une formidable aventure intellectuelle mais aussi sans aucun doute une incroyable aventure humaine. Durant ces trois années, j'ai eu l'occasion de rencontrer et de collaborer avec de nombreuses personnes qui m'ont apporté tant d'un point de vue professionnel que personnel. À travers ces quelques lignes, je tiens à les remercier pour leur soutien et leur aide.

Tout d'abord, j'aimerais remercier Emeric Le Floc'h, mon directeur de thèse, qui a su m'accompagner et me guider au cours de cette thèse. Il a trouvé le bon équilibre en me laissant explorer mes idées mais en me remettant sur la bonne voie lorsque cela était nécessaire. Il m'a permis de découvrir, d'apprendre et d'apprécier le travail de recherche. Tout au long de la thèse, j'ai été ravi de travailler à ses côtés et réaliser des suivis de GRB jusque tard dans la nuit.

Je tiens également à remercier tout particulièrement Aline Meuris, qui m'a non seulement initié à l'instrumentation spatiale mais aussi transmis sa passion pour ce domaine. Elle a toujours su trouver les mots justes et me donner de précieux conseils dans les moments clés de ma thèse. J'ai sincèrement aimé travailler avec elle et je la remercie pour son aide et le temps qu'elle a consacré à ma formation.

Je remercie chaleureusement tous les membres de l'équipe SVOM, en particulier Bertrand Cordier, Karine Mercier, Diego Götz et Philippe Ferrando pour leur bienveillance et leur accompagnement dans mon projet de thèse. J'ai été ravi de rejoindre la mission et de collaborer au développement de ce projet qui promet d'être riche en résultats scientifiques sur le ciel transitoire.

Merci à toute la collaboration Stargate pour leur accueil, leur disponibilité et leurs échanges. Plus particulièrement, je remercie Daniele Malesani, Susanna Vergani, Jesse Palmerio et Damien Turpin pour leurs précieuses explications et conseils sur le suivi des GRBs, souvent à des heures tardives lors d'un nouveau burst.

Je remercie l'ensemble du CEA/DAP, en particulier le LCEG et Mengyuan Xiao, avec qui j'ai pu avoir des discussions passionnantes et enrichissantes qui

m'ont fait prendre du recul et grandir humainement.

Un grand merci à Jérôme Rodriguez, Olivier Limousin et Jérôme Guillet qui ont pris le temps de m'écouter et discuter dans les moments difficiles et qui ont été des alliés précieux pour prendre les bonnes décisions dans mon parcours professionnel. Je tiens aussi à remercier Nicolas Dagoneau pour son aide et soutien infaillibles depuis l'école d'ingénieur à Strasbourg.

Je remercie également l'ensemble du jury et plus particulièrement Johan Richard et Etienne Pointecouteau pour avoir accepté d'être les rapporteurs de cette thèse et pour leur rapport sur ce manuscrit.

Il m'est impossible d'oublier Diana Renaud, Timothée Tollet, Thibault Pichon, Hugo Allaire avec qui j'ai passé des moments incroyables et qui ont toujours été là pour me changer les idées dans les moments difficiles ou marquer le coup lors des grandes étapes de ma vie professionnelle et privée. Merci à eux pour tout ce qu'ils m'ont fait vivre pendant ces trois années et pour les souvenirs qu'ils me laissent.

Enfin, mes derniers remerciements vont à toutes les personnes qui ont eu un lien direct ou indirect avec ma thèse mais dont je n'ai pas pu citer leur nom dans ces quelques lignes même si mes pensées pour eux étaient là au moment de leur écriture.

Benjamin Schneider

Contents

Abbreviations

ACS Advanced Camera for Surveys

ADC Analog To Digital Converter

ADU Analog Digital Unit

AEGIS All-wavelength Extended Groth Strip International Survey

AMR Adaptive Mesh Refinement

ASIC Application-Specific Integrated Circuit

ASPIRED Automated SpectroPhotometric Image REDuction

BA Burst Advocate

BAT Burst Alert Telescope

BATSE Burst and Transient Source Experiment

BL Broad Line

CAGIRE CApturing Grbs InfraRed Emission

CAMEX CMOS Amplifier and MultiplEXer

CANDELS Cosmic Assembly Near-infrared Deep Extragalactic Legacy Survey

CATCH Chasing All Transients Constellation Hunters

CCD Charge Coupled Device

CDF Cumulative Distribution Function

CdTe Cadmium Telluride

CEA Commissariat à l'Énergie Atomique et aux énergies alternatives

CGRO Compton Gamma-ray observatory

CNES Centre National D'Etudes Spatiales

CNN Convolutional Neural Networks

COS Cosmic Origins Spectrograph

COSMOS Cosmic Evolution Survey

COSTAR Corrective Space Telescope Axial Replacement

CP Core Program

CS Charge Sharing

CSFRH Cosmic Star Formation Rate History

CTE Charge Transfer Efficiency

CTI Charge Transfer Inefficiency

DLA Damped Lyman-α Absorber

ECC Energy Calibration via Correlation

ENC Equivalent Noise Charge

EP Einstein Probe

ESO European Southern Observatory

ETC Exposure Time Calculators

F/C-GFT French/Chinese-Ground Follow-up Telescope

FEE Front-End Electronics

FGS Fine Guidance Sensors

FIR Far-Infrared

FM Flight Model

FOV Field Of View

FPA Focal Plane Assembly

FSC French Science Center

FWHM Full With Half Maximum

GCN Gamma-ray burst Coordinates Network

GOODS Great Observatories Origins Survey

GP General Program

GRB Gamma-Ray Burst

GRD Gamma-Ray Detector

GRM Gamma-Ray Monitor

GUI Graphical User Interface

GWAC Ground Wide Angle Cameras

HERMES High Energy Rapid Modular Ensemble of Satellites

HETE-2 High Energy Transient Explorer

HiZ-GUNDAM High-z Gamma-ray bursts for Unraveling the Dark Ages Mission

HLA Hubble Legacy Archive

HR Hardness ratio

HST Hubble Space Telescope

HUDF Hubble Ultra Deep Field

IMF Initial Mass Function

Integral INTErnational Gamma Ray Astrophysics Laboratory

IR Infrared

JFET Junction Field Effect Transistor

KAGRA Kamioka Gravitational Wave Detector

LEAP LargE Area burst Polarimeter

LEO Low Earth Orbit

LLT Low-Level Threshold

LM Levenberg–Marquardt

LOS Line Of Sight

LPF Low-Pass Filter

LyC Lyman continuum

M-Z Mass-Metallicity relation

M/L Mass-to-Light ratio

MAD Median Absolute Deviation

MAST Mikulski Archive for Space Telescopes

MC Monte Carlo

MCAM MXT CAMera

MDPU MXT Data Processing Unit

MISTRAL Multi-purpose InSTRument for Astronomy at Low-resolution

MoonBEAM Moon Burst Energetics All-sky Monitor

MOP MXT OPtical assembly

MOS Metal-Oxide-Semiconductor

MPE Max Planck Institute for Extraterrestrial Physics

MPO Micro-Pore Optic

MS Main Sequence of star-forming galaxies

MXT Microchannel X-ray Telescope

NICMOS Near Infrared Camera and Multi-object Spectrometer

NIR Near-Infrared

NL Non-Linear

NOT Nordic Optical Telescope

NTBT Nuclear Test Ban Treaty

NTE NOT Transient Explorer

NTT New Technology Telescope

OHP Observatoire de Haute Provence

PC Photon-counting

PDF Probability Density Function

PHA Pulse Height Amplitude

PI Principal Investigator

PM Performance Model

PSF Point Spread Function

QE Quantum Efficiency

RRM Rapid Response Mode

S/N Signal-to-Noise ratio

SAA South Atlantic Anomaly

SDB SVOM Database

SDD Silicon Drift Detector

SDSS Sloan Digital Sky Survey

SED Spectral Energy Distribution

SFR Star Formation Rate

SHOALS Swift Gamma-Ray Burst Host Galaxy Legacy Survey

SN Supernova

SNR Supernova Remnant

SOLEIL Source Optimisée de Lumière d'Energie Intermédiaire du LURE

SOXS Son Of X-Shooter

STD STanDard

STIS Space Telescope Imaging Spectrograph

SVOM Space-based multi-band astronomical Variable Objects Monitor

TEC Thermo Electric Cooler

TeV Teraelectronvolt

THESEUS Transient High-Energy Sky and Early Universe Surveyor

ToO Targets of Opportunity

TVAC Thermal Vacuum Chamber

UDS Ultra Deep Survey

UT Unit Telescope

UV Ultraviolet

UVOT Ultra-violet Optical Telescope

VAT Vatlock system

VIS Visible

VLT Very Large Telescope

VT Visible-band Telescope

WFC3 Wide Field Camera 3

WT Windowed Timing

XMM X-ray Multi Mirror

XRF X-ray Flashes

XRR X-ray Rich

XRT X-Ray Telescope

Chapter 1

Introduction

Contents

This chapter presents the general context and framework of my work on gamma-ray bursts. It gives the necessary background and elements to understand the motivations that drove my research activities as part of this PhD. First, gamma-ray bursts are introduced from their discovery, the current models describing their formation and emission mechanism, up to their attractive use as cosmic probes for

the early Universe (Sect. 1.1). Then, their host galaxies and previous work that provided meaningful information about the property of the environments where these phenomena occur are described in Sect. 1.2. Finally, Sect. 1.3 presents the forthcoming SVOM mission and its optimized strategy compared to previous missions, promising new insights into these extreme phenomena.

1.1 Gamma-Ray Bursts

Literally a *gamma-ray burst* (GRB) is a sudden, brief and violent emission of gamma radiation. In astronomy, this term refers to the most energetic and luminous explosions of the Universe since the Big Bang, able to release in a few seconds the same amount of energy as the Sun during its entire lifetime. Although such an event is qualified as a *burst* of γ-rays, the duration and emission of a GRB is far from being limited to the timescale of seconds and gamma ray range. In the temporal domain, the source can be visible minutes, hours, days and up to months or years after its detection. In the spectral domain, the emission covers a large part of the spectrum, from radio to Teraelectronvolt (TeV). In the following sections, a brief description of the history of GRBs is presented. A more detailed description can be found in Vedrenne & Atteia (2009); Kouveliotou et al. (2012); Zhang (2018).

1.1.1 Brief history

The discovery of GRBs was, as is often the case with scientific discoveries, quite unexpected. The scientific adventure started more than sixty years ago and continues to be an active research field with the ongoing development of new satellites to detect, observe and better understand the nature of these phenomena.

1.1.1.1 Geopolitics context

In the late 1960s, the Nuclear Test Ban Treaty (NTBT) between the Soviet Union and the United States prohibited the use of nuclear weapons in the atmosphere or in space. Suspicious about the respect of this treaty, the US developed a series of satellites named *Vela* to detect clandestine nuclear tests. A total of twelve

pairs of satellites (Fig. 1.1) were launched by the US Air Force between 1963 and 1970, and operated on opposite sides of a high geocentric orbit ($\sim 118\,000$ km) to ensure permanent and direct observations of the entire Earth. Each satellite was composed of 12 external X-ray detectors and 18 internal neutron and gamma-ray detectors designed by the Los Alamos Scientific Laboratory and Sandia Laboratories of Albuquerque.

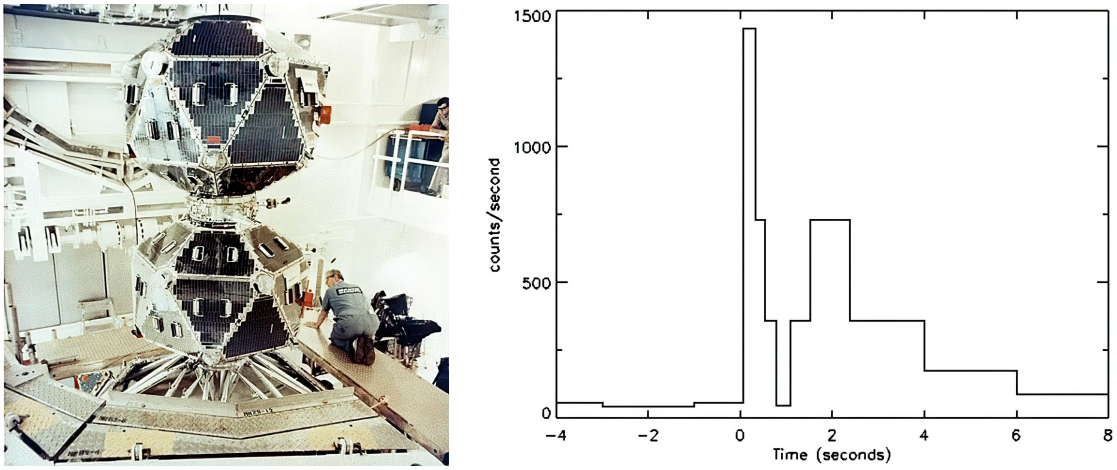

Figure 1.1: *Left panel:* Picture of the Vela-5A/B satellites in their cleanroom. (Credit: Los Alamos National Laboratory). *Right panel:* The light curve of the first gamma-ray burst detected on July 2, 1967 by the Vela 4A/B and the still operational Vela 3 satellites (Credit: Bonnell 1995).

1.1.1.2 First detection

A first flash of gamma radiation was detected on July 2, 1967 by the Vela 4 and Vela 3 satellites. The two distinct peaks of the light curve (see Fig. 1.1) make this event unlikely to be related to a nuclear explosion which would have created an intense burst of gamma rays followed by a gradual decay. Due to the low time resolution of the instruments at that time, the localization of the burst was not determined and the interpretation of this event was postponed. Few years later, using the improved version of Vela satellites, Klebesadel et al. (1973) reported the detection of 16 bursts of gamma radiations. Considering the signal delay between the various Vela detectors, they roughly estimated their location and found that the bursts were created by celestial objects. Moreover, the random distribution of the sources in the sky strongly suggested an origin other than the sun, the moon or an object of the solar system. Finally, no coincidence with a supernova was

reported at the time or in the direction of these events. This led to the discovery of new astronomical objects known as "Gamma-Ray Bursts" and the publication of more than 30,000 articles since 1967.

1.1.1.3 Previous missions

Since the discovery of GRBs, several missions were launched to further characterize GRB emissions and attempt to solve the origin of these mysterious high-energy events. The history of GRB science has not evolved in a linear way but rather step by step with important gaps. One of the reasons for this is that GRBs are detected in gamma-ray light that is absorbed by the Earth's atmosphere and therefore requires the launch of space telescopes. The development of a new generation of instruments using new and improved technologies takes time and is limited by harsh space environments that can damage the telescope. Major space satellites that have contributed to key milestones in GRB science include:

- CGRO (Compton Gamma-ray observatory), 1991 - 2000
- Beppo-SAX (Satellite per Astronomia a raggi X), 1996 - 2003
- HETE-2 (High Energy Transient Explorer), 2000 - 2008
- Integral (INTErnational Gamma Ray Astrophysics Laboratory), 2002 - now
- *Swift*, 2004 - now
- Fermi, 2008 - now

The CGRO satellite was launched into a low Earth orbit in 1991. It was composed of four instruments covering an energy range from 20 keV to 30 GeV. The Burst and Transient Source Experiment (BATSE) was one of these instruments and was dedicated to the study of GRBs. BATSE was an all sky monitor with an energy range from 20 to 1 000 keV.
During its lifetime, BATSE detected a total of 2704 GRBs with a typical error radius of $\sim 0.2 - 18$ deg (Briggs et al. 1999). The large sample of GRBs detected by BATSE allowed important progress in the field of GRBs. At that time, the origin of GRBs, i.e., galactic or extragalactic, was a great subject of debate. The angular distribution of BATSE GRBs (Fig. 1.2) was found to be homogeneously distributed in space (isotropic) and supported a cosmological origin (Briggs et al.

1996; Paciesas et al. 1999). Then, the duration of GRBs is often defined as the time during which the source emits from 5% to 95% of its total measured counts (T_{90}). The distribution of BATSE GRB durations (Fig.1.3) showed that the whole population can be separated around 2 seconds into two sub-populations (Kouveliotou et al. 1993; Paciesas et al. 1999). Bursts with $T_{90} < 2$ sec were named as *short-duration* GRBs and bursts with $T_{90} > 2$ sec as *long-duration* GRBs. Finally, the GRB spectra obtained from BATSE suggested a non-thermal origin and were well-modeled using a broken power law (Band et al. 1993).

Given that the optical sky is crowded of sources, large uncertainties in the positions returned by BASTE prevented the identification of the optical counterpart predicted by the models of the burst and referred as *afterglow* emission (Sect. 1.1.4). BeppoSAX (Boella et al. 1997) was an X-ray satellite launched in 1996 capable to observe objects between 0.1 to 300 keV. In addition to a set of wide field gamma-ray instruments, it was composed of a set of narrow and wide X-ray instruments. Since the X-ray sky is much less crowded than the optical sky and X-ray instruments have a much better localization capability than gamma-ray instruments, BeppoSAX was ideally designed to quickly identify and improve the burst localization. The first X-ray afterglow detections were obtained for GRB 970228 (top panel of Fig. 1.4) and GRB 970508. The improved burst localization enabled the first optical afterglow detection on GRB 970228 by the 10-m Keck II Telescope, visible on the bottom panel of Fig. 1.4 (van Paradijs et al. 1997). Then, briefly the first radio afterglow was detected on GRB 970508 using the Very Large Array (Frail et al. 1997). The first redshift measurement was performed by Metzger et al. (1997) on GRB 970508 with the 10-m Keck II Telescope. They inferred a redshift of $z = 0.835$ for the burst with the Fe II and Mg II absorption lines observed in the spectrum (bottom panels of Fig. 1.5). This measurement definitively confirmed the cosmological origin of GRBs. Later, imaging and spectroscopic observations were again performed with the Keck II Telescope at the GRB position. An actively star-forming dwarf galaxy was found at the same redshift (Bloom et al. 1998), which confirmed the identification and detection of the host galaxy. Then, the gathering of multi-wavelength observations of several bursts allowed to better understand the physics of GRBs and to confirm the power-law decay of the afterglow for all wavelength ranges as predicted by the theory (e.g., Mészáros & Rees 1997).

In 2004, an additional step was made with the launch of the *Swift* satellite (Gehrels et al. 2004) dedicated and optimized to study GRBs. It carries three instruments:

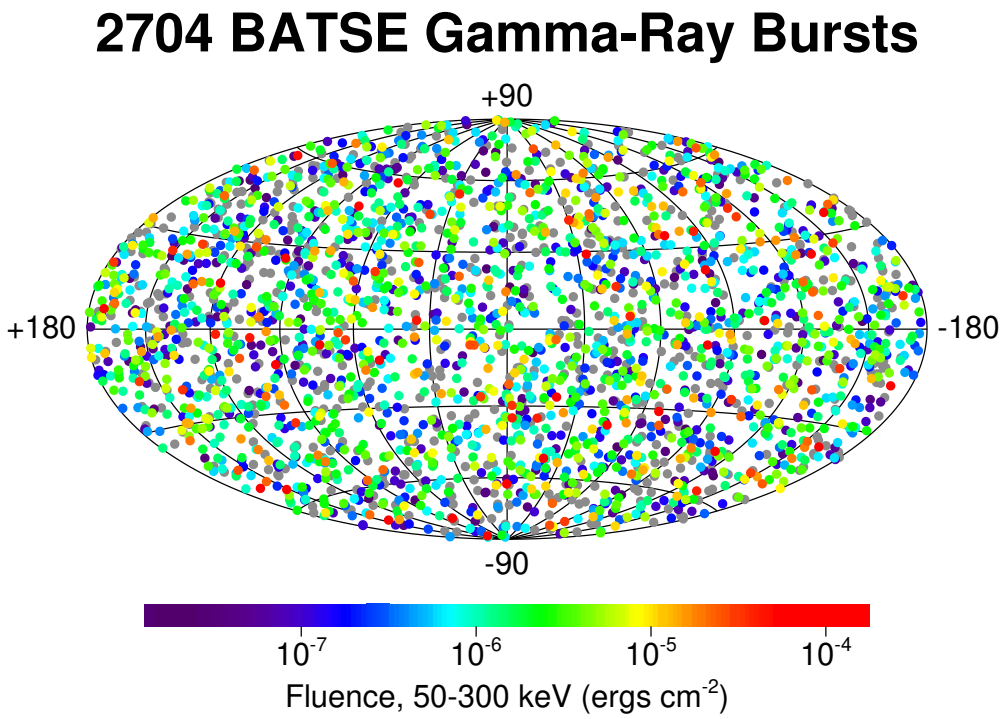

Figure 1.2: Sky distribution of the 2704 BATSE GRBs in galactic coordinates. Bursts are color-coded based on the fluence (i.e., the amount of energy collected per unit area over the total duration of the burst for all BATSE channels). The Galactic plane is located at the middle of the figure along the horizontal line. (Paciesas et al. 1999)

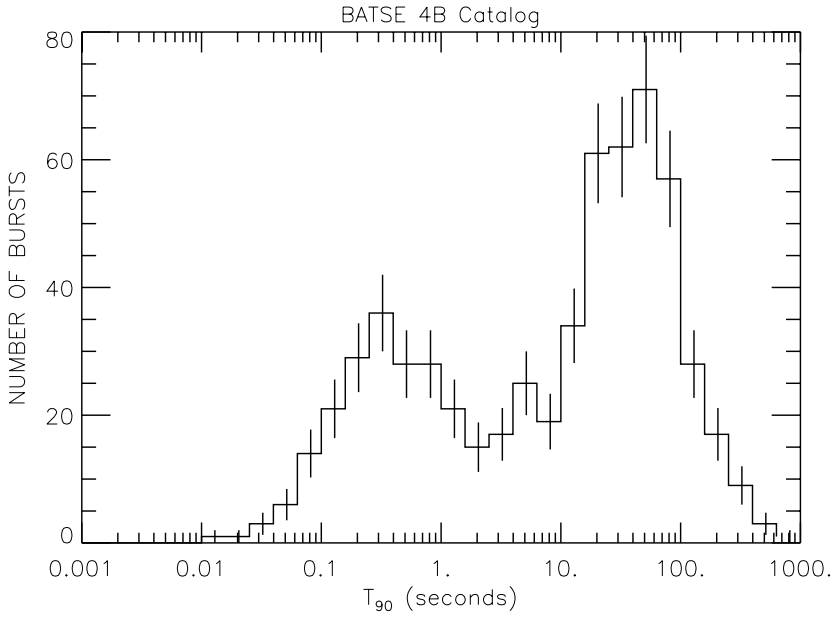

Figure 1.3: Duration (T_{90}) distribution of the 2704 BATSE GRBs. The duration of the burst is defined as the time interval collecting 5% to 95% of the total number of detected counts over all BATSE channels (>20 keV). (Paciesas et al. 1999)

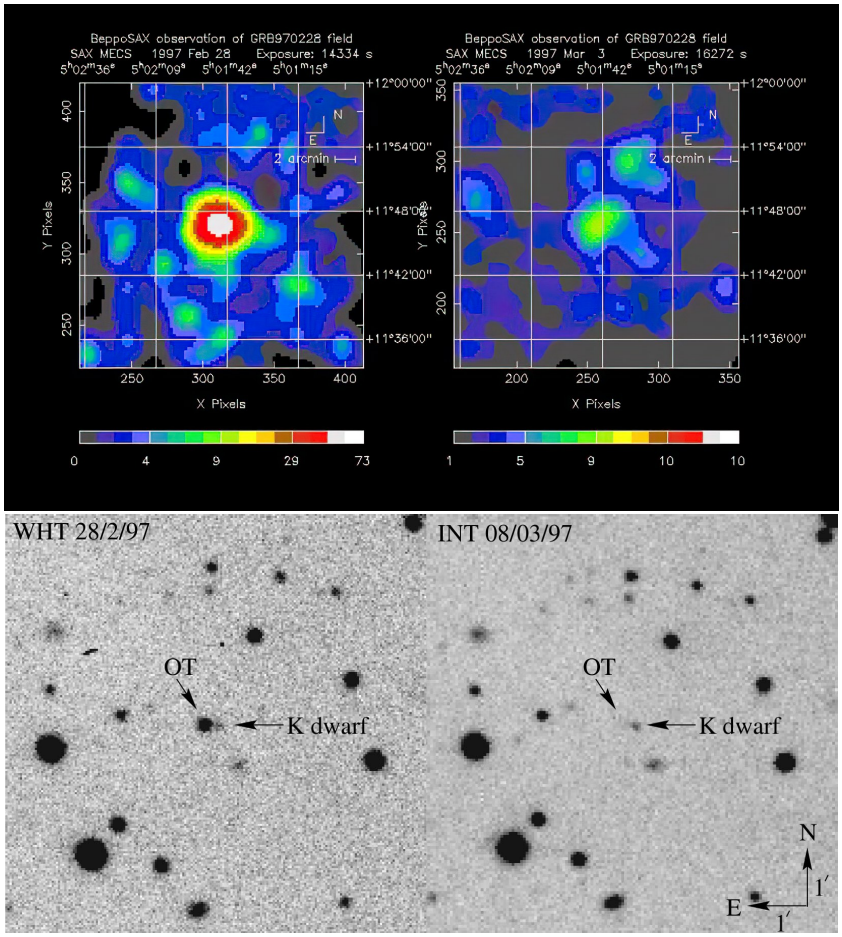

Figure 1.4: First X-ray afterglow of GRB 970228 detected by BeppoSAX (top panels). The left panel shows the first observation 8 hours after the detection and the right panel the observation 3 days after. (Costa et al. 1997) First optical afterglow detected by the William Herschel Telescope (bottom panels). The left and right panels show V-band images with an interval of 8 days. The burst is indicated with the "OT" arrow. (van Paradijs et al. 1997)

(i) a wide field coded mask X-ray imager Burst Alert Telescope (BAT; Barthelmy et al. 2005), (ii) a narrow field X-Ray Telescope (XRT; Burrows et al. 2005) and (iii) a UV-Optical Telescope (UVOT; Roming et al. 2005). The GRB is firstly detected and localized within a few arcmin error box by BAT with its large field of view (FOV) of 1.4 sr and large spectral coverage from 15 to 350 keV. Then the satellite slews in typically less than one minute towards the direction of the BAT error box, and the XRT (0.2-10 keV) and UVOT (170-650 nm) are used to improve the GRB localization and further characterize its emission. For the vast majority of GRBs, the typical error box position returned by XRT is less than 10 arcsec. If an optical counterpart is detected by UVOT, the position is improved at the

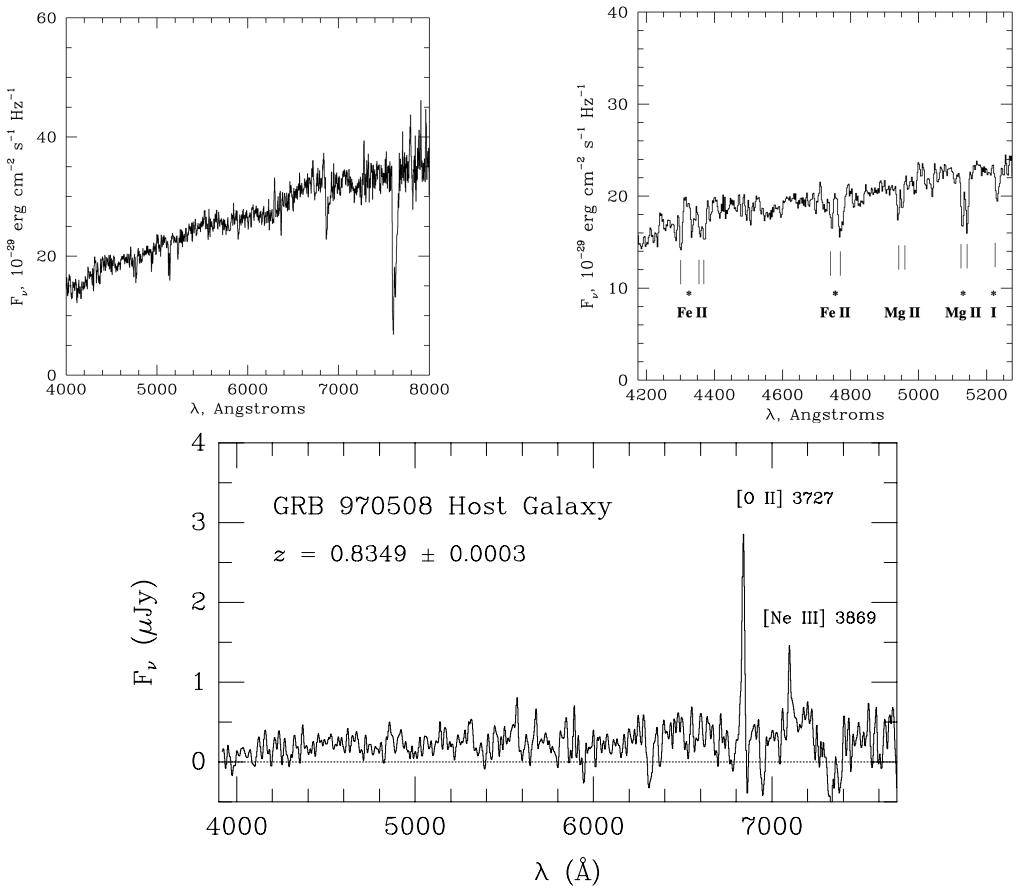

Figure 1.5: Optical spectrum of GRB 970508 obtained with the 10-m Keck II Telescope, allowing to infer a redshift of 0.835 for the burst (top panels). The full spectrum and a zoom are shown on the left and right, respectively. The absorption lines with asterisks correspond to an intermediate system at $z = 0.767$. (Metzger et al. 1997) Optical spectrum of the GRB 970508 host galaxy after 163 days (bottom panel). Two emissions lines are detected and provided a redshift of 0.835. (Bloom et al. 1998)

subarcsec level. These positions are then quickly sent to the ground and shared with the entire GRB community to perform rapid follow-up observations at other wavelengths. With its fast slewing capability, and narrow field on board X-ray and optical instruments, *Swift* has detected a GRB counterpart for the majority of GRBs and has revolutionized the GRB field in many aspects such as the regular redshift measurements and association with the host galaxy, the discovery of an ultra-long GRB class (Levan et al. 2014) or the possibility to study the relative localization of the burst with respect to the host (Blanchard et al. 2016), see Gehrels et al. (2009) for a review about observational progress with *Swift*.

1.1.1.4 Future missions

To further improve the strategy compared to previous missions such as *Swift*, several missions are currently under development. They carry on board a set of instruments with different characteristics (e.g., sensitivity, wavelength coverage) and an optimized synergy with other space and ground telescopes. They are expected to probe a different population of transient sources and provide a larger and more controlled sample of GRBs.

By the end of 2023, two missions dedicated to the detection of transient sources will be launched, the Space-based Multi-band Variable astronomical Objects Monitor (SVOM) mission (Wei et al. 2016; Atteia et al. 2022), which is further described in Sect. 1.3 and represents the central theme within this manuscript, and the Einstein Probe (EP) mission (Yuan et al. 2015). Another project using nano-satellites to probe the X-ray temporal emission is the High Energy Rapid Modular Ensemble of Satellites (HERMES) project (Evangelista et al. 2020) currently under development and scheduled for 2023.

By the 2030s, proposed missions are generally optimized to detect and rapidly identify GRBs at $z > 6$. This goal is achieved using a wide-field X-ray detector and an infrared spectro-imaging telescope to perform a redshift estimate of the source directly onboard the satellite. For instance, the Transient High-Energy Sky and Early Universe Surveyor (THESEUS) mission (Amati et al. 2021a,b), the Gamow Explorer mission (White et al. 2021) albeit non selected so far or the HiZ-GUNDAM (High-z Gamma-ray bursts for Unraveling the Dark Ages Mission) mission (Yonetoku et al. 2014) are proposed missions optimized for high-z GRBs. Moreover, the Moon Burst Energetics All-sky Monitor (MoonBEAM) and the LargE Area burst Polarimeter (LEAP) mission (McConnell et al. 2021) are two NASA missions in competition to study GRBs with a targeted launch in 2027. Finally, an interesting project in development is based on a constellation of 133 X-ray micro-satellites, the Chasing All Transients Constellation Hunters Space Mission (CATCH). The satellites will be capable of performing X-ray follow-up observations in spectroscopy, imaging, and polarization of multiple transient sources at the same time (Li et al. 2022, submitted).

1.1.2 Classification

As anticipated in Sect. 1.1.1.3, the bimodal duration distribution of BATSE GRBs suggested that the whole GRB population is separated into two distinct classes, *short-duration* and *long-duration* types with a separation around $T_{90} \sim 2$ seconds. However, the duration distribution shows a clear overlap between the two classes. It is therefore highly likely that the tails of the two distributions may introduce outliers in each class. In addition, a criterion based on T_{90} may introduce instrumental selection effect given that the measured duration depends on the energy and the sensitivity of the instrument (Qin et al. 2013). For instance, a short GRB detected by a first instrument in a hard energy band (> 100 keV) might be detected as a long GRB by the second using a softer energy band.
Due to the non-negligible overlap in the duration distribution, it is common to consider the spectral hardness of the burst as a second dimension to improve the classification (Kouveliotou et al. 1993). The hardness (HR) is defined as the ratio of the fluences[1] measured during the T_{90} interval from time-resolved spectra fits in the 50–300 keV and 10–50 keV energy bands. It was observed that short GRBs have a hard spectrum and long GRBs a soft one (left panel of Fig. 1.6). Although the HR diagram shows two distinct clusters with a less significant overlap, the boundary is still vague and can lead to mis-classifications. For example, the GRB 200826A had a $T_{90} \sim 1$ s and a hardness consistent with the short burst type. However, considering other observational properties (e.g., spectral behaviors, total energy, host galaxy properties) the burst might be classified as a long GRB (Ahumada et al. 2021; Zhang et al. 2021). In a more general context, this case supports the idea of using multi-observational criteria to correctly classify GRBs (Zhang et al. 2009), such as properties of the host galaxy (Qin et al. 2022). A multi-observational criterion may thus be a powerful method to improve the boundary between short and long bursts in the HR-duration plane, and to find exotic bursts challenging the current models such as GRB 200826A (Zhang et al. 2021).

Several GRBs were detected with a T_{90} longer than 1000 s and were named *ultra-long* GRBs (Campana et al. 2011; Thöne et al. 2011b; Gendre et al. 2013;

[1] In the case of transient phenomena, the fluence is the amount of energy collected per unit area over the duration of the burst.

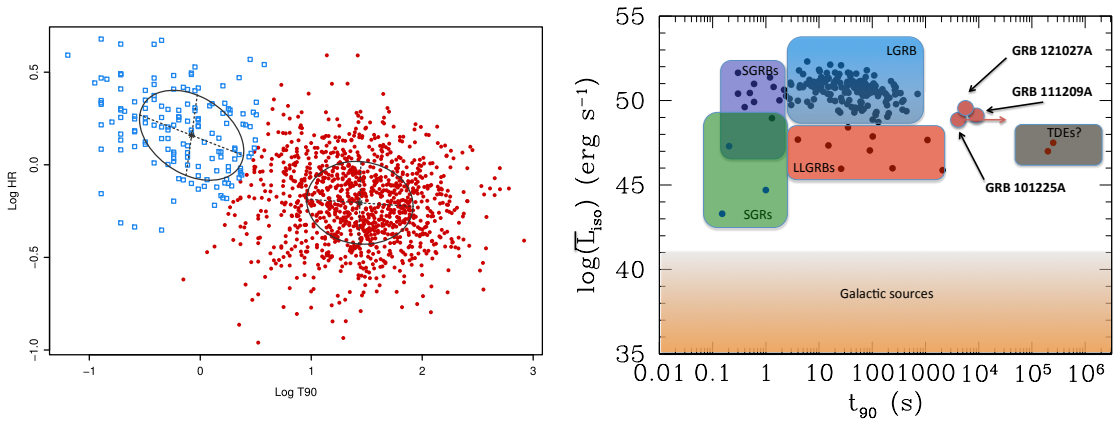

Figure 1.6: *Left panel:* Hardness–duration diagram of the third Fermi GBM GRB catalog. Short-hard bursts are in blue color and long-soft bursts in red color. (Narayana Bhat et al. 2016) *Right panel:* Average luminosity observed during T_{90} as a function of T_{90} for transient sources in the gamma-ray sky. At high luminosity, possible GRB sub-populations are represented by different colors: blue for long GRBs, purple for short GRBs, red for low-luminosity GRBs. Ultra-long GRBs are indicated by large red circles. (Levan et al. 2014)

Stratta et al. 2013). The right panel of Fig. 1.6 shows the average luminosity as a function of duration and demonstrates the extreme nature of these events compared to other GRB populations. The exact origin and nature of these events is still debated. Some authors argued for an origin common to long GRBs due to a long-duration tail of the population (Virgili et al. 2013; Zhang et al. 2014), while others argued for a separate group (Gendre et al. 2013; Levan et al. 2014). The currently limited number of ultra-long GRBs prevents a firm conclusion. The expected rate of ultra-long GRBs detected by the forthcoming SVOM satellite should be at least as much as *Swift* (Dagoneau et al. 2020) and will contribute to better understand the origin of these mysterious events.

1.1.3 GRB progenitors

Using a phenomenological classification scheme, it is clear that two major classes of GRB exist, long/soft and short/hard GRBs. The physical origin and the progenitors of these bursts remained mysterious until the discovery of the first afterglow emissions which allowed to characterize these events and to find some clues on their progenitor.

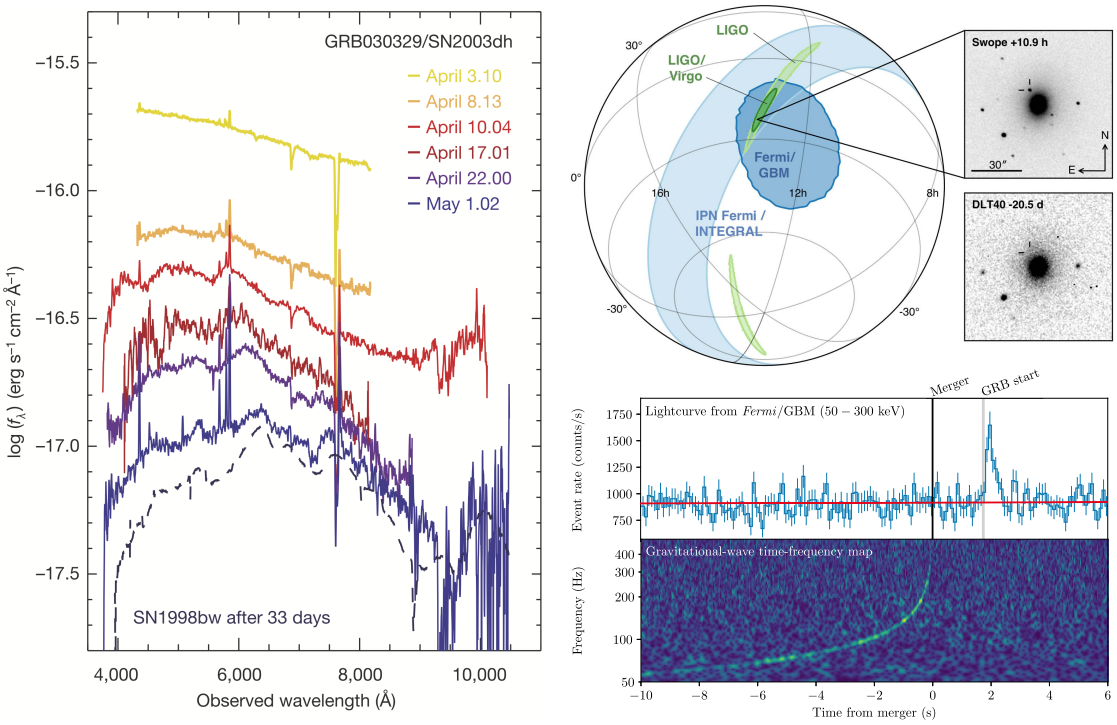

Figure 1.7: *Left panel:* Optical spectroscopy of the GRB030329 afterglow at different epochs with the FORS1/2 instrument of the Very Large Telescope. Each color shows a spectrum obtained at a different day. (Hjorth et al. 2003) *Right panel:* Multi-messenger detection of GW170817 and GRB 170817A. Top panel: Localization of the gravitational-wave by LIGO-Virgo (dark green), the short GRB by Fermi-GBM (dark blue), and optical images prior and post merger. Bottom panel: Fermi/GBM light curve in the 50–300 keV energy range of GRB 170817A and LIGO time-frequency map of GW170817. The merger and burst times are indicated by a vertical black and gray lines, respectively. (Adapted from Abbott et al. 2017a,b)

Long GRBs The first optical spectroscopic follow-up of close GRBs rapidly revealed the evidence of a possible association of the GRB with a supernova (SN), for example SN 1998bw detected in the error box of GRB 980425 (Galama et al. 1998). It was later confirmed by multiple observations of spatial and temporal coincidence of an SN with a GRB (Hjorth et al. 2003; Stanek et al. 2003; Campana et al. 2006a; Pian et al. 2006), such as the case of GRB 030329. An example of the spectral evolution of GRB 030329 is shown in Fig. 1.7. The typical power law decay of a GRB afterglow is firstly observed (yellow), then the fading of the emission gradually gives rise to the detection of the SN 2003dh spectrum (in blue). All GRB supernovae showed spectral similarities. They were observed to be stripped core-collapse supernovae of type Ic (no outer envelope of hydrogen and helium). In

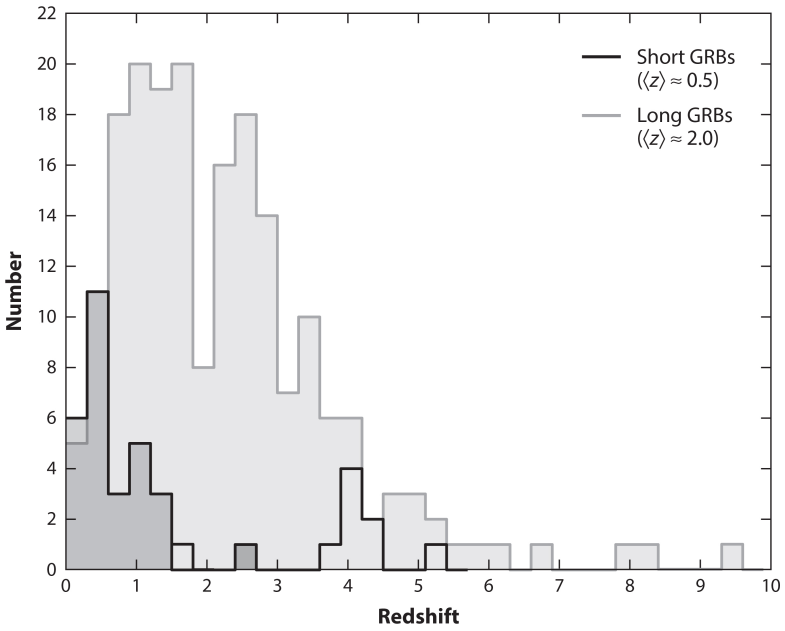

Figure 1.8: Redshift distribution of long GRBs in gray and short GRBs in black. The open histogram shows the redshift upper limits of short GRBs. (Adapted from Berger 2014)

addition, almost all of them exhibited broad lines (BL) indicative of a high outflow velocity ($\sim 30,000$ km s^{-1}). For additional details on the GRB-SN connection, see the review of Cano et al. (2017).

The view of a systematic GRB-SN connection was challenged by the observation of GRB 060505 and GRB 060614, two close GRBs ($z \sim 0.1$) but where no supernova was detected up to 100 times fainter than SN 1998bw (Della Valle et al. 2006; Fynbo et al. 2006; Gal-Yam et al. 2006; Gehrels et al. 2006). The limited number of long GRBs detected locally (Fig. 1.8) where the supernova counterpart can be studied in detail makes the SN-less GRB sample limited. So far, 4 SN-less GRBs were detected, which prevents a firm conclusion on their distinct origin from long GRBs associated with a SN.

It is now clear that long GRBs are related to massive stars (see also the clues from their host galaxies in the Sect. 1.2) but their exact nature remains a question. The *collapsar* model (Woosley 1993) is one of the proposed model to explain the production of long GRBs. In this model, the progenitor ends as a central engine (black hole or magnetar) surrounded by an accretion disk able to create the GRB jet. The formation of the central engine requires a very *massive star* ($\gg 20$ M$_\odot$), for instance a Wolf-Rayet star, and the formation of an accretion disk implies a

direct condition of a *fast-rotating* progenitor. In addition the association observed between GRBs and type Ic supernovae requires the removal of the hydrogen and a part of the helium envelopes of the progenitor. This can be achieved by stellar winds or binary interactions. However, the former are expected to cause a large scale mass loss depending on the progenitor metallicity (Vink et al. 2001) and a significant loss of angular momentum, in contradiction with the requirement of a fast-rotating star.

A single star progenitor remains viable considering that the fast rotation induces a chemically homogeneous evolution of the star (Yoon & Langer 2005; Langer & Norman 2006). This evolution requires a sufficiently low metallicity ($< 0.2\ Z_{\odot}$) but avoids the need for strong stellar winds to remove the hydrogen envelope.

The majority of massive stars were observed to be formed in binary systems (Sana et al. 2012). The presence of a companion offers the possibility to spin up the progenitor via tidal interactions, the accretion of material with high specific angular momentum, or by direct mergers. However, stars may spin down if the system loses mass, producing problems similar to those observed for single star progenitors. One possible scenario involves late mass transfer into the system during the final stage of helium burning in the core and, interestingly, remains viable at high metallicity (Brown & Lee 2004).

The true nature is likely a combination of the two scenarios where single stars and binary stars can produce a GRB. One would also expect the relative contribution of each channel to vary over cosmic time as a function of prevailing environmental conditions at a given time. Further information on GRB progenitors can be found in the review of Levan et al. (2016).

Short GRBs The short GRB afterglows are more challenging to detect due to their faint emission. The progress on the nature of their progenitor was therefore slower than for long GRBs. The detection rate was improved with *Swift* and thanks to its accurate localization, the host galaxies of short GRBs were identified in a larger number (or more easily) (Gehrels et al. 2005; Berger et al. 2005). The lack of SN associations, the mix of ellipticals and spirals in their host population and their wide range of environments (Fong & Berger 2013; Nugent et al. 2022) are in favor of a different formation mechanism. In addition, short GRBs were often found several kiloparsecs from the center of their host galaxies, without strong correlation between the burst location and the stellar light distribution of their hosts (Berger

2010; O'Connor et al. 2022; Fong et al. 2022). All these indirect evidence suggested that the progenitors migrate from their birth sites (e.g., natal kick) to explosion sites. They are consistent with the formation mechanism by the coalescence of two compact objects (Eichler et al. 1989; Narayan et al. 1992) via a binary neutron star system (BNS, Ruffert & Janka 1999; Rosswog et al. 2003) or a neutron star and a black hole (NS-BH, Faber et al. 2006; Shibata & Taniguchi 2011). The connection between short GRBs and BNS mergers was confirmed by the joint detection of the gravitational wave GW170817 and its associated electromagnetic counterpart GRB 170817A (Abbott et al. 2017b; Goldstein et al. 2017). The coincidence of error boxes between Fermi/GBM and LIGO/Virgo are visible in the top right panel of Fig. 1.7. On the bottom panel, the time-frequency map of GW170817 and the GRB 170817A light curve of Fermi/GBM in the 50–300 keV band are shown. A delay of around 2 seconds was observed between the gravitational wave and the electromagnetic counterpart of the BNS merger. This event confirmed that at least one formation channel of short GRBs is due to the merger of compact binary objects. For more discussion on SGRBs, the reader is referred to Berger (2014).

1.1.4 Formation mechanism

The two main types of GRBs are in the vast majority of cases detected with two common characteristic emissions. First, a brief emission mainly in the sub-MeV range is detected, called the *prompt emission*, followed by a longer emission with a broader spectrum, called the *afterglow emission*. Since they are observed for each class of events but on different timescales, the underlying mechanism producing these emissions is expected to be similar. The well-accepted standard scenario is described by the relativistic *fireball* model (Piran 1999; Mészáros 2001). At the end of life of the progenitor, either a fast-rotating massive star for long GRBs or the merger of two compact sources for short GRBs, a newly compact source is formed as the central engine (a black hole or a magnetar[2]). In the central black hole engine scenario, an accretion disk is created at the time of collapse by the high angular momentum of a fraction of the falling material (Fryer et al. 1999). The accretion structure then produces two relativistic jets along the rotation axis of the central engine. The exact process for extracting energy from the accretion disk and producing a GRB is complex and still poorly understood, but one possibility

[2]A magnetar is a highly magnetized neutron star ($\gtrsim 10^{14}$ G).

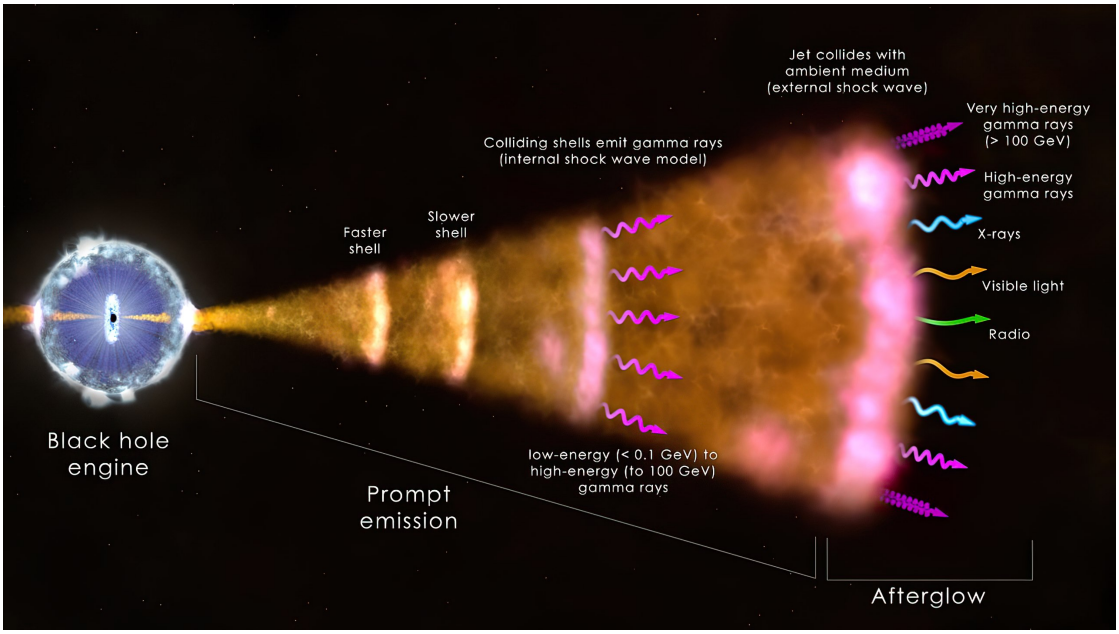

Figure 1.9: Cartoon for the *Fireball* model showing the central engine, the jet, and the two characteristic emitting components of a GRB: the prompt and afterglow emissions. (Credit: NASA)

would be via the Blandford-Znajek effect (Blandford & Znajek 1977).
The first stage of the jets (photosphere region) is optically thick due to the quasi-thermal equilibrium between radiation (photons) and matter (electron-positron). At a larger distance from the source, the expansion and cooling of the jets make them transparent. The second stage produces the prompt emission of the burst which can be observed by an observer in the axis of the jet. This emission is emitted by internal dissipation mechanisms within the jet but the exact mechanism able to produce it is still debated. The model often considered involves the production of the emission via *internal shocks* (Fig. 1.9) between layers of the ejecta with different Lorentz factors (Narayan et al. 1992; Rees & Meszaros 1994). In this scenario, gamma ray photons are generated by accelerated electrons from the dissipated energy, which then release photons by synchrotron radiation and inverse Compton scattering. The two other proposed models involve magnetic field line connection (Spruit et al. 2001) or photospheric emission (Rees & Mészáros 2005) to produce the observed GRB prompt emission. Finally, the afterglow emission is thought to be produced by the *external shock* (Fig. 1.9) between the jet and the interstellar medium or the wind earlier emitted by the progenitor (Paczynski & Rhoads 1993; Meszaros & Rees 1993). The deceleration induced by the circumburst medium on

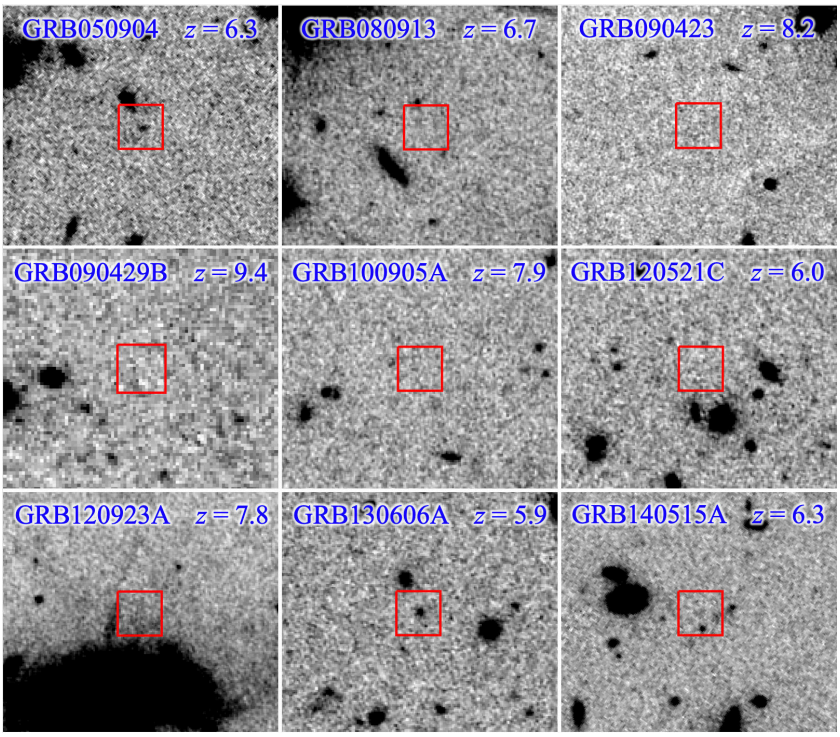

Figure 1.10: Deep HST images of GRB fields at $z > 6$ after the fading of their afterglow. (Tanvir et al. 2021b)

the relativistic jet produces a strong *forward shock* propagating into the medium and a *reverse shock* (Mészáros & Rees 1997; Sari & Piran 1999) propagating into the ejecta itself. At the front of the forward shock, relativistic electrons are accelerated and spiral through magnetic fields generating a non-thermal emission through synchrotron radiation. This produces a broad-band emission from X-rays to radio wavelengths (observable from a few minutes to several days) well-modeled by a power-law (in frequency and time) (Sari et al. 1998), see also Sect. 3.1 for a more illustrative presentation of the GRB afterglows and Kumar & Zhang (2015) for a more theoretical description.

Although the emission mechanism presented here is similar for short and long GRBs, variations in their afterglow emission may be expected due to the different density and composition of the circumburst probed by their respective progenitors.

1.1.5 GRB as probe of the early Universe

GRBs are the most powerful and luminous events known in the Universe. Their energy (E_{iso}[3]) was observed to span about six orders of magnitude ($10^{48} < E_{iso} < 10^{54}$ erg) and their distance to cover a wide range of redshift. Currently the closest long GRB was observed at $z = 0.008$ (GRB 980425, Tinney et al. 1998) and the most distant identified with spectroscopically-confirmed redshift[4] estimate was GRB 090423 at $z = 8.2$ (Tanvir et al. 2009; Salvaterra et al. 2009). Recently, the detection of a bright flash in the Keck MOSFIRE observations of the galaxy GN-z11 at $z \sim 11$ (Jiang et al. 2021a) was suggested to be a possible UV flash produced by a GRB. This report was followed by an intense debate within the community (Kann et al. 2020; Michałowski et al. 2021; Nir et al. 2021; Steinhardt et al. 2021; Jiang et al. 2021b; Padmanabhan & Loeb 2022) where other interpretations such as a flash produced by a satellite or from space debris were proposed as a more likely interpretation. In any case, some GRBs are expected to be produced by Population III stars[5] (Pop III) (Bromm & Yoshida 2011) and therefore detectable at $z > 10$ (Mészáros & Rees 2010; Toma et al. 2011; Yoon et al. 2015).
In addition to their intense luminosity and large redshift range, their transient nature makes them ideal beacons for probing the early Universe. The detection of the prompt emission depends only on the instrument sensitivity given that γ-rays are not strongly affected by the absorption of materials (e.g., dust) along their line of sight (LOS). On the other hand, the afterglow emission is bright enough to imprint the signature of these elements and provide information about the physical conditions close to the burst. The important implication is that the selection function is radically different from the traditional approach such as the galaxy surveys, where the detected objects are limited by the depth of the images. For GRBs, the burst may reveal information about the galaxy, even if the latter is too faint to be detected by current telescopes. This effect is illustrated in Fig. 1.10 for 9 high-z long GRBs, where after the fading of the afterglow, the GRB fields were imaged by deep HST observations. In only 2-3 cases was the host galaxy detected, suggesting that at high redshift, the vast majority of the activity

[3]The isotropic energy of a burst is the equivalent energy released by the source if the object would emit in all the directions.

[4]The most distant GRB with a photometric redshift estimate was found at $z = 9.4$ (Cucchiara et al. 2011).

[5]Pop III stars are the first hypothetical population of stars in the early Universe, very massive ($\gtrsim 300$ $M_\odot$) and formed from a quasi metal-free environment.

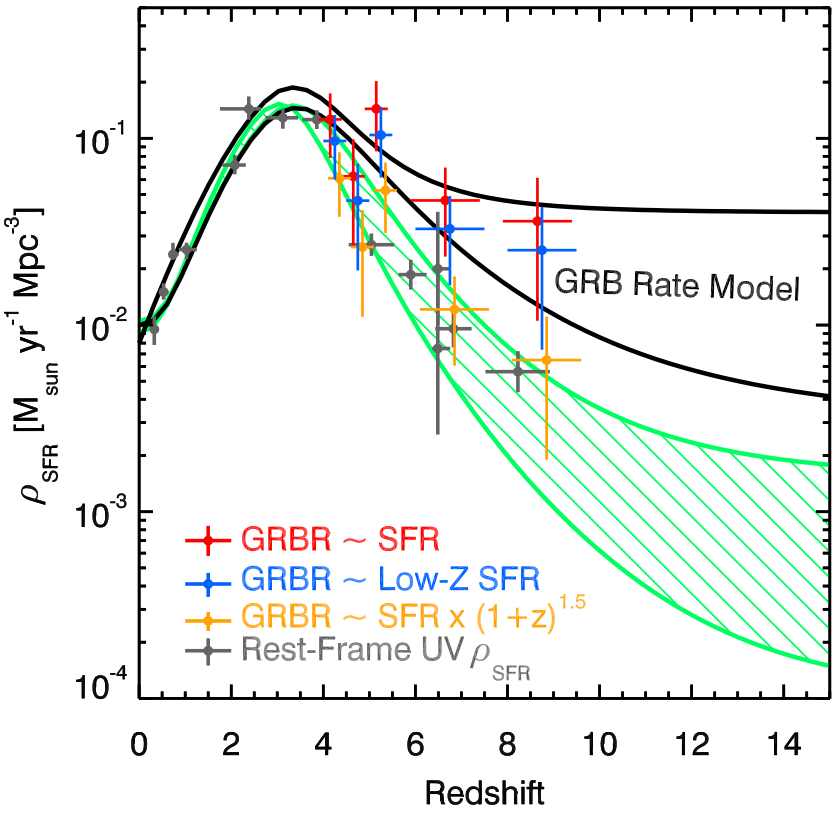

Figure 1.11: Cosmic star formation rate history as a function of redshift derived from UV-selected galaxies (gray circles) and predicted from GRB rates assuming various models (red, blue and yellow circles). (Robertson & Ellis 2012)

from massive stars occurred in galaxies below the current HST sensitivity limits. Moreover, compared to traditional methods using quasars, GRB afterglows offer the unique possibility to probe the cold or neutral gas in the galaxy via absorption lines, and after the fading of the afterglow, the possibility to probe later the galaxy composition using nebular emission.

At $z \sim 2$, the Lyman-α line (1216 Å) becomes accessible for ground spectrometers operating in the optical range. From the optical spectra of GRB afterglows at $z \gtrsim 2$, it is therefore possible to derive the neutral hydrogen column density ($N_{\rm HI}$) by measuring the depth of the absorption around the Lyman-α line (e.g., Tanvir et al. 2019). Furthermore, it is also common to find in their optical afterglow spectra narrow absorption lines from heavier elements such as carbon (C), silicon (S) or iron (Fe). By combining these lines with the estimate of $N_{\rm HI}$ it is possible to infer the metallicity of the gas in absorption within the distant system. A large sample of GRB afterglows at different redshifts thus offers the possibility to probe the chemical enrichment of the Universe independently of the luminosity of the

underlying galaxies (Fig. 1.10). Finally, the intrinsically basic form of the afterglow spectra (power law function) allows a direct measurement of the extinction law and its evolution across cosmic time (e.g., Bolmer et al. 2018), as well as the determination of the Lyman continuum (LyC) escape fraction of their host galaxy (Vielfaure et al. 2020).

As discussed earlier in 1.1.3, the formation of a long GRB is associated with the death of a massive star. Since massive stars consume their fuel very rapidly (< 50 Myr), the detection of a long GRB is related to recent star formation in its host galaxy. Considering the rate of GRBs as a function of redshift, long GRBs are therefore expected to trace the history of the cosmic star formation rate (Kistler et al. 2009; Robertson & Ellis 2012; Kistler et al. 2013; Wang 2013; Ghirlanda & Salvaterra 2022). The comparison between prediction of long GRBs and star-forming galaxies selected by their bright rest-frame ultraviolet (UV) emission is shown in Fig. 1.11. Their predictions differ at $z > 4$ where the star formation rate density is higher using the GRB rate as a direct tracer of star-formation. The exact reason for this deviation is not yet clear and is a subject of debate. Both tracers could suffer from biases causing an over- or underestimation of the true value. For more details about the use of GRBs as cosmic probes, the reader is referred to Schady (2017).

However, long GRBs also have possible drawbacks. The afterglow fades quickly after a few hours or days for bright events. This requires fast and efficient follow-up observations to be able to collect enough information and perform a detailed analysis of the event. In addition, the environment in which these events form can play an important role in their formation (e.g. metallicity) and cause a systematic bias that may impact their study. Proper consideration of these effects is crucial before drawing any firm conclusions from GRBs. In this context, the study of one of the possible effects influencing the GRB formation represents one of the objectives of this manuscript, and will be further discussed in Chapter. 2.

1.2 Long GRB host galaxies

With the discovery of X-ray emission and optical afterglows, the localization accuracy of the bursts was significantly improved. This considerably reduced the number of sources within the error radius and helped to identify the host galaxy. An unambiguous way to associate the GRB with its host galaxy is to measure:

(i) the redshift using fine-structure absorption lines of the afterglow, and (ii) the redshift using emission lines of the galaxy. The underlying assumption made when measuring the redshift on the afterglow is that the most distant absorbing system is the host galaxy. This hypothesis was confirmed by the detection of the variation of fine-structure lines which indicated that the GRB-to-cloud distance is about a few hundred parsecs (Prochaska et al. 2006; Vreeswijk et al. 2007, 2011). However, this method is often not feasible and the standard approach is to estimate the probability of chance coincidence (P_{cc}). For each host candidate within the error radius, the probability that the object is an unrelated galaxy given its magnitude is estimated (see also Sect. 2.2.3.2). The object with the lowest probability of chance coincidence is assigned as the host.

1.2.1 Scientific interests

It is now clear that long GRBs are extragalactic events, with the bulk of the population lying between a redshift of 1 and 3 (Fig. 1.8). Current telescopes capacity does not provide enough resolution to directly resolve their progenitors. Only for a few cases of very local events, studies with an effective spatial resolution of 150-250 pc were conducted using the MUSE instrument at the Very Large Telescope. Two of them showed that the explosion site is consistent with a young stellar population and a massive star progenitor of 20-40 $M_{\odot}$(Krühler et al. 2017; Izzo et al. 2017), but Tanga et al. (2018) found that the SN-less GRB 111005A occurred in a metal-rich environment with a small ongoing star formation constraining the mass of the progenitor below 15 $M_{\odot}$. For GRB hosts at a larger distance, spatially resolved studies are not possible and it is common to use global host properties as a proxy for the local GRB environment. From a sample of GRB hosts, one therefore expects to be able to constrain and infer key properties that trigger or enhance their formation mechanism.

1.2.2 Host galaxy properties

Seminal studies of long GRB host galaxy samples at $z < 1$ showed that GRB hosts were often faint, irregular, low-mass and star-forming galaxies (e.g., Sokolov et al. 2001; Le Floc'h et al. 2003; Christensen et al. 2004; Tanvir et al. 2004; Fruchter et al. 2006; Savaglio et al. 2009).

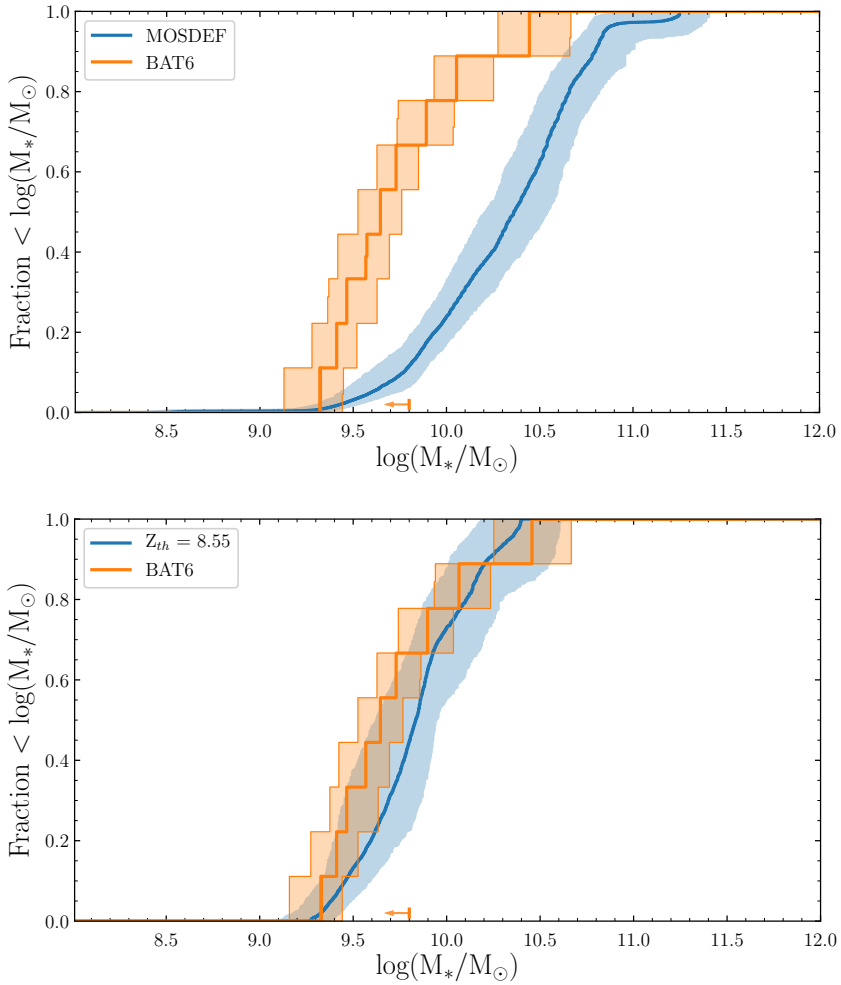

Figure 1.12: Cumulative distribution of stellar mass for the hosts of the BAT6 (orange) and the MOSDEF survey (blue). The top and bottom panels are identical, except that for the bottom panel only MOSDEF objects with a metallicity lower than $12 + \log(\mathrm{O/H}) = 8.55$ are used. (Palmerio et al. 2019)

Then, studies of the burst position within their host galaxy revealed that the GRB explosion site is often (i) centrally concentrated (low galactocentric offset), and (ii) spatially correlated with the bright star-forming regions of their hosts (Fruchter et al. 2006; Svensson et al. 2010; Blanchard et al. 2016; Lyman et al. 2017). Moreover, GRB hosts showed a preference for sub-solar metallicity galaxies (Modjaz et al. 2008; Graham & Fruchter 2013; Boissier et al. 2013; Graham & Fruchter 2017). The large number of well-localized GRBs detected by *Swift* enabled the construction of complete and unbiased samples of GRBs: TOUGH (Hjorth et al. 2012), BAT6 (Salvaterra et al. 2012) and SHOALS (Perley et al. 2016a). Their respective selection criteria vary from sample to sample, but in general, sources

were selected on the basis of their peak flux and favorable observing conditions (e.g., fast XRT localization, low Galactic extinction). In addition, the prompt emission properties do not correlate with the host galaxy properties (Levesque et al. 2010c; Japelj et al. 2016). Thus, their host galaxies are expected to be statistically representative of the entire long GRB host population and to enable the identification of possible biases in the GRB population. Based on these complete and unbiased samples, the bias toward low metallicity environment was confirmed at $z \lesssim 2$ (Vergani et al. 2015; Perley et al. 2016b; Palmerio et al. 2019). The Fig. 1.12 illustrates the preference of GRB hosts for low metallicity environments. At $1 < z < 2$, the cumulative distributions of stellar mass for the GRB hosts of the BAT6 sample and for the MOSDEF survey (Kriek et al. 2015) were compared. A metallicity cut on the MOSDEF sample of $12 + \log(\mathrm{O/H}) < 8.55$ reconciled the two distributions, which strongly suggests that the metallicity is a key regulatory factor to produce a GRB.

The location of the bursts in star-forming regions and the bias toward low metallicity are both consistent with the collapsar model where a massive, fast-rotating progenitor is crucial to produce an ultra-relativistic jet (e.g., Yoon et al. 2006; Woosley & Heger 2006). However, some GRBs were found in super solar metallicity galaxies (Levesque et al. 2010b; Schady et al. 2015; Perley et al. 2016b; Heintz et al. 2018). Their exact origin is not yet well understood. A possible explanation may be a local variation of the metallicity in the vicinity of the GRB site (Niino 2011). Alternatively, given that the metallicity estimate is often measured from strong emission lines such as oxygen, a high oxygen-to-iron ratio [O/Fe] could reconcile these constraints with the collapsar model (Hashimoto et al. 2018). Interestingly, this may also indicate the existence of another GRB formation scenario. Since only a few GRBs are concerned among the entire population detected so far, this channel would likely be marginal and involve a very particular set of parameters.

Earlier work also suggested a molecular gas deficiency in GRB hosts with respect to their star formation rate and stellar mass (Hatsukade et al. 2014; Stanway et al. 2015). This claim was then refuted by new ALMA observations that revealed no particular molecular gas deficiency (Arabsalmani et al. 2018a; Michałowski et al. 2018; Hatsukade et al. 2019, 2020). This suggests that the same mechanism of star formation occurs in GRB hosts and in typical star-forming galaxies.

Recently, a [C II] deficit was found in GRB 080207 host galaxy at $z \sim 2$ (Hashimoto

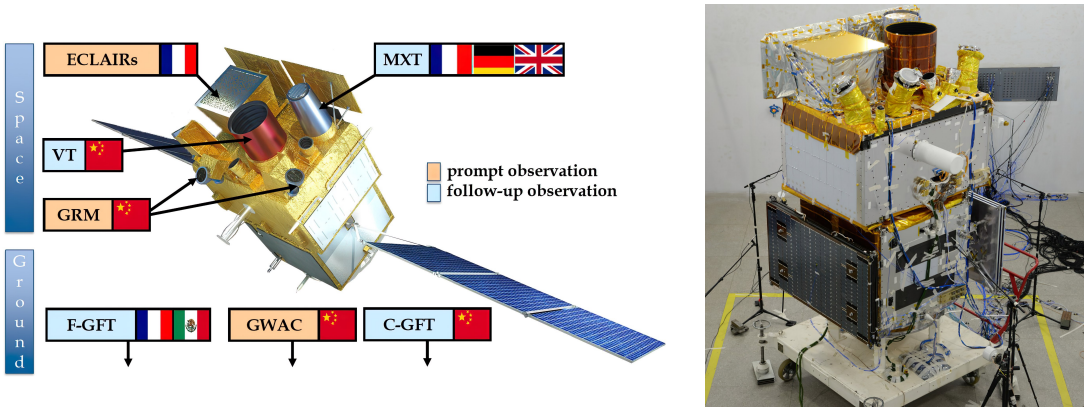

Figure 1.13: The SVOM satellite. *Left panel:* Artist view of the satellite with its onboard and ground telescopes. The names of instruments colored in orange are optimized to detect the prompt emission while instruments in blue are intended for the observation of the afterglow emission. *Right panel:* View of the SVOM qualification model satellite. (SVOM collaboration)

et al. 2019) and could be a new physical property of GRB hosts caused by the influence of the metallicity, IMF or gas density. This possible [C II] deficit needs to be confirmed on a larger sample.

Finally, GRB host galaxies were observed to have a smaller in size compared to typical star-forming galaxies of the field (Conselice et al. 2005; Fruchter et al. 2006; Wainwright et al. 2007; Kelly et al. 2014). Furthermore, they exhibit a preference for high stellar mass surface density and high star formation rate surface density at $z < 1$ (Kelly et al. 2014).

In that context, this thesis is part of the effort of using the global properties of GRB host galaxies to better understand the mechanism of GRB formation and quantify the possible bias in their production efficiency. This is a crucial aspect to establish the link between the long GRB rate and the SFR and thus their ability to trace the cosmic star formation history (Fig. 1.11).

1.3 SVOM mission

The *Space-based multi-wavelength astronomical Variable Object Monitor* (SVOM, Wei et al. 2016; Atteia et al. 2022) is a Chinese-French mission dedicated to the multi-wavelength study of GRBs. The mission concept is based on the success of *Swift* in which GRBs are detected by a wide field instrument and rapidly observed by two narrow field instruments (Fig. 1.13) to improve the burst localization. The

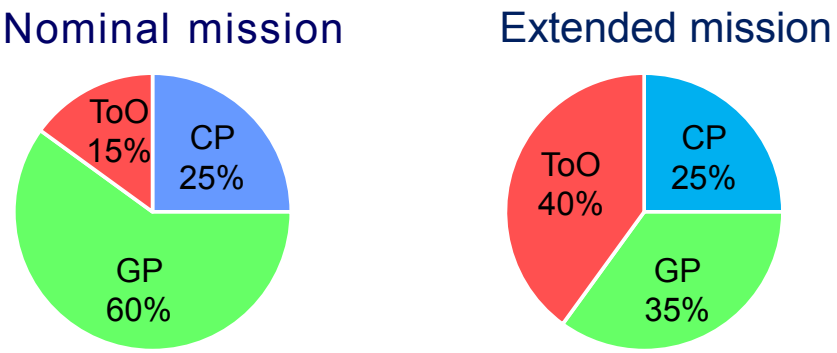

Figure 1.14: Fraction of SVOM observation time according to scientific programs for nominal mission (left) and extended mission (right). The General Program (GP), Target of Opportunity Program (ToO) and Core Program (CP) are colored in green, red and blue, respectively. (SVOM collaboration)

position of the burst will then be quickly transmitted to the ground in < 30 s for 65% of the cases for further follow-up observations and characterization of the source. The nominal lifetime of the mission is 3 years with an additional extension of 2 years.

In Sect. 1.3.1, a brief overview of the mission and its various objectives is presented. Then, the space segment and ground segment of the mission are described in Sect. 1.3.2. Finally, Sect. 1.3.3 discusses the additional synergy with ground telescopes that will improve the time and wavelength coverage of follow-up observations of SVOM alerts. For more details on the mission and its scientific perspectives, the reader is referred to the white paper of SVOM (Wei et al. 2016).

1.3.1 Mission overview

SVOM will have the ability to trigger on the vast majority of GRB types including underluminous, ultra-long GRBs, X-ray rich GRBs (XRR, $30 \leq E_{\rm peak} \leq 50$ keV) and X-ray Flashes (XRF, $E_{\rm peak} < 30$ keV). In this section, the fraction of SVOM time entirely devoted to the detection of new gamma-ray sources and other science programs are described. In addition, the optimized pointing strategy is discussed in order to achieve 2/3 completeness for the redshift measurement of the future SVOM GRB sample.

1.3.1.1 Observation time

The SVOM observation time is distributed into three main parts: the Core Program (CP), the Targets of Opportunity program (ToO), and the General Program (GP). The time split allocates a certain amount of time to each science objective that SVOM was designed to cover. For the extended part of the mission, the time allocated to the three programs will evolve compared to the nominal part of the mission, as shown in Fig. 1.14.

Core program This observation time covers the central objectives of SVOM. It is dedicated to the detection, localization and characterization of prompt and afterglow emissions from GRBs. When a burst is detected, the satellite will observe it for about 1 day (14 orbits). The expected rate of GRBs is about 60-70 per year, which represents a total of 25% of the SVOM available time. Between the nominal and extended phases, the fraction of allocated time will remain the same for this program. This will provide a sample of well-characterized GRBs with good temporal and spectral coverage, and distance measurement (redshift).

General program This program is open to scientists through a call for proposals. It will consist of using SVOM as a more standard space observatory and performing pre-planned observations. During the GP program, the sources will be observed for a minimum of one orbit ($\approx$ 45 min of effective observation, due to Earth occultations). The percentage of time will be about 60% during the nominal mission phase and will decrease to 35% during the extended phase.

Targets of Opportunity program It will offer the possibility to perform rapid unplanned observations of transient events and variable sources, detected by other facilities such as the Vera C. Rubin Observatory or LIGO/VIRGO. This mode is composed of three subclasses: ToO-NOM (nominal), ToO-EX (exceptional) and ToO-MM (multi-messenger alerts). Each subclass is defined by a given observation strategy, such as the delay before starting the observation or the duration of the observation (number of orbits). The allocation will increase from 15% to 40% between the nominal mission phase and the extended mission phase. This will provide more flexibility to take advantage of the opportunities offered by the new era of time-domain astronomy that will begin with the advent of new facilities

such as the Vera C. Rubin Observatory or Advanced LIGO, Advanced Virgo, and the Kamioka Gravitational Wave Detector (KAGRA).

1.3.1.2 Observation strategy

SVOM is scheduled to be launched in 2023 by a Chinese Long March 2C rocket from Xichang in China. The satellite will orbit with a period of 96 min at an altitude of 625 km and a declination of about 30°, which corresponds to a Low Earth Orbit (LEO). Several times per day, SVOM will cross an area where the Earth's magnetic field is weaker, the South Atlantic Anomaly (SAA). In this region, a large number of energetic particles are trapped and all instruments have to be shut down to limit the possible damage produced by these high energy particles. This leads to an overall dead time of ≈ 13-17% per day.
The SVOM pointing strategy (Cordier et al. 2008) will follow the so-called *B1 attitude law*. It consists in pointing the optical axis of SVOM instruments at a maximum of 45° of the anti-solar direction, avoiding bright X-ray sources (Sco-X1, galactic plane) in the field of view (FOV) of ECLAIRs and favoring the area of the sky directly observable from the large ground-based telescopes in Chile, Hawaii and the Canary Islands. This strategy will ensure that the detected source is observable from the nightside hemisphere by telescopes and will increase the chances of detecting a counterpart to infer a redshift of the GRBs. However, this attitude law has the drawback of reducing the duty cycle of the onboard instruments (down to 50-60%) since the Earth will occult the FOV of SVOM instruments during a part of each orbit.

1.3.1.3 Unique features

SVOM is a direct successor of the *Swift* and Fermi missions and is designed to compensate the limitations of previous GRB missions by adding new capabilities. First, the onboard instruments offer a wide energy coverage from 4 keV to 5 MeV, which enables triggering on the vast majority of GRB classes. In particular, its low threshold of 4 keV should provide a larger number of XRF and high-z GRBs than previous missions. In addition, the wide-field gamma-ray instrument is capable of accumulating and stacking images up to ≈ 20 min to improve the detection of (ultra-)long GRBs and high-z GRBs. Then, with the B1 attitude law and its

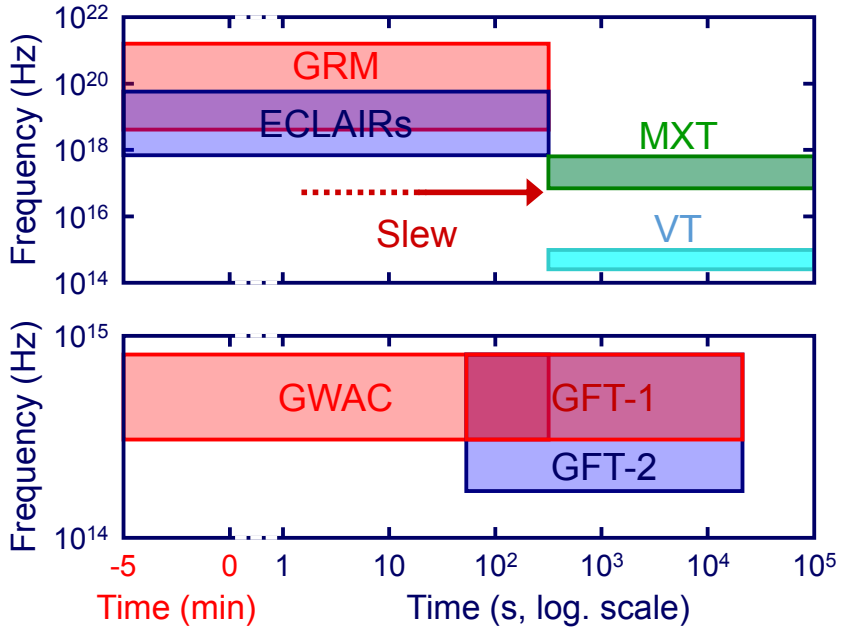

Figure 1.15: Spectral coverage of the SVOM instruments for the prompt and afterglow emissions of the GRB as a function of time. The top panel shows the space instruments and the bottom the ground telescopes. (SVOM collaboration)

dedicated follow-up using ground telescopes, the mission offers the unique feature of a continuous monitoring of the SVOM FOV at optical wavelengths. This will allow in particular to detect and characterize the prompt optical emission of GRBs and to better understand the central engine and the formation mechanism of this emission. Finally, the pointing strategy will ensure that large ground telescopes can quickly perform follow-up observations at optical and near-infrared wavelengths. This will provide well-characterized sources in time, wavelength and redshift (2/3 of the sample) and thus a more homogeneous and controlled GRB sample than obtained with the previous missions.

1.3.2 Scientific instruments

The specificity of the SVOM mission lies in the combination of space instruments and ground telescopes. The space segment is composed of four instruments with wavelength coverage from 200 eV to 5 MeV in the X-ray and gamma-ray domains and from 400 nm to 1000 nm in the visible, described in more details in the Sect. 1.3.2.1. A view of the on-board instruments and their implementation on the satellite can be seen in Fig. 1.13, and the spectral coverage as a function of time

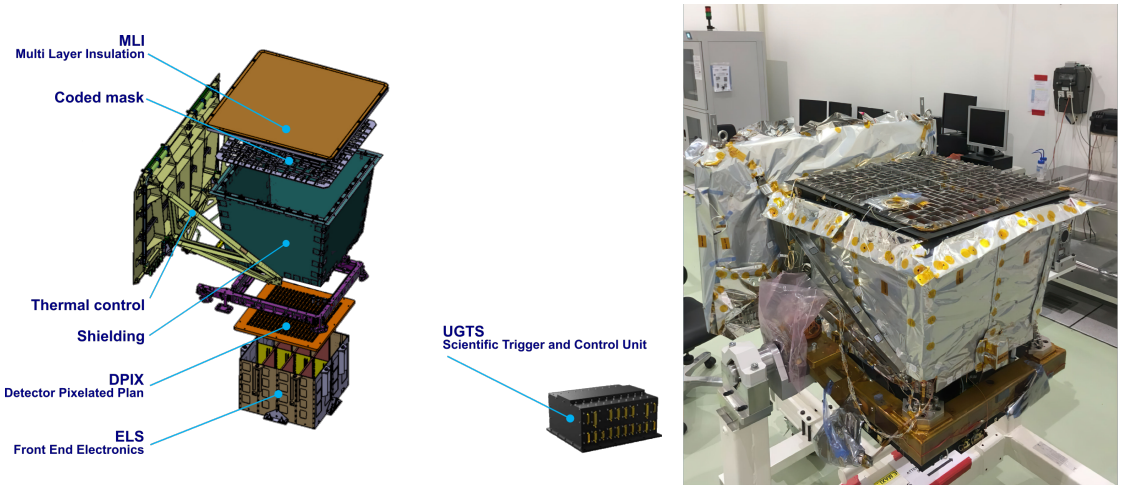

Figure 1.16: View of the ECLAIRs telescope, exploded view with the main components (left) and the structural and thermal ECLAIRs model (right) prior to qualification tests. (SVOM collaboration)

is provided in Fig. 1.15. The ground segment covers the optical and near-infrared bands from 400 nm to 1800 nm and is presented in Sect. 1.3.2.2.

1.3.2.1 On-board instruments

The SVOM mission is mainly a collaboration between Chinese and French laboratories. The responsibility for the four on board instruments was shared between the two countries (Fig. 1.13). An important constraint for the development was the limited allocated mass for the scientific payload ($\sim$ 450 kg). This led to a series of constraints on mass, volume, and power consumption that influenced the design of the instruments. A brief overview of the instruments is provided below.

ECLAIRs is a wide-field spectro-imaging coded mask telescope (Godet et al. 2014) on board SVOM. The focal plane is composed of 6400-pixel CdTe (Cadmium Telluride) detectors sensitive to γ-ray photons from 4 to 150 keV. ECLAIRs will scan the sky to find an excess of gamma-ray photons in the background signal. With its coded mask aperture, it will be able to detect the prompt GRB emission down to 4 keV and locate the source within 2 sr (89×89 deg^2) to an accuracy of about 13 arcmin for most sources (90%). The expected rate of GRBs detected by ECLAIRs is about 60-70 per year. It is one of the instruments under the technical and scientific responsibility of the French community and was developed

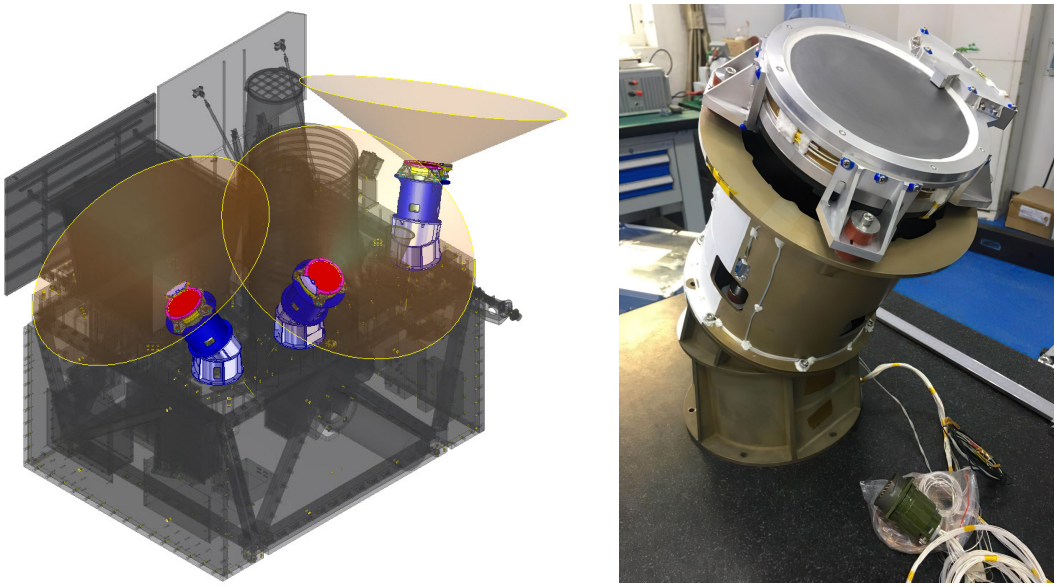

Figure 1.17: View of the Gamma Ray Monitor (GRM) instrument, 3D model of the instrument (left) and the qualification model of one of the gamma ray detectors (right) composing the GRM. (SVOM collaboration)

in collaboration between IRAP (PI), CEA Paris-Saclay, IAP, APC and CNES laboratories. An exploded view of the instrument with its main components is visible in the left panel of Fig. 1.16 and an image of the structure and thermal model of ECLAIRs is presented in the right panel.

GRM (Gamma-Ray Monitor, Dong et al. 2010) is a wide-field γ-ray detector with an energy range between 15 to 5000 keV developed by IHEP Beijing. It is composed of three detection modules (GRDs) made of NaI(Tl) (Sodium Iodide) scintillating crystal, a photomultiplier and its readout electronics. Each GRD has a FOV of $\pm$60 degrees around its central axis and a temporal resolution lower than 20 μs. The three GRDs have different directions to form a common FOV that matches the one of ECLAIRs (2 sr). GRM will be able to localize the bursts with an accuracy of 5 degrees. The rate of GRBs detected by GRM is expected to be higher than 90 per year. A 3D model and arrangement of the three GRDs is visible on the left panel of Fig. 1.17 and an image of the qualification model of one GRD is visible on the right.

MXT (Microchannel X-ray Telescope, Götz et al. 2014) is a narrow field spectro-imaging instrument focusing X-ray photons with a energy range of 0.2-10 keV. It is

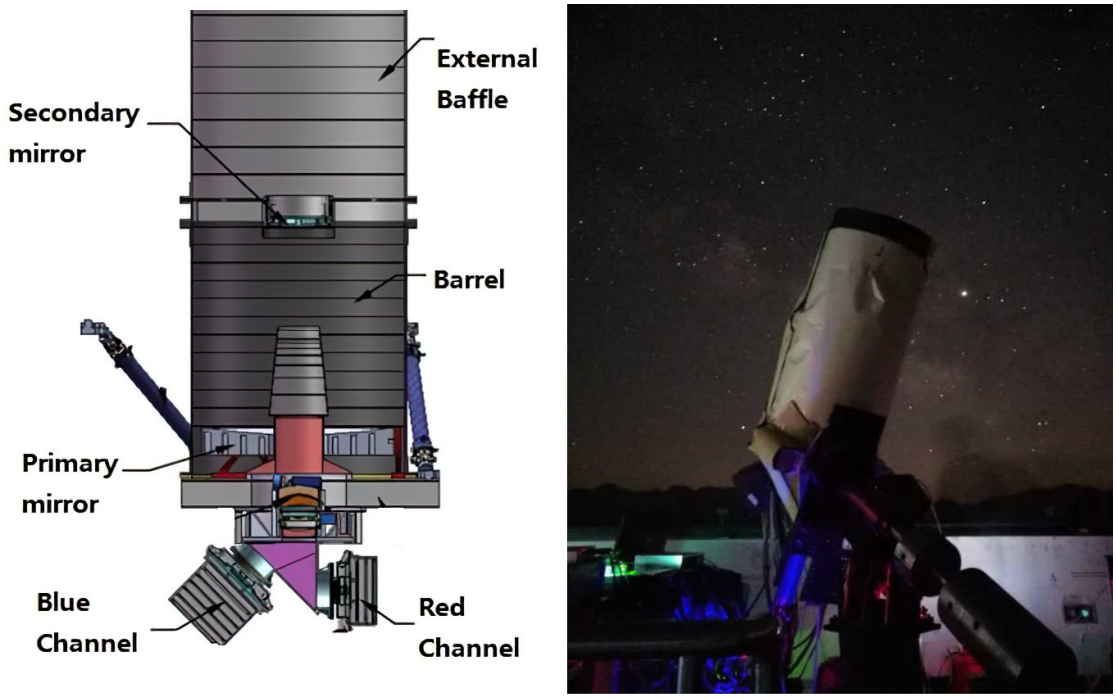

Figure 1.18: View of the Visible Telescope (VT) instrument, schematic diagram with its main components (left) and the qualification model of the VT (right) during the performance campaign at the Xinglong observatory in China. (SVOM collaboration)

a light (42 kg) and compact (1.2 m) instrument based on an innovative optics with a Lobster Eye design. MXT has a FOV of 58×58 arcmin^2 and a spectral energy resolution below 80 eV at 1.5 keV. It will observe the afterglow emission of GRB to monitor the X-ray light curve evolution and improve the ECLAIRs localization below 2 arcmin for most of GRBs. The instrument is under the responsibility of CNES and is developed in collaboration between the University of Leicester, CEA Paris-Saclay (PI), the Max Planck Institute for extraterrestrial physics and CNES laboratories. A more detailed description of the instrument and its scientific characteristics is provided in Sect. 3.3.4 and 4.1.

VT (Visible Telescope, Fan et al. 2020) is a 40 cm Ritchey-Chretien optical telescope composed of a blue channel (400-650 nm) and a red channel (650-1000 nm). The focal plane of each channel is composed of 2k $\times$ 2k CCD detectors, back-illuminated for the blue channel and deep-depleted for the red channel in order to increase the sensitivity at 0.9 μm. Its FOV of 26×26 arcmin^2 will cover the ECLAIRs error box in most cases and provide a localization < 1 arcsec for 80%

Figure 1.19: View of the GWAC system installed at the Xinglong Observatory in China. On the right part, some of the mounts are visible and on the left part, the 30 and 60 cm telescopes are shown. (SVOM collaboration)

of ECLAIRs GRBs. The VT can reach a limiting magnitude of $M_V = 22.5$ in 300 s of exposure and will detect GRBs up to $z \sim 6.5$ through its red channel. The instrument is under the responsibility of NAOC Beijing and XIOPM Xi'an. A schematic diagram with the main components is visible on the left panel of Fig. 1.18 and an image of the VT qualification model during observational tests is shown on the right.

1.3.2.2 Ground segment

Once a GRB is detected and located, the information is quickly transmitted to the ground via VHF antennas (Sect. 1.3.2.3). The SVOM satellite is then supplemented by a ground segment composed of optical and near-infrared telescopes. These systems will provide rapid follow-up to observe prompt optical emissions or estimate the photometric redshift of new events. This section presents the systems that are part of the SVOM mission and will be used routinely to perform follow-up observations of SVOM GRBs.

GWAC (Ground Wide Angle Camera, Xu et al. 2020; Wang et al. 2020) is a set of ground instruments imaging the sky down to R $\sim$ 16 mag at a cadence of 15 s. It is composed of several units each carrying 4 wide-angle optical cameras (JFoV) with a diameter of 18 cm and a small photographic camera (FFoV) with a diameter of 3.5 cm. The JFoV camera has a wavelength coverage from 0.5 to 0.85 μm and a FOV of 150 deg^2. Four units were installed at Xinglong Observatory in China (right part of Fig. 1.19) and additional units will be installed before the launch of SVOM. This will provide a total coverage of about 5000 deg^2 and offer

Figure 1.20: View of the two SVOM ground follow-up telescopes. The French ground follow-up telescope (left), also named COLIBRI, during tests at the Observatoire de Haute Provence (OHP) in France. The Chinese ground follow-up telescope (right panel) installed at the Jilin observatory in China. (SVOM collaboration)

the possibility to simultaneously search for the optical prompt emission within the ECLAIRs FOV. Early observations have demonstrated the ability of GWAC to be used and to detect transient events (Turpin et al. 2020; Wang et al. 2020; Xin et al. 2021). In addition, the system is complemented by two identical 60 cm and one 30 cm diameter telescopes to perform rapid follow-up and further characterize the transient candidates (left part of Fig. 1.19).

GFTs (Ground Follow-up Telescopes) is a network of two robotic telescopes capable of observing in less than a minute the transient alerts sent by SVOM. The F-GFT (also called Colibri, Basa et al. 2022) that will be installed in Mexico and the C-GFT installed in China are separated by about 120° in longitude in order to increase the probability of an immediate observation following a SVOM alert. An image of Colibri is shown in the left panel of Fig. 1.20 and an image of C-GFT in the right panel. The two telescopes have similar characteristics: (i) C-GFT has a primary mirror of 1.2 m, an FOV of 21×21 arcmin^2, a wavelength coverage of

400 to 900 nm, and an R-magnitude limit of 20 mag in 300 s (ii) Colibri has a primary mirror of 1.3 m, a FOV of 26×26 arcmin^2, a wavelength coverage of 400 to 1800 nm, and an R-magnitude limit of 22 mag in 300 s. Both will provide a localization < 1 arcsec. In addition, Colibri will be able to infer a photometric redshift of the source with 10% accuracy for GRBs at $3.5 < z < 8$ (Corre et al. 2018a)

1.3.2.3 VHF alert network

Once a new source is detected and validated onboard by the satellite, a signal is quickly sent to the ground by two onboard VHF antennas. The signal will be received by one of the ~ 45 VHF antennas distributed in the $\pm 30°$ latitude range of the satellite. The alert is then transmitted to the French Scientific Center (FSC) which will format the information to be sent as a GCN and VOEvent. The alert will therefore be quickly shared with the whole community and will ensure an efficient follow-up of the source.
It is worth noting that another communication system (Beidou system, Li et al. 2021) can be used to send short commands to the satellite, for example to quickly start a ToO observation for a high priority transient event.

1.3.3 Follow-up observations

Follow-up observations are a key aspect of the SVOM mission and have to be performed by dedicated optical facilities within minutes or hours after trigger in order to maximize the information collected from the transient source. These observations are used to determine the nature of the source and further characterize it by improving its location, monitoring its light curve over time, inferring its distance, or measuring its spectrum. As mentioned in 1.3.2.2, several facilities are being developed as part of the SVOM mission to provide and ensure a minimal ground follow-up of SVOM alerts. However, the overall coverage of these facilities is limited and observations from the ground are often subject to the observation conditions. For these reasons, the SVOM collaboration has initiated several partnerships with large ground telescopes to complement its strategy and complete the wavelength and time coverage of alerts. The current status of these collaborations are summarized in Fig. 1.21. There are two main types of partnerships: private

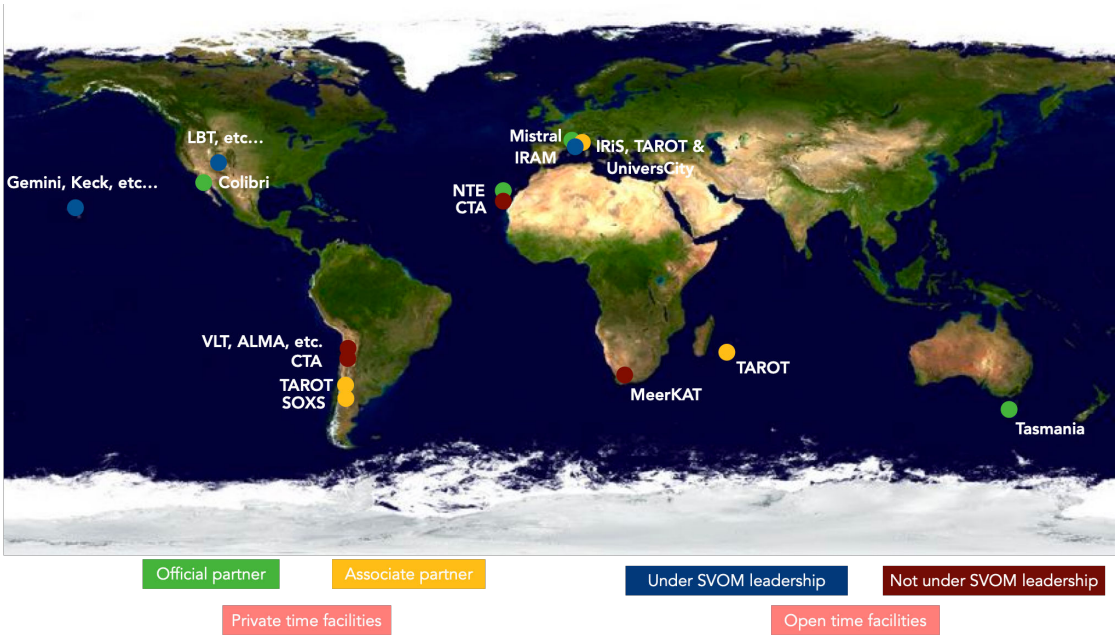

Figure 1.21: Current coverage of ground telescopes that could be used to perform follow-up observations. The colors show the different agreements with the facilities. (SVOM collaboration)

time facility or open time facility. In the first case, SVOM has a guaranteed allocated time to observe the SVOM alerts. In the second case, facilities are open to the whole scientific community and proposals have to be submitted to grant observational time (typically for 6 months or 2 years in the case of large programs). For the private time partnership, two types of agreements are defined: an official partner or an associate partner. The official partner agrees to respond to a significant fraction of the alerts and the collected data are considered as SVOM data and pushed to the SVOM database (SDB). In return, the facility has the same rights as a Co-I and can access to SVOM science products. In contrast, the associated partner responds on a voluntary manner to alerts and a specific agreement defines the rights on the collected data.

For the open time facility, the proposal may be led by a SVOM Co-I (collaboration under SVOM leadership) and the data collected is pushed to the SDB. If the proposal is independent of SVOM, the collaboration is not under SVOM leadership although some SVOM Co-Is may be part of the proposal. In this case, no other proposal is generally accepted on this scientific topic by the facility. The SVOM Co-I members have to respect the rules defined by the team leading the proposal. Recently, two new official partners have joined the SVOM follow-up collabora-

tion, the NOT Transient Explorer (NTE) instrument and the Son Of X-Shooter (SOXS) instrument. The NTE is a new instrument mounted on the 2.5 m of the Nordic Optical Telescope (NOT). The design of the instrument is inspired by the X-Shooter instrument mounted on the Very Large Telescope (Sect. 3.2.3.2). The instrument is composed of three arms (UV, VIS and NIR) and provides an intermediate resolution spectrum from 320 nm to 2.4 μm. The NTE is an official partner of SVOM and offers 80 nights of observations over 3 years. SOXS is a new spectrograph instrument installed on the 3.5 m New Technology Telescope (NTT) at ESO's La Silla Observatory (Chile). It is dedicated to the follow-up observation of transient and variable sources in a wavelength range between 350 to 2000 nm and with a spectral resolution of R $\sim$ 4500. SOXS is an associate partner of SVOM and the agreement ensures that all SVOM alerts will be observed by SOXS and that the redshift measurements will be shared with the SVOM Co-Is. Finally, a new project of follow-up observations was initiated on the MISTRAL instrument of the T193 at OHP. It is a collaboration on an open-time facility under SVOM leadership. The science topic of the proposal and first results are further discussed in Sect. 3.2.2.

1.4 Structure of the manuscript

This manuscript is composed of three main parts, revolving around the preparation of the forthcoming SVOM mission in the long, medium and short term. In the first part (Chapter 2), I present my work on the analysis of a sample of long GRB host galaxies to determine how the properties, in particular, the size and density of the galaxy could influence the formation mechanism of these phenomena. This study contributes directly to the effort of better understanding the efficiency of GRB production and their use as a tracer of star formation through the cosmic age. The analysis of the GRB host galaxies requires a complete, homogeneous and well-characterized GRB sample (e.g. position, redshift measurement) to minimize possible selection effects and biases that might be present in the GRB sample. In this context, an important aspect of the SVOM mission is the synergy between the observations from space and from the ground telescopes to maximize the amount of information collected for each burst. In the second part (Chapter 3), I report my work on the development of the SVOM follow-up network and how these observations are crucial to better characterize the GRB through its afterglow emission

and thus obtain insights into the near environment of the GRB within the host galaxy. Finally, SVOM will perform systematic follow-up observations of the GRB X-ray counterparts with the MXT instrument on board the satellite. In the third part (Chapter 4), I present my work on the preparation of the scientific exploitation of the MXT data. Specifically, I discuss the spectral calibration of the MXT flight model instrument and how a careful processing of the data can provide high quality products to perform reliable scientific analysis.

Chapter 2

Exploring the stellar density of long gamma-ray burst host galaxies

Contents

In this chapter, I present my work on the stellar density of galaxies that hosted a long gamma-ray burst. The challenge of this study lies in the limited number of GRB hosts with sufficient material to perform such an analysis. To derive the stellar density, it is necessary to have a variety of information about the GRB as well as its host galaxy, which is not always available. First, the burst has to be localized with a precision of a few arcseconds to ensure the association of the source and the host galaxy. Then, the distance (i.e., redshift) of the GRB is crucial in order to convert the observables into physical quantities. This is usually measured by large ground-based telescopes equipped with a spectrometer capable of detecting either absorption lines on the GRB afterglow or emission lines from the host galaxy, or both. In addition, the host galaxy has to be observed in several bands, from optical to FIR (in the ideal case) to estimate a robust estimate of the stellar mass and star formation rate. Finally, the estimate of the galaxy size requires a high resolution image to assess the best possible value. After reviewing the general context of this work in Sect. 2.1, the analysis and results for a sample of GRB hosts at $1 < z < 3.1$ are presented in Sect. 2.2. Then, Sect. 2.3 describes the additional tests performed to get reliable galaxy sizes and complementary properties of the GRB host samples at $z < 1$ and $1 < z < 3.1$.

2.1 General context

In this section, I present the scientific landscape, instrument, and tools used to study the stellar density of a GRB host sample. I first discuss the motivation and previous work related to this study. Then, the instrument used to image the galaxy and the 3D-HST survey are presented. Finally, the morphology of galaxy, possible observational effects on their structure, and the different measurement methods for modeling a galaxy are described.

2.1.1 The Hubble Space Telescope

The Hubble Space Telescope (HST) is a space telescope orbiting at low Earth orbit with an altitude of $\sim$ 550 km and an inclination of 28.5°. It was launched in April 1990 by the Space Shuttle Discovery from the NASA's Kennedy Space

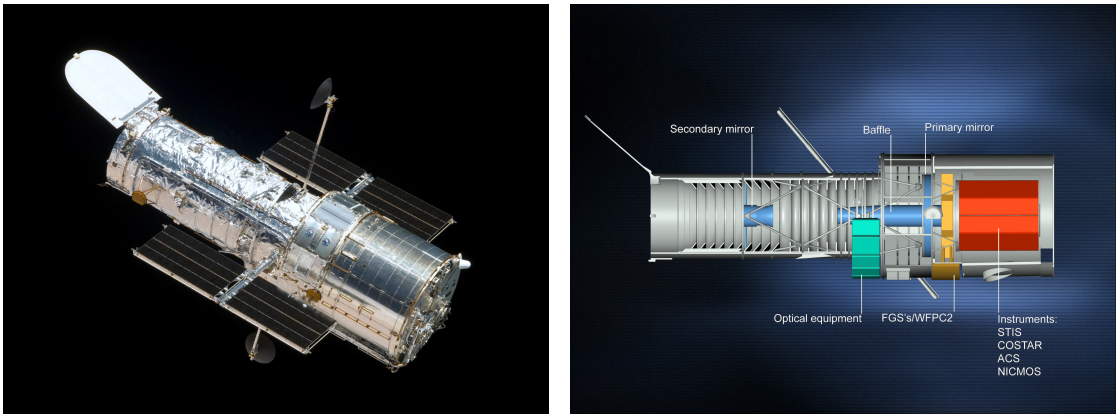

Figure 2.1: *Left panel:* Picture of the HST in 2009 after the fifth and final servicing mission. *Right panel:* Cross-section of the HST. The primary mirror ($\varnothing$ 2.4 m) and secondary mirror ($\varnothing$ 0.3 m) are visible in blue. The radial and axial instrument bays are shown in yellow and red, respectively. The WFC3 is installed in one of the four radial bays on the sides of the telescope. (Credit: NASA, ESA)

Center. Hubble is composed of a 2.4 m diameter, f/24, primary mirror and five main instruments (Fig. 2.1) covering the wavelength range from Ultraviolet (UV) to Near-Infrared (NIR). A few weeks after the successful launch, Hubble's first images showed stars (i.e., point-like sources) surrounded by a large halo of light. The problem was identified as a spherical aberration due to the wrong shape of the primary mirror[1]. For instance, the middle panel of Fig. 2.2 illustrates the blurring effects observed due to the spherical aberration. Beforehand, Hubble was designed to be repaired, maintained, and upgraded with new cameras and detectors by astronauts during in orbit operations. The first servicing mission solved the optical problem by sacrificing one of the instruments and installing instead the Corrective Space Telescope Axial Replacement (COSTAR). By 2002, all instruments requiring COSTAR were removed and replaced by instruments equipped with their own corrective optics. From 1993 to 2009, a total of five servicing missions have maintained Hubble's performance and improved the instruments with new available technologies, making it continuously competitive over the years. The instruments currently installed and in operation are the following:

- ACS - Advanced Camera for Surveys
- COS - Cosmic Origins Spectrograph

[1]The primary mirror was perfectly smooth but too shallow toward its outer edges by 2 μm. As a result, the outer edge of the PSF was blurred and mostly affected observations of faint and diffuse objects.

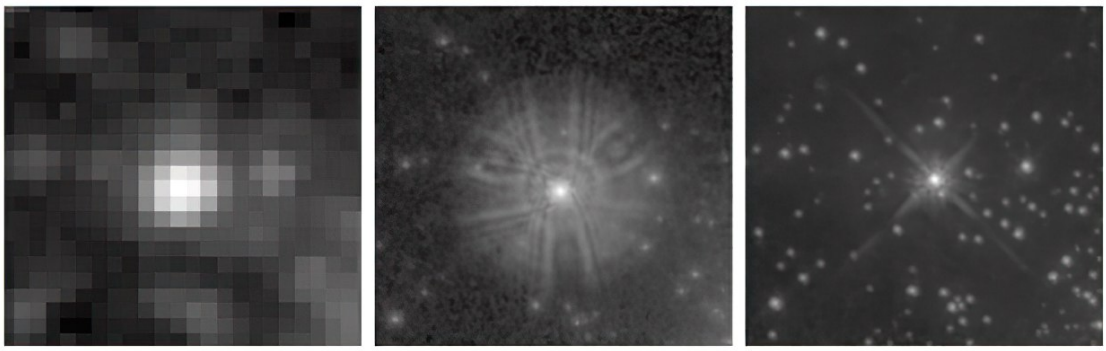

Figure 2.2: Image of the same star field in 30 Doradus (Melnick-34 at the center) with a ground-based telescope under ideal conditions and a resolution of 0.6″ (*left panel*), with the WFPC1 camera before the correction of the Hubble's spherical aberration where a 4″ diameter "skirt" around the central star is visible (*middle panel*), and after the installation of the corrective optics with a resolution of about 0.05″ (*right panel*). Images correspond to a square region of 7 arcseconds. (Credit: NASA)

- STIS - Space Telescope Imaging Spectrograph
- WFC3 - Wide Field Camera 3
- FGS - Fine Guidance Sensors

The ACS is an optimized imaging camera to survey large sky areas from the UV to the NIR (115 - 1050 nm) regions of the spectrum. It is famous for the exceptional images captured of the early universe, e.g., the Hubble Ultra Deep Field (HUDF). ACS is composed of three channels, the Wide Field Channel (WFC), the High-Resolution Channel (HRC), the Solar Blind Channel (SBC). Among them, the most used channel is the WFC due to its large spectral range (350 - 1100 nm) and large effective FOV of 202×202 arcsec^2. The HRC could not be repaired during the servicing mission 4 and is now disabled. The COS is an UV spectrograph covering with two channels the UV light from 90 - 320 nm. It is designed to observe faint, point-like UV sources such as hot stars and quasars, and study the large-scale structures and warm-hot ISM. The STIS is an imager and spectrograph of three detectors complementary to the COS covering a wavelength range of 115 - 1000 nm. It has the ability to observe and get simultaneous spectra from different points across the image. STIS offers the possibility to study black holes, massive stars, IGM and the atmosphere of exoplanets. The WFC3 is an imager configured with two channels, the Ultraviolet-Visible (UVIS) channel from 200 - 1000 nm and the NIR channel from 850 - 1700 nm. It also provides a slitless low-resolution

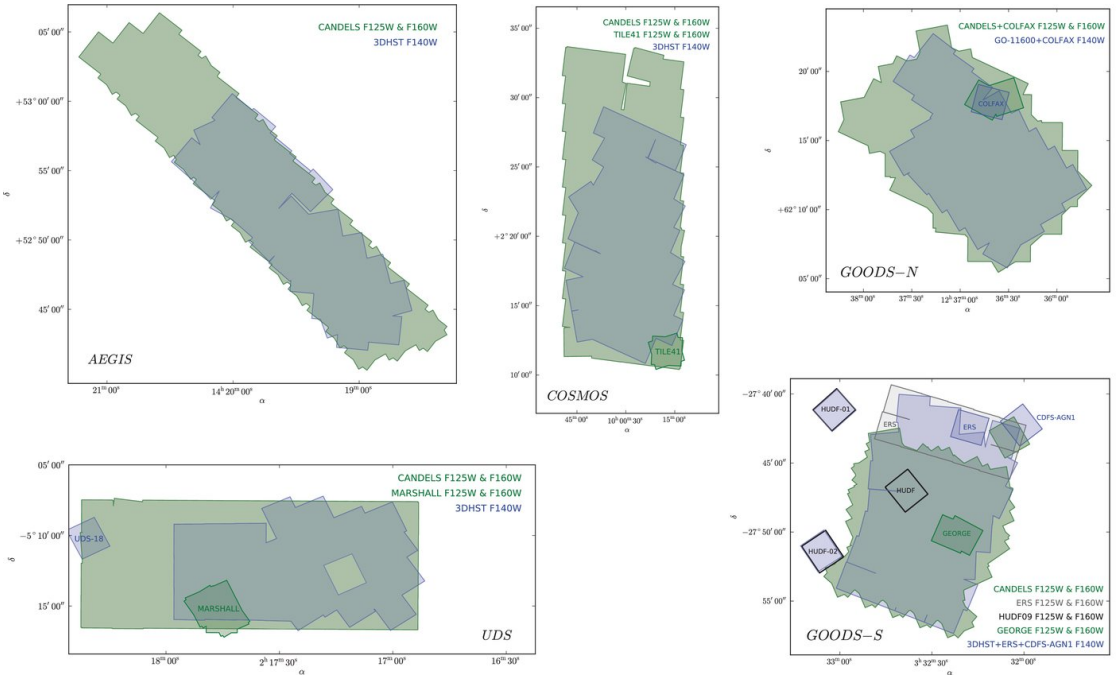

Figure 2.3: Layout of the five extragalactic fields observed with the HST/WFC3 during imaging surveys such as CANDELS or 3D-HST. North is up and East is to the left. (Skelton et al. 2014)

spectroscopy mode using prisms and grisms for both channels over the entire FOV of detectors. The high resolution and the large field of view of the WFC3 coupled with the ACS offer the possibility to observe and probe the distant universe from UV to NIR. Together, they have deeply contributed to revolutionize our vision of the local and very distant universe. The FGS consists of three sensors, two of them are used to accurately measure the position of the guide stars and correct for pointing drift relative to the target position, and the third is dedicated to scientific research for stars (measure relative positions, brightness variations and resolve double-star systems). Note that a sixth instrument is present on board the HST but inactive since 2008, the Near Infrared Camera and Multi-object Spectrometer (NICMOS), an imager and spectrometer covering wavelengths between 0.8 and 2.4 μm.

2.1.2 The CANDELS/3D-HST survey

In astrophysics, a survey defines a project to observe a given part of the sky and collect imaging and/or spectroscopic data. Because the observing time of

a telescope devoted to a given area is always limited, one of the dilemmas for allocated time is to opt for a very deep observation of a small area or a shallower observation of a wide area. An important characteristic of a survey is its limiting magnitude ($m_{\rm lim}$) or *survey depth* defining the limit beyond which a galaxy is not properly detected. This is directly related to the concept of *completeness limit* which indicates the percent of galaxies that the survey is able to detect with respect to the total population. This completeness can be defined in many ways, such as a function of observational quantities (e.g., fluxes) or physical properties of galaxies (e.g., stellar mass, SFR). For instance, using the HST/ACS camera, the Ultra Deep Field (UDF) is a 10 arcmin^2 survey with a limiting NIR magnitude of 29 - 30 mag, while the Cosmic Evolution Survey (COSMOS) is a wider survey of 2 deg^2 with a $m_{\rm lim} \approx 24$ - 26 mag. The wavelength probed by a given filter is affected by the distance from the source (i.e. redshift). Depending on the main scientific objectives of the survey, the selected photometric filter might play a crucial role (See the discussion on the effect of the probed rest-frame wavelength in Sect. 2.1.3.2). For example, to detect and characterize very high redshift galaxies, IR filters are more appropriate than optical or UV filters. It is worth mentioning that the limiting size and depth in galaxy surveys cause systematic effects (i.e., biases) on the observed galaxy population. Ignoring these systematic uncertainties can lead to an incorrect interpretation of the results and wrong conclusions. The two main biases caused by the limiting flux of surveys are the *Malmquist* bias (Malmquist 1922) and the *Eddington* bias (Eddington 1913). The former appears as galaxies with a flux fainter than the limiting flux are not detected, which implies that for a given sample, more luminous sources can be detected at larger distances. The identified objects are therefore only a subsample of the total galaxy population. The latter results from the measurement errors of galaxy properties (e.g, luminosity, stellar mass) around their true value. For example, considering a population of galaxies divided into magnitude bins, the error in the magnitude estimate implies that a fraction of the objects in one bin is moved to an adjacent bin. This bias particularly affects the sample when the number count density is very steep. Finally, the cosmic variance bias (e.g., Blanton et al. 2003) is a consequence of the limited sky area covered by the survey. Because galaxies are clustered in 3D space, surveying a region of low- or high- density can induce a variation on the galaxy number counts which is crucial for determining the galaxy luminosity or mass functions. To limit these possible biases, the strategy often adopted is to combine multiple and close

observations of the same area to improve the size, depth, and wavelength coverage.

The Cosmic Assembly Near-infrared Deep Extragalactic Legacy Survey, (CANDELS, Grogin et al. 2011; Koekemoer et al. 2011) is a multi-wavelength deep imaging survey consisting of 902 orbits ($\sim$ 60 continuous days) of HST completed between 2010 to 2013. The survey was designed to study the galaxy evolution between $z \sim 1.5$ to 8 and characterize Type Ia SNe at $z > 1.5$. The program targeted five well-studied extragalactic sky regions: the All-wavelength Extended Groth Strip International Survey (AEGIS) field, the Great Observatories Origins Survey (GOODS) Northern and Southern fields (GOODS-North and GOODS-South), the Ultra Deep Survey (UDS) field, and the COSMOS field. The observations were performed in a variety of filters (from 0.27 to 1.6 μm) with the WFC3 IR and UVIS channels, in parallel with the ACS WFC channel. The CANDELS layout and coverage with the WFC3 filters (e.g., $F140W$, $F160W$) are visible in green color in Fig. 2.3. CANDELS/Wide covered a total area of approximately 800 arcmin^2 for a $m_{\rm lim}(F160W) \approx 27$ mag at 5σ. Among which, CANDELS/Deep covered 125 arcmin^2 and reached $m_{\rm lim}(F160W) \approx 28$ mag. CANDELS has detected more than 250,000 objects and has significantly contributed to a better understanding of the critical period of galaxy evolution at $1 < z < 3$. However, an important limitation of the survey was the lack of a third dimension (i.e., redshift), the metallicity, and SFR for the detected sources. This gap was filled by the spectroscopic 3D-HST survey (Brammer et al. 2012; Skelton et al. 2014; Momcheva et al. 2016) which consisted of surveying with 248 orbits of HST the same five fields as CANDELS. The observations were performed with WFC3/G141 grism and ACS/G800L grism, and covered a total of $\sim$600 arcmin^2. The results provided for a large fraction of objects a spectroscopic redshift, which allowed to estimate galaxy properties (e.g., stellar mass, rest-frame photometry) with a better accuracy. The combined CANDELS and 3D-HST surveys is currently, and at least until the forthcoming first JWST survey, the optimal and most appropriate survey to study the evolution of galaxies at $1 < z < 3$.

2.1.3 Galaxy morphology

Once the extragalactic nature of galaxies was firmly established and a collection of objects was available, astronomers began classifying them into subsamples based

on their physical properties. This is the first and most natural step in understanding a population, as it has been done for animals or insects on Earth. In addition, it is now clear that galaxies evolved over time, particularly at $1 < z < 3$ where galaxy activity reached its maximum (Madau & Dickinson 2014). However, the processes or forces responsible for the formation of galaxies and their properties are not clear. Studying galaxy morphology offers an interesting way to trace these processes and better understand them. In this section, I will briefly review the different classification methods, the caveats and precautions that the classification of galaxies requires, as well as more recent methods for studying the structural properties of galaxies. Additional details on galaxy evolution and morphology can be found in the review of Conselice (2014).

2.1.3.1 Classification of galaxies

The first classification of galaxies was established from a visual inspection of 400 local galaxies by the astronomer Edwin Hubble (Hubble 1926, 1936). He was the pioneer and the first to distinguish three major classes of galaxies (elliptical, spiral and irregular), which is now known as the Hubble sequence. Later, the Hubble classification was revised and expanded with additional and intermediate classes (e.g., lenticular) by de Vaucouleurs (1959). During the same period, it was progressively established that physical properties of local galaxies correlate with morphology (e.g., Holmberg 1958). It was observed that spiral galaxies are blue, low-mass and star-forming, while elliptical galaxies are massive, red and form only a small amount of new stars. In the local universe, the fraction of spiral, elliptical or lenticular, and irregular or peculiar galaxies is about $\sim 61\%$, $\sim 34\%$, and $\sim 5\%$, respectively (de Vaucouleurs 1959). Note that, regarding the stellar mass distribution, the fraction is quite different, and spheroid-like[2] galaxies count for 73% of the total mass budget (Fukugita et al. 1998). The evolution of the Hubble sequence with the redshift is not yet well established, mostly due to the limited angular resolution and the rest-frame wavelength range probed for galaxies at $z > 3$ by current instruments, see Sect. 2.1.3.2. It was found that at $z < 0.3$ the Hubble sequence as observed in the local Universe, with the modern form of spirals and ellipticals, is in place (Abraham & van den Bergh 2001). Then, at

[2]It regroups objects with a round or elliptical shape and a dense core such as elliptical and lenticular types.

higher redshift, the detailed features (spirals arms, bulges and bars) are less and less visible. For this reason, galaxies are only classified into three major types: disk-like, spheroid-like or peculiar. It was observed that the fraction of spirals and ellipticals is progressively reduced with z in favor of peculiar and clumpy galaxies, which become dominant at $z > 2$ (Mortlock et al. 2013). However, preliminary results from deep imaging of the galaxy cluster SMACS 0723 by the JWST showed that some aspect of the Hubble sequence such as the existence of spheroid-like and disk-like objects, might be already in place at $z \sim 6$ (Ferreira et al. 2022).

2.1.3.2 Observational effects

It is important to keep in mind that the structure and the morphology of a given galaxy depends on several observational effects. I will present here a non-exhaustive list of the possible biases that the analysis and the conclusions drawn from the image of an object may suffer.

Projection effect Galaxies move in a three-dimensional space while the images collected by a space or ground-based telescope are a projection of the object in a two-dimensional space. This means that all galaxies are observed from a certain viewing angle defined by our position in the Universe. Using a parametric approach (see Sect. 2.1.3.3), the galaxy size is given by the major axis effective radius of the object. Therefore, a spiral galaxy seen face-on has an apparent size smaller than a spiral galaxy seen edge-on. For instance, this is the proposed explanation by Mowla et al. (2019) for compact and massive star-forming galaxies observed at $z \sim 2.5$. Although this effect may cause a part of the dispersion observed in the size-mass plane, it is likely marginal at high redshift since the galaxies are more often peculiar, perturbed and less structured.

Wavelength probed The morphology of a galaxy depends strongly on the wavelength. This is clearly illustrated by Fig. 2.4 where several objects are shown for the F775W and F160W filters. For distant galaxies, the former probes the rest-frame UV morphology and the latter the rest-frame optical morphology. This effect is called *morphological K correction* by analogy to the K correction factor. The immediate consequence is that the size of a galaxy is not unique and depends on the properties of the rest-frame emission probed by the filter that has been used.

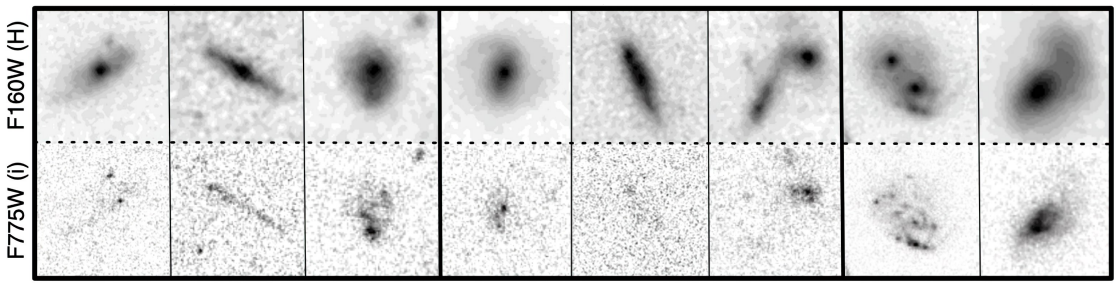

Figure 2.4: Comparison of randomly selected HUDF galaxies observed with the WFC3/IR (top) and ACS (bottom) cameras. Three different types of objects are visible separated by a thick black line, from left to right: spheroid, disk and merger. (Grogin et al. 2011)

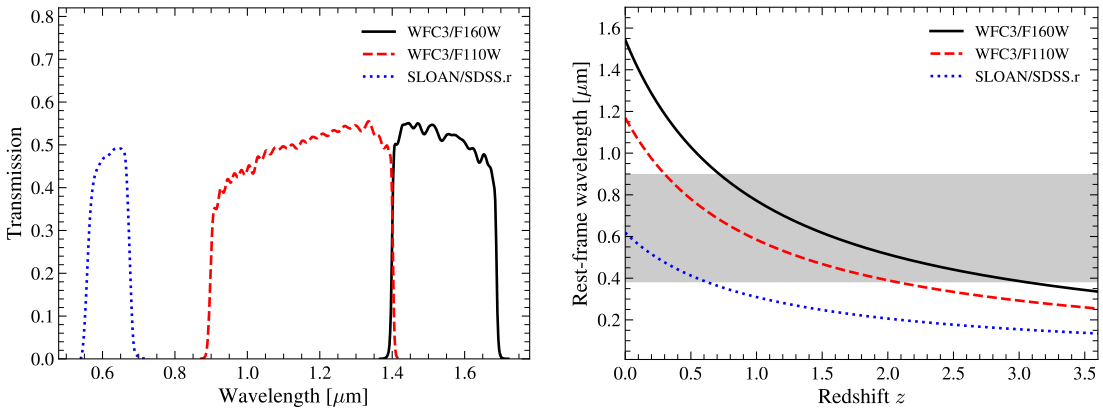

Figure 2.5: *Left panel:* Transmission curves for the WFC3 $F160W$ (black) and $F110W$ (red) filters, and the SDSS red filter. *Right panel:* Rest-frame wavelength probed by λ_{mean} for the filters presented in the left panel as a function of redshift. The gray area shows the rest-frame optical light of galaxies from 0.38 to 0.9 μm.

This morphological variation with wavelength is caused by two reasons. The first is the distinct color and light emitted by stellar populations. UV light is produced mostly by star-forming regions composed of young, massive, blue O stars, while NIR light is emitted by old, low-mass, red stars. Young stellar populations are often observed sporadically (e.g., in spiral arms) in the galaxy, while old stellar populations are observed more dispersed from the bulge to the disk due to their longer lifetimes. The second is the extinction caused by dust. Dust preferentially absorbs UV light and can therefore influence the apparent morphology of a galaxy. Spiral galaxies that are composed of a larger fraction of young stellar populations and dust are generally more affected by these morphological effects. These galaxy are seen clumpy and irregular in UV, and smoother in the NIR. In contrast, elliptical galaxies appear to be less subject to this variation because of their more

homogeneously distributed population of old stars in the galaxy. It is commonly accepted that the rest-frame optical redder than the Balmer break (3646 Å) is a good compromise to probe the true stellar mass distribution (mixture of stars at different ages) and measure a realistic size of galaxies.

To determine the size of GRB host galaxies, I have used HST data from the WFC3 instrument in the IR band. The two commonly used filters were the $F160W$ and $F110W$. Their transmission curves can be seen in the left panel of Fig. 2.5. The observed wavelength range falls in the NIR and the mean wavelength is ~ 1.54 μm and ~ 1.16 μm for $F160W$ and $F110W$, respectively. The redshift distribution of the GRB host sample considered in the analysis is spread between 1 to 3. The right panel of Fig. 2.5 shows the rest-frame λ_{mean} probed as a function of redshift up to $z = 3.5$. The optical wavelength range (0.38 - 0.9 μm) is illustrated as a gray area. For the GRB host sample, this confirms that the optical rest-frame wavelengths are properly probed by the WFC3 data, and that the bulk of the stellar mass is probed by the $F160W$ filter up to $z \sim 3$. The structural and morphological properties of GRB hosts determined from these images are thus dominated by long-lived stars and marginally affected by dust. This is supported by the smooth visual appearance of the objects in the WFC3/IR images in Appendix 2.2.2.C.

Dimming and spatial resolution Images of distant galaxies are degraded by the object distance and the instrument performance. These distance effects have to be properly considered to study with accuracy the galaxy evolution. The two major effects depending on the redshift are: the *surface brightness dimming* (Tolman 1930, 1934) and the instrument *angular resolution*.
Dimming is a cosmological effect due to the nonEuclidean geometry of the Universe and the contribution of time dilatation, redshift, and curvature. It diminishes the surface brightness of all sources through a $(1 + z)^{-4}$ scaling. The consequence is that the fraction of light detected in the outer regions of a source is progressively reduced with z, resulting in a smaller apparent size of an extended object. For instance, a simulation of the dimming effect and angular resolution (described below) on a sample of disk galaxies is visible in Fig. 2.6. It shows the difference between real galaxies observed at $z = 0$ and the same galaxies simulated at higher redshift that WFC3/IR in $F160W$ could observe (see Conselice et al. 2011, for additional details on the simulation method). Clearly, the fine galaxy features

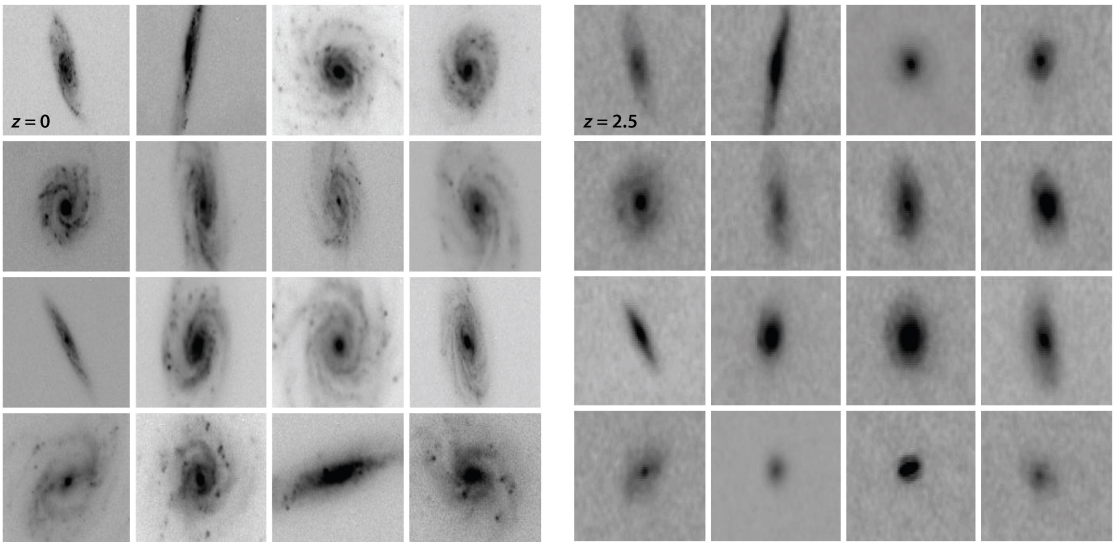

Figure 2.6: Comparison of local galaxies observed at $z = 0$ in optical B-band (left panel) and simulated at $z = 2.5$ in the rest-frame B-band probed by the WFC3/IR camera (right panel). (Conselice 2014)

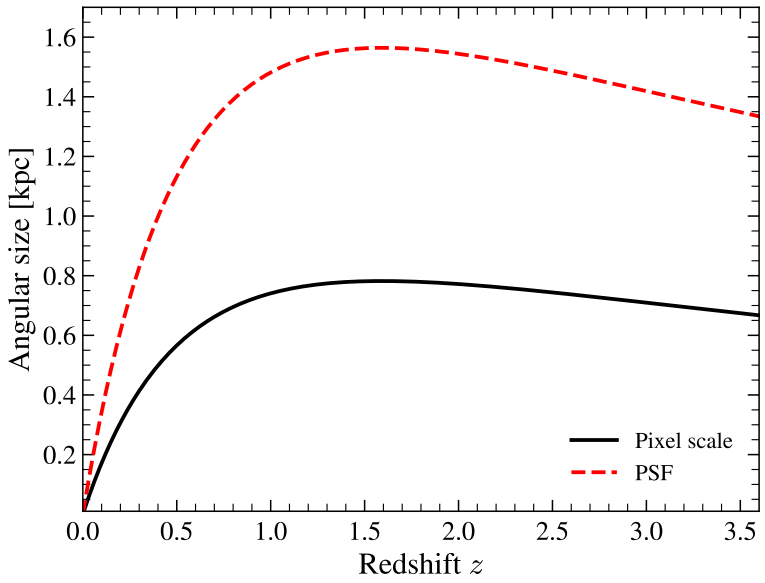

Figure 2.7: Angular size in kpc as a function of redshift for a PSF size of 0.18″ (in red) and a pixel scale of 0.09″ (in black) typical of WFC3/IR images in the $F160W$ filter. For an object at $1 < z < 3$, the resolution reached is about 1.5 kpc.

such as spiral arms are not visible at $z = 2$, challenging visual and non-parametric methods (see Sect. 2.1.3.3) to properly classify the galaxy morphology.
The angular resolution is the ability of a telescope to distinguish details of a given object. The fundamental limit for the resolution of a telescope is due to the wave-like nature of light which produces the diffraction phenomena. This limit is determined by the Rayleigh criterion. For a circular aperture (diameter D) and assuming a small angular separation (θ), the Rayleigh criterion is given by:

$$\sin(\theta_{\rm min}) \approx \theta_{\rm min} \approx 1.22\frac{\lambda}{D} \tag{2.1}$$

where θ is in rad, and λ and D are in m.
Regarding the HST WFC3/IR camera, the resolution limit for the $F160W$ filter determined from the Rayleigh criterion corresponds to $\theta_{\rm min} = 0.164$ arcsec. For a diffracted-limited telescope, the response of a point-like source, i.e., the point spread function (PSF), may be inferred from the Fourier transform of the aperture configuration. In practice, additional instrumental defects and imperfections imply that telescopes are often not diffracted-limited, and the PSF is thus larger. For instance, by combining the point-like sources (stars) from the field around the GRB hosts observed in the F160W filter, I modeled a PSF and determined a Full Width at Half Maximum (FWHM) of about $\sim$ 0.18 arcsec (see Sect. 2.2.4.1), consistent with but slightly larger than the Rayleigh criterion described above. Figure 2.7 shows for the F160W filter the minimum resolved structure (i.e., PSF) in kpc as a function of redshift[3]. It appears that the angular resolution allows to probe structures of > 1.5 kpc at $1 < z < 3$. Finally, an important aspect is to properly sample the PSF. For the WFC3/IR camera, the physical pixel size of the detector is 0.18 μm. Given the telescope focal length of 29 m for this instrument, one pixel of the detector corresponds to a pixel scale of 0.13 arcsec/pixel. For this reason, the native pixel scale of the WFC3/IR detector undersamples the PSF (Nyquist–Shannon sampling theorem). To improve this aspect, the observations are usually performed with a slight shift between each exposures and then, during the data reduction process the Drizzle algorithm (Fruchter & Hook 2002) produces images with a lower pixel scale. For instance, the pixel scale of the HLA images is 0.09 arcsec/pixel and satisfies the Nyquist–Shannon criterion for correctly sampling

[3]It may appear surprising that the angular size decreases after $z \sim 1.5$. This is due to the faster decrease of the Universe size with z than the increase of the covered size of the considered solid angle.

(by at least two pixels) the PSF of ~ 0.18 arcsec.

As described above, studying the morphology of galaxy in a context of galaxy evolution might therefore suffer from multiple observational biases. However, it is worth mentioning that in the case of my work, I compared a population of GRB hosts to a population of star-forming galaxies at a given redshift and stellar mass. This means that the effects described previously affect both populations at a comparable level. If a difference between the two populations is observed, it will more likely be related to a possible environmental effect than to the observational effects described above.

2.1.3.3 Size measurement and galaxy classification methods

The morphology of galaxies is a key ingredient to understand their formation and evolution across cosmic time. Since the first observations, astronomers classified the objects into different classes and tried to find relations between them. Over the years, different methods were developed to determine the most important and fundamental parameters describing the structure of galaxies. In this section, I will review the main existing methods to classify and measure the size of galaxies.

Visual morphology Visual inspection is the historical and traditional method for classifying galaxies (Hubble 1926, 1936; de Vaucouleurs 1959; Nair & Abraham 2010). However, the main limitation of this method is that it is person-dependent and easily biased by the opinion of a single person. For nearby galaxies, the clearly visible features characterizing spiral and elliptical galaxies mitigate the risk of misclassification. For distant galaxies, observational effects (see Sect. 2.1.3.2) make the exercise more difficult. In the case of a reasonable sample of objects, a possible solution is to ask a small group of independent astronomers to classify each galaxy. For larger surveys, a smart alternative is to create a collaborative environment and ask volunteers to classify the objects. This was originally proposed in 2007 by a group of scientists, known as the *Galaxy Zoo* project (Lintott et al. 2008, 2011). In total, the project permitted so far to classify around 1.5 million galaxies, the entire Sloan Digital Sky Survey spectroscopic sample and all existing HST surveys. Each object was classified more than 40 times, which considerably reduces the misclassification and associated uncertainties. Lintott et al. (2008)

demonstrated that the accuracy obtained with this approach is comparable to a classification from expert astronomers. Currently the project is still running and includes many other surveys (e.g., the Galaxy And Mass Assembly Survey and the Dark Energy Camera Legacy Survey) and cosmological hydrodynamic simulations such as Illustris. This method is generally robust to variations in the S/N of the images and is very efficient for nearby and intermediate redshift objects.

Non-parametric method The time consuming nature of visual inspection has pushed researchers to find more autonomous methods to classify galaxies. The most common non-parametric method of measuring the galaxy light distribution is the Concentration (C), Asymmetry (A), Clumpiness (S) (CAS) system (Abraham & Merrifield 2000; Bershady et al. 2000; Conselice 2003). The concentration parameter measures how the light of an object is distributed in the center compared to the outer parts. It is defined as

$$C \equiv 5 \times \log\left(\frac{r_{80}}{r_{20}}\right), \tag{2.2}$$

where r_{80} and r_{20} are the circular radii that contain 20% and 80% of the galaxy total flux, respectively. A large value of C means that a larger fraction of the light is contained in the central region than in the outer part of the object.
The asymmetry (A) index is measured by the difference between the original image (I) and the same image rotated by 180° (R) from its center. It is expressed as

$$A \equiv \frac{\text{abs}(I - R)}{I}, \tag{2.3}$$

where abs($I - R$) is the sum of the absolute pixel values resulting from the subtraction of R from I that cover the object. It provides an indicator of the fraction of light in the non-symmetric components of the galaxy.
The clumpiness (S) parameter estimates the fraction of light present in the clumps of the galaxy. It is determined by the difference between the original image and the same image blurred (B) by a convolution with a Gaussian filter. It is defined as

$$S \equiv \frac{I - B}{I}, \tag{2.4}$$

where $I - B$ is the sum of the pixels resulting from the difference between the I and B images covering the object. A large value of S might reveal that the object

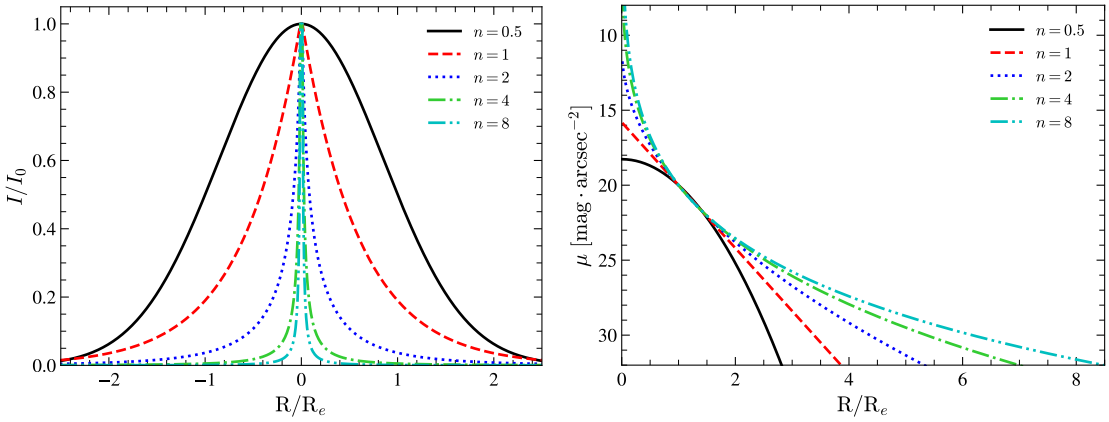

Figure 2.8: Examples of Sérsic functions for different values of n. *Left panel:* Surface brightness normalized to I_e as a function of radius normalized to $R_{\rm e}$. *Right panel:* Surface brightness expressed in magnitude $\cdot$ arcsec^{-2} as a function of radius normalized to $R_{\rm e}$ considering a magnitude at $R_{\rm e}$ (μ_e) of 20.

has regions of ongoing star-formation (H II regions).

Note that other non-parametric systems also exist, such as Gini-M_{20} indices (Abraham et al. 2003; Lotz et al. 2004) which are related to the distribution of light pixel to pixel.

The non-parametric approaches present some limitations, especially regarding their robustness to the S/N and to the image resolution (Lisker 2008; Andrae et al. 2011). In addition, they are often used to classify galaxies but are not optimized to provide accurate structural properties such as the galaxy size of compact objects.

A possible non-parametric method to determine the size of a galaxy is to use `SExtractor` (Bertin & Arnouts 1996). Based on aperture photometry, `SExtractor` is able to provide an estimate of the radius that encloses a given fraction of the total flux. The strengths of this technique are that it does not depend on the shape of the object (i.e. it is model independent), and its simplicity implies that it can be applied to a large variety of galaxy shapes and sizes. However, this method does not take into account the PSF of the instrument. For compact sources close to the PSF size or pixel scale, the size measurement becomes inaccurate and unreliable. In addition, aperture photometry requires an estimation and subtraction of the sky. In the case of a low S/N or crowded environments, an overestimate of the sky can result in an underestimate of the object size.

Parametric method Galaxies are extended objects and their "true" extent can be difficult to define. By convention, a common quantity used to describe galaxy sizes is the half-light radius (R_e) or effective radius. It is defined as the radius which contains 50% of the total flux of the galaxy. To determine this quantity for distant and faint objects, the visual inspection and the non-parametric approach described previously appear inadequate. A more quantitative approach relies on modeling the surface brightness (I) as a function of the radial distance (R) from the object center. de Vaucouleurs (1948) was the first to propose a law (de Vaucouleurs profile) to describe the variation of the surface brightness with R for an elliptical galaxy. Later, Sérsic (1963); Sersic (1968) has generalized the de Vaucouleurs profile to reproduce the surface brightness profile of different types of galaxies. The Sérsic profile is defined such that

$$I(R) = I_e \exp\left\{-b_n\left[\left(\frac{R}{R_e}\right)^{1/n} - 1\right]\right\}, \tag{2.5}$$

where n is the Sérsic index, I_e is the surface brightness at R_e, and b_n is a dimensionless parameter that depends of n. See also Graham & Driver (2005) for various mathematical expressions of the Sérsic profile. The function b_n is defined by the relation

$$\Gamma(2n) = 2\gamma(2n, b_n), \tag{2.6}$$

where Γ and γ are the Gamma function and lower incomplete Gamma function, respectively. For $0.5 < n < 10$, b_n is well approximated by $b_n = 1.9992n - 0.3271$ (Capaccioli 1989). Figure 2.8 shows the profile of the Sérsic functions for different values of n expressed in linear scale and dimensionless unit (left panel) or in logarithmic scale and mag $\cdot$ arcsec^{-2} unit (right panel). It can be seen that the Sérsic index n determines the degree of curvature of the profile. For a large value of n (i.e. $n > 2$), the profile is steeper in the center and more extended at a larger radius compared to $n < 2$. This is illustrated in the left panel of Fig. 2.9 where the fraction of light within a given radius is provided. Besides, using the formula derived by Miller et al. (2019), it is also possible to derive r_{80} and r_{20} for a given value of n and determine the profile concentration based on the CAS definition. The right panel of Fig. 2.9 shows that the concentration (C) is a monotonically increasing function of the Sérsic index.

For $n = 4$, the Sérsic profile corresponds to the special case of the de Vaucouleurs profile, whereas the case $n = 1$ corresponds to an exponential light distribution

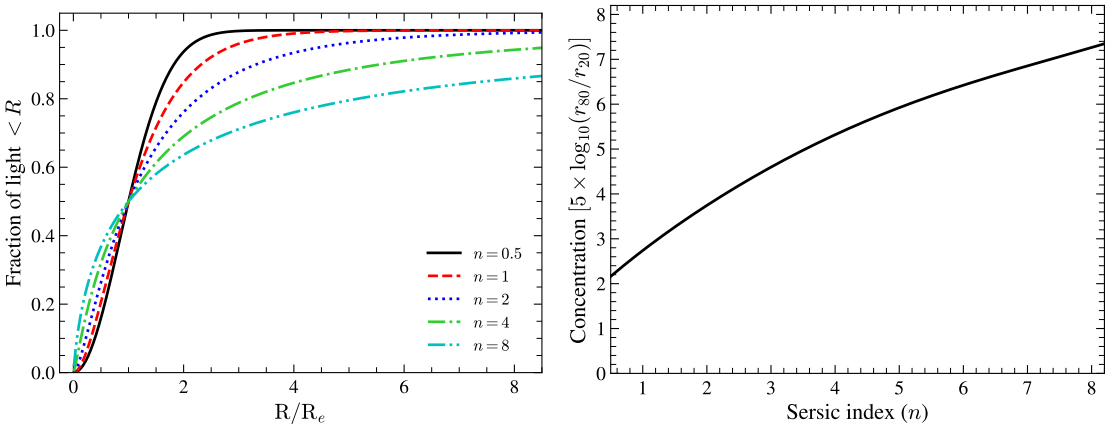

Figure 2.9: Light concentration of Sérsic functions for different values of n. *Left panel:* Cumulative distribution of the light as a function of the radius. *Right panel:* Concentration of the Sérsic function as defined by the CAS system versus Sérsic index.

and $n = 0.5$ to a Gaussian profile. Previous works using a single Sérsic function to fit the surface brightness of sources showed that galaxies can have a large diversity of n, from 0.5 to 10. The elliptical galaxies, the bulge of spiral galaxies or the objects showing a dense central core are often characterized by a Sérsic profile with a high Sérsic index, between 2 to 10. Disks of galaxies and disk-like galaxies have shown a good agreement with a profile having $n \approx 1$ and flatter structure such as bars of galaxies by a function with $n \lesssim 0.5$ (e.g., Kelvin et al. 2012; Lange et al. 2015). An example of the diversity of 2D Sérsic profiles that can be observed for galaxies with the WFC3/IR $F160W$ filter is visible in Fig. 2.10. The top panels show flatter profiles ($n \leq 1$) and bottom panels show more profiles with a compact and dense central core ($n \geq 4$).

Studies have found that when a single Sérsic function is used to model objects, the difference between early types (spheroid-like) and later types (disk-like) can be separated by $n \approx 2.5$. Although a single Sérsic model is often a fair assumption for distant objects, nearby objects often have multiple components and more than one profile is usually required. A standard approach is to decompose the object into two Sérsic functions, one for the bulge ($n = 4$) and one for the disk ($n = 1$). From this decomposition, two quantities measuring the relative importance of the bulge and disk can be derived, the bulge-to-total (B/T) and the bulge-to-disk (B/D) luminosity ratios. These two quantities correlate with the Hubble sequence and can be used to determine a morphological classification of the sample (e.g.,

Graham & Worley 2008; Weinzirl et al. 2009).
It is worth noting that it exists another definition to describe the radial profile of a galaxy in a distance-independent way, the Petrosian profile (Petrosian 1976). It is defined as the ratio (η) between the surface brightness at a distance of R to the average surface brightness within R. At the center of the object, $\eta = 1$ and decreases to zero at the outskirts of the object. The Petrosian radius ($R_{\rm petro}$) is often chosen such as $\eta = 0.2$.

Several softwares have been developed to fit 2D Sérsic profiles to galaxy images, such as Gim2D (Simard et al. 2002), `GALFIT` (Peng et al. 2002, 2010), PyMorph (Vikram et al. 2010), GALFIT-CORSAIR (Bonfini 2014), MORFOMETRYKA (Ferrari et al. 2015; Lucatelli & Ferrari 2019), ProFit (Robotham et al. 2017), iFit (Breda et al. 2019), GaLight (Ding et al. 2021). They all have slightly different functionalities, are written in different languages and use different minimization algorithms (e.g. Levenberg-Marquardt, Metropolis). Therefore, depending on the scientific objective, one might be more appropriate than another.

The strengths of the parametric approach are multiples. First, it takes into account the PSF to fit and optimize the model. It is thus possible to measure and constrain the shape of the galaxy up to the central region of the object. For instance, the convolution of the model with the PSF is particularly important for small and distant objects with an apparent size close to the PSF or pixel scale resolution. Then, the method is more robust in complex environments with surrounding objects, because several functions can be fit simultaneously and reduce the possible contamination of neighboring objects. Finally, the parametric method considers at the same time the flux from the source and its expected noise given the observed flux. This means that even if the edges of an object are not detected, the method will try to optimize models that are consistent with the well-detected central region and considering that at the edge, the models might not be zero. In comparison, size measurements based on aperture photometry only measure the size of the detected part of the object and might therefore underestimate the "true" size (e.g., see Fig. 2 of Ichikawa et al. 2012). However, the parametric approach has some weaknesses. First, this method is model-dependent and regarding the large variety of observed morphologies, the functions considered to model galaxies might not be valid for all of them and can affect their luminosity and size measurements. Then, the method might suffer from parameter degeneracy, i.e., the same function

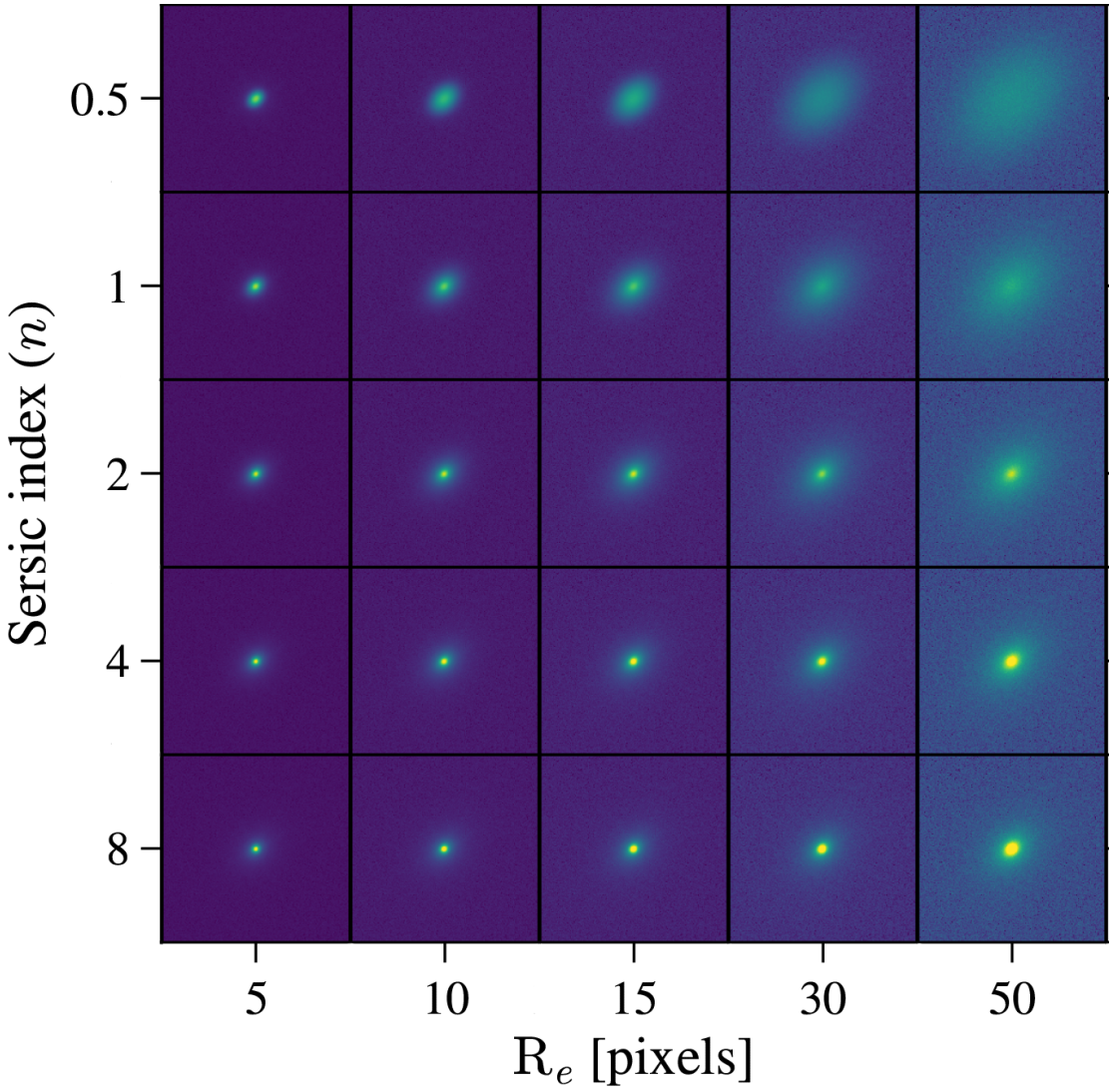

Figure 2.10: Examples of `GALFIT` models for a single Sérsic component considering different values of R_e and n. The axis ratio is maintained at a value of 0.7 and the position angle at 45 deg. Models are convolved with the PSF of the WFC3/IR $F160W$ filter and a Poisson noise is added to produce more realistic profiles.

with different parameters can model the object with a similar accuracy. Finally, the number of components and the neighboring objects to be fit simultaneously, and how to determine the reliability of a given fit, often represent a difficult choice with multiple possibilities.

GALFIT procedure To determine the size of GRB host galaxies, I chose to use the parametric approach, which seems the most appropriate in this case of small and distant objects ($1 < z < 3$). Among the previously listed softwares, I decided to use GALFIT for two main reasons. First, GALFIT has been intensively tested since many years and therefore has demonstrated its reliability for size measurement, and has a vast quantity of materials available. Secondly, GALFIT was used to determine the galaxy size of the reference star-forming sample used to compare the GRB host population. The use of the same software might minimize the possible systematic bias between size measurement methods.
GALFIT is a software providing an environment to perform the fitting of two-dimensional PSF-converted functions, such as the Sérsic function, on an image. It is written in C and runs on the Linux distribution and MacOS X. GALFIT uses the χ^2_ν statistics and Levenberg-Marquardt (LM) algorithm to find the best-fit parameters of the model(s). The fitting parameters are the center position of the galaxy ($x,\ y$), the AB magnitude, the half-light radius along the semi-major axis (R_e), the Sérsic index (n), the axis ratio q (semi-minor axis over semi-major axis) and the position angle (PA). Before the fitting optimization, GALFIT needs a first guess for the parameters of the models considered in the fit. The first guess can be obtained by hand or by using another software such as SExtractor. To avoid the contamination from surrounding sources and parameter degeneracy, it is also recommended to mask the objects close to the target. GALFIT is therefore not adapted nor conceived to do automated batch fitting of galaxies.
To automate the steps before running GALFIT on survey mosaics, the wrapper GALAPAGOS (Barden et al. 2012) has been developed. However the code is written in IDL, a software with expensive license, less and less used by astronomers. Furthermore, to have more flexibility, I preferred to develop my own GALFIT wrapper to automate the process described in Fig. 2.11 and in more details in Sect. 2.2.4.1. Only the main steps are recalled here. First, the area of interest in the science image is selected and extracted, usually a square area of 200×200 pixels around the targeted object. Then, SExtractor is run to find a first estimate of the model

parameters and to mask the surrounding objects. A noise map is provided to `GALFIT` (or determined internally by `GALFIT`) as well as a PSF adapted to the science image. Finally, `GALFIT` is run to determine the parameters of the best-fit model.

Machine learning Recently a new kind of algorithm has been developed for galaxy morphology classification and for measuring the galaxy size based on convolutional neural networks (CNN) (Dieleman et al. 2015; Huertas-Company et al. 2015; Tuccillo et al. 2018). Once trained, these algorithms are significantly faster than traditional methods with similar accuracy. Therefore, they are ideal methods to handle the large amount of data that upcoming projects like EUCLID or LSST will produce. However, machine learning algorithms require a large training sample with a time-consuming training period. In addition, the results are strongly dependent on the training set used to learn the neural networks. Given the very small size of my long GRB host selected sample (< 50 objects), this approach was not a viable option for measuring galaxy sizes in my analysis. Machine learning and deep learning are a very active field of research and possible solutions to these limitations will probably emerge in the coming year.

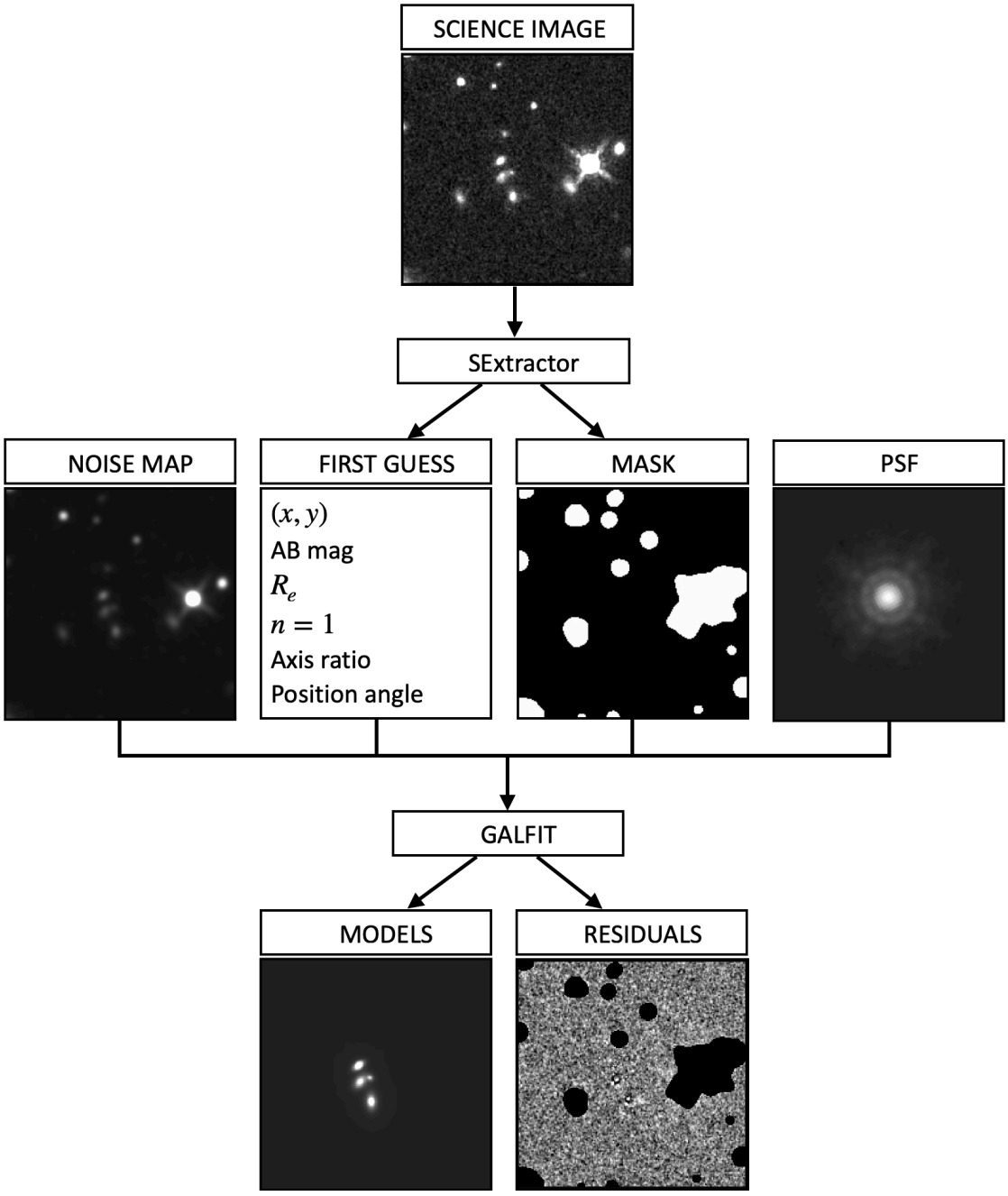

Figure 2.11: The standard `GALFIT` procedure used to model sources with a single Sérsic component. `SExtractor` allows to mask bright objects around the target sources and determine the initial parameters of the Sérsic function. In addition, a noise map and a PSF adapted to the science image are provided to `GALFIT`. After the optimization, the `GALFIT` returns in a single file: the original image, an image with the models, and a residual map (the difference between the original and model images).

2.2 Are the host galaxies of Long Gamma-Ray Bursts more compact than star-forming galaxies of the field? (B. Schneider et al., 2022, A&A, 666, A14)

In this section, I report on my work on the stellar density of a sample of LGRB host galaxies at $z > 1$ observed with the HST/WFC3 instrument in the IR band. This study was published in the Astronomy and Astrophysics journal[4]. Only minor "cosmetic" changes are made compared to the published version. The differences are mainly designed to fit the format of this manuscript (e.g., typography, size of figures).

2.2.1 Abstract

Context. Long gamma-ray bursts (GRBs) offer a promising tool for tracing the cosmic history of star formation, especially at high redshift, where conventional methods are known to suffer from intrinsic biases. Previous studies of GRB host galaxies at low redshift showed that high surface density of stellar mass and high surface density of star formation rate (SFR) can potentially enhance the GRB production. Evaluating the effect of such stellar densities at high redshift is therefore crucial to fully control the ability of long GRBs for probing the activity of star formation in the distant Universe.

Aims. We assess how the size, stellar mass, and star formation rate surface densities of distant galaxies affect the probability of their hosting a long GRB, using a sample of GRB hosts at $z > 1$ and a control sample of star-forming sources from the field.

Methods. We gathered a sample of 45 GRB host galaxies at $1 < z < 3.1$ observed with the Hubble Space Telescope WFC3 camera in the near-infrared. Our subsample at $1 < z < 2$ has cumulative distributions of redshift and stellar mass consistent with the host galaxies of known unbiased GRB samples, while our GRB host selection at $2 < z < 3.1$ has lower statistics and is probably biased toward the high end of the stellar mass function. Using the GALFIT parametric approach, we

[4] https://www.aanda.org/articles/aa/abs/2022/10/aa43367-22/aa43367-22.html

modeled the GRB host light profile with a Sérsic component and derived the half-light radius for 35 GRB hosts, which we used to estimate the star formation rate and stellar mass surface densities of each object. We compared the distribution of these physical quantities to the SFR-weighted properties of a complete sample of star-forming galaxies from the 3D-HST deep survey at a comparable redshift and stellar mass.

Results. We show that similarly to $z < 1$, GRB hosts are smaller in size and they have higher stellar mass and star formation rate surface densities than field galaxies at $1 < z < 2$. Interestingly, this result is robust even when separately considering the hosts of GRBs with optically bright afterglows and the hosts of dark GRBs, as the two subsamples share similar size distributions. At $z > 2$, however, GRB hosts appear to have sizes and stellar mass surface densities more consistent with those characterizing the field galaxies. This may reveal an evolution with redshift of the bias between GRB hosts and the overall population of star-forming sources, although we cannot exclude that our result at $z > 2$ is also affected by the prevalence of dark GRBs in our selection.

Conclusions. In addition to a possible trend toward a low-metallicity environment, other environmental properties such as stellar density appear to play a role in the formation of long GRBs, at least up to $z \sim 2$. This might suggest that GRBs require special environments to enhance their production.

2.2.2 Introduction

Long-duration gamma-ray bursts (GRBs) are extremely luminous ($\sim 10^{53}$ erg s^{-1}) and powerful explosions with a typical prompt emission duration longer than 2 seconds. Two types of progenitors have been proposed to explain these extreme phenomena: a single massive star (Woosley 1993; Woosley & Heger 2006; Yoon et al. 2006) known as the collapsar model or a binary system of massive stars (Fryer & Heger 2005; Cantiello et al. 2007; Chrimes et al. 2020). In both cases, they connect long GRBs to the death of massive (> 40 M$_\odot$) and fast-rotating stars. The strongest support for this association lies in multiple observations of the spatial and temporal coincidence between a type Ic-BL supernova (SN) and a GRB (Hjorth et al. 2003; Stanek et al. 2003; Xu et al. 2013). Observations of their host galaxies also support this connection by identifying that actively star-forming galaxies favor GRBs production (Sokolov et al. 2001; Bloom et al. 2002;

Le Floc'h et al. 2003; Perley & Perley 2013; Hunt et al. 2014; Greiner et al. 2015; Palmerio et al. 2019) and that GRBs mostly occur in the UV-bright regions of their hosts (Fruchter et al. 2006; Blanchard et al. 2016; Lyman et al. 2017). Due to the short lifetime of massive stars (< 50 Myr), long GRBs are linked to recent star formation activity in their host environment. The rate of GRBs could thus offer a unique opportunity to constrain the cosmic star formation rate history (CSFRH), especially at high redshifts ($z > 5$), where GRBs are still detectable (Salvaterra et al. 2009; Tanvir et al. 2009) and where the uncertainties affecting the estimates from UV-selected galaxies become predominant. The comparison of the two approaches reveals that at high redshifts the GRB rate predicts a substantially higher star formation rate (SFR) density than the one inferred from UV-selected galaxies (Kistler et al. 2008; Robertson & Ellis 2012; Ghirlanda & Salvaterra 2022). Recent discovery of massive dusty star-forming galaxies at $z > 3$ (Wang et al. 2019) points out that UV-selected galaxy samples miss these galaxies and may indeed underestimate the CSFRH at high-z. On the other hand, long GRBs might require specific conditions to form, depending on, for instance, metallicity or local density, which could also introduce biases in the CSFRH determination.

At the end-life of the progenitor, a high angular momentum is needed to launch the GRB jet. In order to have this critical requirement, the collapsar model requires a low metallicity ($Z < 0.3\ Z_{\odot}$, Yoon et al. 2006). Indeed, stars with higher metallicity produce stronger stellar winds that remove angular momentum and inhibit GRB production. For binary system models, tidal interaction and mass transfer in binaries can spin up the system (Petrovic et al. 2005) to produce the relativistic jet and thus require a lower constraint on the metallicity (Chrimes et al. 2020). Because GRB progenitors are not directly observable, the characterization of GRB host (GRBH) galaxies offer an indirect but precious tool to explore the GRB environment and further constrain the physical conditions which favor their formation. Studies based on GRB host galaxies showed that GRBs tend to avoid high metallicity galaxies (Vergani et al. 2015; Perley et al. 2016b; Palmerio et al. 2019) and support the hypothesis of a bias toward a low-metallicity environment. For instance, Palmerio et al. (2019) found that GRB production is significantly reduced for galaxies with $Z \gtrsim 0.7\ Z_{\odot}$. Spatially resolved spectroscopic studies of nearby GRB host galaxies (Levesque et al. 2011; Krühler et al. 2017) show that the integrated host metallicity may differ from the GRB site metallicity by about $0.1 - 0.3$ dex, which could reconcile the apparent discrepancies between

the theoretical predictions of the collapsar model and the current observational constraints. On the other hand, several studies reported GRB host galaxies with super-solar metallicity (Levesque et al. 2010b; Savaglio et al. 2012; Heintz et al. 2018), which sets into question the existence of a hard metallicity cap. Although there is a consensus that metallicity plays a role, the precise way it affects the GRB occurrence rate remains unclear.

In a cosmological context, such a metallicity condition would not affect the relation between GRB and cosmic star formation rate at $z \gtrsim 3$, because sub-solar metallicities are typical of galaxies in the early universe. Hence, long GRBs may trace the star formation rate in an unbiased way assuming that no other biases are involved. However, the discrepancies on the metallicity constraints reported above may also suggest other possible influences, as discussed in several studies of GRB hosts. For instance, Perley et al. (2015) suggested that GRB explosions are enhanced in intense starburst galaxies (see also Arabsalmani et al. 2020) in addition to a trend toward low metallicity environment. Michałowski et al. (2016) focused on GRB 980425 and observed clues of a possible recent atomic gas inflow toward its host that may have triggered the formation of massive stars able to produce a GRB. Arabsalmani et al. (2015, 2019) also reported evidences of a companion dwarf galaxy interacting with the host of GRB 980425. They suggested that the interaction of galaxies can favor GRB formation. Moreover, GRB hosts show a higher specific star formation rate (star formation rate per unit mass) compared to field galaxies (Salvaterra et al. 2009; Schulze et al. 2018). Finally, GRB hosts are found to be more compact and smaller than field galaxies (Conselice et al. 2005; Fruchter et al. 2006; Wainwright et al. 2007). In particular, Kelly et al. (2014) showed that at $z < 1$ GRBs tend to occur in compact and dense environments, that is, in galaxies with star formation and stellar mass surface densities higher than observed in field galaxies at comparable stellar mass and redshift. However, the existence of this trend toward more compact environments and its link to metallicity, if any, has not been explored at $z > 1$. This remains a crucial aspect to establish the link between the long GRB rate and the SFR in the distant Universe. Furthermore, determining the influence of stellar density on the GRB occurrence rate could also shed indirect lights into our understanding of the main drivers or the relative importance of progenitor models in the formation of long GRBs.

In this work, we quantify the stellar mass surface density ($\Sigma_{\rm M}$) and the star

formation surface density ($\Sigma_{\rm SFR}$) in GRB host galaxies up to $z \sim 3$ and assess how these physical properties compare with those observed in field galaxies at similar redshift. We present results based on a sample of long GRB host galaxies observed with the Hubble Space Telescope (HST) and more particularly with the Wide Field Camera 3 (WFC3) instrument in the infrared (IR) band. The high-resolution images of the HST provide a possibility of precisely measuring the galaxy size, avoiding contamination by nearby galaxies. Our analysis is mostly based on images obtained with the $F160W$ filter ($\lambda_{mean} \sim 1.54\,\mu$m), where the observed emission is more sensitive to the bulk of the galaxy stellar mass compared to data at shorter wavelengths, which also minimizes the effect from dust obscuration. This paper is organized as follows. In Sect. 2.2.3, we introduce the GRB host galaxy sample, the control star-forming galaxy sample and the limit of completeness of both samples. In Sect. 2.2.4, we describe the methods for deriving the structural and physical parameters for the GRB hosts galaxies. Section 2.2.5 presents our results and their comparison with the field galaxies. Section 2.2.6 presents a discussion of our results more broadly and their implications. Finally, the conclusions are presented in Sect. 2.2.7. Throughout the paper, we use the ΛCDM cosmology from Planck Collaboration et al. (2020) with $\Omega_{\rm m} = 0.315$, $\Omega_\Lambda = 0.685$, and $H_0 = 67.4$ km s^{-1} Mpc^{-1}. Stellar masses (M_*) and SFRs are reported assuming a Chabrier (2003) initial mass function (IMF).

2.2.3 Data

2.2.3.1 Sample selection

We consider all long GRBs with a redshift measurement (spectroscopic or photometric) in $1 < z < 4$ from J. Greiner's database[5]. This page gathers all GRBs detected and localized since 1996 by high-energy space observatories such as HETE, INTEGRAL, Fermi, and *Swift*. For each GRB, the page provides a collection of information (localization, error box, T_{90}, and redshift, if available) collected from Gamma-ray Coordinates Network (GCN) messages and referenced publications. We find a total of 317 GRBs in the range of redshift considered. We query these objects in the Mikulski Archive for Space Telescopes (MAST) database and select the ones performed with the WFC3/IR instrument of the HST. We extract the

[5] https://www.mpe.mpg.de/~jcg/grbgen.html

enhanced data products available in the Hubble Legacy Archive (HLA) database[6]. These products are generated with the standard HST pipeline (`AstroDrizzle` software) which corrects geometric distortion, removes cosmic rays, and combines multiple exposures. The images are north up aligned and have a final pixel scale of 0.09 arcsec. Most of the sample is located at $z < 3.1$, with one single source lying at $z = 3.5$. For this reason, we restrained our study at $1 < z < 3.1$.

To verify that all HST observations have been included in the HLA database, we cross-checked standard products available in the HST archive with the enhanced HLA products. Two additional observations have been found in the HST archive (GRB 060512 and GRB 100414A). However, HST observations of GRB 060512 have poor quality with visible star trails and the data of GRB 100414A correspond to another object (NGC 4698) because no observations were performed for this GRB field. We excluded these two objects from our analysis.

Our sample is composed of 42 long GRB host galaxies observed in the $F160W$ filter. At $1 < z < 3.1$, we additionally find in the HLA database a total of two GRB hosts solely observed in the $F110W$ filter (GRB 070125 and GRB 080207). We include them in the final sample because the wavelength probed by this filter ($\lambda_{\rm mean} \sim 1.18\,\mu$m) is close to that of $F160W$ filter ($\lambda_{\rm mean} \sim 1.54\,\mu$m). Therefore, we do not expect significantly different size measurements between these filters. We also include the peculiar GRB 090426, classified as a short GRB based on its $T_{90} < 2s$ (Levesque et al. 2010a) but as a long one regarding the properties of the host galaxy (Thöne et al. 2011a). Finally, we excluded the unsecured case of GRB 140331A due to multiple candidate hosts and a photometric redshift value close to 1.

All HST observations (except for GRB 160509A) were taken at a late time after the GRB detection, when the afterglow had faded significantly. For GRB 160509A, two HST observations were performed after 35.3 and 422.1 days in the $F160W$. In the HLA database, only products for the observations at 35.3 days are available. Because of the short delay between the detection and the observations, a possible contamination of the afterglow cannot be excluded. Kangas et al. (2020) showed that the remaining afterglow at 35.3 days is very weak ($H_{F160W} = 26.07$ mag) compared to the host galaxy. We conclude (for this object) that the HST observations considered are not strongly affected by the GRB afterglow and that the host galaxy is assumed dominant.

[6] http://hla.stsci.edu/

The final GRB host sample is shown in Table 2.1. It is composed of 44 bursts mainly ($\sim$ 90%) detected by *Swift*. Among them, only two (GRB 090404 and GRB 111215A) have a photometric redshift estimated from the spectral energy distribution (SED) of the host galaxy. These redshifts are less reliable than spectroscopic determinations, but since they represent only a small fraction ($< 5\%$) of the full sample, we do not expect a significant impact on our results. In our analysis, we divided the sample into two bins of redshift, $1 < z < 2$ and $2 < z < 3.1$ to enclose the cosmic noon at $z \sim 2$ (Madau & Dickinson 2014; Förster Schreiber & Wuyts 2020), where the cosmic star formation rate volume density has reached its maximum.

2.2.3.2 Host assignment

Since the launch of *Swift* in 2004, GRB positions are often determined with an accuracy of $\sim$ 1". Because long GRBs are associated with the death of massive stars (Hjorth et al. 2003), the GRB site is expected to be close to the center or the brightest region of its host galaxy (Fruchter et al. 2006; Blanchard et al. 2016; Lyman et al. 2017). An unambiguous way to assign a host galaxy to a GRB is to match the redshift measured from the fine-structure lines of the GRB afterglow with the redshift obtained from the emission lines of the host candidate. Unfortunately, this is not always possible, especially for dark GRBs, where faint or no optical counterpart is detected. In this case, to assign the burst to its host galaxy, a standard approach is to use the probability of chance coincidence ($P_{\rm cc}$). The $P_{\rm cc}$ can be estimated from the Poisson probability of finding a galaxy in a given radius around the transient event localization (see Bloom et al. 2002). Another possible approach relies on a Bayesian inference framework (Aggarwal et al. 2021). The majority of our GRBs have already been well studied in the literature. Blanchard et al. (2016) and Lyman et al. (2017) assigned host galaxies using $P_{\rm cc}$ on HST images but the coordinates of the identified hosts are not reported.

As a starting point, we extracted the best GRB coordinates available in the literature (e.g., Perley et al. 2016b). We then let `SExtractor` (Bertin & Arnouts 1996) find the closest object to the best GRB position. We cross-checked the objects found by `SExtractor` with images provided in Blanchard et al. (2016) and Lyman et al. (2017). We successfully identified the host galaxies for the majority of

our sample. Only the hosts of GRB 150314A and GRB 160509A have not yet been reported in the literature. For these two cases, we considered the Bayesian formalism of Aggarwal et al. (2021) and use the provided PYTHON package *astropath*. For each GRB, we first extracted the best afterglow position and errors from the literature. Then, all objects within or crossing the error circle of the afterglow position were considered as possible host galaxies. Following the recommendations of Aggarwal et al. (2021), we estimated the galaxy centroids, magnitudes, and angular sizes of objects with a nonparametric approach (i.e., `SExtractor`). It is common to consider that the host is undetected when HST observations reveal either a blank region with no obvious source or if the detected object has a larger projected offset than typically observed for previous GRBs (> 10 kpc, Bloom et al. 2002; Blanchard et al. 2016; Lyman et al. 2017). For GRB 150314A and GRB 160509A, one or more extended objects with $H_{F160W} \lesssim 24$ mag can be seen within the 1.5" *Swift* error box region. Based on Hubble's Ultra Deep Field (UDF), the number of sources with a limiting H-band magnitude of 24 within 1.5" was estimated to be about 0.075 (Rafelski et al. 2015). We therefore assumed a probability of zero ($P(U) = 0$) that the host galaxy is not detected. It means that the GRB host is necessarily one of the objects detected by the HST near the afterglow position. This hypothesis is supported by the $F160W$ magnitudes (Table 2.1) determined by `GALFIT` (Peng et al. 2002, 2010), which are consistent with the other magnitudes of GRB hosts at similar redshift and stellar mass. For the prior probability that the object, i, is the host galaxy, $P(O_i)$, we considered the "inverse" prior. This formalism is inspired from the $P_{\rm cc}$ calculation and gives higher prior probability to brighter candidates. In addition, the angular distance of the object from the GRB position was taken into account by the $p(\omega|O_i)$ prior and set to the "exponential" model. We assigned as the host galaxy the object with the highest posterior probability. We found for GRB 150314A and GRB 160509A a probability of 0.92 and 0.54, respectively. Finally, a total of six GRBs were rejected because no host galaxies were detected on the HST observations. The 3σ $F160W$ magnitude limits found by Blanchard et al. (2016); Lyman et al. (2017) reveal extremely faint hosts (≥ 26.7 mag). These galaxies would lie below the stellar mass completeness limit of the 3D-HST survey that we further use for our control sample.

Finally, we note that Krühler et al. (2015) quantified the possible number of misidentifications in their sample of 96 targets. They found a probability of $\sim 30\%$

for having 2 over 96 sources with an erroneous association. Our sample is similarly composed of well-localized GRBs from *Swift*, we therefore did not expect a larger number of misidentified objects nor a great impact on our results.

2.2.3.3 Control sample

To compare the properties of GRB host galaxies with those of field galaxies, we used a population of star-forming galaxies from the Cosmic Assembly Near-infrared Deep Extragalactic Legacy Survey (CANDELS) and 3D-HST surveys. CANDELS[7] (Grogin et al. 2011; Koekemoer et al. 2011) is a deep near-infrared imaging survey carried out with the near-infrared WFC3 and optical Advanced Camera for Surveys (ACS) instruments on board the HST. The survey targets five well-known extragalactic fields (AEGIS, COSMOS, GOODS-N, GOODS-S, and UDS) and represents a total area of ~ 0.25 degree^2 with more than 250,000 galaxies. The 3D-HST[8] survey is a near-infrared spectroscopic survey with the WFC3 and ACS grisms on board the HST (Brammer et al. 2012; Momcheva et al. 2016). The survey provides a third dimension (i.e., redshift) for approximately 70% of the CANDELS survey. The photometric analysis of the resulting CANDELS + 3D-HST mosaic plus other wavelengths from ground- and space-based observatories is presented in Skelton et al. (2014).
Within the 3D-HST catalog, we selected the star-forming galaxies with the rest-frame $U-V$ and $V-J$ colors method (Wuyts et al. 2007; Williams et al. 2009). For the resulting objects, the stellar masses and star formation rates considered are described in Appendix 2.2.2.A. We found consistent values with the well-established main sequence of star-forming galaxies (e.g., Whitaker et al. 2014). The structural parameters used were extracted from van der Wel et al. (2014). The light profile modeling is based on a single Sérsic model (Sérsic 1963; Sersic 1968) fit by `GALFIT` (Peng et al. 2002, 2010) and `GALAPAGOS` (Barden et al. 2012). Details of the methodology are presented in van der Wel et al. (2012). This paper uses the data products released in the version 4.1.5, available through the 3D-HST website and described in Momcheva et al. (2016).

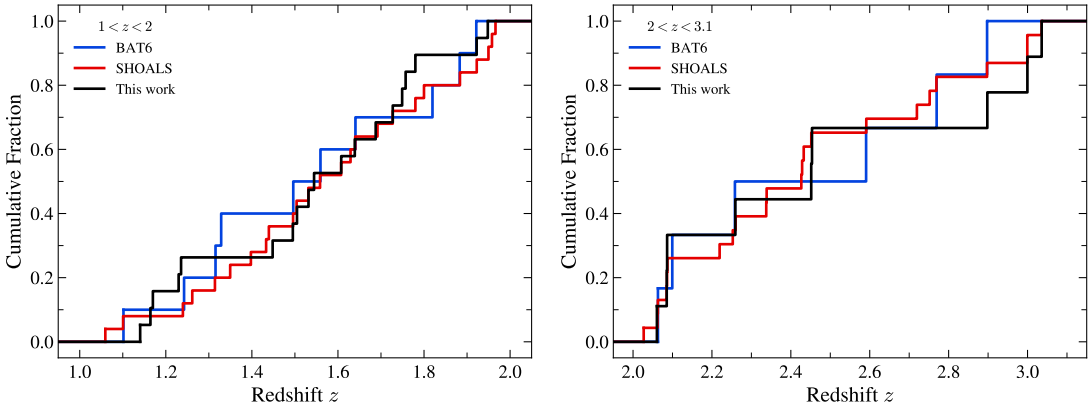

Figure 2.12: Redshift cumulative distributions of our GRB host sample, compared to the host galaxies of unbiased GRB samples (SHOALS and BAT6). Objects are divided into two bins of redshifts. Top panel with GRB hosts at $1 < z < 2$. Bottom panel with GRB hosts at $2 < z < 3.1$.

2.2.3.4 Completeness of the samples

In deep imaging surveys, the number of sources detected is limited by the depth of images and instrument performances. At a given redshift, the resulting sample is only a subsample of all existing galaxies at that age of the Universe. The stellar mass completeness of the 3D-HST/CANDELS survey is discussed in Tal et al. (2014). In our analysis, for the star-forming galaxies, we combined several physical quantities such as stellar mass, SFR, and half-light radius extracted from various studies (Momcheva et al. 2016; Whitaker et al. 2014; van der Wel et al. 2014). Consequently, each object does not necessarily have an estimate for all its properties (e.g., the size when `GALFIT` has not successfully converged) and it would not be fair to consider the same mass-completeness limits as determined by Tal et al. (2014). We combined the SFR estimates obtained by adding the UV and IR light ($\mathrm{SFR_{UV+IR}}$) with the UV-SFR corrected from dust extinction ($\mathrm{SFR_{UV,corr}}$) to have at least one SFR value for objects having a stellar mass (see Appendix 2.2.2.A for more details) and thus we preserved the mass-completeness limits determined by Tal et al. (2014). Hence, the most limiting factor lies in the galaxy size measurements. van der Wel et al. (2012) showed that accurate and precise measurements of galaxy sizes can be obtained down to a magnitude of $H_{F160W} = 24.5$ mag, corresponding to a 95% magnitude completeness (Skelton

[7] http://arcoiris.ucolick.org/candels/index.html
[8] https://archive.stsci.edu/prepds/3d-hst/

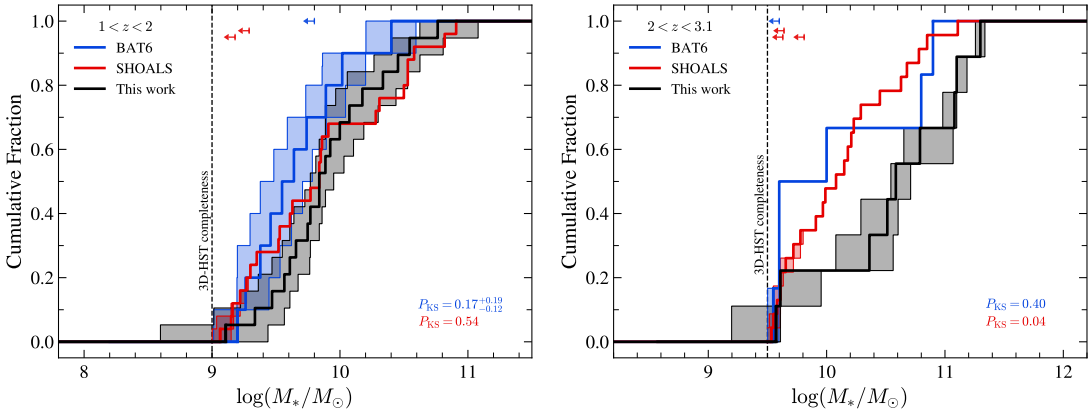

Figure 2.13: Stellar mass cumulative distributions of our GRB host sample, compared to the host galaxies of unbiased GRB samples (SHOALS and BAT6). Two bins of redshift are distinguished: with GRB hosts at $1 < z < 2$ (top panel) and with objects at $2 < z < 3.1$ (bottom panel). Upper limits are represented as arrows at the top of the plots. The 1σ uncertainty on the cumulative distribution is given by the shaded region around the curve. The $p-$value returned by the two-sided K-S test is provided in the right bottom part of both panels and color-coded according to the unbiased sample selected to compute the test. The vertical dashed line symbolizes the stellar mass completeness limit of the 3D-HST survey.

et al. 2014). On this basis, van der Wel et al. (2014) provided the equivalent stellar mass completeness limits per bin of 0.5 redshift. We considered the mean value of their mass-completeness limits included in our redshift bins. For $1 < z < 2$ and $2 < z < 3.1$, we obtained a completeness limit of 10^9 $M_\odot$ and $10^{9.5}$ $M_\odot$, respectively.

Regarding the GRB samples, their host galaxies, observed thus far with HST/WFC3 at $z > 1$, represent only a small fraction of all GRBs currently identified at these redshifts. In addition, these observations result from different HST programs with distinct objectives, with a clear trend toward dark GRB host galaxies. For this reason, the selection function is not simple to model. To get an insight into the effect that our selection method introduces, we compared the redshift and stellar mass cumulative distribution functions (CDFs) of our GRB host sample to the host galaxies of complete unbiased GRB samples of BAT6 (Salvaterra et al. 2012) and SHOALS (Perley et al. 2016a). The CDFs were computed at $1 < z < 2$ and $2 < z < 3.1$ based on a method that is similar to the one developed by Palmerio et al. (2019) and described further in Sect. 2.2.4.4. We extracted stellar masses from Perley et al. (2016b) for the SHOALS sample and from Palmerio et al. (2019) and Perley et al. (2016b) for the BAT6 sample. We note that for the BAT6 sam-

ple all objects at $2 < z < 3.1$ are included in the SHOALS sample. The choice of stellar masses used for our GRB host sample is discussed in Sect. 2.2.4.2. In the subsequent analysis, we only considered GRB hosts with a stellar mass above the mass-completeness limit of the 3D-HST sample described earlier. We therefore perform a comparison between the different GRB host samples using a similar constraint.

The distributions of redshifts and stellar masses at $1 < z < 2$ and $2 < z < 3.1$ are shown in Figs. 2.12 and 2.13. In the literature, the stellar masses of the SHOALS sample are provided without uncertainties. The uncertainties associated with the CDF, red shaded area in Fig. 2.13, are only produced by the upper mass limit present in the sample. At $1 < z < 2$, the results show good agreement between the hosts associated with the two unbiased GRB samples and ours. We note however a small offset between the BAT6 sample and the two other samples. At this redshift bin, the majority of GRB hosts (8/10) in the BAT6 sample are also included in SHOALS. For these sources, the stellar masses reported by Perley et al. (2016b) are, on average, higher than the ones derived by Palmerio et al. (2019) (see also Fig. 2.15). However, only three (over 22) stellar masses from Perley et al. (2016b) are used in our own sample. This might suggest that the small offset observed at $1 < z < 2$ between our sample and BAT6 has a different origin than the one observed between SHOALS and BAT6. At $2 < z < 3.1$, our sample appears to be biased toward more massive GRB host galaxies. We note that our samples are composed of $\sim 60\%$ and 100% of dark GRBs ($\beta_{\rm ox} < 0.5$, Jakobsson et al. 2004) at $1 < z < 2$ and $2 < z < 3.1$, respectively. The estimated fraction of dark GRBs in the overall GRB population is not well constrained but it seems that approximately $25 - 40\%$ of *Swift* GRBs are dark (Fynbo et al. 2009; Greiner et al. 2011) and that fraction likely increases with the host stellar mass (Perley et al. 2016a). In our sample, the large number of dark bursts is probably due to an important part of HST programs (proposals ID: 11840, 12949, 13949) dedicated to dark GRB host galaxies. This population appears to be more massive, more luminous, redder, and dustier than the hosts of optically bright GRBs (e.g., Krühler et al. 2011; Svensson et al. 2012; Perley et al. 2013, 2016b; Chrimes et al. 2019). This likely explains why GRB hosts at the high-mass end are over-represented in our sample at $2 < z < 3.1$, compared to the mass distribution of host galaxies drawn from unbiased GRB samples. To summarize, we conclude that our two subsamples are globally consistent with unbiased populations of GRBs studied

previously, although we note a trend for GRB hosts with larger stellar masses in our highest redshift bin.

2.2.4 Methods and measurements

2.2.4.1 GALFIT modeling of GRB hosts

Profile fitting We determined the structural parameters of the GRB host galaxies using a parametric approach based on GALFIT (Peng et al. 2002, 2010). GALFIT is a software using a 2D fitting algorithm to model the surface brightness of galaxies. It allows for the fitting of commonly used astronomical brightness profiles including exponential, Sérsic, Nuker, Gaussian, King, Moffat, and PSF. We fit the GRB host galaxies using a unique single Sésic profile to have a similar approach to the 3D-HST sample (van der Wel et al. 2012, 2014). Because we have more than a few galaxies to analyze, we automated the following process in PYTHON. First, we created a cutout of 200 × 200 pixels around the host galaxy position. We then ran SExtractor (Bertin & Arnouts 1996) on the resulting cutout to detect all objects present in the image. We used the segmentation map returned by SExtractor to mask all unnecessary sources. Close, large, or bright sources to the target object are fit simultaneously to reduce their possible contamination. However, fitting many objects increases the number of free parameters and can make GALFIT converge to a local minimum. To choose the neighboring objects to be included in the analysis, we used similar conditions, as described in Vikram et al. (2010). We observe that their conditions based on the isophotal surface and semi-major axis of objects give good results. For the remaining unmasked objects, we modeled them using single Sérsic profile. We initialized the parameters of each component to the values returned by SExtractor through MAG_AUTO, FLUX_RADIUS, ELONGATION, and THETA_IMAGE. We note that the empirical formula, $R_{\rm e} = 0.162 \times \mathrm{FLUX\_RADIUS}^{1.87}$, determined by Häussler et al. (2007) can help to converge in some cases. Finally, we started the Sérsic index at an exponential profile ($n = 1$). If GALFIT was not shown to converge, we progressively increased the value.

SExtractor tends to overestimate the sky level (Häussler et al. 2007). For this reason, we set the input sky level at the SExtractor value and let GALFIT

optimize simultaneously the sky value and the other components. We also let GALFIT internally determine its own sigma image (noise map). The calculation is described in the GALFIT user's manual (Eq. 33). It takes into account the Poisson source noise in addition to the uncertainty on the sky estimation. HLA products are given in electrons/s and have to be converted in electrons before computing the noise map (GALFIT requirement). We multiplied the image by the EXPTIME keyword from the fits header to go back in e^- unit. GALFIT considers two additional keywords from the fits header: GAIN (detector gain) and NCOMBINE (number of combined images). As we were already working in electrons unit (not in counts), we set the GAIN keyword to 1. For HLA products, the EXPTIME value already includes the total exposure time from each individual frame. We thus set the NCOMBINE keyword to 1.

GALFIT needs the instrumental response, also known as the point spread function (PSF), to convolve its models and improve the fitting process. To create a PSF model for the HST, three methods are possible: using an empirical model by stacking isolated and bright point-like sources from observations, using a synthetic model from TinyTim modeling software, or using a combination of the two. Models created by TinyTim (Krist et al. 2011) are often not adapted for data analysis due to instrumental effects such as spacecraft jitter or instrument breathing. They need to be corrected for a better matching. Moreover, it is not feasible to derive an empirical PSF model for each GRB host image. Some GRB host fields are very poor in stars (e.g., GRB 060719). The resulting PSF models would have a low signal to noise ratio (S/N) and may introduce artifact in the GALFIT model. To obtain a PSF model with a high S/N, we extracted and combined the stars from all GRB host fields. We isolated a total of 35 stars that we provide to PSFEx (Bertin 2011) to generate a PSF. Then we investigated the possible effects of the PSF modeling. To do so, we applied our wrapper with different PSF models on all GRB hosts at $1 < z < 2$. We used two PSFs derived in a rich-stars and poor-stars fields in addition to the one combining stars from all fields. The three PSFs have a similar radius profile but the S/N is progressively degraded as the number of stars used to generate the PSF decreases. We find a good agreement for all parameters, only the Sérsic index varies with the PSF used, as it tends to increase as the S/N of the PSF decreases. Since our study is mainly focused on the half-light radius of GRB host galaxies, we conclude that using the PSF combining stars from multiple fields would not significantly affect our results.

We investigated whether our values determined by GALFIT are consistent with those inferred by van der Wel et al. (2014). Our measurements on the randomly selected objects from the 3D-HST catalog show a good agreement with their estimates (see Appendix 2.2.2.B for details). The half-light radii are recovered within 10% at a magnitude of 21.5 (bottom panel of Fig. 2.25). We tended to progressively overestimate the R_e as the magnitude increases until reaching 50% at a $F160W$ magnitude of 26. Given that our GRB hosts above the 3D-HST mass-completeness limit have magnitudes below 25, we conclude that our fitting procedure is consistent with that of van der Wel et al. (2014) and that the comparison between GRB hosts and 3D-HST objects does not suffer from a strong systematic bias.

Uncertainties It is widely known that GALFIT tends to underestimate the uncertainties associated with the model parameters (Häussler et al. 2007). To improve the uncertainty estimates for GRB host models, we use a Monte Carlo (MC) approach. First, we consider the best-fitting models returned by GALFIT to create artificial sources. We then inject these sources into randomly selected 50-pixels[9] empty regions of the science image. For all objects, the box size is maintained constant to probe environments with similar neighboring objects. We perform one hundred realizations for each object. Finally, the uncertainties are given by the standard deviation between the realizations and the best model. This method mainly captures the uncertainty from the sky estimation. For most of the objects, we find a higher uncertainties than those of GALFIT, especially for the magnitudes and half-light radii. In some cases when the S/N becomes small or the neighbor contamination is dominant, our MC method determines an error lower than the one derived by GALFIT. For this reason, we consider in our analysis the largest uncertainty returned by GALFIT or the MC approach.

Alternative approach If GALFIT does not converge, we use an alternative procedure to obtain an equivalent GALFIT model. First, we run GALFIT with R_e fixed at the SExtractor value. If GALFIT successfully converges to a realistic model (no parameters between '*' and $n < 8$), we re-run GALFIT with all parameters except R_e fixed at the new model values. Using this method, we can estimate for each object (which has not converged with the standard procedure) a GALFIT model

[9]We cut all models when the flux goes below 0.5% of the maximum and note that $\sim$ 80% objects have a final size lower than 50×50 pixels.

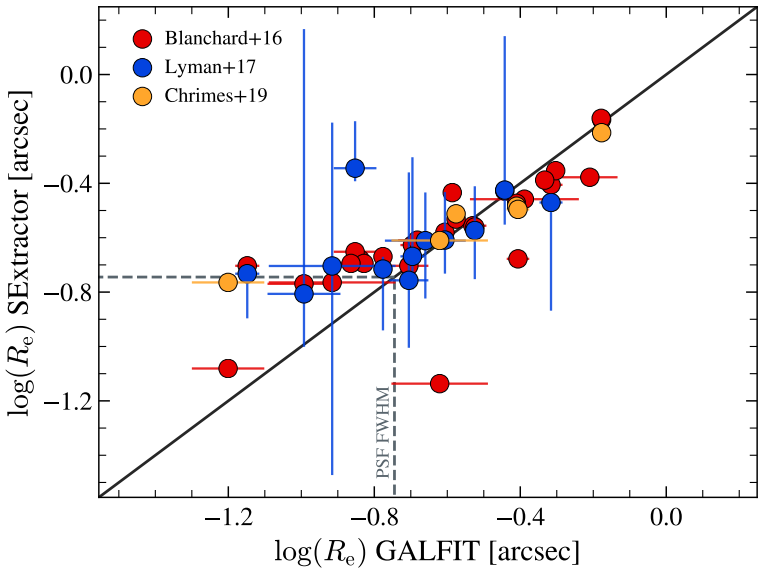

Figure 2.14: Half-light radius of GRB hosts estimated by `GALFIT` in this work (*x axis*) compared to estimates based on `SExtractor` extracted from the literature (*y axis*). The FWHM of the PSF is visible as a gray dashed line.

and its uncertainties. The models are thus consistent with the standard approach, except that they are constrained by the `SExtractor` input value. We used this method for two objects of the full sample (see Sect. 2.2.4.2).

2.2.4.2 GRB hosts properties

Structural parameters The structural parameters and their uncertainties are presented in Table 2.1. We provide, for each host galaxy, the $F160W$ AB magnitude, the half-light radius, the Sérsic index, and the axis ratio returned by `GALFIT`. A total of 35/37 GRB host galaxies converge successfully to realistic parameters. The models and the residuals maps are visible in Appendix 2.2.2.C (Figs. 2.26-2.26).

We used a specific treatment for the host galaxy of GRB 080319C. Perley et al. (2009) and Lyman et al. (2017) reported that a bright foreground galaxy is probably superimposed on the true host galaxy. The redshift of this object was determined from absorption lines in the GRB afterglow. No spectroscopic observations were performed to confirm the association with the host galaxy. The results of `GALFIT` using a single Sérsic model show a residual source located to the south-east of the main object. This source is consistent with the GRB position and

Table 2.1: Physical and structural properties of GRB hosts at $1 < z < 3.1$.

GRB	z	$\log(M_*/M_\odot)$	SFR ($M_\odot$/yr)	AB Mag	R_e (arcsec)	n	q	Ref.
050315	1.95	9.77	> 7.57	23.67 ± 0.08	0.20 ± 0.02	1.86 ± 0.52	0.37 ± 0.04	9, 1
050408	1.24	$9.37^{+0.21}_{-0.24}$	...	23.48 ± 0.07	0.30 ± 0.03	1.01 ± 0.41	0.19 ± 0.06	1
060502A[c]	1.51	...	...	...	...	...	...	
060719	1.53	9.84	$7.1^{+18.9}_{-3.9}$	23.24 ± 0.08	0.21 ± 0.03	4.12 ± 0.99	0.37 ± 0.06	9, 10
060814	1.92	$10.43^{+0.12}_{-0.12}$	56.0^{+9}_{-9}	23.04 ± 0.03	0.29 ± 0.01	1.61 ± 0.18	0.36 ± 0.02	2, 2
061007	1.26	$8.9^{+0.4}_{-0.5}$	$4.4^{+6.2}_{-2.1}$	23.70 ± 0.05	0.36 ± 0.02	0.60 ± 0.10	0.50 ± 0.04	4, 7
070125[b]	1.55	...	...	...	...	...	...	
070208	1.17	$9.87^{+0.26}_{-0.19}$	...	22.35 ± 0.01	0.26 ± 0.01	0.36 ± 0.03	0.60 ± 0.01	1
070306	1.50	$10.48^{+0.06}_{-0.06}$	38.0^{+2}_{-2}	21.71 ± 0.04	0.14 ± 0.01	4.50 ± 0.73	0.35 ± 0.01	2, 10
071122	1.14	$9.75^{+0.26}_{-0.22}$	...	22.56 ± 0.06	0.48 ± 0.04	1.45 ± 0.17	0.47 ± 0.02	1
080319C	1.95	$8.82^{+0.37}_{-0.52}$	...	25.35 ± 0.09	0.09 ± 0.03	0.24 ± 1.11	0.64 ± 0.28	1
080325	1.78	$10.75^{+0.07}_{-0.07}$	$66.09^{+24.3}_{-24.3}$	22.50 ± 0.02	0.50 ± 0.01	0.31 ± 0.03	0.61 ± 0.02	5, 11
080520	1.55	$9.2^{+0.27}_{-0.31}$	...	24.06 ± 0.12	0.14 ± 0.02	2.14 ± 0.85	0.72 ± 0.12	1
080603A	1.69	$10.04^{+0.44}_{-0.23}$	...	22.75 ± 0.04	0.15 ± 0.01	1.69 ± 0.26	0.75 ± 0.05	1
080605	1.64	$10.09^{+0.15}_{-0.15}$	$44.9^{+22.9}_{-22.9}$	22.34 ± 0.04	0.07 ± 0.01	4.48 ± 1.51	0.33 ± 0.07	5, 10
080707	1.23	$9.68^{+0.27}_{-0.24}$	...	22.87 ± 0.05	0.25 ± 0.01	2.04 ± 0.24	0.37 ± 0.02	1
080805	1.51	$9.53^{+0.22}_{-0.22}$	20.6^{+12}_{-12}	23.09 ± 0.04	0.30 ± 0.02	1.77 ± 0.23	0.31 ± 0.04	5, 10
080928[b]	1.69	...	...	...	...	...	...	
081008[b]	1.97	...	...	...	...	...	...	
090113	1.75	9.89	$17.9^{+10.1}_{-4.8}$	22.87 ± 0.02	0.27 ± 0.01	1.11 ± 0.08	0.74 ± 0.02	8, 10
090407	1.45	$10.02^{+0.11}_{-0.11}$	$14.06^{+4.87}_{-4.87}$	22.92 ± 0.04	0.39 ± 0.02	1.16 ± 0.15	0.31 ± 0.02	5, 10
090418A	1.61	9.61	...	23.58 ± 0.04	0.17 ± 0.01	1.27 ± 0.26	0.43 ± 0.04	9
091208B[b]	1.06	...	...	...	...	...	...	
100615A	1.40	$8.6^{+0.2}_{-0.2}$	$8.6^{+13.9}_{-4.4}$	23.90 ± 0.04	0.06 ± 0.01	3.50 ± 1.65	0.36 ± 0.12	4, 10
120119A	1.73	$9.58^{+0.14}_{-0.14}$	$25.5^{+14.1}_{-14.1}$	23.24 ± 0.12	0.14 ± 0.02	5.28 ± 2.15	0.49 ± 0.06	5, 10
140331A	$1.00^{a\,+0.11}_{-0.04}$	$11.22^{+0.11}_{-0.17}$	$5.3^{+4.3}_{-2.4}$	...	...	...	...	6, 6
150314A	1.76	$10.01^{+0.45}_{-0.26}$	...	23.00 ± 0.07	0.27 ± 0.03	3.05 ± 0.48	0.73 ± 0.04	1
160509A	1.17	$9.8^{+0.26}_{-0.22}$	...	22.53 ± 0.03	0.26 ± 0.01	1.98 ± 0.13	0.36 ± 0.03	1
050401	2.90	9.61	> 3.17	25.03 ± 0.09	0.10 ± 0.02	2.45 ± 1.93	0.30 ± 0.20	9, 1
050406X[c]	2.44	...	> 1.69	...	...	...	...	1
060124	2.30	$8.7^{+0.47}_{-0.54}$	...	25.83 ± 0.21	0.12 ± 0.05	0.39 ± 0.99	0.99 ± 0.43	1
070521	2.09	$10.65^{+0.21}_{-0.002}$	$49.85^{+72.33}_{-2.86}$	22.93 ± 0.18	0.22 ± 0.06	5.92 ± 2.08	0.51 ± 0.06	3, 3
070802	2.45	$9.57^{+0.19}_{-0.19}$	$32.2^{+17.8}_{-17.8}$	23.74 ± 0.28	0.41 ± 0.14	3.76 ± 1.48	0.63 ± 0.09	5, 10
071021	2.45	$11.08^{+0.05}_{-0.05}$	90.0^{+5}_{-5}	23.20 ± 0.05	0.30 ± 0.02	1.68 ± 0.26	0.40 ± 0.03	2, 2
071031[b]	2.69	...	...	...	...	...	...	
080207	2.09	$11.3^{+0.02}_{-0.02}$	250.0^{+13}_{-13}	23.38 ± 0.84	0.67 ± 0.02	0.33 ± 0.05	0.76 ± 0.03	2, 2
080603B[b]	2.69	...	...	...	...	...	...	
080607	3.04	$10.44^{+0.13}_{-0.13}$	$35.2^{+13.9}_{-13.9}$	24.01 ± 0.19	0.62 ± 0.11	1.99 ± 0.37	0.56 ± 0.05	5, 5
081121	2.51	9.24	...	24.70 ± 0.09	0.20 ± 0.02	1.63 ± 0.60	0.26 ± 0.07	9
081221	2.26	$10.58^{+0.02}_{-0.02}$	35.0^{+2}_{-2}	23.23 ± 0.03	0.46 ± 0.01	0.29 ± 0.05	0.37 ± 0.02	2, 2
090404	$3.00^{a\,+0.83}_{-1.82}$	11.1	381.0	23.74 ± 0.06	0.66 ± 0.03	0.68 ± 0.08	0.33 ± 0.02	13, 13
090426S	2.61	$9.0^{+0.46}_{-0.5}$	14.4^{+2}_{-2}	25.53 ± 0.14	0.05 ± 0.03	2.25 ± 4.08	0.14 ± 0.57	1, 14
110709B	2.09	9.2	...	24.58 ± 0.21	0.24 ± 0.07	3.87 ± 1.85	0.60 ± 0.13	9
111215A	$2.06^{a\,+0.10}_{-0.16}$	$10.5^{+0.1}_{-0.2}$	34.0^{+33}_{-13}	22.41 ± 0.05	0.39 ± 0.03	1.92 ± 0.23	0.53 ± 0.02	12, 12

Notes. [a] Photometric redshift ; [b] No host detected ; [c] `GALFIT` has not converged . Names in bold are dark GRBs.

References. (1) This work; (2) Hsiao et al. (2020); (3) Hashimoto et al. (2019); (4) Palmerio et al. (2019); (5) Corre et al. (2018b); (6) Chrimes et al. (2018); (7) Vergani et al. (2017); (8) Krühler & Schady (2017); (9) Perley et al. (2016b); (10) Krühler et al. (2015); (11) Hashimoto et al. (2015); (12) van der Horst et al. (2015); (13) Hunt et al. (2014); (14) Levesque et al. (2010a).

supports the hypothesis that an object is overlapping the true host. We use two Sérsic components to model and mitigate the contamination of the superimposed object. We then add a single Sérsic component to the overall `GALFIT` model to fit the residual source near the GRB location. The host galaxies of GRB 070802 and GRB 090404 do not converge to realistic parameters ($n > 8$) with the standard approach. We note that bright sources are close to the host galaxy and likely contaminate it. For these objects, we used the procedure described in Sect. 2.2.4.2, where the R_e is maintained at the `SExtractor` value. Finally, the host galaxies of GRB 060502A and 050406X do not converge even when keeping the R_e fixed at the first guess of `SExtractor`. These objects are very faint sources with a low S/N and might diverge numerically easily due to contamination by neighboring objects.

Blanchard et al. (2016), Lyman et al. (2017), and Chrimes et al. (2019) reported the measurement of half-light radii using `SExtractor` for GRB hosts mainly observed by the WFC3 in the $F160W$ filter. A fraction of our GRB hosts matches their objects. The comparison between their `SExtractor` and our `GALFIT` values is shown in Fig. 2.14. We find good agreement for objects with a R_e greater than the full width at half maximum (FWHM) of the PSF. For objects with a half-light radius derived by `SExtractor` and close to the FWHM, we find that `GALFIT` returns smaller R_e. We expect this behavior because `GALFIT` convolves its models with the PSF function. It can therefore capture smaller structures of the galaxy.

Stellar mass The stellar masses of GRB host galaxies used in this work were mostly gathered from the literature. For some objects, we find multiple estimates where most of them were obtained with SED fitting using several photometric points. Only stellar masses from Perley et al. (2016b) were derived using a single photometric point (*Spitzer*/IRAC 3.6 μm band) and a method based on a mass-redshift grid of galaxy SED models. We compare all these estimates in Fig. 2.15 (top panel) and we note a significant discrepancy in many cases (up to ~ 0.9 dex). The SED fitting codes based on an energy balance principle (e.g., CIGALE, Noll et al. 2009; Boquien et al. 2019) can model the stellar luminosity absorbed by dust and its re-emitted luminosity in the IR. If a far-infrared (FIR) band is used to constrain the models, a more realistic attenuation value can be derived and thus we expect a more accurate stellar mass. For this reason, we selected (preferentially) the estimates in the following order: (1) SED fitting with optical/near-IR

(NIR) and FIR measurements using an energy balance code; (2) SED fitting with optical/NIR measurements; and (3) a mass-to-light ratio.

For GRB hosts with no stellar mass reported in the literature and not enough photometric points to determine a stellar mass from a SED fitting, we derived our own estimate based on a mass-to-light (M/L) ratio (Bell & de Jong 2001) applied to the $F160W$ magnitude determined by `GALFIT`. We used the COSMOS2015 (Laigle et al. 2016) catalog to find a relation between stellar mass and NIR luminosity at a given redshift. The COSMOS2015 survey covers a larger area (~ 2 degree^2) than the 3D-HST/CANDELS survey and gives access to a larger number of galaxies ($> 500\,000$ objects). The catalog provides a total of 16 photometric bands from the ultraviolet to the mid-infrared, including the H band ($\lambda_{\rm mean} \sim 1.64$ μm) of the *VISTA* infrared camera. Given that magnitudes of GRB hosts are obtained with WFC3/$F160W$ filter ($\lambda_{\rm mean} \sim 1.54$ μm), we applied a color correction on each GRB host magnitude. To estimate this value, we matched the objects that were observed in the 3D-HST/COSMOS field and the COSMOS2015 catalog. We measured a mean difference of 0.08 mag between the two filters. Finally, we corrected the GRB host galaxy magnitudes for the Galactic extinction using the measurements from Schlafly & Finkbeiner (2011).
To determine the M/L ratio, we first selected all the star-forming galaxies `(CLASS=1)` from the COSMOS2015 catalog at $z_{\rm target} \pm 0.1$. We then fit a linear relation between H_{VISTA} magnitudes and stellar masses of the identified objects. We finally used the linear model and the GRB host magnitudes earlier corrected for color excess and Galactic extinction to obtain the stellar mass. We note that our M/L ratio is based on magnitude in COSMOS2015 determined from aperture photometry using `SExtractor`, while our magnitude is determined by `GALFIT`. Skelton et al. (2014) showed that for the 3D-HST catalog the median difference is lower than 0.04 mag in the range $21 < H_{F160W} < 24$ between `SExtractor` and `GALFIT` measurements. We did not correct for this effect, which would have only a minimal consequence on the estimated stellar mass. In addition, we compared the stellar masses derived using the COSMOS2015 catalog with those calculated from the M/L ratios of the 3D-HST catalog. We find a good agreement between the two estimates for the entire sample of GRB hosts. In our analysis, we used the estimates from the COSMOS2015 catalog, which are based on a larger statistic. The uncertainties are derived by propagating the uncertainty of the `GALFIT` magnitude

models[10]. We select all galaxies inside $z_{\rm target} \pm 0.1$ and with a $\rm mag_{target} \pm \delta mag_{target}$. We then computed the 1σ error by taking the $16^{\rm th}$ percentile and $84^{\rm th}$ percentile of the resulting galaxy distribution.

As a sanity check, we also applied this M/L procedure to the hosts with stellar masses determined in the literature and selected according to the requirements described above. The comparison between the two is visible in Fig. 2.16, where we color-code the GRB hosts according to their redshift. We find an overall agreement between the two estimates, but we also note a linear trend evolving with stellar mass, where low (high) stellar mass galaxies tend to be overestimated (underestimated). In particular, two GRB hosts have mass estimates differing by more than 0.8 dex (GRB 071021 and GRB 090404). These sources are located at $z > 2.4$ where the WFC3/$F160W$ filter probes bluer wavelengths, more subject to dust extinction. As GRB host magnitudes are not corrected for galaxy attenuation, they might lead to underestimate the stellar mass derived from a M/L ratio. In addition, we use a single Sérsic profile to model each GRB host galaxy. This enabled us to catch most of the flux for the majority of objects, but in some cases (e.g., GRB 080207, GRB 111215A), more components would have been required to improve the fit and the magnitude estimate. This might have contributed to underestimate their total flux and therefore their stellar mass. With this caution in mind, we note however that the few GRB hosts with mass estimates relying on this M/L approach (see Table 2.1) have redshifts and stellar masses in the range where Fig. 2.16 reveals consistent results with the more conventional SED fitting method. This supports therefore the reliability of our measurements, which should not introduce any additional systematics given their otherwise large statistical uncertainties.

Star formation rate The star formation rates of GRB host galaxies are also gathered from the literature. In a similar way to stellar masses, we show in Fig. 2.15 (bottom panel), the dispersion of SFR measurements obtained for a same sources. We yet observe a better agreement between SFRs than previously found for $\rm M_*$. We note in several cases that the SED fitting solution used to estimate these star formation rates (e.g., Corre et al. 2018b; Palmerio et al. 2019) was constrained using SFR measurements determined from emission lines fluxes published in other

[10]More particularly, we use the largest uncertainty values returned by `GALFIT` or the MC approach, as described in the Sect. 2.2.4.1.

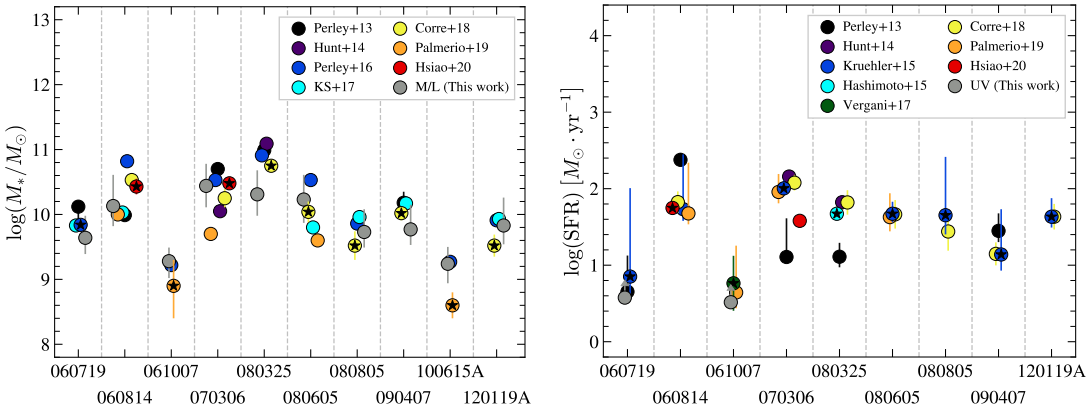

Figure 2.15: Compilation of stellar mass (top panel) and SFR (bottom panel) estimates for GRB hosts at $1 < z < 2$. Each circle corresponds to an estimate from the literature or determined as described in Sect. 2.2.4.2. The circles marked with a star represent the estimates used in our analysis.

works (e.g., Krühler et al. 2015). This contributes to reduce the dispersion between estimates observed in Fig. 2.15. In general, it is expected that estimates including observations in the FIR give a more reliable SFR because the thermal emission of cold dust heated by O/B stars is more accurately modeled. We therefore preferentially select the SFR estimated by (1) SED fitting with optical/NIR and FIR measurements using energy balance code, (2) Dust corrected H_α luminosity (3) SED fitting with optical/NIR measurements. Only for GRB 070306, we consider the SFR based on H_α luminosity instead of the SED fitting with FIR observations. Indeed, the SED of the galaxy in Hsiao et al. (2020) does not match correctly the *Herschel*/PACS observations. The model seems to underestimate the IR luminosity and thus the total SFR of the galaxy, as also suggested by the higher SFR estimate obtained from H_α. At $1 < z < 2$ we have a majority (10/11) of SFRs from H_α and one estimate based on SED fitting including a FIR measurement (ALMA detection). The tracers are more diversified at $2 < z < 3.1$ with 5 over 9 objects from SED fitting with ALMA detection, one from H_α, two from SED fitting with optical/NIR measurements and one from the rest-frame UV continuum emission.

If no SFR is found in the literature, we derived a lower limit value based on the R-band magnitude of Hjorth et al. (2012). This filter probes the UV rest-frame of the galaxy at $z > 1$. The UV light is mainly radiated by young and short-lived stars. It is another indicator of recent SFR in the galaxy. However,

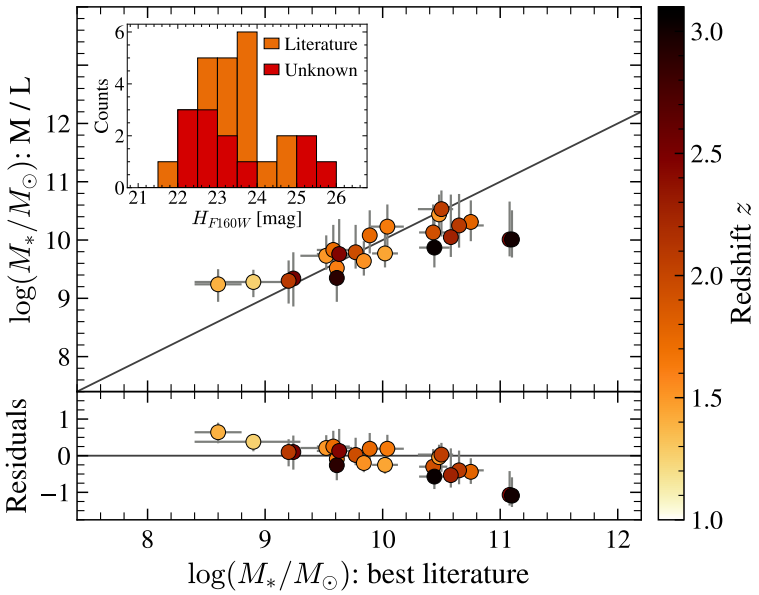

Figure 2.16: Stellar mass of GRB hosts estimated from mass-to-light ratios, compared with the best estimates selected from the literature (Sect. 2.2.4.2). The residuals are shown in the bottom panel. Each GRB host is color-coded according to its redshift. The inset represents their associated $F160W$ magnitude distribution (orange histogram) and the distribution of the GRB hosts for which no stellar mass measurement exists in the literature (red histogram).

the UV radiation is subject to dust reddening caused by the Galactic center or the galaxy itself. We corrected UV magnitudes from the Galactic extinction using Schlafly & Finkbeiner (2011) measurements. We then derived a $\mathrm{SFR_{UV}}$ using the relation from Kennicutt (1998). Nevertheless, we only considered these values as lower limits of the SFR since the UV luminosities are not corrected for the dust attenuation in the host itself.

2.2.4.3 Stellar mass and star formation surface densities

For GRB hosts and star-forming galaxies, the stellar mass density is given by

$$\Sigma_{\mathrm{M}} = \log\left(\frac{\mathrm{M}/2}{\pi R_e^2}\right), \tag{2.7}$$

where M is the stellar mass in $\mathrm{M_\odot}$, and the star formation surface density by

$$\Sigma_{\mathrm{SFR}} = \log\left(\frac{\mathrm{SFR}/2}{\pi R_e^2}\right). \tag{2.8}$$

The M_* and SFR are divided by the galaxy projected area defined by the half-light radius. As it contains half of the total light of the galaxy, a correction factor of 1/2 is applied to the M_* and SFR while assuming that the matter is uniformly distributed inside the galaxy. We derived the $\Sigma_{\rm M}$ and $\Sigma_{\rm SFR}$ errors by propagating the uncertainties of the stellar masses, the star formation rates, and the half-light radii.

2.2.4.4 Statistical tests

We applied the Kolmogorov-Smirnov (K-S) test to compare the CDFs of GRB hosts and field galaxies. We considered a similar Bayesian inference framework as described by Palmerio et al. (2019). This approach considers that each parameter value ($R_{\rm e}$, $\Sigma_{\rm M}$, $\Sigma_{\rm SFR}$) is described by an asymmetric Gaussian. The center of the distribution is given by the value in Table 2.1 and the asymmetrical standard deviation is given by errors associated with that value. We sampled each Gaussian probability density function (PDF) with 10 000 (N_{real}) MC realizations. We then built N_{real} different CDFs for the GRB hosts and 3D-HST samples. Finally, we computed N_{real} MC realizations of the two sided K-S test from the previous samples of CDFs. We thus obtained a distribution function of D-statistic and $p-$values that provide confidence bounds on the K-S test.

2.2.5 Results

2.2.5.1 $R_{\rm e}$-M_* relation

In Fig. 2.17 (top panel), we show the half-light radii ($R_{\rm e}$) against stellar masses for the GRB hosts and 3D-HST star-forming galaxies. As mentioned previously, it is commonly accepted that long GRBs are related to recent star formation activity in their host. If GRB hosts trace the star-forming sources with no bias, then galaxies with higher SFR should have a higher probability of producing a GRB. Based on this assumption, we weighted the control sample by its SFR to mimic a population of galaxies that should host GRBs with no environmental dependence. The resulting SFR-weighted $R_{\rm e}$-M_* relation (cyan curve) is close to the median relation characterizing the field galaxies (gray curve). This is expected because for a given stellar mass, the radius does not depend much on the SFR, as can be

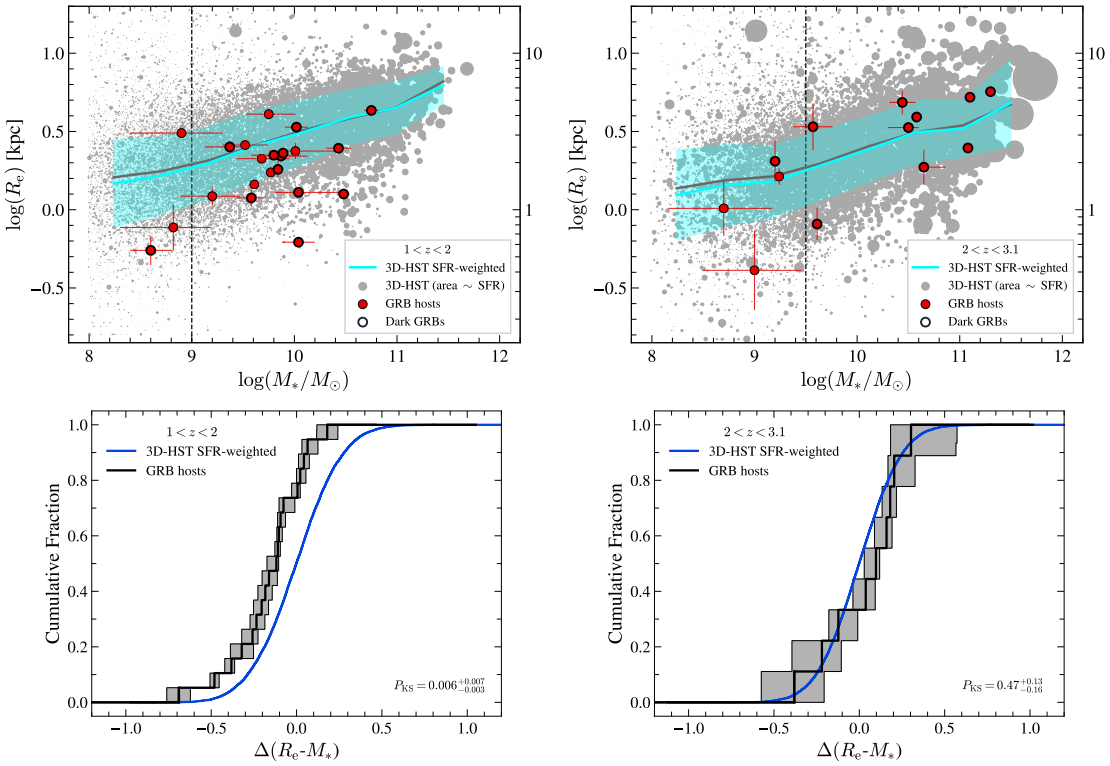

Figure 2.17: Size-mass relations and size deviations of GRB hosts from star-forming galaxies. Top panels: Half-light radius against stellar mass for GRB hosts and star-forming galaxies at $1 < z < 2$ (left panel) and $2 < z < 3.1$ (right panel). The GRB host galaxies are displayed as red circles and the 3D-HST star-forming galaxies are shown as gray circles with an area proportional to their SFR. The median of the star-forming population is shown as a dashed gray line. The dashed cyan line represents the expected median of a GRB hosts population that does not suffer from bias to trace the SFR (gray circles weighted by their SFR). The 1σ uncertainty of the cyan median is given as a shaded cyan region. The vertical dashed black line is the mass-completeness limit of the 3D-HST survey. Bottom panels: Cumulative distribution of $\Delta(R_e\text{-}M_*)$ at $1 < z < 2$ (left panel) and $2 < z < 3.1$ (right panel). The $\Delta(R_e\text{-}M_*)$ represents the distance between GRB hosts and the SFR-weighted $R_e\text{-}M_*$ relation of the top panels. The blue curve is a Gaussian CDF with a mean of 0 and a standard deviation defined by the 1σ errors of the shaded cyan area at the GRB hosts positions. The $p-$value returned by the two-sided K-S test is provided in the right bottom part of panels.

seen from the sizes of the gray circles in Fig. 2.17. The 1σ uncertainty associated with the SFR-weighted R_e-M_* relation (cyan region) was derived using the median absolute deviation (MAD) estimator.

Figure 2.17 (top left panel) clearly shows that GRB hosts are markedly different from the general population. Indeed, we note a larger number of GRB hosts below the SFR-weighted relation at $1 < z < 2$. If GRB hosts were truly representative of the overall population of star-forming sources, we would expect approximately equal numbers above and below the SFR-weighted relation. For GRB hosts at $2 < z < 3.1$, we observe however a more uniform distribution of sizes with respect to field galaxies, and a better agreement with the SFR-weighted relation. The predominance of dark GRB hosts in the samples and how these results are representative of the whole GRB host population will be further discussed in Sect. 2.2.5.3. Because GRB hosts commonly occur in faint and low stellar mass galaxies (Fruchter et al. 2006) and given the positive trend of the R_e-M_* relation (massive galaxies are also larger), a straight comparison between the distribution of their sizes and that of the overall population of star-forming sources, irrespective of their stellar mass, would necessarily be biased. To quantify if GRB host galaxies are not smaller only because they explode in faint galaxies, we measure for each GRB host the distance between its position in Fig. 2.17 (top panel) and the SFR-weighted R_e-M_* relation at the same stellar mass, denoted as $\Delta(R_e\text{-}M_*)$ hereafter, such that

$$\Delta(R_e\text{-}M_*) = \log\left(R_{e,\,\mathrm{GRBH}}\right) - \log\left(R_{e,\,\mathrm{3D\text{-}HST\,SFR\text{-}weighted,\,median}}\right). \tag{2.9}$$

If GRB hosts are representative of field star-forming sources, we should expect that the CDF of $\Delta(R_e\text{-}M_*)$ to be distributed around zero. To test this assumption, we applied a K-S test, as described in Sect. 2.2.4.4, only considering GRB hosts and field galaxies above the 3D-HST mass-completeness limits quoted earlier. We compared the $\Delta(R_e\text{-}M_*)$ CDF to a Gaussian CDF centered on zero and with a standard deviation given by the median value of the 1σ uncertainties associated with the SFR-weighted relation at each GRB host position. The CDFs and their associated uncertainties are shown in Fig. 2.17 (bottom panel). For GRB hosts at $1 < z < 2$, the two sided K-S test returns a probability of $P_{\mathrm{KS}} = 0.006$. We can rule out the null hypothesis that the two samples are drawn from the same underlying population. At $2 < z < 3.1$, we obtain a K-S probability of $P_{\mathrm{KS}} = 0.47$. In this case, the null hypothesis of the K-S test cannot be rejected and we cannot

rule out the possibility that both samples are drawn from the same distribution.

2.2.5.2 $\Sigma_{\rm M}$-$M_*$and $\Sigma_{\rm SFR}$-M_* relations

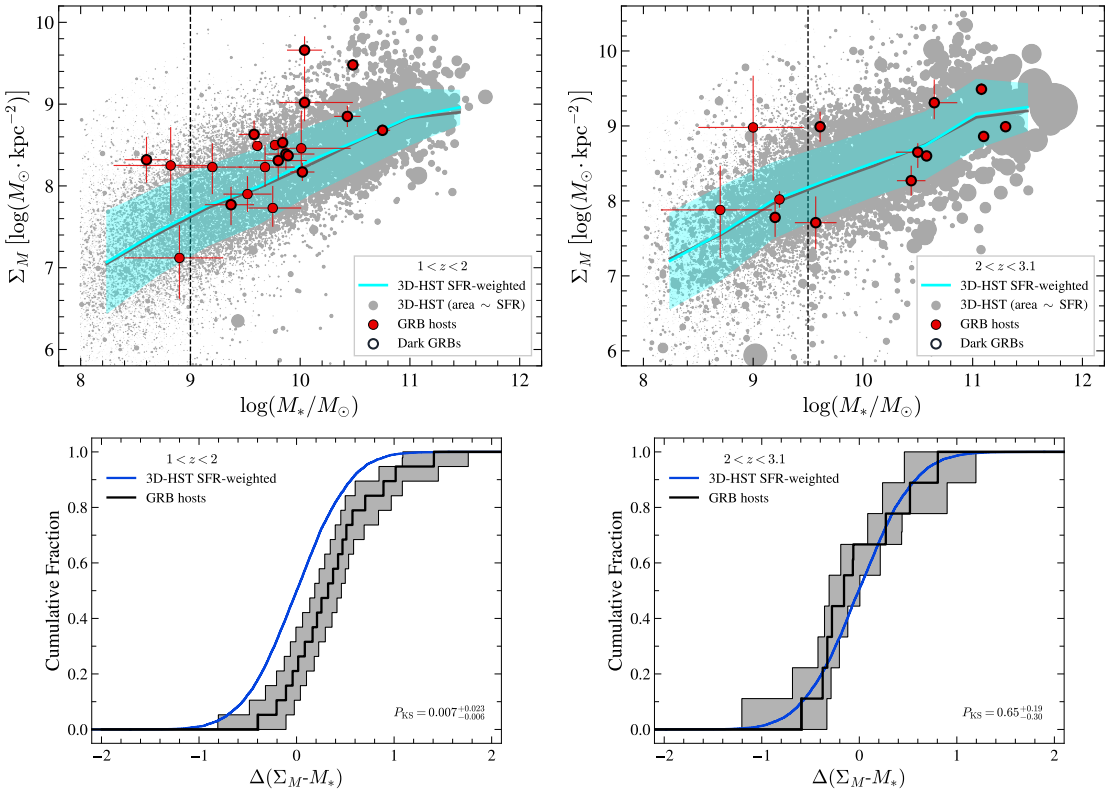

Figure 2.18: Stellar mass surface density ($\Sigma_{\rm M}$) against stellar mass for GRB hosts and star-forming galaxies (top panels) and cumulative distribution of $\Delta(\Sigma_{\rm M}$-$M_*)$ (bottom panels). The symbols are identical to those of Fig. 2.17.

Figures 2.18 and 2.19 (top panels) show stellar mass and star formation surface densities against stellar mass for GRB hosts and field galaxies. At $1 < z < 2$, we note for the $\Sigma_{\rm M}$-M_* and $\Sigma_{\rm SFR}$-M_* planes (top left panels) that the GRB sample is clearly different from the general population, with GRB hosts being placed in a region with higher density values. Regarding the stellar mass densities, we find indeed a larger number of GRB hosts above the SFR-weighted $\Sigma_{\rm M}$-M_* relation at $1 < z < 2$, while a more homogeneous distribution of host galaxies is found at $2 < z < 3.1$ with respect to the field. This is probably a direct consequence of the trend discussed earlier regarding the size distribution of GRB host galaxies, as the hosts at $1 < z < 2$ appear to be smaller (and therefore denser) than typical star-forming sources at comparable stellar masses (see Fig. 2.17). Similarly, we see

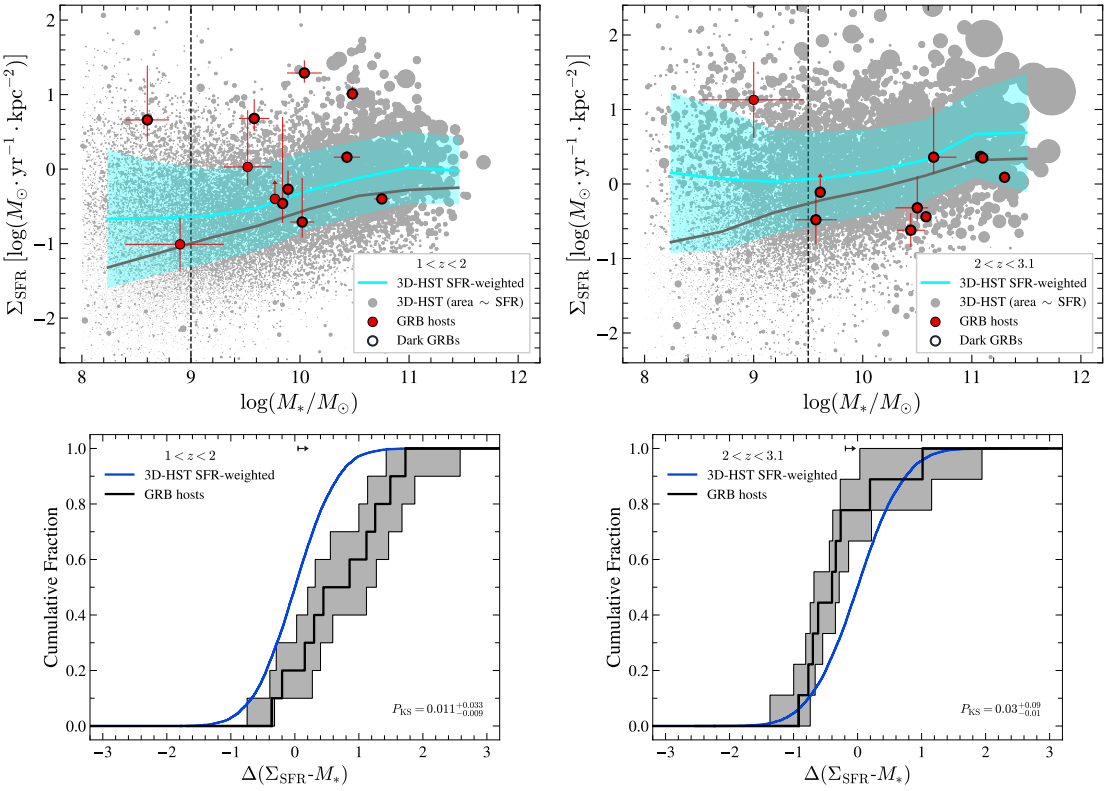

Figure 2.19: Star formation rate surface density ($\Sigma_{\rm SFR}$) against stellar mass for GRB hosts and star-forming galaxies (top panels) and cumulative distribution of $\Delta(\Sigma_{\rm SFR}$-$M_*)$ (bottom panels). Lower limits are represented as arrows and other symbols are identical to those of Fig. 2.17.

that GRB hosts at $1 < z < 2$ exhibit star formation surface densities often higher than typically measured in the field, as a larger number of GRB hosts lie above the SFR-weighted $\Sigma_{\rm M}$-M_* relation. At $2 < z < 3.1$, our results are nonetheless more intriguing, as we observe an opposite trend where the majority of GRB hosts are below the SFR-weighted $\Sigma_{\rm SFR}$-M_* relation.

In a similar way to the approach we followed to compare the size distribution, we then measured the distance between the GRB hosts and the SFR-weighted $\Sigma_{\rm M}$-M_* relation, denoted as $\Delta(\Sigma_{\rm M}$-$M_*)$, and expressed as

$$\Delta(\Sigma_{\rm M}\text{-}M_*) = \Sigma_{\rm M,\,GRBH} - \Sigma_{\rm M,\,3D\text{-}HST\,SFR\text{-}weighted,\,median}, \tag{2.10}$$

and the distance between the GRB hosts and the SFR-weighted $\Sigma_{\rm SFR}$-M_* relation,

denoted as $\Delta(\Sigma_{\rm SFR}\text{-}M_*)$, such that

$$\Delta(\Sigma_{\rm SFR}\text{-}M_*) = \Sigma_{\rm SFR,\,GRBH} - \Sigma_{\rm SFR,\,3D\text{-}HST\,SFR\text{-}weighted,\,median}. \quad (2.11)$$

We then computed their CDFs using the prescriptions given in Sect. 2.2.4.4. The CDFs are shown in the bottom panels of Figs. 2.18 and 2.19. We compare these CDFs to a CDF centered on zero defined in a similar manner as for the $\Delta(R_{\rm e}\text{-}M_*)$ parameter. At $1 < z < 2$, for both parameters we observe a fraction $> 70\%$ of GRB hosts with a distance > 0 to their SFR-weighted relation. We obtain a $p-$value of $P_{\rm KS} = 0.007$ and $P_{\rm KS} = 0.011$ for the $\Delta(\Sigma_{\rm M}\text{-}M_*)$ and $\Delta(\Sigma_{\rm SFR}\text{-}M_*)$, respectively. We can rule out the null hypothesis in both cases. In other words, the K-S test suggests that the GRB host sample is a distinct population from the general star-forming galaxy population. At $2 < z < 3.1$, the median of K-S realizations for $\Delta(\Sigma_{\rm SFR}\text{-}M_*)$ rejects the null hypothesis at the 3% significance level but can also be reconciled with the null hypothesis given the K-S uncertainty. Finally at $2 < z < 3.1$ for $\Delta(\Sigma_{\rm M}\text{-}M_*)$, the K-S test confirms that GRB host galaxies have stellar mass surface densities consistent with those typically found among star-forming sources with similar stellar mass.

2.2.5.3 Hosts of GRBs with dark versus optically bright afterglows

We further investigate whether the deviations found may be due to a predominance of dark GRB hosts in the sample and how these results may be extended to the whole GRB host population. Previous studies on the nature of dark bursts and the properties of their host galaxy found a population of galaxies more massive, with a typical stellar mass of about 10^{10} $\rm M_\odot$, more luminous and with redder colors than optically bright GRB hosts (Krühler et al. 2011; Rossi et al. 2012; Svensson et al. 2012; Perley et al. 2013; Hunt et al. 2014; Perley et al. 2016b). Only a few cases of dark GRBs with low-mass host galaxies have been reported (e.g., GRB 080605 and GRB 100621A, Krühler et al. 2011). The apparent relation between dark GRBs and massive galaxies suggests that the GRB obscuration is mainly due to the dust within the host rather than a dense local environment (clumps) surrounding the GRB. Although a more complex situation with a combination of the two is more likely to be realistic, Corre et al. (2018b), for instance, showed that for half of their sample, a very clumpy local dust distribution near the burst is necessary to reproduce the galaxy attenuation curves. Furthermore, Chrimes et al. (2019)

analyzed a sample of 21 dark GRBs observed with the HST in F606W and F160W filters. They found that dark GRB host galaxies are physically larger but have a morphology (i.e., spirals or irregulars) similar to those of optically bright GRB hosts. They reported no particular evidence of differences in concentration, asymmetry, or ellipticity between the two populations. These findings support the view that dark and optically bright GRB hosts share common morphological properties, except, not surprisingly, for the galaxy size (galaxies with higher stellar mass are also larger, van der Wel et al. 2014).

At $1 < z < 2$ and for $9 \leq \log(\mathrm{M}_*/\mathrm{M}_\odot) \leq 10.2$, the two host subpopulations of dark and optically bright GRB afterglows exhibit properties that overlap each other (as seen in the top left panel of Fig. 2.17). For these sources, we first investigated the distributions of dark versus optically bright GRB hosts in the R_e-M_* plane. To prevent the effect of the positive mass-size trend, we used the $\Delta(R_\mathrm{e}$-$M_*)$ and calculate a median value for each population. We found a median offset of -0.113, -0.105, and -0.109 dex (i.e., $\sim 22\%$ smaller) for dark hosts, optically bright hosts, and the whole subsample, respectively. This indicates that at this redshift range, the size distributions of the two population are consistent with each other, and that the tendency for GRB host galaxies to be smaller than the field is not driven by the large number of dark GRBs within our initial selection. In addition, we note that the median Sérsic index and axis ratio are also similar for both populations, which supports that the dark and optically bright GRB hosts share similar morphological properties, at least for this stellar mass range. As suggested by the R_e-M_* plane, we also find that the two populations are consistent in terms of $\Delta(\Sigma_\mathrm{M}$-$M_*)$. In the case of $\Delta(\Sigma_\mathrm{SFR}$-$M_*)$, the lower statistic makes the comparison more challenging. We note, however, that the two remaining optically bright hosts are in favor of a consistent trend between the two populations.

At $2 < z < 3.1$, our sample is mainly composed of dark GRB hosts with $\log(\mathrm{M}_*/\mathrm{M}_\odot) > 10.5$. Therefore, it is not possible to extend the comparison between the two subpopulations of host galaxies as discussed above and additional HST observations of the hosts of bright afterglows would be needed to draw a firm conclusion about the properties of the whole GRB host population in this redshift range. Because the radii of dark GRB hosts appear more consistent with the size of field galaxies at $2 < z < 3.1$, we argue that a different behavior for the size of the hosts of optically bright GRB afterglows would be difficult to interpret. In this

case, indeed, we would have to explain either why the latter remain more compact than the host of dark GRBs despite their lower obscuration or why they become on the other hand much larger than field sources. However, in the absence of clear observational constraints on their physical size, we acknowledge that caution should be considered regarding the interpretation of our results for this redshift range.

2.2.5.4 Evolution across z

The results previously described in Sects. 2.2.5.1 and 2.2.5.2 reveal that a deviation between GRB hosts and field star-forming galaxies on the R_e-M_*, Σ_M-M_* and Σ_{SFR}-M_* planes exists at $1 < z < 2$. We further investigate how this deviation compares with the trend previously discussed in the literature for GRB hosts at $z < 1$.
At $0.3 < z < 1.1$, we use a GRB host sample extracted jointly from Kelly et al. (2014) and Blanchard et al. (2016). Their respective selections are not drawn from unbiased GRB samples. We use a similar method to the one described in Sect. 2.2.3.4 and evaluate how the CDFs in redshift and stellar mass are distributed compared to the hosts of unbiased GRB samples (BAT6 and SHOALS). The results are presented in Fig. 2.20. We find that the CDFs are consistent with each other for both parameters. This confirms that our sample at $0.3 < z < 1.1$ probes a similar range of stellar masses as the host galaxies of unbiased GRB samples and that our sample does not suffer from an important bias toward low- or high-mass galaxies.

In addition, to enable a comparison as fair as possible with our previous work at $z > 1$ and limit the potential systematic bias between the different studies, we only considered the size measurements reported by these authors. We then re-computed the Σ_M and Σ_{SFR} using M_* and SFR extracted from literature in a way similar to the one described in Sect. 2.2.4.2. From Kelly et al. (2014), we selected the r_{50} determined from the *SDSS* photo pipeline. A part of their sample matches the sample of Wainwright et al. (2007) who used `GALFIT` and a single Sérsic profile to measure galaxy sizes. The comparison of estimates shows good agreement between the two methods. This confirms that using sizes from the *SDSS* photo pipeline should not introduce a significant bias compared to our method. From

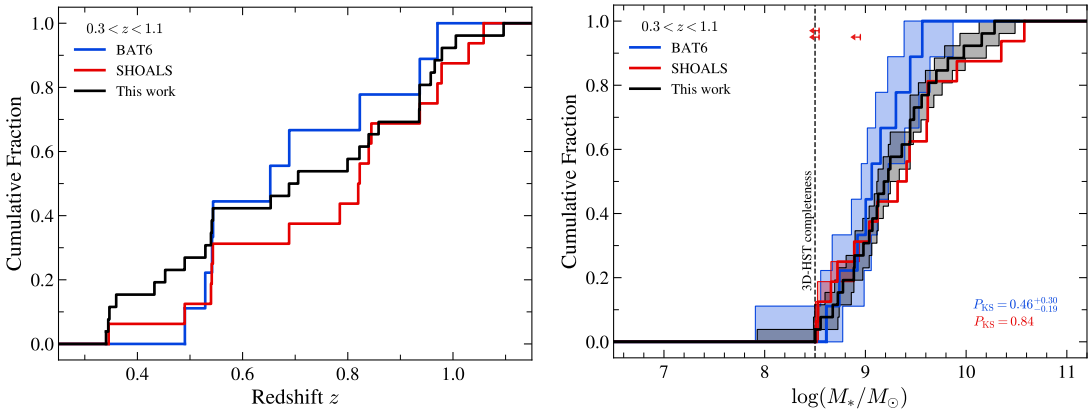

Figure 2.20: Cumulative distributions as in Fig. 2.12 (top panel) and Fig. 2.13 (bottom panel) but showing the GRB host sample combined from Kelly et al. (2014) and Blanchard et al. (2016) at $0.3 < z < 1.1$.

Blanchard et al. (2016), we select R_e determined by `SExtractor`. In Fig. 2.14, we show that the majority of size measurements are consistent between `GALFIT` and `SExtractor`, except when the galaxy size becomes close to the PSF size. Given that only 2/18 objects at $z < 1$ are smaller than the PSF size, this effect should not significantly affect the results. Finally, the majority of the objects (13/18) were observed with the $F160W$ filter of the WFC3/IR camera. The others were targeted with a filter close to the R-band, which also mostly probes the bulk of the stellar component for these sources at low redshift. Hence, it should not introduce any additional bias to our study. In Kelly et al. (2014), GRB hosts are compared to a sample of star-forming galaxies from the Sloan Digital Sky Survey (*SDSS*) DR10 catalog at $z < 0.2$. Because a non-negligible fraction of our combined GRB host low-redshift sample is located at $z > 0.2$, we were able to perform a new comparison by considering a control sample from the 3D-HST survey at similar redshift, applying the same analysis method as performed at $1 < z < 2$ and $2 < z < 3.1$. Although 3D-HST may be more suited to galaxies at larger distances (i.e., $z > 1$), we note that this survey remains the most appropriate when combining estimates of redshift, size, stellar mass, and star formation rates for sources at low to intermediate redshifts. It represents therefore the best available control sample to study the densities of GRB hosts at $0.3 < z < 1.1$. Our combined sample of GRB host galaxies at $0.3 < z < 1.1$ yields similar results to those obtained by Kelly et al. (2014). We indeed found that the majority of GRB hosts are located above the SFR-weighted Σ_M-M_* and Σ_{SFR}-M_* relations of field galaxies, while they fall below the R_e-M_* relation driven by the control sample of

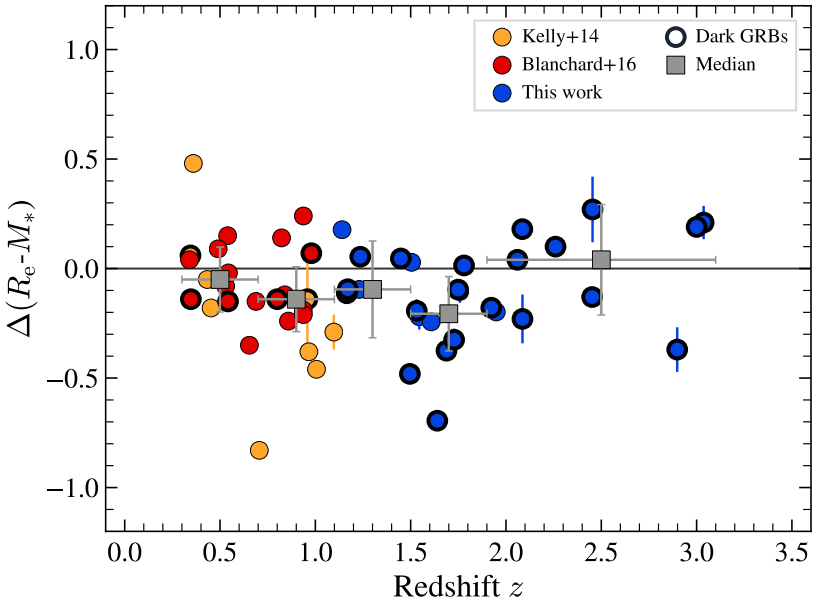

Figure 2.21: $\Delta(R_e\text{-}M_*)$ as a function of the redshift for GRB host galaxies. The orange and red circles are GRB hosts at $z \lesssim 1$ from Kelly et al. (2014) and Blanchard et al. (2016), respectively. The blue circles are the GRB hosts considered in this study. Dark GRBs are highlighted by a thick black circle. The gray squares are the median of the $\Delta(R_e\text{-}M_*)$ for each redshift bin. The associated error bars are the standard deviation using the MAD estimator. The black line at $y = 0$ represents the expected median values for a GRB hosts population that do not suffer from environment bias.

star-forming sources. However, the apparent deviations that we measure are much less pronounced than those derived by Kelly et al. (2014), which may be due to the different control sample used in their analysis. We computed the CDFs for each parameter and perform K-S tests. The results reveal that we can reject the null hypothesis with a significance level of $\lesssim 5\%$ for all parameters ($P_{\rm KS} = 0.01$, $P_{\rm KS} = 0.04$ and $P_{\rm KS} = 0.006$ for $\Delta(R_e\text{-}M_*)$, $\Delta(\Sigma_M\text{-}M_*)$ and $\Delta(\Sigma_M\text{-}M_*)$, respectively). In Fig. 2.21, we show the evolution of $\Delta(R_e\text{-}M_*)$ at $0.3 < z < 3.1$. We divided the redshift range in five bins and determine the corresponding median value for each redshift bin. At $z \lesssim 2$, we observe that the median $\Delta(R_e\text{-}M_*)$ is systematically negative, with an offset that appears statistically significant despite the relatively large scatter of the individual estimates. This shows again that the overall population of GRB host galaxies at $z \lesssim 2$ tend to exhibit smaller sizes than typical star-forming sources with comparable stellar masses. As already noticed in Sect. 2.2.5.1 from our sample at $2 < z < 3.1$, the median value at $z \gtrsim 2$ is, however,

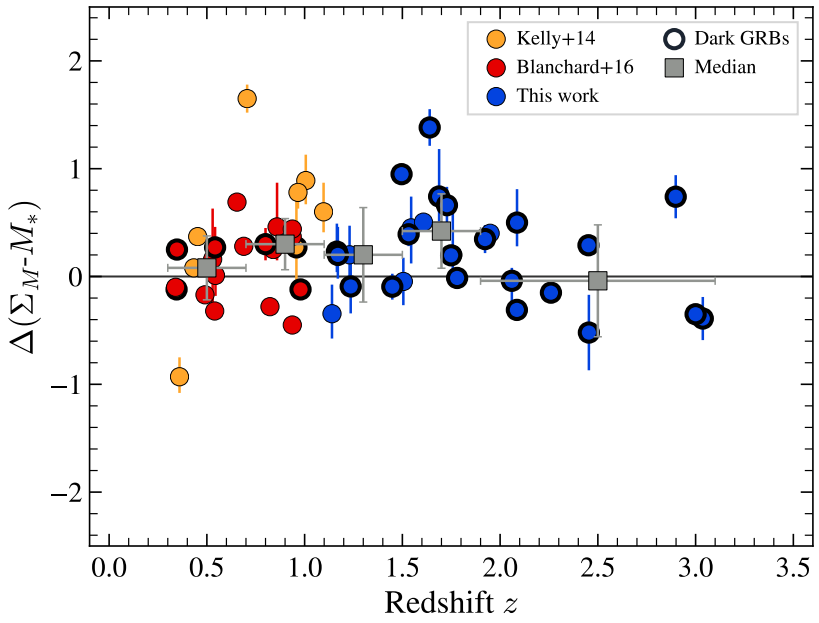

Figure 2.22: $\Delta(\Sigma_{\rm M}\text{-}M_*)$ against redshift for GRB host galaxies. The symbols are identical to those of Fig. 2.21.

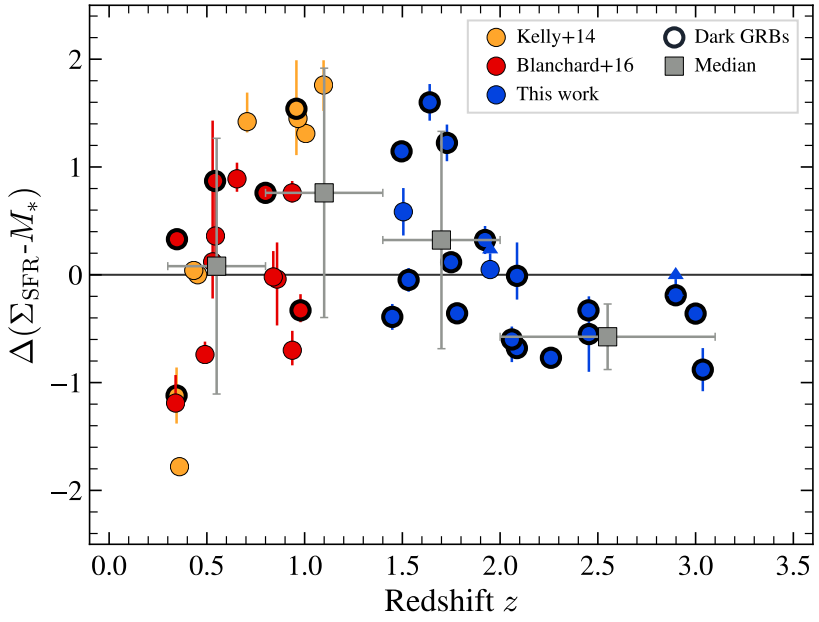

Figure 2.23: $\Delta(\Sigma_{\rm SFR}\text{-}M_*)$ against redshift for GRB host galaxies. Lower limits are represented as arrows and other symbols are identical to those of Fig. 2.21.

closer to a null deviation, meaning that GRB hosts at higher redshifts tend to be more homogeneously spread around the SFR-weighted R_e-M_* relation. Similarly, we find an opposite behavior for $\Delta(\Sigma_M$-$M_*)$ (Fig. 2.22), which reveals a statistically significant positive deviation up to $z \sim 2$, and a median value consistent with zero at higher redshift. Finally, the $\Delta(\Sigma_{SFR}$-$M_*)$ is shown in Fig. 2.23. We reduce the number of redshift bins due to the smaller number of GRB hosts with a SFR value. We find that GRB host galaxies may show a slight preference toward high star formation density at low to intermediate redshifts, but all median values are also consistent with a null deviation given the large associated uncertainties.

2.2.6 Discussion

The non-negligible scatter observed in Figs. 2.21, 2.22, and 2.23 unfortunately prevents us from deriving an unambiguous interpretation of the data. However, our analysis strongly suggests that GRB host galaxies up to $z \sim 2$ tend to exhibit smaller sizes and larger densities of stellar mass and star formation than what we could expect for a SFR-weighted population of star-forming galaxies. It thus confirms and extends to higher redshifts the trend already observed for GRB hosts at low z, even though the offset that we find between the two populations is not as prominent as previously measured (e.g., Kelly et al. 2014). We stress again that our comparison was performed by properly matching the GRB host sample and the population of field sources in redshift and stellar mass. This indicates that our results cannot be explained by the combination of the more frequent occurrence of long GRBs in low-mass sources (at least up to $z \sim 2$) with the general mass-size relationship and its evolution with cosmic time. Similarly, we showed that it cannot be due to systematic uncertainties in the determination of physical parameters (e.g., mass, size) between field galaxies and GRB hosts. Finally, we believe that this effect cannot be simply due to the GRB host sample selection and in particular the larger number of GRBs with a dark afterglow compared to the overall population of long GRBs. A higher number of dark GRBs may indeed bias the host sample toward larger and more massive sources (Perley et al. 2013; Chrimes et al. 2020), but this should not affect the comparison with field galaxies at fixed stellar mass. In addition, we do not observe any apparent difference between dark and optically bright GRB hosts at $1 < z < 2$, when quantifying their size, stellar mass, and SFR density offset with the field (Figs. 2.17, 2.18, and 2.19).

This is also what we find with the sample at $0.3 < z < 1.1$, which is composed of a majority of optically bright GRBs and that shows a similar trend toward compact and dense environments.

2.2.6.1 Effects of the size-metallicity relation on GRB hosts

Previous works have pointed to the conclusion that the production efficiency of long GRBs is mostly ruled by metallicity, with GRB formation being switched off in galaxies with metallicity higher than a threshold that is still currently debated in the literature (Modjaz et al. 2008; Graham & Fruchter 2013; Krühler et al. 2015; Vergani et al. 2015; Perley et al. 2016b; Palmerio et al. 2019). Given the additional bias toward compact galaxies found in our analysis for GRB hosts, we further investigate the possible link between the size and metallicity of galaxies. Ellison et al. (2008a) used a sample of star-forming sources from the *SDSS* to study the possible influence of the galaxy size on the mass-metallicity (MZ) relation (Tremonti et al. 2004; Mannucci et al. 2010; Wuyts et al. 2014; Zahid et al. 2014). They observed an anti-correlation between size and metallicity at a given stellar mass. This means that for the same stellar mass, galaxies with a smaller size are also richer in metallicity, (i.e., the metallicity increases by 0.1 dex when the size is divided by a factor of 2). This result has been corroborated by Brisbin & Harwit (2012); Harwit & Brisbin (2015) and it was also observed at higher redshifts by Yabe et al. (2012, 2014) using a sample of star-forming galaxies up to $z \sim 1.4$. The tendency for GRB hosts to occur in denser environments could thus appear intriguing at first sight. In fact, GRB-selected galaxies appear to track the mass–metallicity relation of star-forming sources but with an offset of 0.15 dex toward lower metallicities (Arabsalmani et al. 2018b). If this offset is due to the intrinsic nature of GRB hosts and not to systematic effects, the possibility that GRB hosts are more compact (and not larger) than field galaxies may indicate that the physical conditions and the environments in which long GRBs form are more complex than what has been assumed so far. Our results could also imply that the impact of metallicity and compactness separately considered is even stronger than has actually been seen, and their inter-correlation at a given stellar mass mitigates the global trends that we can observe among GRB hosts. Interestingly, based on the EAGLE cosmological numerical simulations, Sánchez Almeida & Dalla Vecchia (2018) found a similar size-metallicity anti-correlation up to $z \sim 8$ and explored its

possible physical origin. It is worth noting that their simulation reproduced well-known observed scale relations such as the MZ relation at $z < 5$ (De Rossi et al. 2017) but was not designed to reproduce the relation between size and metallicity. They explored three potential explanations of this relation: (1) a recent metal-poor gas inflows that increased the size and reduced the metallicity of the galaxy; (2) a more efficient star formation process in compact galaxies, whereby the denser gas transforming more efficiently into stars, resulting in a faster enrichment of the gas; and (3) an effectiveness of metal-rich gas outflows reduced in compact galaxies due to a deeper gravitational potential. The EAGLE simulation supports cause (1) and discards causes (2) and (3). In this scenario, we may infer that long GRBs cannot be linked to young star formation triggered by recent inflow of gas at low metallicity, which would have otherwise increased the size of their hosting environment.

To investigate this possible relationship between metallicity and stellar density in greater detail in our GRB host sample, we turned to previous studies (Hashimoto et al. 2015; Krühler et al. 2015) to extract the gas-phase metallicity measurement determined from strong emission lines ($Z_{\rm emiss}$). We only consider GRB hosts in $1 < z < 2$, where the trend toward compact galaxies is more clearly observed. We find only a small fraction of GRB hosts (10/22) with a metallicity measurement. We also find an additional GRB host with gas-phase metallicity measurement determined using the GRB afterglow absorption lines ($Z_{\rm abs}$) in Arabsalmani et al. (2018b). However, due to the insecure relation between $Z_{\rm emiss}$ and $Z_{\rm abs}$ especially at high-z (Metha & Trenti 2020; Metha et al. 2021), we omit this measurement. Unfortunately, our data do not reveal any obvious trend between the metallicity of GRB hosts and the deviation of their size from field galaxies at comparable stellar mass. This may be explained by the poor statistics of the sample and, therefore, we cannot confirm or rule out a different relation for GRB hosts compared to field galaxies regarding these physical parameters.

To further complicate the picture, we finally point out that minor interactions could also play a role in shaping the inter-dependency of size and metallicity in these different populations. Using a local sample of star-forming galaxies from the *SDSS*, Ellison et al. (2008b) observed that galaxies with a companion have indeed a lower metallicity for a given stellar mass and size. Detailed studies of individual GRB host revealed that GRBs can be found in interacting environments

(Thöne et al. 2011a; Arabsalmani et al. 2019). It is also supported by previous work (Wainwright et al. 2007; Ørum et al. 2020) reporting that GRB hosts are often found in interacting systems with major companions ($\sim 30\%$). This may suggest that a recent interaction of the host galaxy could also affect the conditions required to produce a long GRB, in addition to metallicity and stellar density.

2.2.6.2 A possible redshift-dependent bias

At $z \gtrsim 2$, the picture arising from our sample is different than the one observed at lower redshifts. The apparent deviation that we found at $z \lesssim 2$ between GRB hosts and field galaxies seems to disappear. Admittedly, the large uncertainties measured at $2 < z < 3.1$ and the much lower statistics characterizing our GRB host sample at such redshifts do not allow us to draw a firm conclusion that this evolution is real and statistically robust, as suggested by the significance of our K-S tests as well. The SFR density of GRB hosts at $2 < z < 3.1$ may even be lower than expected from the field according to our analysis (see Fig. 2.19), although we believe this reversal is probably due to the small number of sources in our sample. However, the data do suggest that the size and stellar mass density of GRB hosts at these higher redshifts are globally more representative of the overall population of star-forming galaxies in the field. From a qualitative point of view, we could argue that this evolution of the size and density of GRB hosts compared to the field is consistent with the idea that the bias, which is clearly established between the overall population of star-forming galaxies and the hosts of long GRBs at low redshifts, which is progressively reduced as the redshift increases. This may thus support the hypothesis that long GRBs represent a more accurate tracer of star formation in the distant Universe than they actually do at lower redshifts. On the other hand, we note that the stellar mass range probed by our sample in this redshift range ($M_* > 10^{10.5}$) is substantially larger than the one probed at $1 < z < 2$ ($M_* < 10^{10.5}$), and our GRB host selection at $z \gtrsim 2$ is also exclusively drawn from dark GRBs. While we found no apparent difference in the size and stellar densities between the hosts of optically bright and dark GRBs at lower stellar mass and redshift, we cannot firmly exclude a possible dependence of the size deviation with stellar mass. This means that the offset observed at $z \lesssim 2$ could plausibly remain at $2 < z < 3.1$, if we had also included GRB hosts with lower stellar mass ($M_* < 10^{10.5}$) or more massive hosts selected with optically

bright GRBs.

2.2.6.3 Stellar density and GRB progenitor models

Considering the proposed progenitor models, GRB production may be expected to depend on the density environment in addition to any metallicity bias. Several observational and theoretical studies reported that the fraction of star formation happening in young bound star clusters (Γ) may depend on the environmental properties of the host galaxy. In particular, they found that the $\Sigma_{\rm SFR}$ correlates with Γ (Goddard et al. 2010; Adamo et al. 2011; Kruijssen 2012; Silva-Villa et al. 2013; Adamo et al. 2015). Owing to a greater amount of stars, these clusters may more frequently produce binary systems of massive stars which are one of the candidates to form GRBs. However, this has to be set against the results of Chandar et al. (2017) (see also Chandar et al. 2015; Kruijssen & Bastian 2016), which showed that the relation between $\Sigma_{\rm SFR}$ and Γ presents no particular trend. The previously reported correlation would be due to a bias in the selection of galaxies leading to an estimation of Γ mixing young and old clusters. As a consequence, young (old) clusters were systematically associated with high (low) $\Sigma_{\rm SFR}$ creating an apparent correlation between Γ and $\Sigma_{\rm SFR}$. On the other hand, several studies suggest that the IMF can evolve to top-heavy (overabundance of high mass stars) when the density of the environment increases (Marks et al. 2012; Haghi et al. 2020). If the number of massive stars increases, the probability to produce a GRB also increases. This provides a plausible explanation for the reported trend that associates GRBs with compact and dense environments.

2.2.7 Summary and conclusions

In this work, we study a sample of long GRB host galaxies observed with the HST/WFC3 in the IR band at $1 < z < 3.1$. We compared their sizes, stellar masses, and star formation rate surface densities to the measurements of typical star-forming galaxies of the 3D-HST survey. Prior to the comparison, we minimized the systematics and biases that measurement methods may introduce between samples observed under different conditions. We also verified that no systematic offset is present between the GRB hosts and the star-forming galaxies in the determination of their physical properties. In addition, we confronted our GRB

host sample to the host galaxies of unbiased GRB samples (BAT6 and SHOALS). At $1 < z < 2$, we found that they are consistent with each other in terms of stellar mass and redshift distributions while at $2 < z < 3.1$ we noted an offset toward more massive galaxies. We performed a fair comparison between the GRB hosts and the field galaxies by fixing their redshift range and stellar mass to remove any dependency that the measured properties may have on these two parameters. At $1 < z < 2$, the results clearly showed that GRB hosts are smaller in size and have higher stellar mass and star formation rate surface densities than expected if they had truly been representative of the overall population of star-forming galaxies. We also noted that the galaxy size and stellar density are consistent for the dark and optically bright GRB host populations. At $2 < z < 3.1$, the trend appears to evolve and GRB hosts seem to be more consistent with star-forming galaxies of the field. We even found an inversion of the tendency for the $\Sigma_{\rm SFR}$ parameter, where GRB hosts have a lower star formation rate surface density than field sources. However, because of the small sample size at this redshift, we cannot rule out the possibility of a purely statistical effect. Furthermore, we cannot exclude a possible bias in our results at $z \gtrsim 2$ due to the predominance of galaxies selected from dark GRBs. We inserted our results into a broader context and considered at $0.3 < z < 1.1$ the size measurements from Kelly et al. (2014) and Blanchard et al. (2016). We performed a similar analysis to the one at $1 < z < 3.1$ and found that up to $z \sim 2$, GRB hosts have a smaller size and a higher stellar mass and star formation surface densities than field galaxies. Finally, we investigated the possible relation between the size and metallicity bias found in the GRB host population. However, due to the limited number of metallicity measurements available in the literature for the GRB hosts in our sample, we cannot confirm or refute the anti-correlation reported for star-forming galaxies in the literature between size and metallicity at a given stellar mass.

These results are part of the effort to better understand long GRB formation and the ability to trace the CSFRH, especially at high-redshift where the trend is still poorly constrained by observations. Future works will be focused on expanding the GRB host sample to confirm the trend observed at $z < 3$ and extend the analysis at higher redshifts. The forthcoming *SVOM* mission (Wei et al. 2016; Atteia et al. 2022) and its dedicated follow-up network will allow us to rapidly identify high-z bursts candidate and will contribute to a better controlled and homogeneous GRB host sample. Its synergy with the upcoming James Webb Space Telescope (Gard-

ner et al. 2006) offers a promising opportunity to detect and characterize GRB host galaxies at very high redshift.

Appendices

2.2.2.A Stellar mass and star formation rate of GRB hosts and field galaxies

For star-forming galaxies of the 3D-HST survey, we use the star formation rates (SFR) determined by Whitaker et al. (2014) and stellar masses derived from the SED fitting code `FAST` (Kriek et al. 2009). The $\mathrm{SFR_{UV+IR}}$ of Whitaker et al. (2014) is determined by adding the rest-frame UV light (unobscured light produced by young stars) and the IR light (obscured and remitted light by dust). The total IR luminosity is estimated from the *Spitzer*/MIPS 24 μm flux density and the total UV luminosity is based on the 2800 Å luminosity obtained from best stellar population models (see Whitaker et al. 2014, for additional details).
For objects with no *Spitzer*/MIPS detection (S/N < 1), we derive a UV-SFR corrected from dust extinction ($\mathrm{SFR_{UV,corr}}$). We extract for each object the observed UV luminosity at 1600 Å available in the 3D-HST catalog. We then correct it from extinction by applying an attenuation factor (A_{1600}) derived from the rest-frame UV continuum slope β and the Meurer et al. (1999) relation. Finally, we use the relation from Kennicutt (1998) to convert the UV-corrected luminosity to a SFR. Because the GRB host properties used in this work were determined by SED fitting procedures differing from FAST, the impact of possible systematics arising from the different codes available in the literature should be properly considered. Fortunately, all these codes (including FAST) assume standard star formation histories (e.g., exponential declining, delayed star formation) and similar dust extinction laws, which should strongly limits the risk of large systematics. For instance, typical offsets of only $0.2 - 0.3$ dex for the stellar mass estimates were found from one code to another (Pforr et al. 2012; Mobasher et al. 2015). For SFR determinations, it is generally acknowledged that larger scatter can be seen when relying on SED fitting at optical and NIR wavelengths (Pacifici et al. 2015; Carnall et al. 2019). However, we favored as much as possible the use of more accurate SFR estimates, relying on determinations either based on mid-infrared photometry for the 3D-HST catalog or using Hα and submillimeter fluxes for the majority of GRB

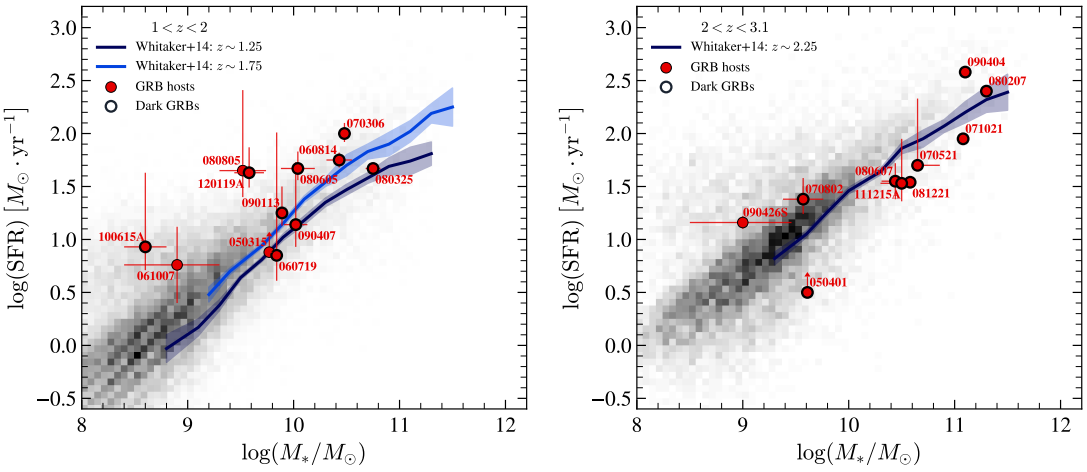

Figure 2.24: Star formation rate against stellar mass for GRB hosts and star-forming galaxies of the 3D-HST survey. Two redshift bins are considered, at $1 < z < 2$ (top panel) and $2 < z < 3.1$ (bottom panel). The star-forming galaxies selected in the analysis combining $\mathrm{SFR_{UV+IR}}$ and $\mathrm{SFR_{UV,corr}}$ values are plotted in background as a 2D gray histogram. The blue and dark blue curves are the main sequence relations derived by Whitaker et al. (2014) at $1 < z < 2.5$.

host galaxies. We thus believe that our comparisons between GRB hosts and field galaxies should not be hardly affected by these effects. In addition, the slight slope of the galaxy mass-size relation should strongly limit the impact of a systematic offset between stellar mass values on our main conclusions.

In Fig. 2.24, we show the sample of star-forming galaxies used in the analysis as a gray-scale density plot and the GRB host galaxies as red circles at $1 < z < 2$ and $2 < z < 3.1$. We also overlay the main sequence (MS) of star-forming galaxies at $z \sim 1.25$, $z \sim 1.75$ and $z \sim 2.25$ from Whitaker et al. (2014). We find a good agreement between the 2D background histogram and the MS relations. This confirms that the sample of star-forming galaxies considered, combining $\mathrm{SFR_{UV+IR}}$ and $\mathrm{SFR_{UV,corr}}$ follows the trend of the MS. Finally, we note that the majority of the GRB hosts are in the typical ~ 0.3 dex scatter of the MS and follow its trend at both redshifts.

2.2.2.B Comparison between methods to estimate the structural parameters

We sought to verify that our method of measuring GRB hosts structural parameters is consistent with the one of van der Wel et al. (2014) used for the reference

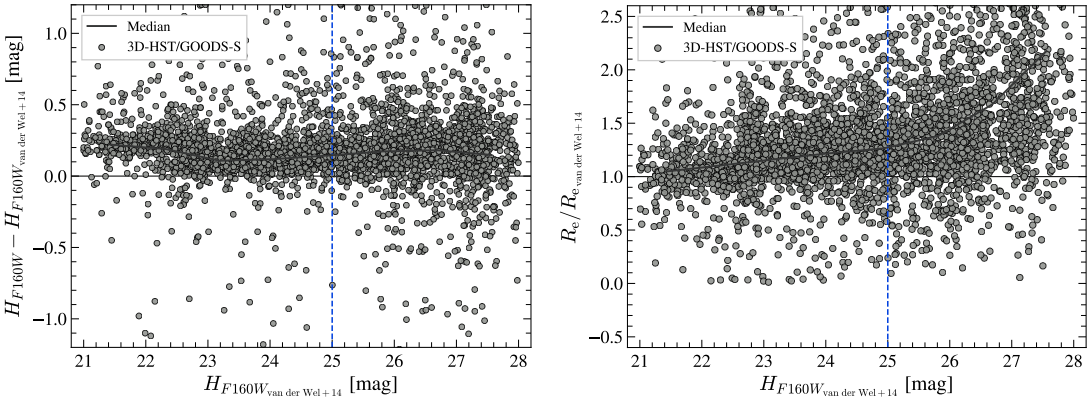

Figure 2.25: Comparison between $F160W$ magnitudes (top panel) and half-light radii (bottom panel) derived by van der Wel et al. (2014) and our `GALFIT` modeling as a function of van der Wel et al. (2014) magnitudes. Each gray point represents an object of the 3D-HST/GOODS-S field. The gray curve is the median of the points and symbolizes the systematic offset for each parameter between the two methods. The vertical dashed blue line represents the maximum magnitude reached by GRB hosts above the 3D-HST mass-completeness limit, while our median H-band magnitude reaches ~ 23.1 mag.

sample. This ensures that no systematic bias is present when comparing GRB hosts and 3D-HST field galaxies. From the catalog of van der Wel et al. (2014), we considered all objects in the 3D-HST/GOODS-S field with a good fit ($flag = 0$). Among them, we randomly select $\sim$ 4 000 objects with $21 < H_{F160W} < 28$. We then ran our pipeline in a similar manner as described in Sect. 2.2.4.1. The pipeline failed for about 100 objects. The majority (75%) of them are not detected by our `SExtractor` configuration. The source extraction method used by van der Wel et al. (2014) is based on the "hot" and "cold" modes developed in `GALAPAGOS`. It is optimized to extract faint sources and properly deblended bright sources in mosaics. The undetected object are probably faint galaxies captured with the optimized source extraction algorithm of `GALAPAGOS`.

In Fig. 2.25, we show the results for the half-light radius and the magnitude. We find a systematic offset of only ~ 0.1 mag between the two magnitude estimates, and note that we also tend to systematically overestimate the half-light radius with our own procedure. At $H_{F160W} = 21.5$ mag, we recover R_e values within 10%, and the median offset then increases progressively with the magnitude until reaching 50% at $H_{F160W} = 26$ mag. This behavior is not surprising since the accuracy of the fitting process depends to first order on the S/N and that the uncertainty in the background estimate becomes dominant at $H_{F160W} > 25.5$ mag (van der

Wel et al. 2012). However, the large majority (90%) of our GRB host sample is brighter than $H_{F160W} = 24$ mag, i.e., where our fitting method reveals consistent results with the one used to estimate the R_e in the 3D-HST catalog. We have only four objects with a magnitude higher than 25 that are excluded once the 3D-HST mass-completeness limit is applied. We thus conclude that these small offsets should have a negligible impact on our results. Finally, in Sect. 2.2.5, we emphasize that the sizes of GRB hosts measured with our code are globally smaller than the size of field sources from the 3D-HST catalog. Removing the systematic effect observed in Fig. 2.25 would thus make this difference between the two populations even more significant, since our size determination tends to overestimate the sizes constrained by van der Wel et al. (2014).

2.2.2.C `GALFIT` models of GRB hosts

In Figs. 2.26, 2.26, and 2.26, we show the best-fitting Sérsic profile derived by `GALFIT` for the sample of GRB hosts. In several cases (e.g., GRB 060814), multiple objects are fit simultaneously to reduce their contamination and improve the fitting process. Masked objects from the `SExtractor` segmentation map are visible as black areas. For the majority of cases, the residual maps show that we managed to remove the flux of the target object. To get a more quantitative indication of the fit goodness, a common method is to use the reduced χ^2 returned by `GALFIT`. However, it can easily be misleading if the fitting process of nearby objects or the masking process is not properly performed. In order to have a better estimate of the remaining signal for each target object, we determined the fraction of pixels within $2 \times R_e$ that have a residual greater than three times the sigma map in the same area. The majority of the objects (33/35) have a residual fraction of $\lesssim 5\%$ confirming the quality of the models considered. Only two objects (GRB 070306 and GRB 080605) have a residual fraction of $\sim 30\%$. Regarding GRB 080605, a plausible explanation is that the two nearby and bright stars probably contaminate the target object and thus interfere with the fitting process. For GRB 070306, the HST observations were performed several years after the GRB detection, thus excluding a possible contamination of the GRB afterglow that could affect the fitting process. We note that adding a PSF model in addition to the Sérsic model improves the fitting process and reduces the residuals to $\sim 10\%$. The resulting size determined by `GALFIT` evolves by a factor of 2 (from 0.14" to 0.28"). This may

indicate an obscured active galactic nucleus or a recent burst of star formation in the host galaxy. Because these two objects represent only a small fraction of the total sample and the models appear realistic despite the large residual fraction, we decided to include them in our analysis. Finally, several objects (e.g., GRB 080207, GRB 111215A) would require more components to improve the residual maps. However, due to the constraint of using a single Sérsic component to model the objects, we did not add additional components to improve the residual maps.

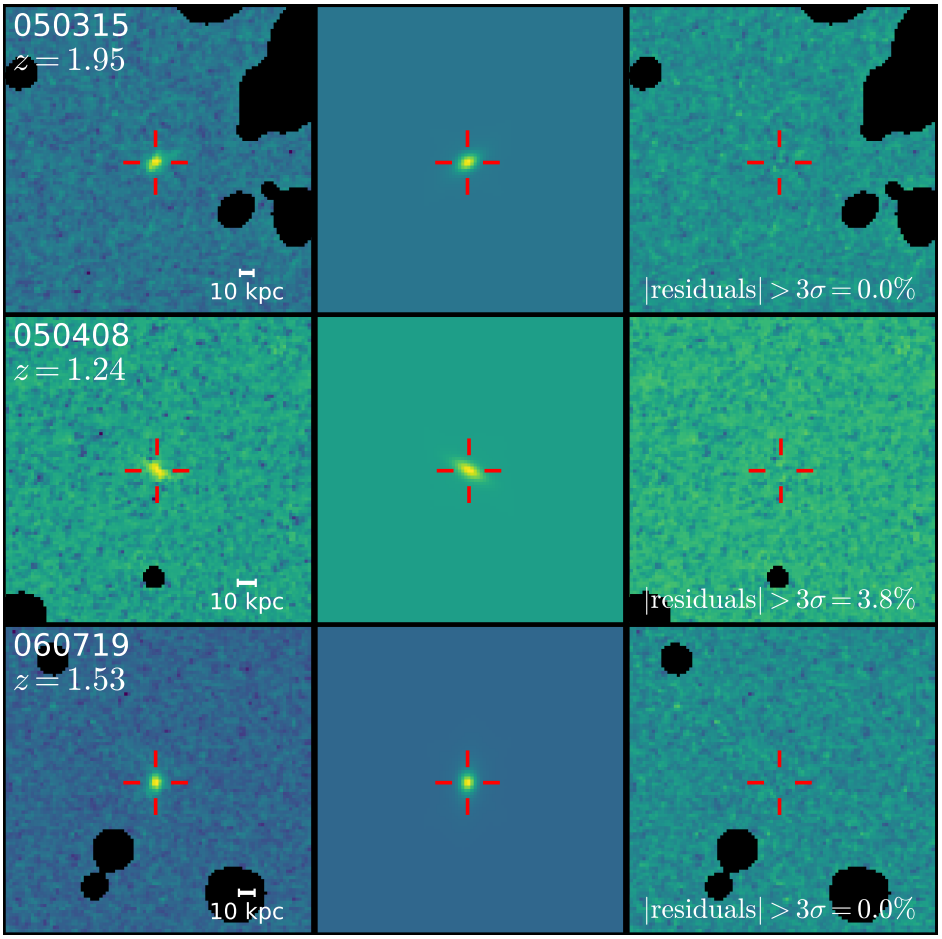

Figure 2.26: GRB hosts images from WFC3/$F160W$ observations (left), their best `GALFIT` models (middle) and the residual maps (right). Images are centered on the best positions of the host galaxies determined by `GALFIT` and corresponds to a square region of 9 arcsec, where north is up and east is to the left. The red marks emphasize the objects considered as the GRB host galaxies. The black regions are the objects masked during the fitting processes based on the `SExtractor` segmentation map. The fraction of pixels with a residual greater than three times their noise within $2 \times R_e$ of the target object is visible in the lower part of the residual map.

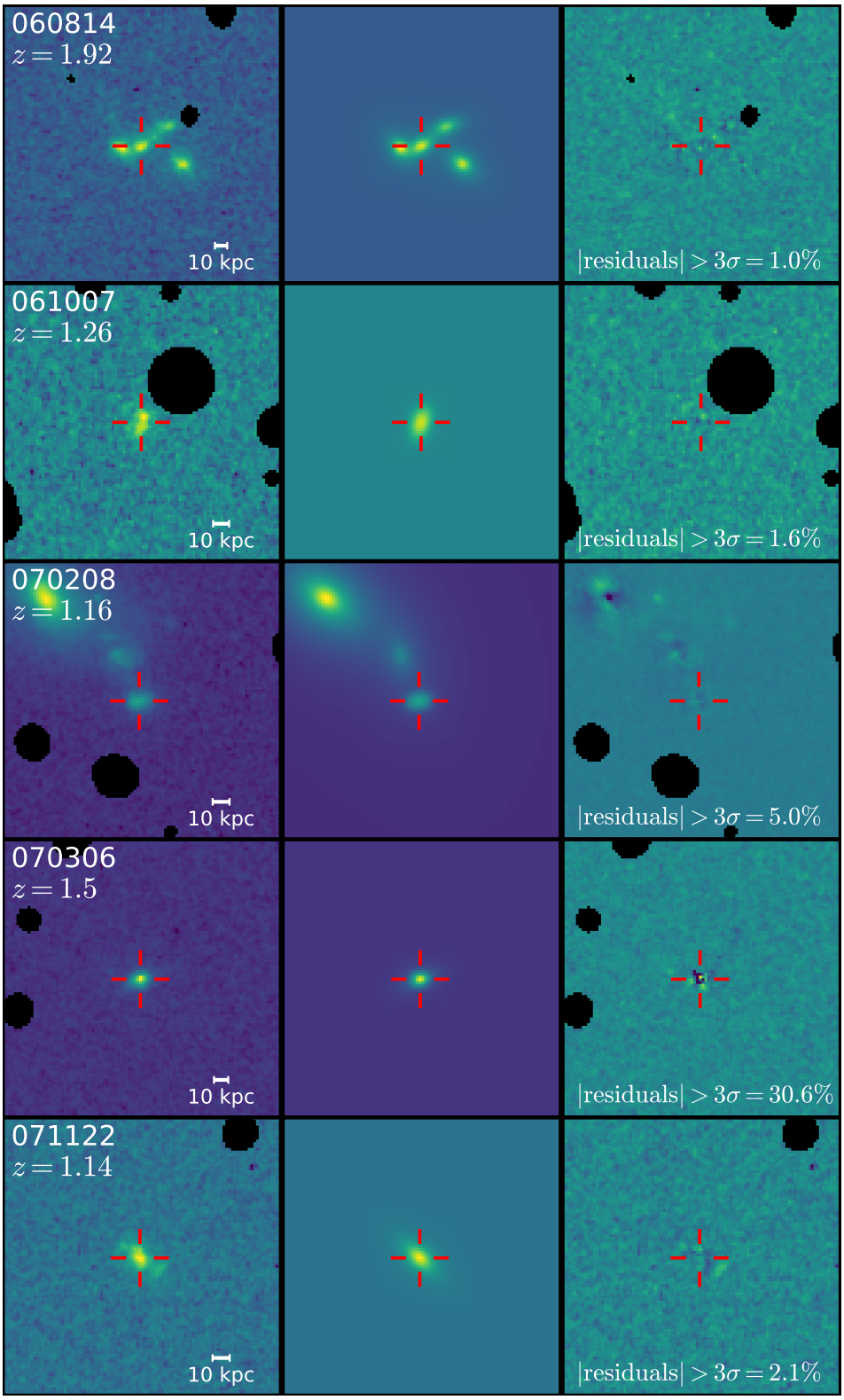

Figure 2.26: (Continued)

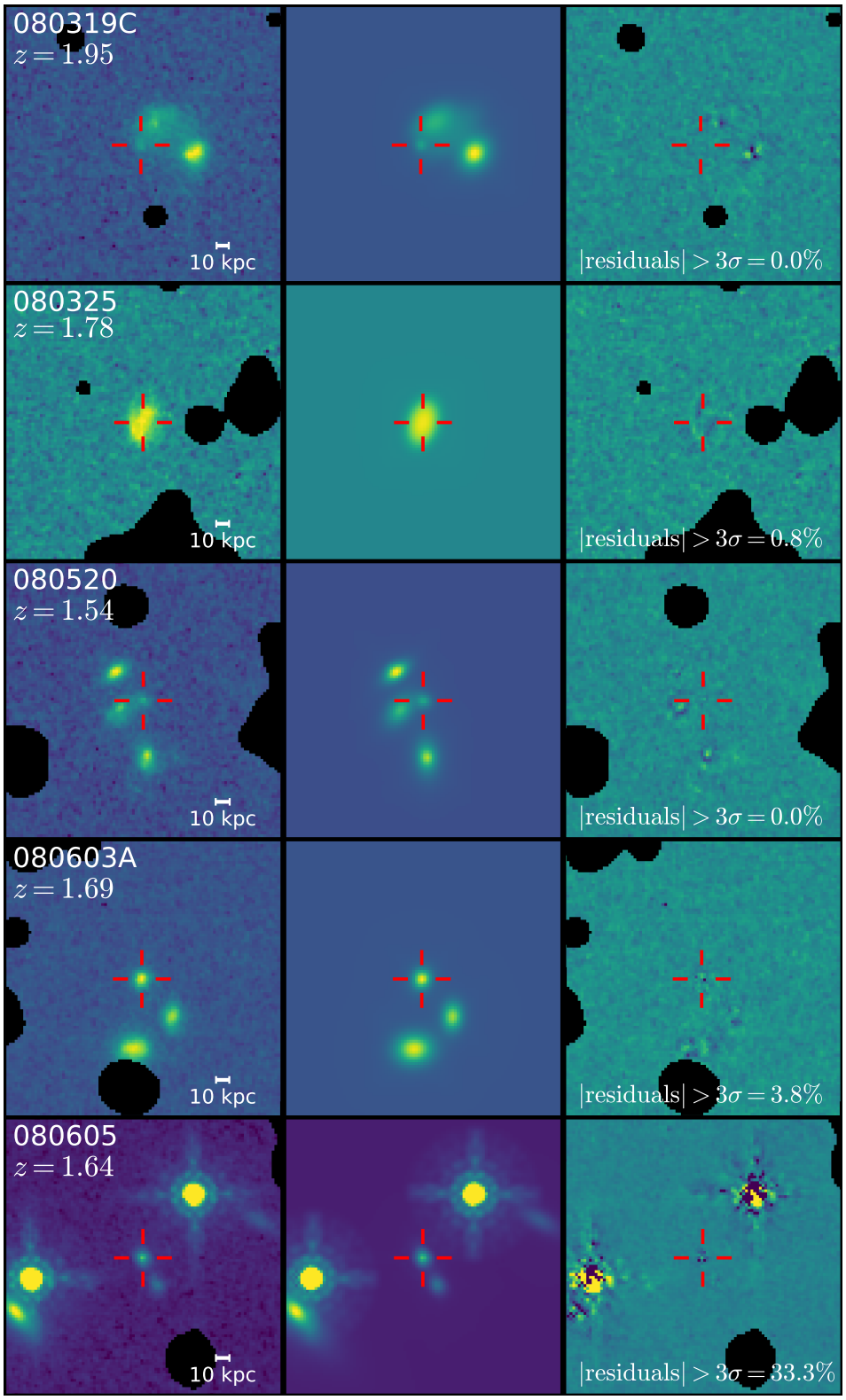

Figure 2.26: (Continued)

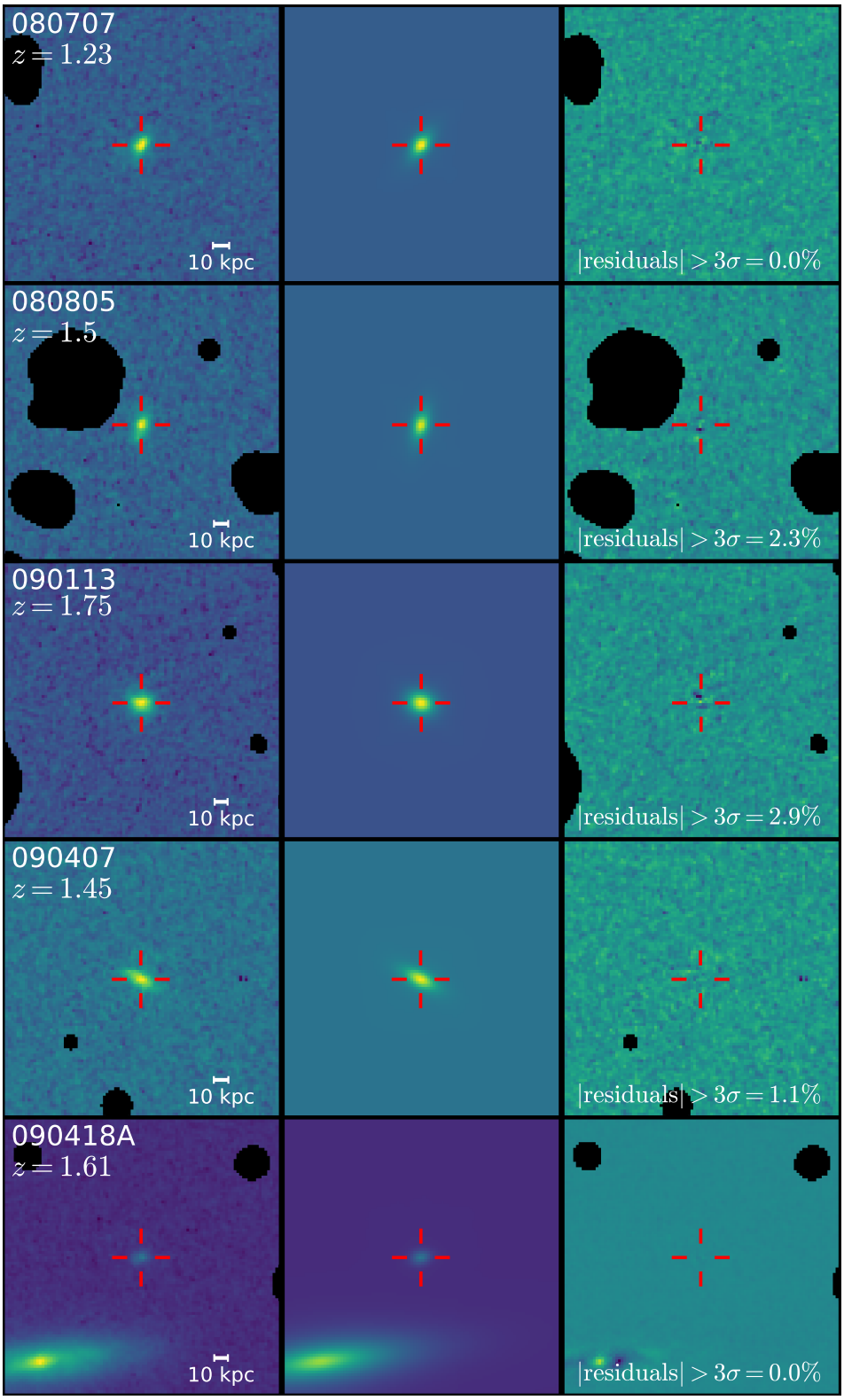

Figure 2.26: (Continued)

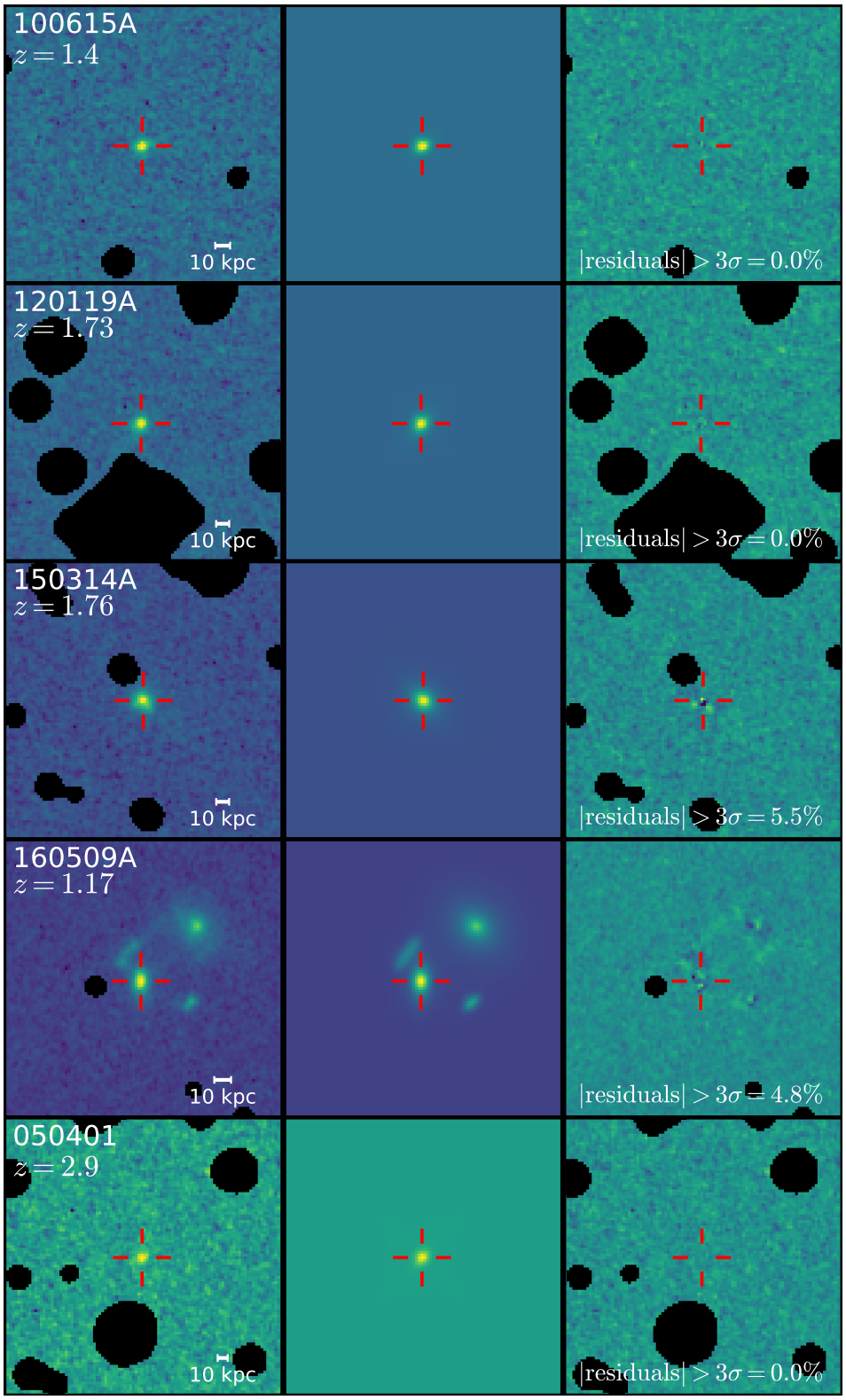

Figure 2.26: (Continued)

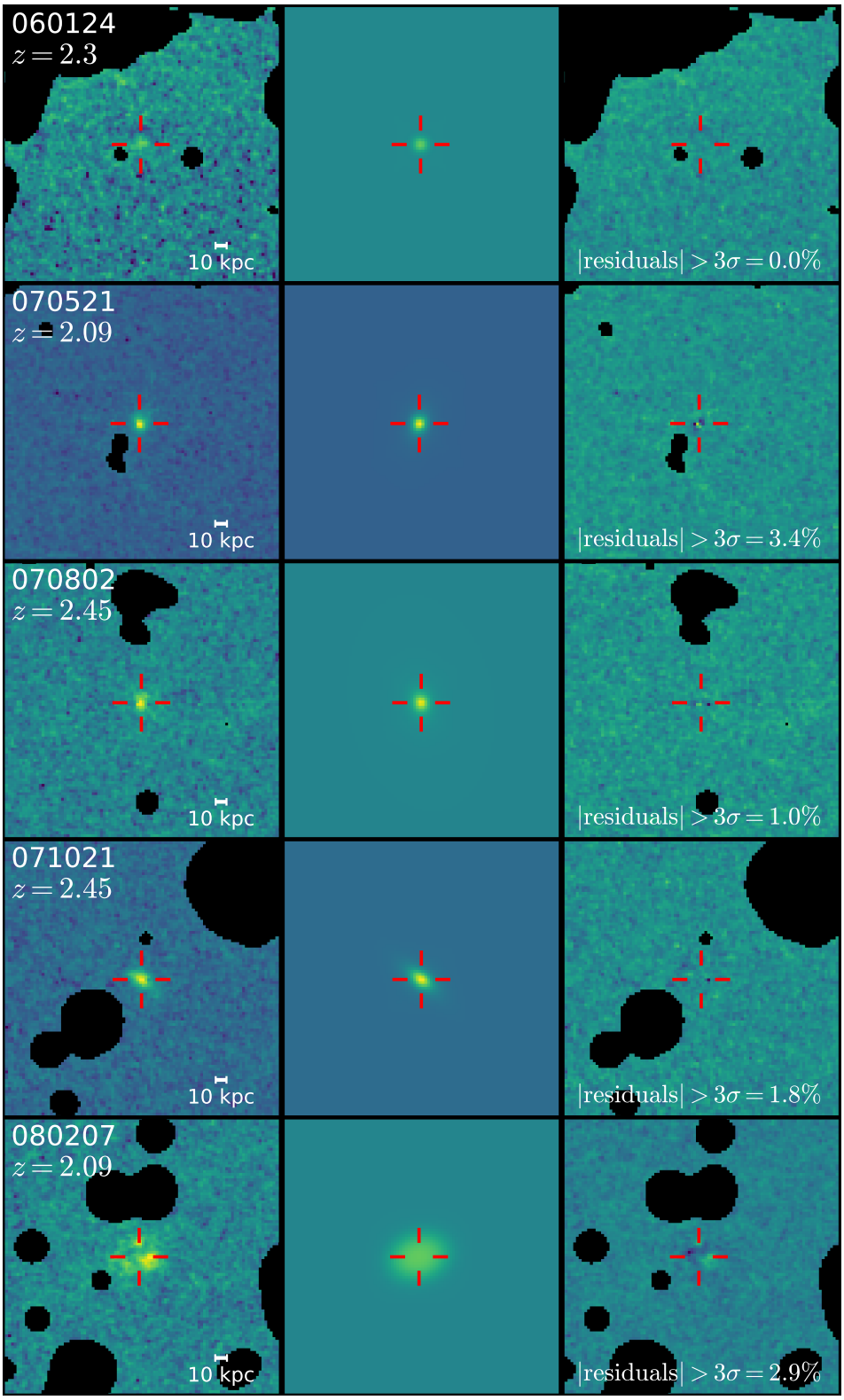

Figure 2.26: (Continued)

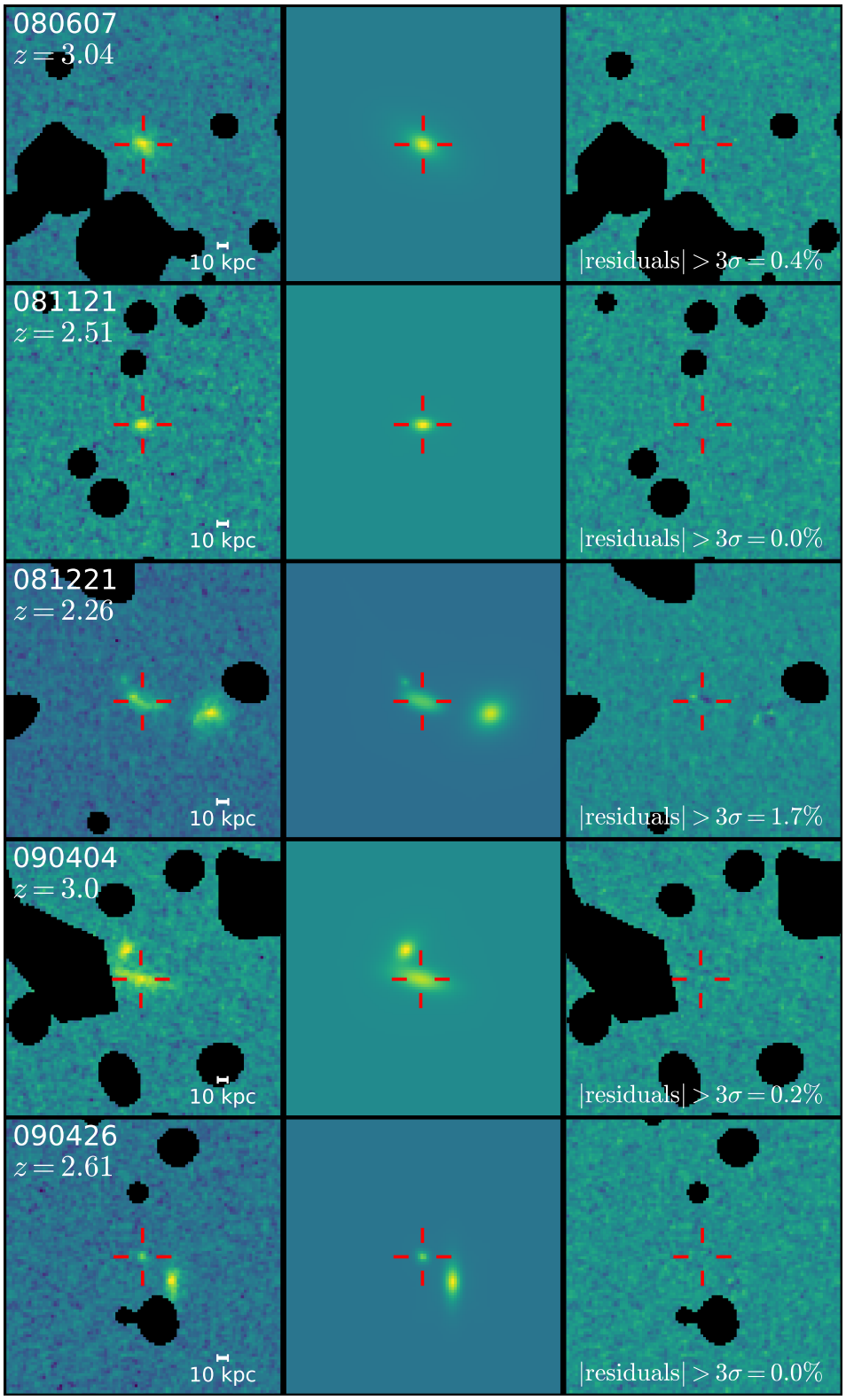

Figure 2.26: (Continued)

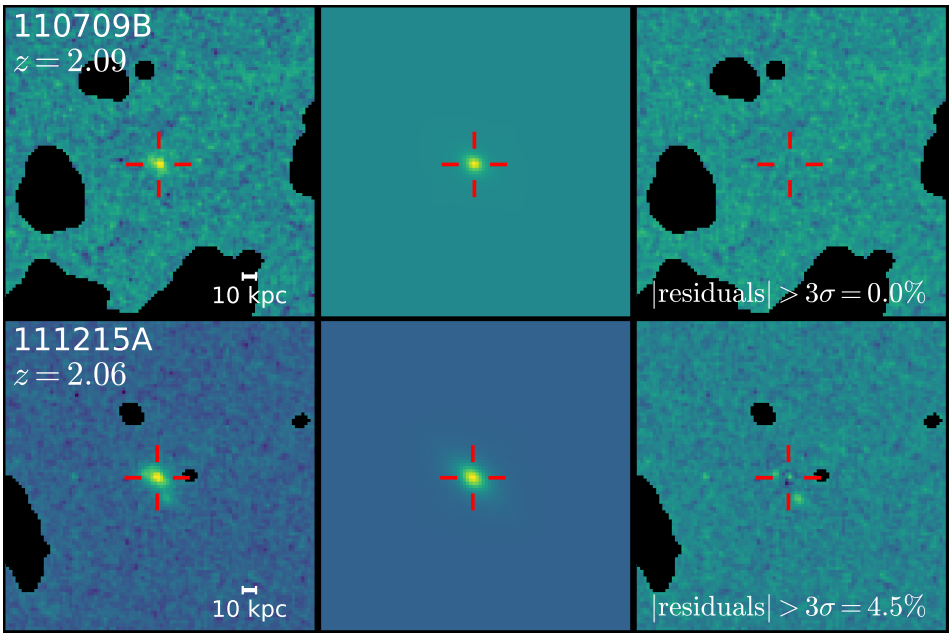

Figure 2.26: (Continued)

2.3 Complementary materials

In this section, I provide further information about the methods that I developed and the analysis performed to obtain the results presented in Sect. 1.2. In particular, additional details are reported on the galaxy modeling and the properties of the GRB host galaxies at $z < 1$ and $1 < z < 3.1$.

2.3.1 Galaxy modeling

A critical aspect of the study was the modeling of the galaxy light profiles and how to determine reliable sizes. I discuss here in a more quantitative way the choice of the PSF function used by `GALFIT` and how more robust uncertainties were derived.

2.3.1.1 PSF of the WFC3/IR camera

As mentioned in Sect. 2.2.4.1 `GALFIT` convolves the light profile models with the instrumental PSF to improve the fitting process. Figure 2.27 shows examples of PSF profile for the WFC3/IR camera in the $F160W$ filter. On the left panel, two PSF profiles were determined from a star-poor (GRB 060719) and star-rich (GRB 080325) fields. We can clearly see that the PSF obtained with a lower number of stars is noisier at the edges and less regular close to the center. This highlights the importance of selecting a sufficient number of stars and the impossibility of determining a PSF for each GRB fields. The use of a PSF with a low S/N introduces artifacts and may affect the size measurement.
In order to limit the possible systematic biases induced by the PSF considered to model the object, the first idea was to use the same PSF as the 3D-HST team, but resampled to the pixel size of the HLA images. To obtain the resampled PSF, several algorithms were tested such as *Lanczos* or *Bicubic* interpolations. However, the resampled profiles showed distortions near the center and caused similar issues to the low S/N PSFs in the models returned by `GALFIT`. For this reason, I decided to model with `PSFex` a PSF tailored to HLA images by extracting and stacking bright stars from HST images of GRB host fields. This provides the best compromise to have a PSF adapted to a pixel scale of 0.09 arcsec/pixel and a good S/N. On the right panel of Fig. 2.27, the comparison between the PSF profile of

the 3D-HST team used to measure the size of the control sample and the PSF obtained from `PSFex` is illustrated. The two PSF profiles show similar features in the central part, with small bumps corresponding to the series of concentric rings around the central spot (Airy patterns). Although the PSF from GRB fields tends to be more noisier at the edges than the 3D-HST one, the visual inspection of the best-fit models does not reveal any particular artifacts.

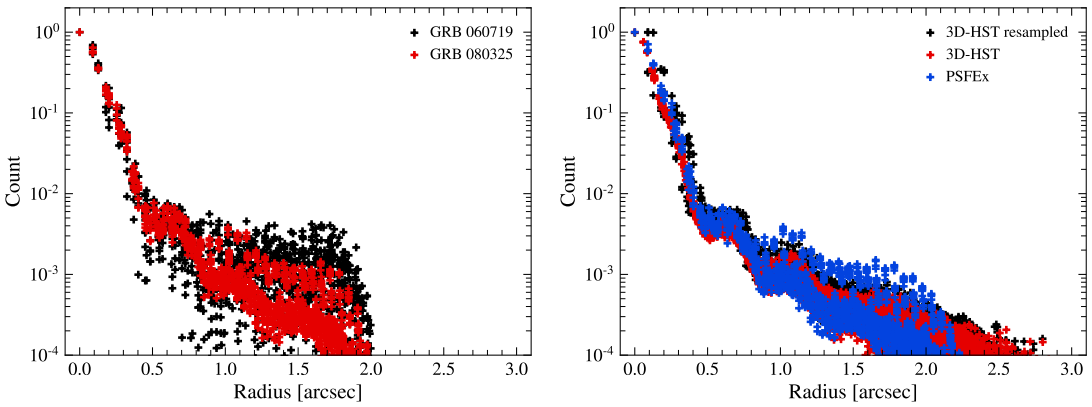

Figure 2.27: Normalized intensity as a function of radius for the WFC3/IR PSF obtained from the field of GRB 060719 (black) and GRB 080325 (red) (left panel), and for the PSF of the 3D-HST team (red) compared to that determined with `PSFex` using a sample of bright-stars from all GRB fields (blue) (right panel).

2.3.1.2 `GALFIT` uncertainties

The interest of deriving more realistic errors associated to the `GALFIT` measurements was firstly motivated by the findings of Häussler et al. (2007). The trend of `GALFIT` to underestimate errors was also observed by comparing the uncertainties derived by van der Wel et al. (2012) and obtained from `GALFIT` for the randomly selected objects in the 3D-HST/GOODS-S field (see Sect. 2.2.2.B). van der Wel et al. (2012) determined more robust uncertainties by considering the same objects in images with different depth (e.g., deep and wide CANDELS mosaics). On the top panels of Fig. 2.28, the difference between the uncertainties of van der Wel et al. (2012) and those returned by `GALFIT` are shown for the magnitude and half-light radius estimates. For both parameters, the errors returned by `GALFIT` are systematically lower than the one derived by van der Wel et al. (2012). For the magnitude errors, the difference is negligible (< 0.1 mag) up to $H_{F160W} \sim 25$ mag and then increases to reach ~ 0.15 mag at $H_{F160W} > 27$ mag. For the $R_{\rm e}$, the

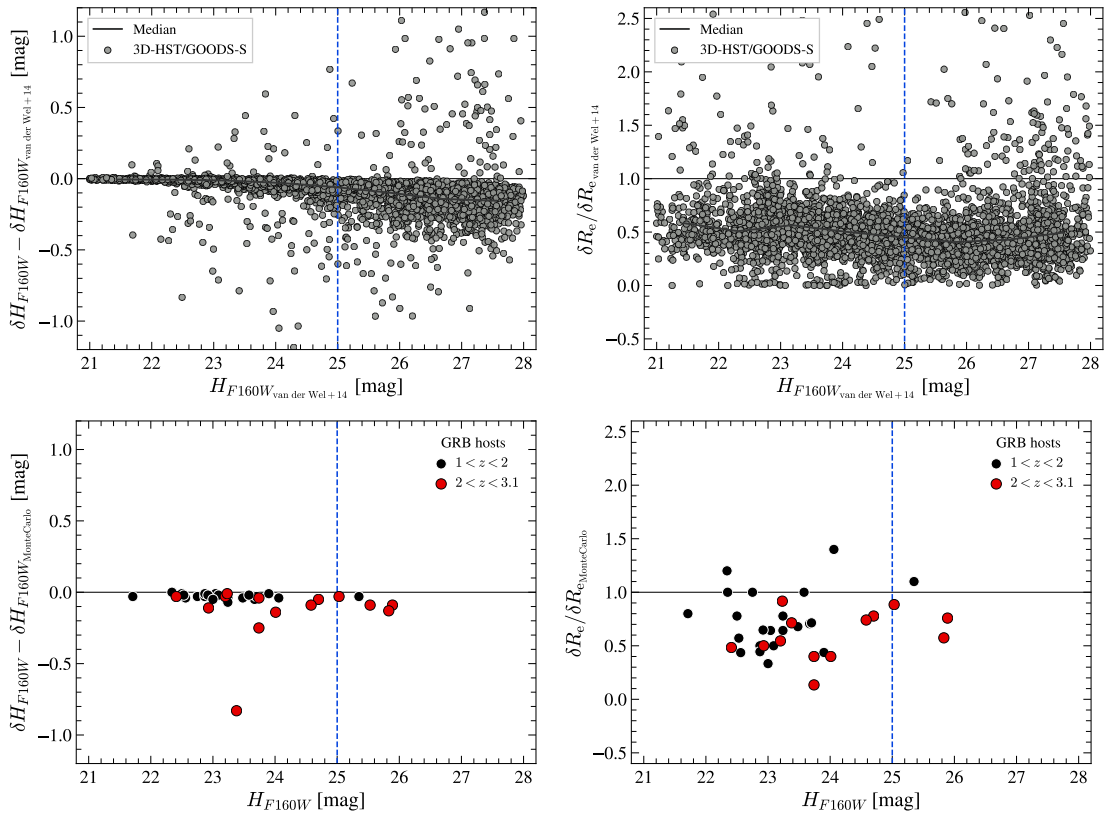

Figure 2.28: Uncertainties on galaxy models. *Top panels:* Difference of magnitude errors (left panel) and R_e errors (right panel) as a function of magnitude obtained by GALFIT and van der Wel et al. (2014) for randomly selected 3D-HST objects. The median of the objects is shown in dark gray. *Bottom panels:* Same as top panels but showing the difference of uncertainties between GALFIT and MC simulations for GRB hosts at $1 < z < 2$ (black) and $2 < z < 3.1$ (red).

difference is larger and the GALFIT errors are underestimated by a factor 2 for all magnitudes.

In Sect. 2.2.4.1, the method to determine more realistic uncertainties was described. The MC approach consists in randomly injecting the best-fit GALFIT models inside empty regions of the science image and fit the new sources with an identical procedure (Fig. 2.11). The method provides an estimate of the systematic and random (mainly from background measurement) uncertainties associated to the models. The bottom panels of Fig. 2.28 show the difference of uncertainties determined by GALFIT and the MC approach versus object magnitudes for both GRB host samples. The trend is similar to the one observed between GALFIT and van der Wel et al. (2014) where magnitude errors are < 0.1 mag and R_e errors underestimated by approximately a factor 2. For three objects the errors estimated

by the MC method is lower than `GALFIT`. This might be explained by a larger contamination of the models from neighboring objects that the approach does not take into account, since by construction the models are injected into empty areas without any close objects. A possible alternative to determine robust uncertainties consistent with those from van der Wel et al. (2014) would be to consider in the 3D-HST sample the N (e.g., 200) galaxies the most similar to the target object and compute the mean value of errors associated to each parameters.

2.3.2 GRB hosts at $z < 1$

The trend toward compact and dense environment observed for GRB hosts at $1 < z < 2$ was also investigated at $z < 1$ in an homogeneous way by only considering the galaxy size measurements of Kelly et al. (2014) and Blanchard et al. (2016) (see Table 2.2 and Sect. 2.2.5.4). On the left panels of the Fig. 2.29, the half-light radius, the stellar mass surface density, and the star formation surface density as a function of stellar mass is shown. Similarly to $1 < z < 2$, it is clearly visible that the GRB hosts are more compact and denser in stellar mass and star formation rate than star-forming galaxies. This was further confirmed statistically by the KS test performed using the measured deviation of the GRB hosts from the control sample (right panels of the Fig. 2.29).
The evolution of this deviation with z for $\Delta(R_{\rm e}\text{-}M_*)$, $\Delta(\Sigma_{\rm M}\text{-}M_*)$, $\Delta(\Sigma_{\rm SFR}\text{-}M_*)$ are shown in Fig. 2.21 to 2.23. Given the observational effect mentioned in Sect. 2.1.3.2, it is worth noting that without precautions, this comparison might suffer from a bias in the wavelength probed by the $F160W$ filter through z. For instance, comparing GRB host sizes across z without applying a morphological K-correction would necessarily be biased. However, in the analysis, the comparison was fairly performed by using the distance measured at a given mass and redshift range (i.e., Δ) between two populations observed in the same filter. This ensures that the evolution of the deviation with z is not artificially caused by a change in the morphology of galaxies with the wavelength.

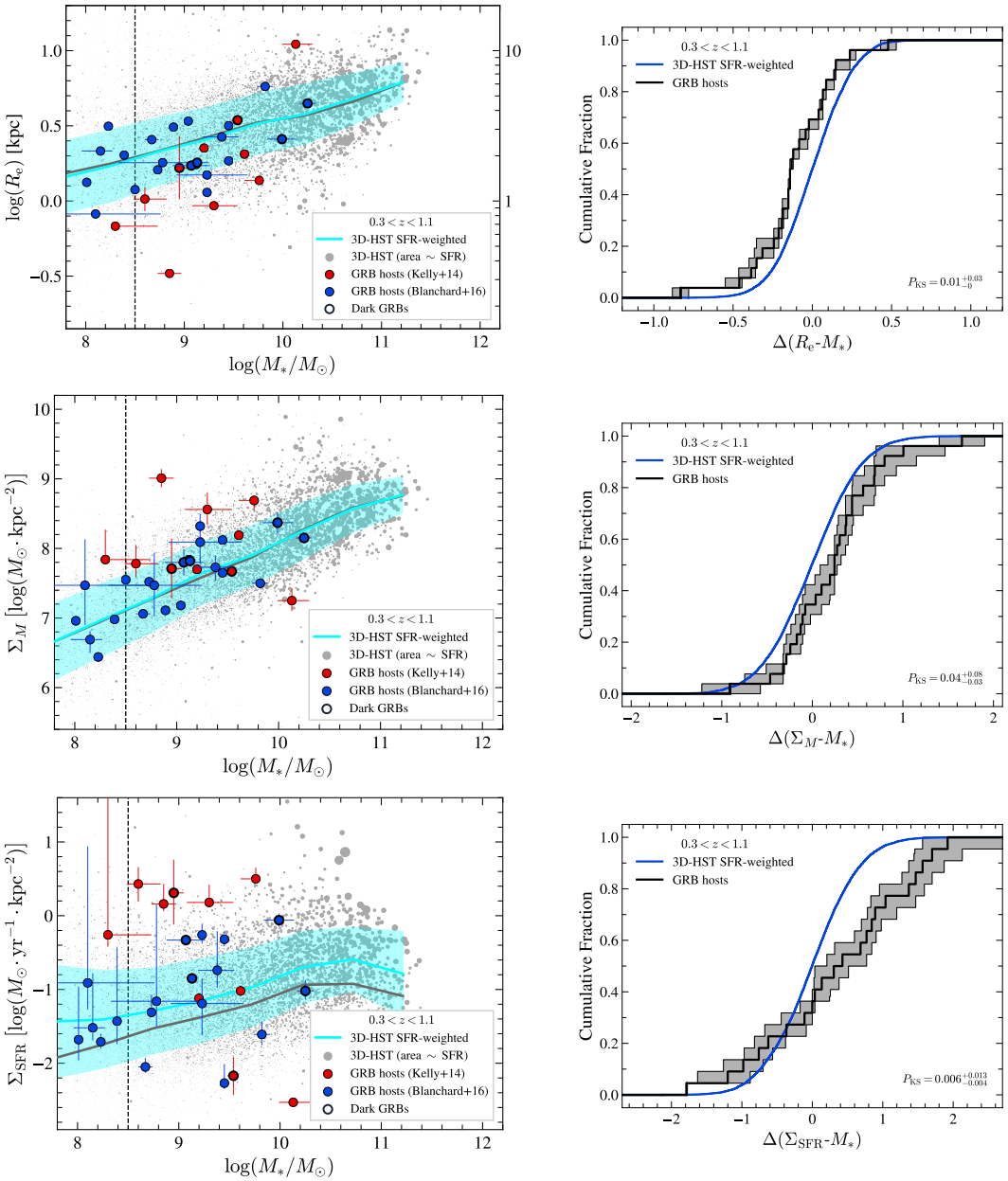

Figure 2.29: Stellar density of GRB hosts at $z < 1$ from Kelly et al. (2014) and Blanchard et al. (2016). *Left panels:* Half-light radius (top), stellar mass surface density (middle) and star formation rate surface density (bottom) against stellar mass for GRB hosts and star-forming galaxies. *Right panels:* Cumulative distribution of $\Delta(R_e\text{-}M_*)$ (top), $\Delta(\Sigma_M\text{-}M_*)$ (middle) and $\Delta(\Sigma_M\text{-}M_*)$ (bottom). The symbols are identical to those of Fig. 2.17.

Table 2.2: Physical and structural properties of GRB hosts at $z < 1.1$.

GRB	z	$\log(M_*/M_\odot)$	SFR ($M_\odot$/yr)	R_e (kpc)	Ref.
970508	0.84	$8.30^{+0.43}_{-0.01}$	$1.6^{+12.7}_{-0.6}$	0.68 ± 0.01	8, 8, 7
970828	0.96	$8.95^{+0.10}_{-0.05}$	$35.0^{+12.6}_{-7.6}$	1.66 ± 0.80	8, 8, 7
980613	1.10	$8.60^{+0.22}_{-0.11}$	$17.9^{+6.70}_{-7.3}$	1.03 ± 0.19	8, 8, 7
980703	0.97	$9.76^{+0.03}_{-0.15}$	$37.0^{+13.1}_{-3.3}$	1.37 ± 0.04	8, 8, 7
990712	0.43	$9.20^{+0.05}_{-0.03}$	2.39	2.25 ± 0.08	8, 9, 7
991208	0.71	$8.85^{+0.12}_{-0.12}$	$1.0^{+0.6}_{-0.2}$	0.33 ± 0.02	8, 8, 7
010921	0.45	$9.61^{+0.05}_{-0.02}$	2.50	2.05 ± 0.02	8, 9, 7
011121	0.36	$10.13^{+0.17}_{-0.14}$	2.24	11.04 ± 0.64	8, 9, 7
021211	1.01	$9.30^{+0.24}_{-0.22}$	$8.3^{+4.6}_{-0.7}$	0.93 ± 0.02	8, 8, 7
040924	0.86	$9.23^{+0.41}_{-0.31}$	$0.9^{+0.7}_{-0.9}$	1.49	8, 8, 3
050416A	0.65	9.23	$4.5^{+1.6}_{-1.2}$	1.14	2, 5, 3
050525	0.61	$8.1^{+0.15}_{-0.57}$	$0.52^{+2.21}_{-0.43}$	0.82	6, 6, 3
050824	0.83	8.23	$1.20^{+0.3}_{-0.26}$	3.14	2, 5, 3
051016B	0.94	9.45	$10.2^{+2.6}_{-2.0}$	1.85	2, 5, 3
051022	0.80	$9.99^{+0.15}_{-0.15}$	$36.68^{+7.91}_{-7.91}$	2.58	1, 1, 3
060729	0.54	8.39	$0.96^{+2.21}_{-0.69}$	2.02	2, 5, 3
060912A	0.94	$9.82^{+0.08}_{-0.08}$	$5.1\ ^{+2.1}_{-1.6}$	5.78	1, 5, 3
061110A	0.76	8.01	$0.23^{+0.38}_{-0.15}$	1.33	2, 5, 3
070318	0.84	8.73	$0.79^{+0.44}_{-0.24}$	1.61	2, 5, 3
071010A	0.98	...	...	1.33	3
071010B	0.95	...	...	2.09	3
071112C	0.82	8.89	...	3.10	4, 3
080319B	0.94	8.50	...	1.19	4, 3
080430	0.77	$8.15^{+0.12}_{-0.19}$	$0.87^{+1.49}_{-0.35}$	2.15	6, 6, 3
080916A	0.69	9.12	...	1.75	4, 3
081007	0.53	$8.78\ ^{+0.47}_{-0.45}$	$1.41^{+4.25}_{-1.11}$	1.80	6, 6, 3
081109	0.98	$10.25^{+0.08}_{-0.08}$	$11.80^{+4.1}_{-2.9}$	4.46	1, 1, 3
090417B	0.35	$9.54^{+0.03}_{-0.06}$	$0.5^{+0.3}_{-0.3}$	3.45 ± 0.06	8, 8, 7
090424	0.54	$9.38\ ^{+0.17}_{-0.19}$	$8.18^{+10.01}_{-4.60}$	2.67	6, 6, 3
090618	0.54	9.04	...	3.40	4, 3
091127	0.49	$8.67^{+0.07}_{-0.07}$	$0.37^{+0.1}_{-0.07}$	2.56	6, 5, 3
100621A	0.54	$9.07^{+0.19}_{-0.19}$	$8.70^{+0.8}_{-0.8}$	1.72	1, 1, 3
130427A	0.34	9.45	$0.34^{+0.2}_{-0.06}$	3.17	2, 5, 3
130925A	0.35	9.13	$2.9^{+0.5}_{-0.4}$	1.80	2, 5, 3

Notes. Names in bold are dark GRBs.

References. (1) Corre et al. (2018b); (2) Krühler & Schady (2017); (3) Blanchard et al. (2016); (4) Perley et al. (2016b); (5) Krühler et al. (2015); (6) Vergani et al. (2015); (7) Kelly et al. (2014); (8) Perley et al. (2013); (9) Savaglio et al. (2009).

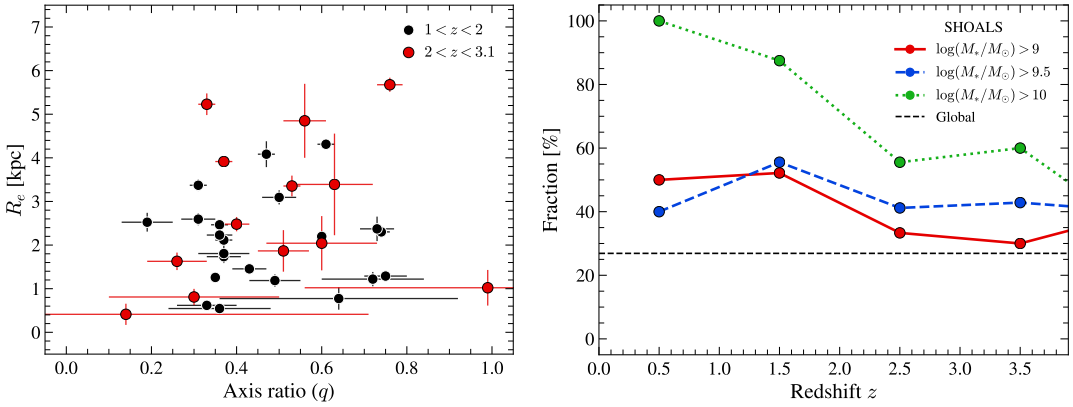

Figure 2.30: *Left panel:* Half-light radius along major axis as a function of axis ratios (q) for GRB hosts at $1 < z < 2$ (black) and $2 < z < 3.1$ (red). *Right panel:* Fraction of dark GRB hosts as a function of redshift for the SHOALS sample at different stellar mass cuts. The black dashed line shows the mean value considering all GRBs in the SHOALS sample.

2.3.3 GRB hosts at $1 < z < 3.1$

2.3.3.1 Axis ratio

The projection effect mentioned in Sect. 2.1.3.2 might cause an apparent deviation between the GRB host population and the control sample if GRB hosts considered were all observed, for instance face-on. Even if there is no particular reason that the galaxies were all observed with the same viewing angle, the modest sample sizes might cause such a statistical effect.

A visual inspection of the HST images (see Figs. 2.26 to 2.26) reveals that at least a few galaxies were observed under different viewing angles such as face-on (e.g., GRB 080603A) or edge-on (e.g., GRB 090404). A more quantitative approach is to test how the major axis size correlates with the axis ratio. For a biased population, there should be a correlation between the major axis and the axis ratio, where the small and large disk-like galaxies would have an axis ratio close to 1 and 0.1, respectively. For the GRB host population, this relation is shown on the left panel of Fig. 2.30. There is no strong correlation observed, and objects with small or large R_e have a uniform distribution of axis ratios. Therefore, there is no evidence that the deviation found between the GRB hosts and the control sample is due to a projection effect.

2.3.3.2 Fraction of dark GRBs

The Sect. 2.2.3.4 briefly mentioned that the observed fraction of dark GRB detected by *Swift* is approximately $25 - 40\%$ (e.g., Greiner et al. 2011). Because dark GRBs tend to be found in dusty and massive galaxies, an interesting aspect is to consider how this fraction evolves with redshift and stellar mass of the host galaxy. The evolution of this fraction was investigated using the unbiased GRB sample of SHOALS and the Table 3 of Perley et al. (2016a) where evidence of dark GRB afterglows based on β_{OX} or optical-NIR colors are reported. In the SHOALS sample, the overall measured fraction of dark GRBs is about 28%, consistent with previous fractions reported in the literature. On the right panel of Fig. 2.30, the evolution of the fraction per 0.5 redshift bin is visible for GRB hosts with stellar mass greater than 10^9, $10^{9.5}$ and 10^{10} $M_\odot$. As anticipated, the fraction increases with the stellar mass to reach approximately $40 - 50\%$ for a population of GRB hosts with a stellar mass $> 10^9$ or $> 10^{9.5}$ $M_\odot$.
At $1 < z < 2$, the fraction of GRBs hosts with dark afterglows found in the sample was larger (60%) than the overall observed fraction of dark for *Swift* GRBs. This higher dark fraction results from a likely selection effect of the HST proposals considered in the analysis. However, it appears to be mitigated by the 3D-HST completeness limit ($> 10^9$ $M_\odot$) applied to the set of GRBs samples in this redshift range (top panel of Fig. 2.13). This may be the result of a possible dependence of dark GRBs with the stellar mass of the host galaxy, as illustrated in the top panel of Fig. 2.30 with host galaxies of the SHOALS sample. Therefore, one would expect to find more dark GRB host galaxies if low-mass galaxies ($< 10^9$ $M_\odot$) are excluded from the GRB host population under study.

2.3.3.3 Stellar mass from M/L

The absence of multi-wavelength photometric data for several GRB hosts of our sample prevents a robust estimate of their stellar mass by SED fitting. Yet, removing these sources would significantly reduce the size of our parent population, given the modest number of GRB hosts observed with the HST/WFC3 camera and considered for this study. In order to maximize the number of objects in our sample, an alternative approach was considered to derive a stellar mass even for galaxies with a single photometric estimate. The approach is based on the corre-

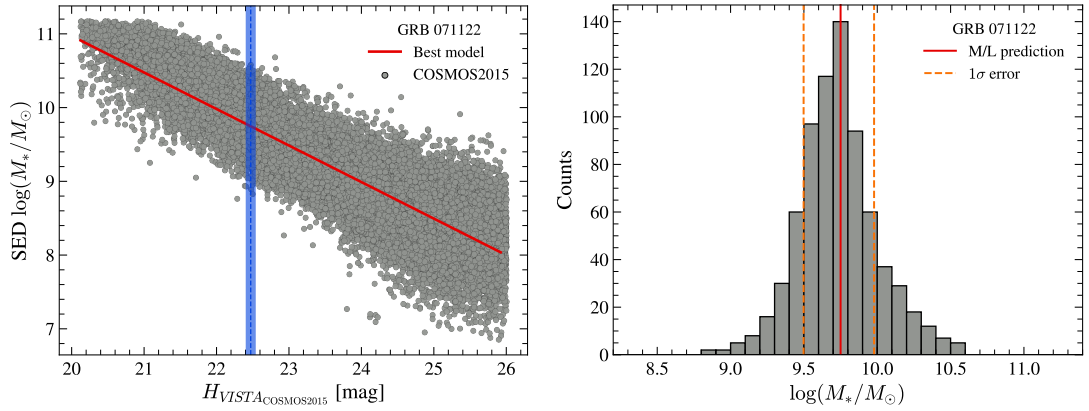

Figure 2.31: Stellar mass from M/L ratios determined for GRB 071122. *Left panel:* Stellar mass from SED fitting as a function of the H_{VISTA} magnitude for COSMOS2015 objects at $z = 1.14 \pm 0.1$. The best-fit model and the GRB host magnitude are shown in red and blue lines, respectively. *Right panel:* Stellar mass distribution of objects considered within the blue area of the left panel. The red line shows the stellar mass estimated for the GRB host and the 1σ errors are visible in dashed orange lines.

lation between the light and the stellar mass observed in large surveys of galaxies. An example of the process performed for each object is visible in Fig. 2.31. The left panel shows the relation between stellar masses inferred from SED fitting and H-band magnitudes, where high stellar mass galaxies are more luminous due to a significant amount of old stars emitting NIR light. The right panel reveals the large distribution of stellar masses for a given magnitude and its error, and highlights the limitation of this method on the accuracy of the derived stellar mass.

2.3.3.4 Dispersion of properties

At $1 < z < 2$, a large dispersion of stellar masses and SFRs extracted from the literature was found for a given GRB host galaxy (see Sect. 2.2.4.2). A similar analysis was performed for the GRB hosts at $2 < z < 3.1$. The observed trend is similar to the one at $1 < z < 2$, where the stellar masses (left panel of Fig. 2.32) and SFRs (right panel of Fig. 2.32) present a large dispersion for the same GRB host galaxy. At $2 < z < 3.1$, it is also interesting to point out that the stellar masses estimated from the M/L ratio appear to be systematically underestimated compared to SED fitting values. This might be due to the presence of very dusty

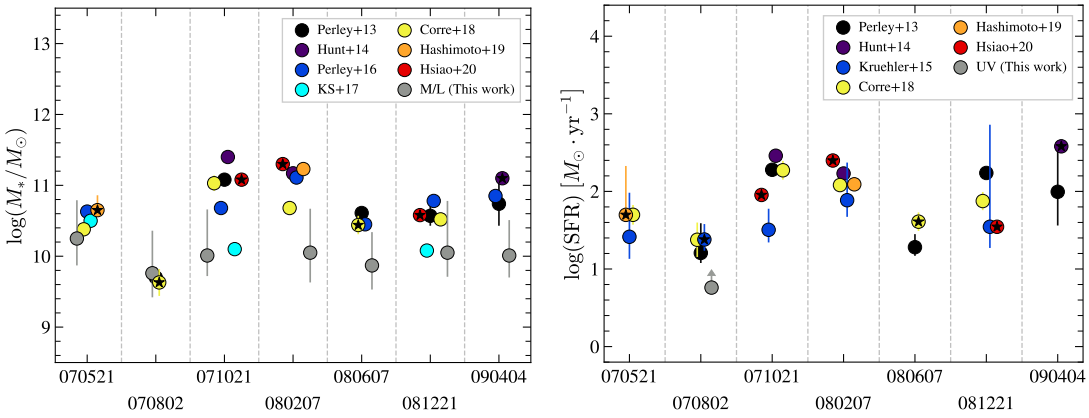

Figure 2.32: Compilation of stellar mass (left panel) and SFR (right panel) estimates for GRB hosts at $2 < z < 3.1$. Each circle corresponds to an estimate from the literature or determined as described in Sect. 2.2.4.2. The circles marked with a star represent the estimates used in the analysis.

host galaxies at this redshift since 100% of the detected GRBs were flagged as dark. Furthermore, at $z > 2$, the rest frame probed by $F160W$ might be slightly affected by dust extinction, resulting in an underestimated luminosity to derive the host stellar mass.

Chapter 3

The science using gamma-ray burst afterglows

Contents

The SVOM mission will benefit from an improved observational strategy between its optimized pointing law and the large number of ground facilities available to perform rapid follow-up observations of transient sources. SVOM is thus expected to provide a more homogeneous and complete sample of GRBs than previous missions. For instance, the number of GRBs with a redshift measurement is expected to reach 2/3 of the full sample, compared to 1/3 for the previous *Swift*

mission. In addition, the synergy between space and ground observations will also permit to quickly identify high-z GRB candidates and trigger larger and more sensitive facilities to further characterize these events.
The mission launch is planned for end 2023 with the first GRB alerts in 2024. The preparation of future follow-up observations is essential to be ready and to be able to react quickly to the first SVOM GRBs. On the French side, the expertise of these observations is progressively developed to ensure a quick and efficient response to the upcoming SVOM alerts. In this chapter, I present my contribution and experiences to develop and prepare future follow-up observations with SVOM. The context and scientific interest of follow-up observations are presented in Sect. 3.1. In Sect. 3.2, my contribution to the optical follow-up with the MISTRAL and VLT/X-Shooter instruments is described and finally in Sect. 3.3 the X-ray follow-up and the expected localization capacity of MXT are discussed.

3.1 Context and scientific objectives

The GRB emission is composed of two main phases, the prompt emission of a few seconds and an afterglow emission of a few minutes up to several days. For both emissions, a broad-band emission is expected, from radio to TeV range. Due to the very short duration of the prompt emission and current instrument capabilities, this emission is mainly characterized in the γ-ray range. The longer duration of the afterglow emission allows to perform follow-up observations using space and ground telescopes.
The multi-wavelength nature of the GRB afterglows was explained by the synchrotron external shock model (Mészáros & Rees 1997; Sari et al. 1998; Zhang et al. 2006) caused by the interaction between the ejecta of the central engine (jet) and the circumburst medium. The model describes the GRB spectrum as a power law with multiple breaks produced by different physical processes during the external shock process (electron Lorentz factor, synchrotron self-Compton and synchrotron cooling). In addition, a reverse shock propagating backwards through the ejecta is expected to produce an emission in the lower frequency part of the early GRB afterglow. Finally the multiple components of the jet such as the jet cocoon (Izzo et al. 2019; Chen et al. 2020) might produce additional emissions in the GRB afterglow spectrum, see for example Sharan Salafia & Ghirlanda (2022) for a review about the jet structure. Recently, for the first time, the GRB after-

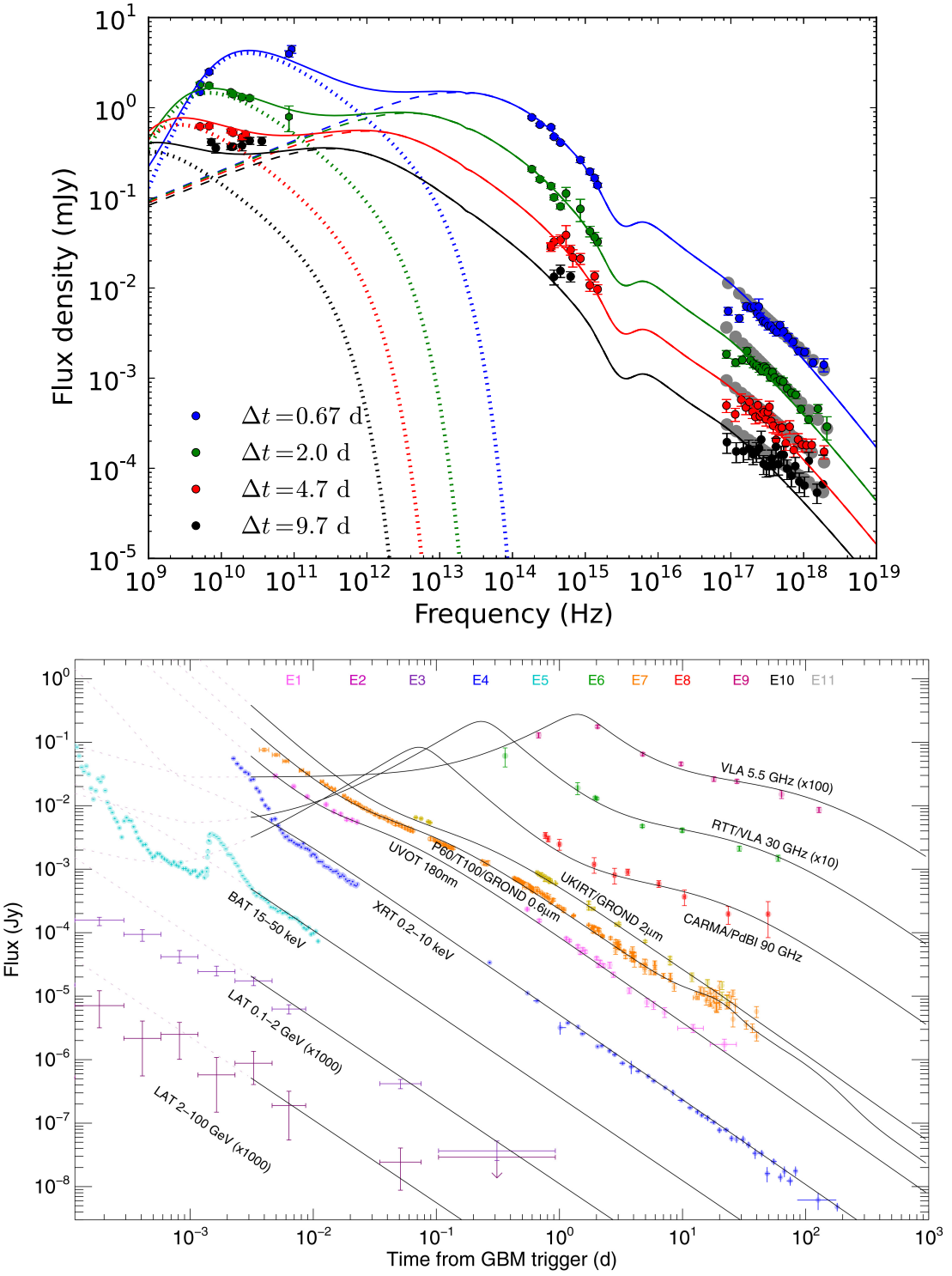

Figure 3.1: *Top panel:* Spectral energy distribution of GRB 130427A at different epochs. The combined model (solid lines) is composed of two components, a forward shock model (dashed lines) and reverse shock model (dotted lines) (Laskar et al. 2013). *Bottom panel:* Multi-wavelength light curves of GRB 130427A from radio to 100 GeV (LAT bands). (Perley et al. 2014)

glow emission in the teraelectronvolt range (1 TeV) was detected (Abdalla et al. 2019; MAGIC Collaboration et al. 2019a,b) and supports the possibility that synchrotron self-Compton radiation is commonly produced in GRBs.
As the blastwave decelerates, the strength of the shock decreases, causing a fading of the afterglow. The light curves at all wavelengths are thus expected to decay with time as a power law. In practice, the picture is more complicated as other physical processes can introduce energy and change the decay phase (see Sect. 3.2.1 and 3.3.1).
The broad-band nature of the afterglow was since confirmed by numerous multi-wavelength follow-up. The GRB 130427A at $z = 0.34$ was among the brightest GRBs detected so far and allowed us to collect a large set of multi-wavelength data at different epochs (e.g., Maselli et al. 2014; Kouveliotou et al. 2013; Laskar et al. 2013; Perley et al. 2014). In the top panel of Fig. 3.1, the spectral energy distribution (SED) of GRB 130427A afterglow is shown at different epochs. The SED is decomposed into two components, (i) a typical synchroton emission expected from the forward shock indicated by dashed lines and consistent with the optical and X-ray range, and (ii) a component expected from a reverse shock model (dotted lines) to explain the bump in the early radio observations. The radio observations of GRB 130427A represent a robust detection of the presence of a reverse shock in GRB afterglows. The bottom panel of Fig. 3.1 shows multi-wavelength light curves of GRB 130427A and their typical (broken) power law decays.

The large SED of GRB afterglows provides a rich quantity of information about the GRB formation mechanism. In addition, their bright afterglows allow to probe in absorption all materials present in the burst line of sight (LOS). First, this offers a direct way to infer the redshift of the source. Then, given that GRBs can be detected from low to high redshift (Tanvir et al. 2009; Salvaterra et al. 2009), the imprinted lines can be used to map the cosmic chemical evolution in the ISM of star-forming galaxies (Laskar et al. 2011; Arabsalmani et al. 2018b). The detection of a Lyman continuum in some GRB afterglows and their very simple intrinsic shape provide a way to measure the escape fraction of ionizing radiations in faint star-forming galaxies (Vielfaure et al. 2020, 2021). Finally, it can provide insight into the shape of dust extinction law on the GRB line of sight (Bolmer et al. 2018; Zafar et al. 2018; Bolmer et al. 2019; Zafar et al. 2019).
It is worth emphasizing that the GRB afterglow probes only one line of sight in the galaxy. Using hydrodynamical simulations, Metha & Trenti (2020); Metha et al.

(2021) (see also, Arabsalmani et al. 2022, submitted) showed that the metallicity probed by the GRB in absorption can be significantly different from the metallicity measurement in emission. A statistical sample averaged over many lines of sight under random viewing angles is therefore essential to limit the possible bias of this approach.
The limited duration of GRB afterglows makes their follow-up observations challenging and subject to many uncertainties (e.g., observational conditions, availability of instruments). The information obtained from each instrument/team is essential to improve the observational strategy, and to encourage additional follow-up observations in the case of a particularly interesting target, such as very bright or high$z$ GRBs. It is therefore usual to share preliminary results of fresh observations with the entire community using the gamma-ray burst coordinates network (GCN) system.

3.2 Optical follow-up

For the vast majority of GRBs, if the source was sufficiently well localized and observed within a few minutes or hours after the alerts, an optical counterpart was detected (e.g., Kann et al. 2010, 2011). The fraction of GRBs with faint or no optical afterglow represents between 20% and 40% of the total GRB population and are named optically dark GRBs. Current ground optical telescopes are routinely used to perform follow-up observations of transient events and to further characterize their optical emission. In this section, I describe my participation and contribution to the optical follow-up of GRBs using 2-meter (Sect. 3.2.2) and 8-meter (Sect. 3.2.3) class telescopes. The results discussed are part of the preparation for the SVOM follow-up and more generally in the effort to better characterize GRBs and their host galaxy.

3.2.1 Optical afterglows

The spatial resolution of optical imaging and spectroscopy is usually better than that of X-ray instruments. This allows to determine a GRB localization at sub-arcsecond accuracy (< 1 arcsec). An accurate localization ensures the association between the GRB and its host galaxy, and permits to quantify the burst locations

within the host or star-forming regions (Fruchter et al. 2006; Blanchard et al. 2016; Lyman et al. 2017).

Optical photometry of the source allows to study the decay of the optical light curve and to better understand the physics of the jet (e.g., jet components, jet breaks, the central engine). In addition to the typical power law decay, a complex and rich diversity of features were observed such as re-brightening features (Nardini et al. 2011) or optical flares (Swenson et al. 2013), and up to eight different components were identified by (Li et al. 2012). Kann et al. (2010, 2011) provided a collection of optical light curves of *Swift*-era bursts. The luminosity distribution of the sample gave the typical expected R-band magnitude range at $T_0 + T$ after the burst detection and emphasizes the importance of rapid follow-up to be able to detect the optical counterpart with a medium-sized ground telescope.

The GRB emissions illuminate all the material between the burst and the observer. A fraction of the light can be absorbed by elements present along the line of sight. Optical spectroscopy allows a detailed study of these imprints and provides a rich source of information. For example, the absorption lines can provide a direct measurement of the redshift of the burst (see Sec. 3.2.3.5) or an estimate of metal and dust abundances in the GRB environment and its host. Finally, a temporal optical spectroscopy follow-up of low-z bursts can provide information on the supposed supernova associated with the GRB (e.g., Hjorth et al. 2003).

Optical follow-up of GRBs is therefore a powerful tool to better understand and characterize their progenitor, their nearby environment and their host galaxy.

3.2.2 Imaging and long-slit spectroscopy with MISTRAL

The Haute-Provence Observatory (OHP) is an historical astronomical observatory located in the south-eastern of France at 650 m altitude. The average seeing is about 2 arcsec and the observational conditions are favorable about 60% of the nights, and totally cloudless for 47% of them. On the site four main telescopes are installed, with a primary mirror of diameter 1.93 m (hereafter T193), 1.52 m, 1.20 m and 80 m. The OHP is ideally located between the C-GFT at Xinglong observatory (China) and Colibri at San Pedro Mártir (Mexico) to perform optical follow-up of SVOM alerts. This section reports the current progress and first follow-up observations using the OHP/T193 telescope.

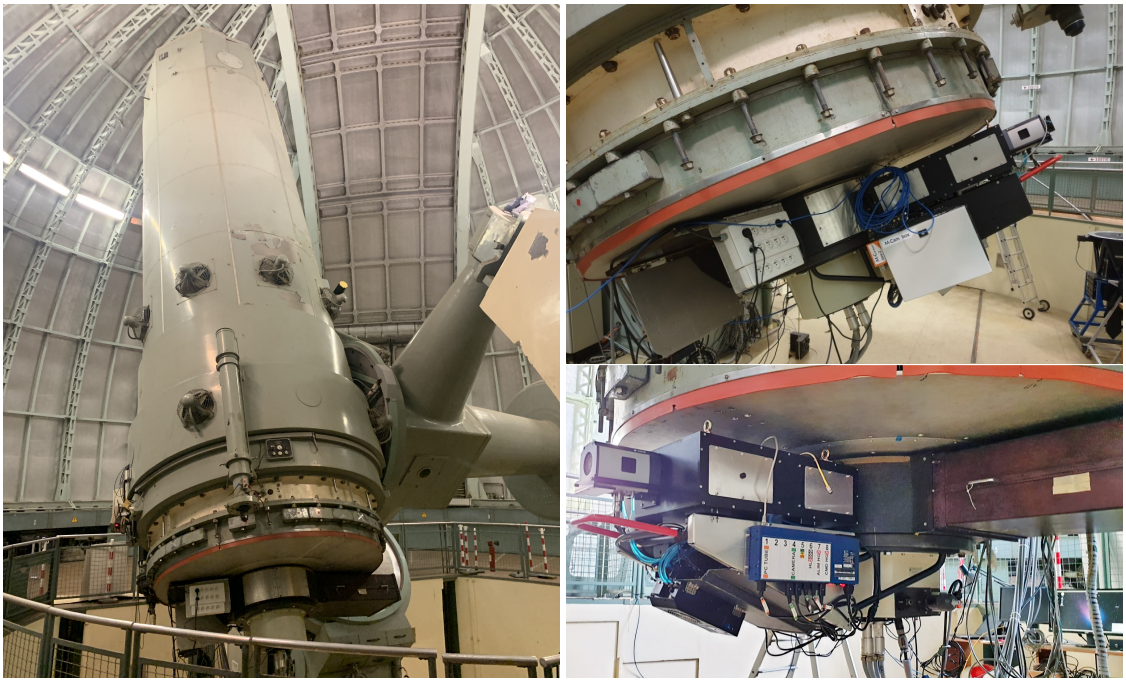

Figure 3.2: Pictures of the OHP/T193 telescope (left) and the MISTRAL spectro-imager installed at the folded-Cassegrain focus (right). Note that on the left picture MISTRAL was not mounted and therefore is not visible.

3.2.2.1 MISTRAL instrument

The OHP/T193 telescope was built and installed in 1958 at OHP. Currently, it is the only remaining telescope at OHP to be entirely dedicated to science. The telescope is composed of a 193 m diameter primary mirror with three different focus: Newton (f/5), Cassegrain (f/15) and Coudé (f/32). Using the high resolution ELODIE spectrograph mounted on the T193, Michel Mayor and Didier Queloz discovered the first exoplanet outside our Solar System (Mayor & Queloz 1995) and won half of the Nobel Prize in Physics 2019 for this discovery. Currently two instruments are mounted on the T193, the SOPHIE spectrograph at the straight Cassegrain focus since 2006 and the Multi-purpose InSTRument for Astronomy at Low-resolution (MISTRAL) spectro-imager at the folded-Cassegrain focus since 2021. The two instruments can be switched in less than one minute without any mechanical operation by moving a 45° commutation mirror. A picture of the T193 and the MISTRAL instrument are shown in Fig. 3.2.

MISTRAL is an imager equipped with an ANDOR deep depletion CCD 2K×2K

Table 3.1: Main MISTRAL characteristics.

Wavelength range	4200-8200 Å (blue setting) 5800-9950 Å (red setting)
Resolution	~ 750 at 6000 Å
Field of View	5.1 arcmin (full), ~ 9 arcmin (total)
Split width	1.9 arcsec
Filter wheel	SDSS g′, r′, i′, z′, Y, Hα, [OIII], SII, Hβ
CCD	Andor series iKon-L 936, 2048×2048 pixels
Pixel size	13.5 μm
Pixel scale	0.48 arcsec/pixel
Gain	1.03 e^-/ADU
Saturation	$\sim 60\,000$ ADU

camera capable of low resolution spectroscopic measurements using an elongated and narrow slit followed by a grism. The detector is cooled down to $-90°$ to $-95°$ with a five-layer Peltier device resulting in a very low dark current (< 3 e^- per hour per pixel). The spectroscopy mode has two independent settings using a blue grism (4200-8000 Å) and red grism (5800-9950 Å) with an average resolution of $R \sim 750$. The instrumental response was characterized using several observations of standard spectrophotometric stars, Feige 15 for blue dispersor/lens and HR1544 for red dispersor/lens. The average spectral response[1] is maximum at 7000 Å and 8500 Å for blue and red configurations, respectively. A major limitation of the current configuration is the impossibility of changing the dispersor (red or blue) during night operation. The manipulation requires the intervention of technical staff during the working day. For the imaging mode, the filter wheel provides access to a total of 12 photometry filters (SDSS g′, r′, i′, z′, Y)[2]. The main characteristics of MISTRAL are given in Table 3.1. The CCD can be read using two modes, a fast mode (3 MHz) and a slow mode (50 kHz). The former has a reading time of 0.7 s and readout noise of 11 e^- rms. It is used for technical operations such as telescope focus or pointing. The latter has a reading time of 40 sec for 4 e^- rms and is used for science operations. Associated with the development of MISTRAL, an upgrade phase of the T193 was initiated. The guidance system was improved with a new and more powerful camera. The new system offers better stability and

[1] http://www.obs-hp.fr/guide/mistral/sub2.html
[2] http://www.obs-hp.fr/guide/mistral/filter_characteristics.html

a larger FOV (70 arcmin^2) for finding guiding stars. In addition, a new system to accelerate the focus between SOPHIE and MISTRAL was installed to reduce the commutation time between the two instruments. The current configuration allows to switch between the two instruments in less than 20-30 minutes.
Since March 2022, MISTRAL was opened to the community for visitor mode and ToO mode through calls for INSU programs. The ToO mode is designed for fast observations of transient sources in the context of the new time-domain era (e.g., LIGO-Virgo, Zwicky Transient Facility or SVOM). The ToO observations can be triggered using two methods, during the day-time by contacting the OHP director or during night-time with the night operator for an immediate reaction (< 1 hour). All nights are opened for ToO observation except during technical events on the instruments/telescope. In addition, the internal rules at OHP limit the possible trigger to one every 3 nights and for a maximum time of 2 hours per trigger. It is worth noting that the ToO mode is for the first time offered at the OHP/T193. For this reason, the procedures, the night operators and the system are in learning phase to improve and reduce the reaction time.
A crucial aspect to perform (reliable) follow-up observations of transient sources is to know the limitations of the instrument. This point was investigated by the MISTRAL team during technical runs of the instrument. For the imaging mode, two exposure time calculators (ETCs) are available to estimate the observational capacity and time required for detecting the target. These calculators are based on an N-parameter space model produced from a combination of observations under different observational conditions (airmass, sky transparency, seeing) between 1 to 60 minutes. The ETC2 provides an estimate of the typical exposure time to reach a given S/N and the ETC3 to ensure the detection of a given percentage of objects. The simulation needs some inputs on the expected properties of the target such as its spatial characteristics (extended or point like), its intrinsic size (FWHM) and magnitude. In addition, the selected filter and expected observational conditions (Moon illumination, seeing, airmass, ...) are considered to provide the most realistic estimate possible. In a similar way for the spectroscopic mode of MISTRAL, the ETC1 gives an estimate of the exposure time for the target considering the slit width, required S/N, expected spectral properties (absorption or emission lines). The Table 3.2 reports typical magnitude limits reached for ~ 10 min of observation in imaging mode for several filters (top). The magnitude limit of the target source to perform a spectroscopic follow-up and get a higher S/N of 3 for the expected

Table 3.2: MISTRAL estimated exposure times for imaging (top) and spectroscopic (bottom) observations. The imaging was determined using several observations under various conditions and gives estimates under a "mean" OHP observational conditions (airmass, sky transparency, seeing). The spectroscopy limits are for a point source observed during one hour under a seeing of 2.5 arcsec to get a minimal S/N of 3 for the expected most intense Absorption (Abs) and Emission (Em) lines. (Adapted from MISTRAL CookBook)

Imaging (filters)	Duration (min)	Limit magnitude (AB)
g'	20	~ 20.5
r'	10	~ 20
i'	10	~ 21
z'	10	~ 19.5
Y	10	~ 18.5
Spectro. (setting)	Duration (min)	Limit magnitude (AB)
Abs. lines (blue)	60	$V < 19.5$
Abs. lines (red)	60	$V < 19.5$
Em. lines (blue)	60	$V < 20.5$
Em. lines (red)	60	$V < 20$

most intense spectral line in one hour is given in the bottom part of Table 3.2. Additional details can be found in the online MISTRAL CookBook.

3.2.2.2 Follow-up program

As mentioned previously, the OHP is ideally located between China and Mexico. In addition, the current number of spectroscopic instruments available to conduct ToO observations in Europe and more generally in the northern hemisphere is limited and often located West of OHP (e.g., Canaries Island, North America). Finally, telescopes such as the T193 are more likely to be available than large (> 8 m) ground telescopes. For these reasons, MISTRAL can play a key role in performing follow-up observations of future Northern Hemisphere SVOM alerts during European nights. With its spectro-imaging capability, it may contribute to (i) locate the counterpart and characterize its photometric properties, and (ii) determine the GRB redshift and study the absorption lines along the line of sight. Furthermore, because of the imminent start of the SVOM operations in approximately two years, it becomes urgent to prepare and train the French community

to quickly react to transient alerts.
In this context, the SVOM collaboration initiated and proposed a follow-up program (PI: E. Le Floc'h) on the MISTRAL spectro-imager taking advantage of the available ToO mode. The proposal was accepted and granted with 18.7 hours, i.e. 10-12 alerts over the 2022A semester (March - September). A similar proposal was resubmitted and accepted for the 2022B semester (October - March). It will permit to continue the effort and training. This ToO GRB follow-up program allows on the OHP side to practice the ToO procedure and on the SVOM side to quickly react and analyze the data.

In the vast majority of cases, MISTRAL is able to reach in a reasonable time a magnitude of about 20.5 mag for photometry and 19 mag for spectroscopy (see Table 3.2). Based on a *Swift* GRB sample, Kann et al. (2010) showed that a large majority of GRB afterglows are brighter than 21 mag in the R-band if observed within 4 hours after the trigger time (see Fig. 3.3). This means that most GRBs should be detectable using MISTRAL photometry if they are observed within typically less than 4 hours. Among them, GRB afterglows brighter than 19 mag could be observed by the MISTRAL spectroscopic mode to further constrain metal absorption lines and determine the GRB redshift.

3.2.2.3 Sample selection

Until the launch of SVOM, the MISTRAL follow-up program consists in developing and improving the follow-up strategy using the *Swift* GRBs. The current rate of *Swift* alerts is about 1 every week or two weeks. Typical location errors returned by XRT (Burrows et al. 2005) are less than 5 arcsec and if UVOT detects an optical afterglow, positions are improved to better than 1 arcsec. In comparison, the expected error box provided by SVOM will have a similar error box for VT but slightly larger for MXT (see Sect. 3.3.4). Therefore, the *Swift* localizations are fully compatible with future SVOM alerts and provide a realistic training set. Note that, for the two missions, the error box is also compatible with the MISTRAL FOV of 5 arcmin and allows to quickly identify the possible GRB counterpart in the images. A common criterion among the GRB follow-up community is to trigger on events localized outside the Galactic plane ($A_V < 0.5$). This avoids a possible bias due to a too strong extinction from the Milky Way on the GRB line

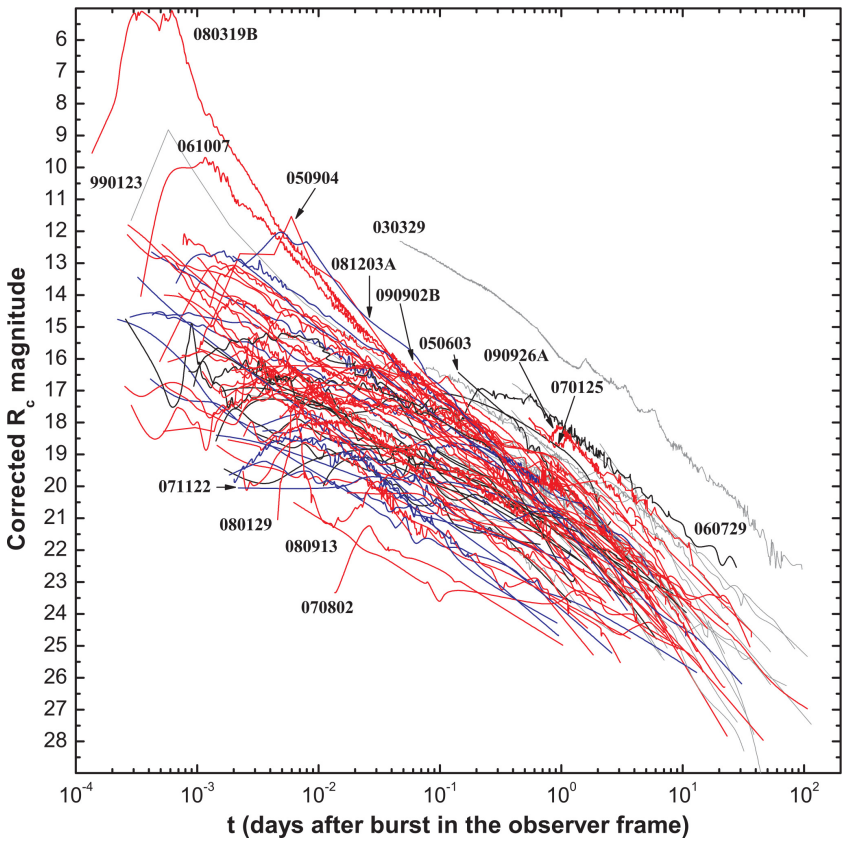

Figure 3.3: Light curve of optical long GRB afterglows detected by *Swift*. The R-band corresponds to the observed wavelength range and is corrected from Galactic extinction and possible host contamination. (Kann et al. 2010)

of sight. The sample selection can be summarize as follow:

1. *Swift* alert with at least an XRT detection (error box $\lesssim$ 10 arcsec)
2. Visibility $>$ 1 hour above 30° at OHP
3. $T_{\rm obs} < T_0 + 4$ hours
4. Low Galactic extinction: $A_V < 0.5$
5. No nearby bright stars

These criteria are not exclusive, and in some cases such as a very bright afterglow or a high-z candidate, the criteria mentioned above can be relaxed to trigger MISTRAL. The target visibility can be checked with the astro-Colibri tool (Reichherzer et al. 2021; Schüssler et al. 2022). It provides in real time the alerts

of transient and have a friendly user interface to visualize the target visibility at several observatories.

3.2.2.4 Observation strategy

Once triggered and MISTRAL ready to observe, a first imaging sequence starts for a typical duration of 20 min. By default under "mean" observational conditions, the images are in the r-band. If previous GCNs information indicate a low or high redshift, weak or strong dust extinction, the strategy might be optimized using other filters in order to increase the probability to detect the counterpart. If before or during the trigger a GCN or a team reports no detection with an upper limit higher than MISTRAL sensitivity, the trigger is canceled. During this imaging phase, in near real-time, the data are processed and analyzed (see Sect. 3.2.2.5) by the proposal members. The objective is to identify the GRB counterpart and choose the next sequence to run. Two sequences are then possible:

- A GRB counterpart is identified and localized with a magnitude lower than 19^{th} mag in the r-band. MISTRAL is switched to the spectroscopic mode for a integration time of 60 min (Table 3.2).
- Too faint ($> 19^{\text{th}}$ mag) or no counterpart is identified. The imaging mode continue to increase the image depth for a detection, or to further constrain the afterglow fading behavior. Successive images of 10 min are collected up to a duration of 60 min.

In total, the ToO sequence is defined in order to have a total duration of 2 hours: 20 min to go from SOPHIE to MISTRAL, 20 min for the first sequence, 60 min for the second sequence and 20 min to go back to SOPHIE instrument. The two sequences were therefore optimized in order to maximize the detection chance given the MISTRAL performance and the ToO time constraint.

A major limitation of the MISTRAL instrument is its inability to switch easily from the blue to the red setting and vice versa. For daytime trigger, technical staff can be contacted to change the setting from one to the other. However, a night trigger implies that the installed dispersor/lens configuration is fixed. For this reason, the choice of the default setting is important. The current criterion

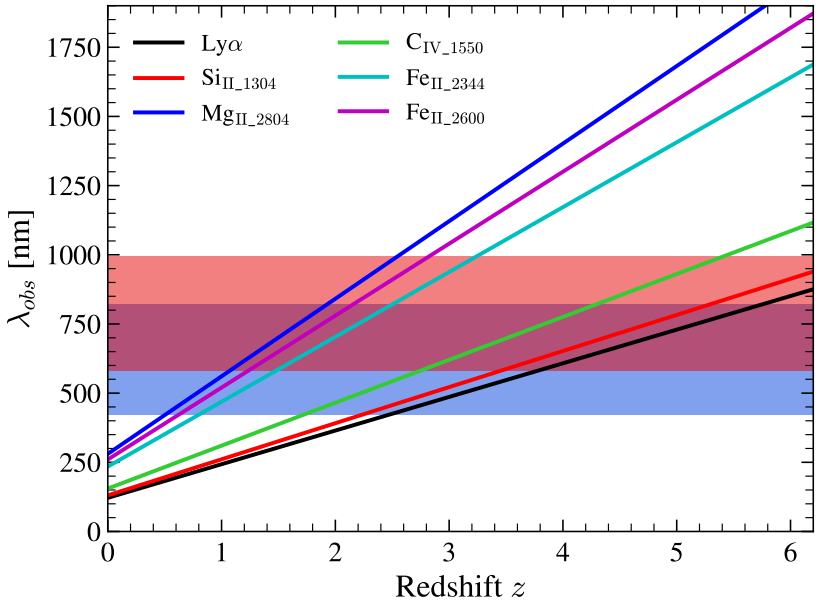

Figure 3.4: Observed wavelength of selected absorption lines as a function of redshift. The wavelengths covered by the blue and red settings are shown by the blue and red area, respectively.

considered to choose the configuration was to increase the probability of identifying a GRB and performing a spectroscopic follow-up. For imaging, the r-band is usually the best compromise and can be observed with both settings. It is therefore not the most limiting element to choose one configuration over another. For the spectroscopic mode, the question is equivalent to: what is the setting where the maximum number of absorption lines can be detected given the redshift distribution of the GRBs? The typical redshift distribution of long GRBs was provided in Fig. 1.8. Moreover, Fig. 11 of Wei et al. (2016) gave the simulated redshift distribution of ECLAIRs GRBs. For both, the majority of GRBs are located at $1 < z < 3$. In Fig. 3.4, the observed wavelengths of expected absorption lines as a function of redshift are provided. The selected lines are strong absorption lines often observed in GRB afterglows (e.g., Fynbo et al. 2009) that MISTRAL is able to resolve and detect. Given the redshift distribution of the GRBs, it is clear that the blue setting maximizes the probability of measuring a redshift for a random GRB. For this reason, the blue dispersor was chosen as the default setting for the MISTRAL GRB ToO observations. Figure 3.4 also illustrates that in the case of a high-z candidate ($z > 5$), the blue setting is not appropriate to provide a redshift. Again, the setting choice is motivated to maximize the probability of

a spectroscopic detection with MISTRAL. With a different science objective, the considerations below may be different and evolve. The possibility of changing this setting during night operations by developing a new mechanism is under discussion and is one of the improvements considered by the MISTRAL technical staff.

3.2.2.5 Data reduction development

The ToO sequence starts with a photometry phase to detect the GRB afterglow, estimate its magnitude and position the slit if a spectroscopic observation is possible. When an exposure is done, the data are pushed in real time to a data cloud. The data are then quickly reduced using a basic `Python` script. The imaging processing consists in a bias subtraction and a flat-fielding using static calibration files. The dark is not subtracted given the very low dark current measured during the technical tests (less than 3 e^-/hour/pixel). When multiple images are available, they are aligned and stacked together to increase the S/N and the image depth. The astrometry and photometry are performed using `STDpipe`[3] Python package. `STDpipe` also provides a routine to detect the transient in the image but given the small error box provided by *Swift*, if detected, finding the source is relatively straightforward.
The spectral quicklook reduction uses the Automated SpectroPhotometric Image REDuction (`ASPIRED`)[4] (Lam et al. 2021) Python package. The scripts used in our ToO program are inspired from the quicklook developed by the MISTRAL staff to reduce the spectra. Since data reduction is often performed at night, I optimized and automated the creation of the configuration files required by ASPIRED. This speeds up the process and reduces the risk of errors. This version of the pipeline with a tutorial and examples were provided to the co-PIs of the ToO program.
The spectral data reduction starts from a raw 2D science spectrum. The image is reduced in a similar way to the imaging mode with a bias subtraction and a flat-fielding using static calibration files. Then, the trace is extracted from the 2D spectra and the sky is subtracted using regions on the edge of the image (see Fig. 3.5). The 1D spectrum is then calibrated in wavelength using an automatic line detection and a line identification from the calibration spectrum (arc lamp spectrum). It is worth noting that ASPIRED is able to correct spatial deviation

[3] https://github.com/karpov-sv/stdpipe
[4] https://github.com/cylammarco/ASPIRED

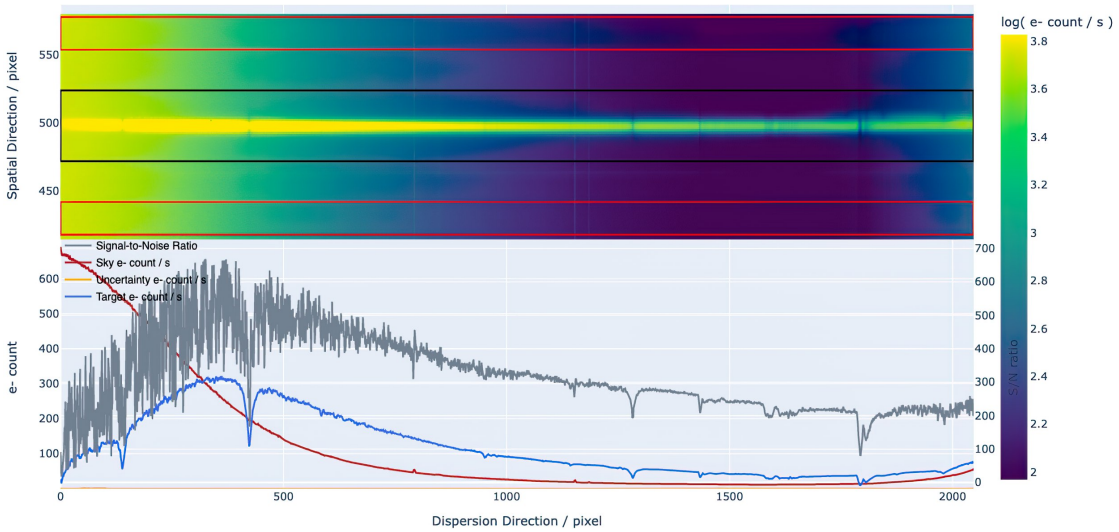

Figure 3.5: Example of a MISTRAL spectrum reduced with ASPIRED. The top panel shows the 2D spectrum. The black box indicates the region used to extract the 1D spectrum (bottom panel) and red boxes are the regions where the sky is measured.

(tilted or curved spectrum) along the dispersion direction of the trace. This effect was not strongly observed during MISTRAL tests and is therefore not considered in the current version of the scripts. A flux calibration can also be performed by ASPIRED using a standard source observed under the same conditions as the scientific target but is not mandatory for a quicklook analysis of the spectra during the night. Currently, a new version of the quicklook is under development in collaboration with people of the Institut d'Astrophysique de Paris (IAP) to perform a wavelength calibration of the 2D MISTRAL spectra.

3.2.2.6 First triggers and results

For the first semester of our ToO program with MISTRAL (March-September 2022), the telescope was triggered three times. However, no spectroscopic data were collected. Instead, we performed imaging observations and tried to constrain the optical light curve decay. We observed the field of GRB 220623A at $T_0+15.2$ h, GRB 220708B at $T_0+19.5$ h and GRB 220711B at T_0+4 h during about 60 minutes (6×10 min exposures) each. GRB 220708B and GRB 220711B were observed with the nominal configuration (blue setting and r′ filter) while GRB 220623A was observed with the red setting and the i′ filter. The change in configuration was

motivated by reported observations with a higher magnitude limit in the r-band than MISTRAL could reach in 60 min of exposure. The criterion on the T_{obs} was not satisfied for GRB 220623A and GRB 220708B but this constraint was relaxed knowing that the probability of detecting the afterglow would be lower. The resulting stacked images are shown in the left panels of Fig. 3.6. For each of them, we did not detect any new source inside or close to the XRT error box. We reported these observations as upper limits via GCN notices (Schneider et al. 2022; Turpin et al. 2022). GRB 220708B was a high-z candidate and additional details regarding this GRB are given in Sect. 3.2.3.5.

The limiting magnitudes of the stacked images were estimated using two independent methods and both provided similar values. The first approach consists in extracting all the source with `SExtractor` at ± 300 pixels around the expected source position. This limits contamination by artifacts on the edge of the image. The distribution of the source magnitudes follows that of standard source number counts, with the number of objects increasing progressively with the magnitude, before dropping because of the instrument sensitivity. An estimate of the limiting magnitude is therefore given by this break in the number counts, which is clearly visible on the right panels of Fig. 3.6. The second and more accurate method consists in determining the variation of the sky values using aperture photometry (for example, with a radius of 5 pixels) at different empty regions of the image. The dispersion at 3σ of the distribution gives an estimate of the limiting magnitude of the image (S/N > 3). Given the uncertainties of both methods (e.g., photometry calibration, artifacts), we determined a limiting magnitude of $i' > 21.5$ for GRB 220623A and $r' \gtrsim 22$ mag for GRB 220708B and GRB 220711B. In addition to the magnitude constraints reported by other groups in the literature, these values could help to constrain the fading of the GRB light curve.

3.2.3 Spectro-imaging with the VLT

The use of larger telescopes ($>$ 5 m-class telescope) is essential to perform a detailed characterization of optical afterglow of transient sources (e.g., dust and molecular elements along the GRB line of sight) where a higher S/N and resolution is required. Larger telescopes also mean that it is more difficult to grant time. Smaller telescopes are thus essential to select the most interesting targets and the rare events for further study with larger facilities. This section discusses my contri-

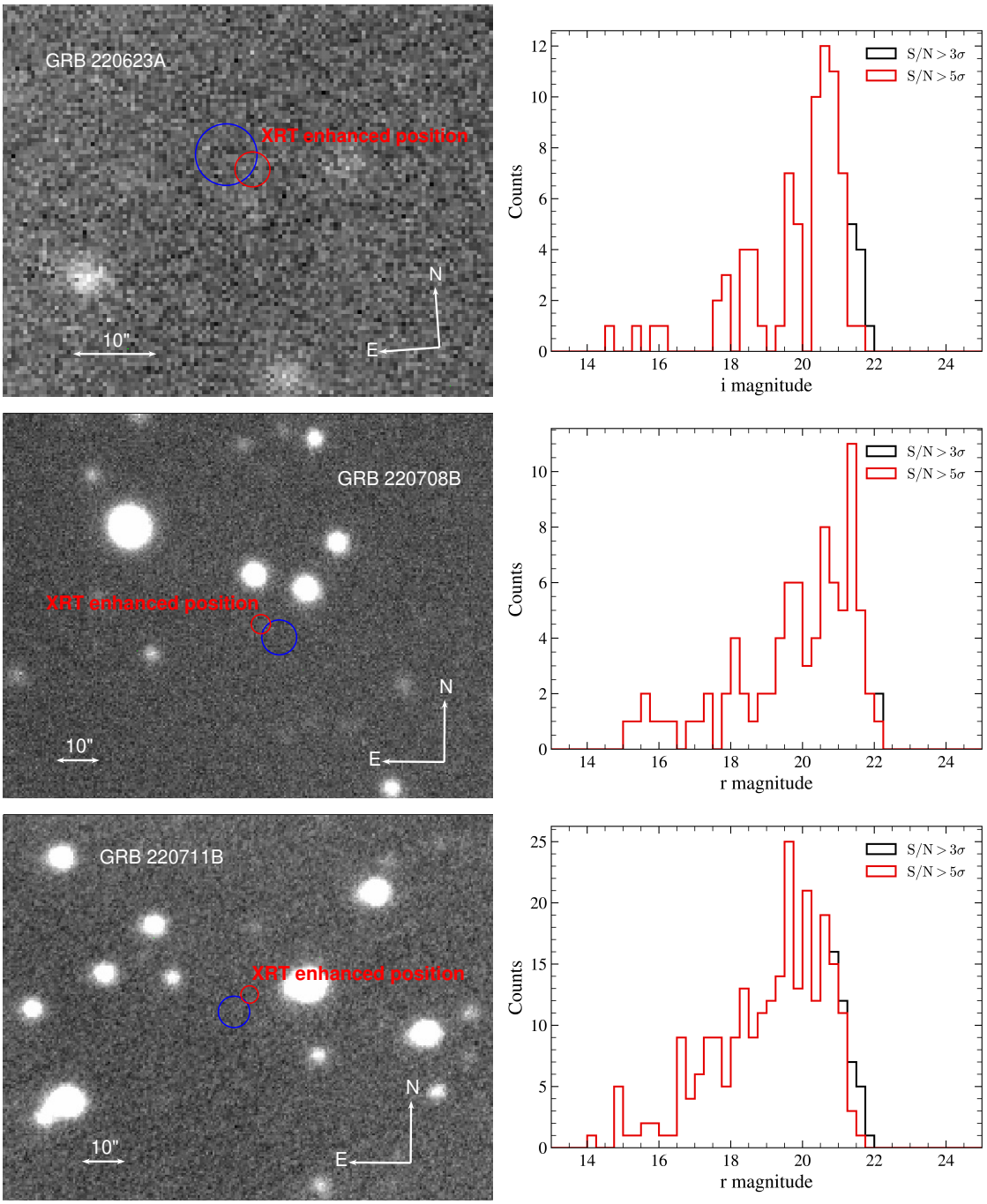

Figure 3.6: *Left panel:* Images of GRB220623A in i′-band (top), GRB220708B in r′-band (middle) and GRB220711B in r′-band (bottom) fields of 60 minutes exposure with the OHP/T193 MISTRAL instrument. The first and enhanced XRT error boxes are indicated in blue and red color, respectively. *Right panel:* Distributions of detected sources within ± 300 pixels around the XRT positions of the image shown in their respective left panel.

bution to the follow-up observations among the *Stargate* consortium (Sect. 3.2.3.3) using the ESO Very Large Telescope in Chile. In particular, the observations with the X-Shooter instrument that I had the opportunity to trigger and the prompt data analyses that I performed are reported.

3.2.3.1 The Very Large Telescopes

The Very Large Telescope (VLT) is a European ground arrangement of four Unit Telescopes (UTs) with a primary mirror of 8.2 m in a Ritchey-Chrétien reflector system. It is located at Cerro Paranal in the Atacama Desert (Chile) at 2 635 m and is operated by the European Southern Observatory (ESO). The observational conditions are excellent with about 340 clear nights per year. The vast majority of the time, the four telescopes are used individually, but they can also be combined together in inteferometric mode. The four UTs are named Antu (UT1), Kueyen (UT2), Melipal (UT3) and Yepun (UT4), see Fig. 3.7. The first light was obtained on Antu in 1998. Each UT is equipped with a set of instruments arranged at the different telescope foci, covering the near-ultraviolet (300 nm) to the mid-infrared wavelengths (24 μm). The VLT is also equipped with an adaptive optics system to correct the effects of atmospheric turbulence and improve the images. In addition to the UTs, four Auxiliary Telescopes (ATs) with a primary mirror of 1.8 m are available and fully dedicated to the interferometric mode. The ATs are mounted on tracks and can be moved to change their configuration.
The VLT had produced a huge quantity of science results and had a significant impact on the observational astronomy. In particular, it contributed in a major way to the detailed study of the GRB afterglows and the redshift measurement of the most distant GRBs currently known (Tanvir et al. 2009; Cucchiara et al. 2011). The instruments of the VLT are regularly upgraded to remain competitive over the years. Currently, several instruments are in development such as MOONS (Cirasuolo et al. 2014) or MAVIS (McDermid et al. 2020) and will be installed at the VLT in the coming years.
To perform follow-up observations of transient events, two modes are proposed at VLT: (i) a standard ToO mode with a reaction time of more than 30 min that can interrupt the Service Mode and Visitor Mode (if visitors agree), and (ii) a Rapid Response Mode (RRM) with an almost immediate follow-up interrupting the current observation whatever the mode.

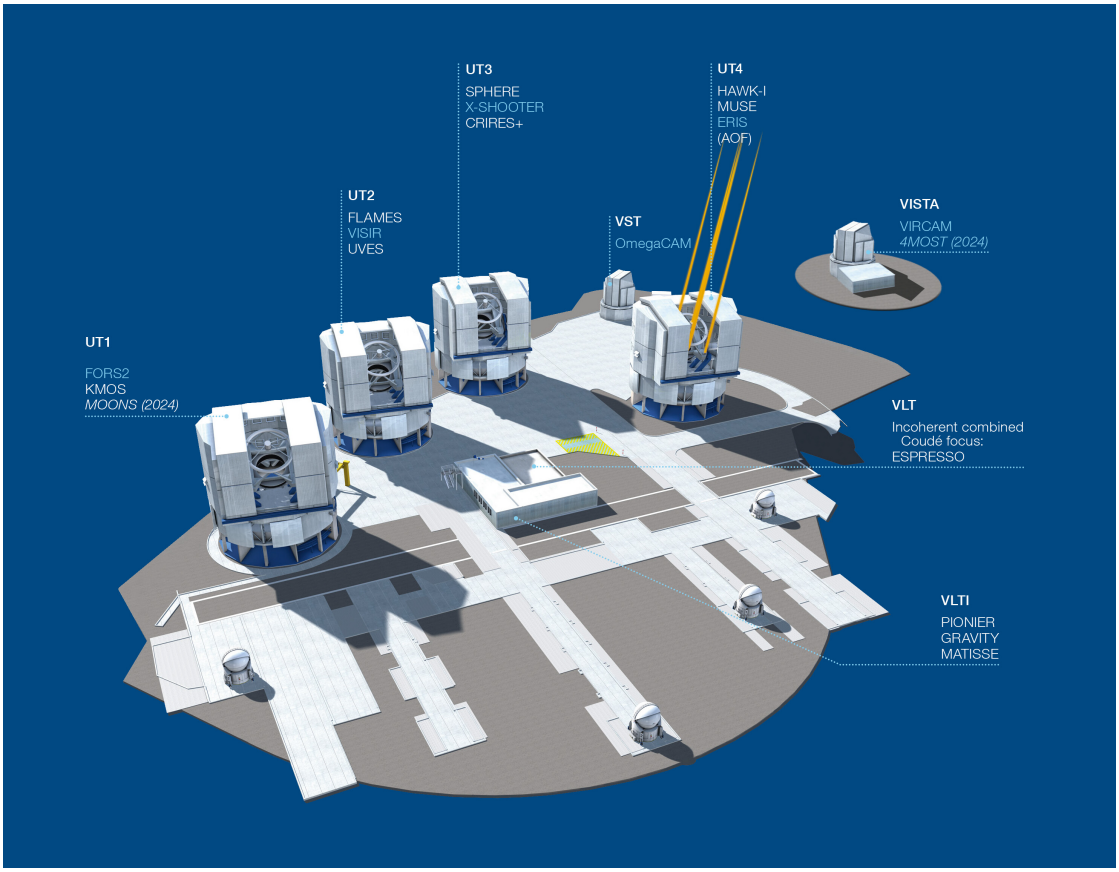

Figure 3.7: The four Unit Telescopes and instruments of the Very Large Telescope on Paranal. Instruments listed in blue color are at the Cassegrain focii of the telescopes. (Credit: ESO)

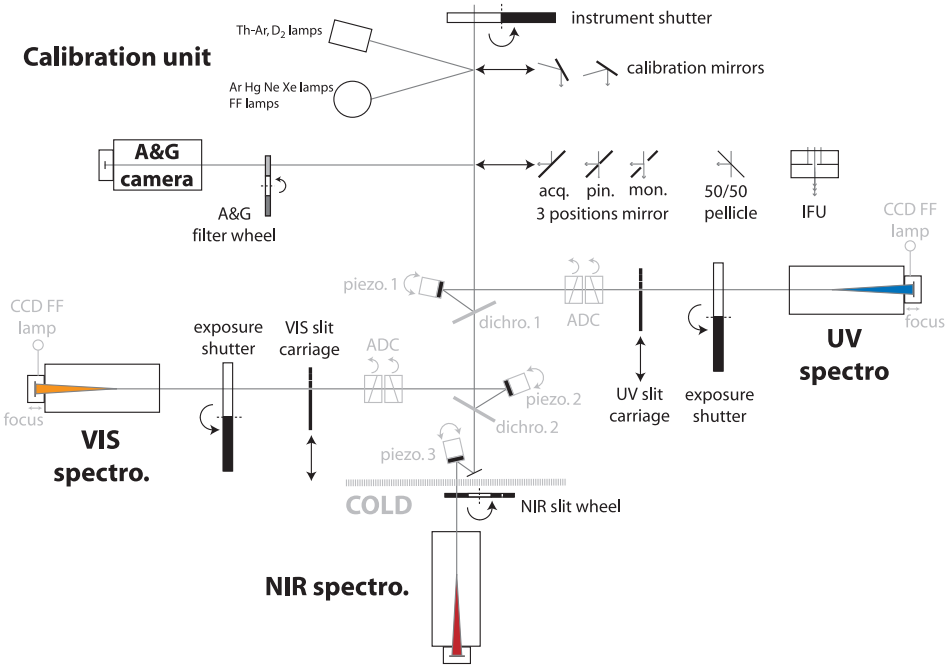

Figure 3.8: Schematic view of the X-Shooter instrument. The light path is from the top to the bottom. The three arms are shown by a different color. (Vernet et al. 2011)

3.2.3.2 X-Shooter instrument

The X-Shooter instrument (Vernet et al. 2011) is a medium-resolution spectrograph of the VLT. It is installed at the Cassegrain focus of the UT3 Melipal telescope. X-Shooter is composed of three arms named, UVB (300-559.5 nm), VIS (559.5-1024 nm) and NIR (1024-2480 nm), see Fig. 3.8. This configuration permits to obtain simultaneously a spectrum of the object from 300 nm to 2.5 μm. The first light of the instrument was in 2009. X-Shooter offers multiple slit widths from 0.4" to 1.6" but all have a fixed length of 11". The resolution varies from 3 000 to 2 0000 depending on wavelength and slit width. Under average observing conditions, the limiting AB magnitude to obtain a spectrum with a S/N of 10 in 1 hour of exposure is about 21.5 mag in the UVB, decreasing to 20.5 mag in the NIR due to atmospheric absorption. The image of the field and the object is obtained by the acquisition and guiding A&G camera. The limiting magnitude obtained with the A&G camera is $r' \sim 21$ mag for a exposure times of 60-120 s. Additional information about the instrument characteristics are provided on the ESO website (`https://www.eso.org/sci/facilities/paranal/instruments/xshooter/inst.html`). X-Shooter offers different observing modes: staring (fixed position on sky), nodding along the slit, offsetting to a fixed sky position (alternating between object and sky), or sequence of offsets (mapping). The nodding mode consists in slightly moving the telescope between two observations along the slit. This mode allows to improve the sky subtraction and is classical for near-infrared observations. An example of an X-Shooter spectrum using nodding mode is shown in Fig. 3.9, with the reduced 2D spectrum (top) and the extracted 1D spectrum (bottom) of the GRB 210905A afterglow. GRB 210905A is among the rare well-constrained GRBs detected at $z \gtrsim 6$ by spectroscopic and imaging follow-up (with five others, so far). The X-Shooter observation started ~ 2.6 hours after the trigger via the *Stargate* Large Programme for GRB follow-up (Sect. 3.2.3.3) and provided an excellent measurement with a S/N > 15. In the VIS spectrum, a clear break around 9000 Å is observed and interpreted as the Lyman-α break. In addition, other lines such as Fe II, Al II, C IV and Si II and fine structure lines were detected and confirmed its redshift of 6.31 (Tanvir et al. 2021a), see also Rossi et al. (2022).

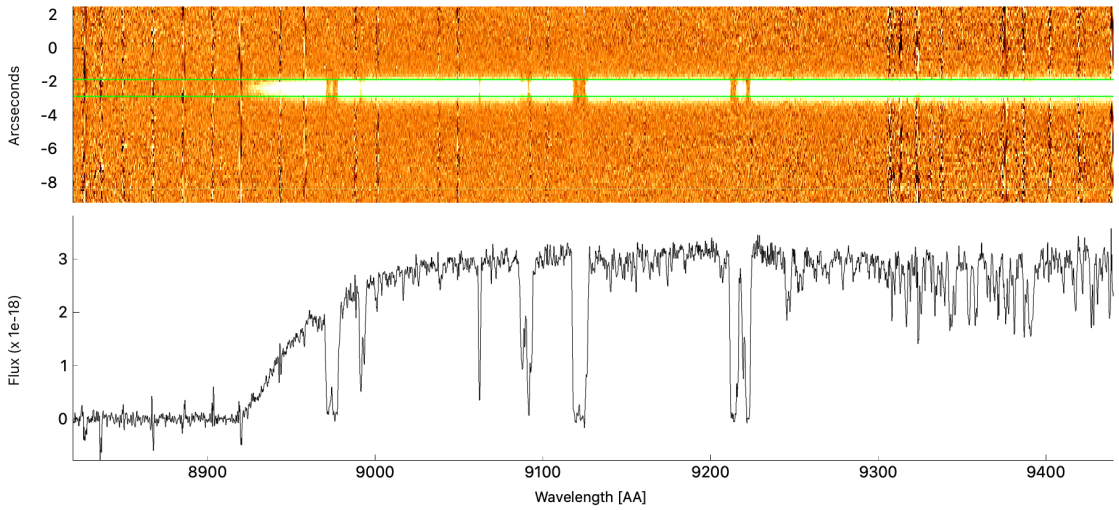

Figure 3.9: X-Shooter spectrum of GRB 210905A at $z = 6.31$. The 2D spectrum is visible at the top panel. The green lines show the region corresponding to the 1D spectrum in the bottom panel.

3.2.3.3 Stargate consortium

Stargate is an international collaboration of GRB experts to perform follow-up observations of well-localized transient events at the VLT. During my thesis, I joined the consortium as Burst Advocate (BA) and achieved several shifts (each for a duration of one week). The collaboration was born from the merging of several GRB programs carried out by different groups. The objectives are to simplify the process for ESO and to improve the efficiency and scientific production.
It is proposed as a long-term proposal (PIs: N. Tanvir, S. D. Vergani, D. Malesani) and was awarded more than 130 hours in the past on various VLT instruments. It was recently accepted for 4 more semesters between October 2022 to September 2024. This means that this program will likely overlap with the first year of SVOM operations and will provide a valuable support to the SVOM follow-up strategy. The program provides access to $\sim$ 30 h/semester on X-Shooter, FORS2, HAWK-I, MUSE and UVES instruments. The strategy of the follow-up observations is optimized in real-time and depends on the transient nature. For "sample" GRBs (as selected in Sect. 3.2.2.3), X-Shooter is the default choice to detect absorption lines in the GRB afterglow given its medium-resolution and large frequency coverage. If X-Shooter is not available, FORS2 is a good alternative for imaging and low-resolution spectroscopy. For more exotic cases such as very bright optical afterglows, UVES is used to get a high-resolution spectrum or FORS2 to perform

polarimetry. Finally, for short GRB candidates, in addition to X-Shooter spectroscopy for redshift measurement, FORS2 and HAWK-I imaging are interesting to constrain the light curve fading and support HST kilonova[5] (Metzger et al. 2010) searches. The exposure time of the requested observations depends on the intrinsic brightness of the event and the delay between the trigger and the effective observation at VLT. It is worth mentioning that another long-term follow-up program is being conducted by the ENGRAVE consortium to detect the electromagnetic counterparts of gravitational waves.
The follow-up observations at VLT are triggered in 95% of cases with the ToO mode. In the rare case of high priority targets immediately visible from Paranal, the RRM mode is activated robotically to get a spectrum within a few minutes following the burst detection. For instance, the RRM mode can be used to investigate the variation of fine structure lines in GRB afterglows that were observed at early time (D'Elia et al. 2009).
Since GRBs are unpredictable events and can be detected at any time, it is not possible to be active and ready to react 24/7 during several months. The monitoring of alerts is arranged by a two-person team (BAs) for a period of one week. The collaboration is composed of more than 100 members, among which about 30 members composed of senior scientists and PhD students performed regular BA shifts. The frequency of the shifts is thus about 1 week every 3 months. A BA shift consists of being ready to quickly react at any time (including night) to an alert and initiate a follow-up observation with the appropriate instrument and settings. This ensures that no transient is "lost". Although the trigger is sent by a single BA to Paranal, the preliminary discussion includes a core group of active members via the *Stargate* mailing list. The discussion helps to define the best strategy for performing efficient observations given the trigger time ($T_0 + T$) and taking into account previous information reported by other teams via GCN notices.

3.2.3.4 Data analysis

The need to reduce and analyze the data is not mandatory to become a *Stargate* BA. Once the trigger is executed, the data are rapidly pushed to the ESO portal by the VLT staff. Frequently, the data are quickly reduced by a *Stargate* member

[5] A kilonova is a transient source occurring after the merging a compact binary system (BNS or NS-BH) powered by the radioactive decay of heavy elements (r-process nuclei).

and shared with all members. The data analysis is then carried out very quickly and the results are reported in less than a few hours via a GCN notice. Given the expertise of the members and their desire to share their experiences, I decided to take the opportunity to learn how to reduce and analyze X-Shooter observations. The X-Shooter calibration files from the night of acquisition are transferred and available a few hours after the raw science data. The first "fast" reduction is usually performed by the `XSH QuickReduction`[6] pipeline and uses static calibration files to reduce the data. This pipeline is a wrapper of the ESO X-shooter pipeline written in `Python`. The reduction is performed for each X-shooter arm and it takes less than 5 minutes to reduce all three arms. For my personal use of the pipeline, I slightly modified the original script and improved it. The reduction parameters (mode, arm), input files, output files can be managed from a single `yaml`[7] file. Since this reduction is often carried out during the night or early in the morning, it has the advantage of being more user-friendly and limits the risk of errors.
Once reduced, each member can analyze the (2D or 1D) spectra with his/her own scripts or online tools such as "Sandbox" of GRBSpec database (de Ugarte Postigo et al. 2014). To analyze the spectra, I usually use the python Graphical User Interface (GUI) named `zHunter`[8] recently released by a *Stargate* member (J. Palmerio). `zHunter` provides an interactive interface to visualize and manipulate 1D or 2D spectra. It also permits to infer the GRB redshift (+ absorbing systems) using the ratio of absorption lines frequently observed in GRB afterglows. I also actively contributed to the improvement and bug correction of this tool. Finally, I initiated and supported the possibility of using this tool to analyze MISTRAL spectra (Sect. 3.2.2).

3.2.3.5 First triggers and results

Throughout the thesis, I carried out a total of 5 shifts of one week with *Stargate*. During these shifts, I triggered two times the X-Shooter instrument in ToO mode to perform follow-up observations of *Swift* alerts.
The first one was for GRB 211207A. With the X-Shooter data collected, we inferred a redshift of $z = 2.27$, and reported it as a GCN (Schneider et al. 2021). It was often observed that GRB host galaxies have high neutral hydrogen columns and

[6] https://github.com/jselsing/XSH_QuickReduction
[7] Yaml is a language designed for human interaction and often used for configuration files.
[8] https://github.com/JPalmerio/zHunter

are classified as damped Lyman-α absorbers (DLAs, $\log(N_{\rm HI}) > 20.3$ atoms/cm^2), see for example Tanvir et al. (2019). A trough was observed in the UVB X-Shooter spectrum of GRB 211207A around 3960 Å (see Fig. 3.10). This gave a first hint about the possible redshift of the source assuming that this absorption is caused by the Lyman-α absorption ($\lambda_{\rm Ly\alpha} = 1216$ Å) of the surrounding GRB environment (mostly the host galaxy). Then, multiple absorption lines were observed in the continuum emission. They were consistent with the absorption lines frequently observed in GRB afterglows and the first clue provided by the strong absorption around 3960 Å (left top panel of Fig. 3.11). Furthermore, it was observed in the NIR spectrum an emission line at 16390 Å consistent with an emission of [O III] 5007 from the GRB host galaxy (left bottom panel of Fig. 3.11). The gas-phase metallicity of the GRB host galaxy can be determined using the ratio of strong nebular lines [O II], [O III], [N II] and the Balmer emission lines (Hα, Hβ), depending on the different metallicity diagnostics, see for example Kewley & Ellison (2008). Because the [O III] line was detected in addition to the afterglow emission, this may suggest that the host has many H II regions that may produce other strong nebular lines detectable by ground-based telescopes. On the other hand, the metallicity could also be obtained from the hydrogen and metal absorption lines measured by X-Shooter in the GRB afterglow. This object is therefore an interesting candidate where metallicity measurements could be independently obtained in absorption and emission. For the moment, such an estimate with both approaches was achieved only for one GRB (Friis et al. 2015). A larger sample will provide a better understanding of how the metallicity probed by a single sight line is representative of the overall metallicity of the host galaxy. The sample may soon increase with the time granted on the JWST/NIRSpec to study a sample of 10 GRB hosts at $z \sim 2$ (Schady et al. 2021). Finally, the right panel of Fig. 3.11 shows the GRB 211207A field with error box positions determined by *Swift* and the X-Shooter slit in the r′-band for an exposure of 60 s.

For the second GRB observed during my shift (GRB 220711B), the ToO was not executed due to bad weather conditions in Paranal and pointing restriction. As mentioned earlier in Sect. 3.2.2.6, MISTRAL was triggered but no optical counterpart was detected in the r-band down to 22 mag. The Nordic Optical Telescope (NOT) also observed the field of GRB 220711B and reported no detection in the r-band but a detection of a viable afterglow in the z-band (Malesani et al. 2022a). The fading of the source was later verified thanks to new NOT observations, which

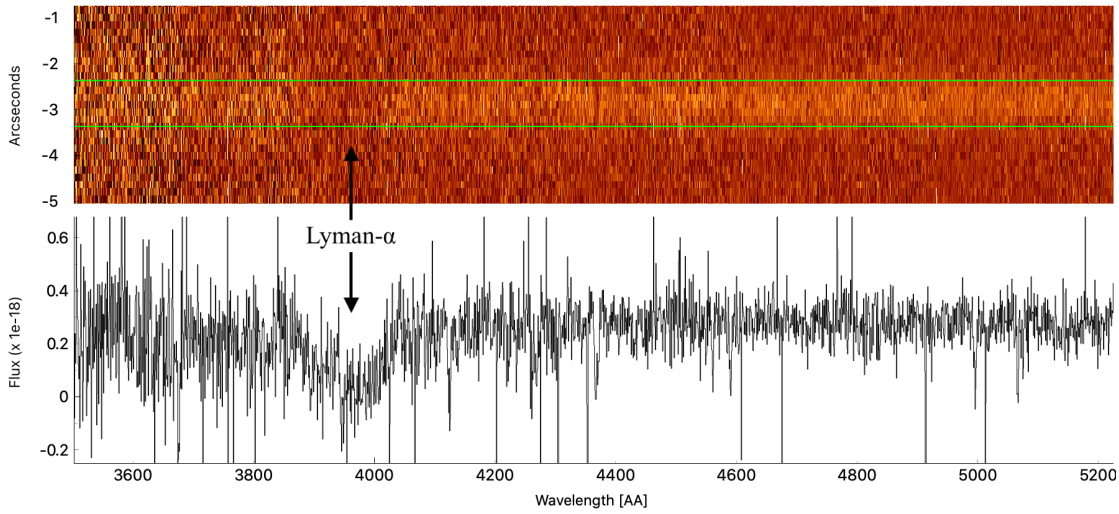

Figure 3.10: X-Shooter spectrum of GRB 211207A at $z = 2.27$. The 2D spectrum is visible in the top panel. The S/N ratio is about 2-3 depending on the wavelength range considered. The green lines show the region corresponding to the 1D spectrum in the bottom panel. The arrow indicates the Lyman-α absorption visible in the 2D and 1D spectrum. (Schneider et al. 2021)

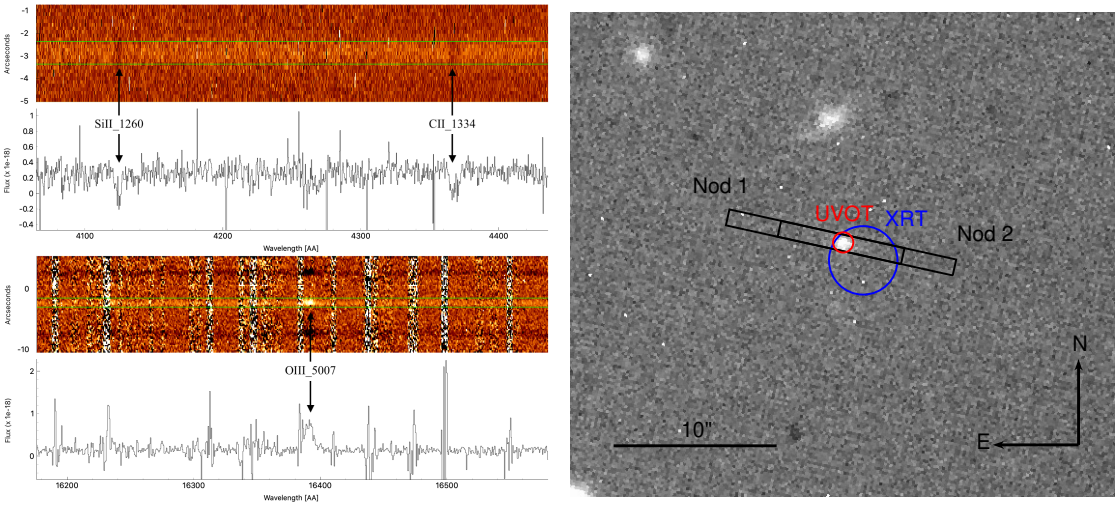

Figure 3.11: *Left panel:* Zoom of the X-Shooter spectrum of GRB 211207A showing two absorption lines (top panel) and one emission line (bottom panel). *Right panel:* X-Shooter imaging of the GRB 211207A in the r-band. The best GRB position returned by UVOT and XRT are shown in red and blue, respectively. The X-Shooter slit (with the nodding) is visible as a black box. (Schneider et al. 2021)

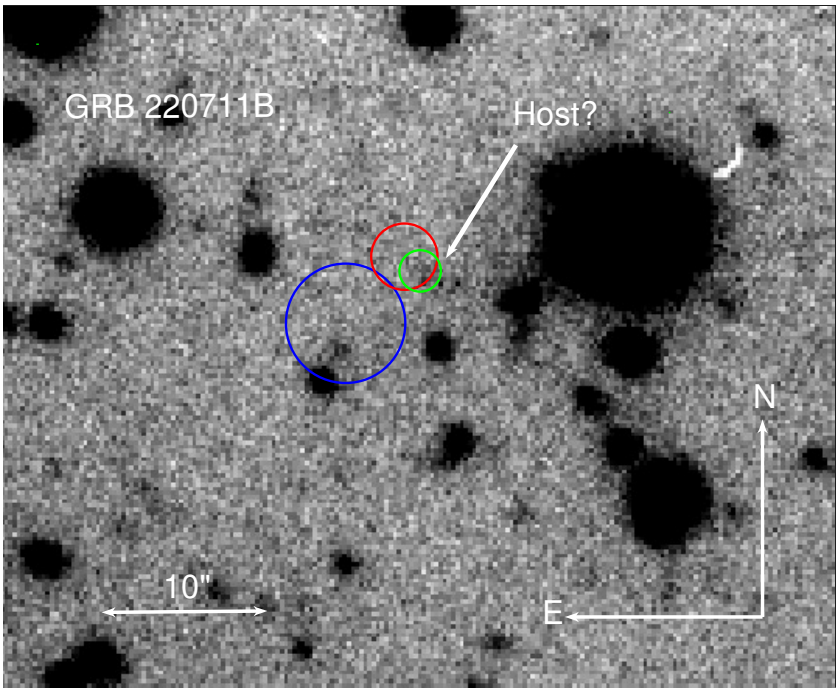

Figure 3.12: Deep FORS2 imaging of GRB 220711B field. The blue and red circles are the first and enhanced XRT error positions. The green circle shows the optical afterglow position found in the z-band NOT observations.

confirmed the GRB origin of this source (Malesani et al. 2022b). These findings suggested a possible high-z GRB with an i-dropout spectrum or a highly extinguished GRB at moderate redshift. No spectroscopic observations were performed from other large telescopes to determine its redshift and to break the degeneracy between these two scenarios. Given that host galaxies of GRBs with dark afterglows were often observed to be relatively red and bright (Chrimes et al. 2019), we triggered a deep integration in the R-band with FORS2. The observations were executed at $T_0 + 13$ days and consisted in 8×300 s (40 minutes) exposures. I reduced and combined the individual exposures in a single image to increase the image depth. The resulting stacked image is shown in Fig. 3.12. A faint source is marginally detected at a position consistent with the one reported by the NOT observations in the z-band. This possible detection of the host galaxy suggests that GRB 220711B was a highly extinguished GRB and not a high-z source.
Finally, I contributed to the analysis of other events such as GRB 220427A, observed ~ 8 hours after the trigger with X-Shooter. However no useful spectroscopy was secured due to the weak afterglow brightness at that time. We reported AB magnitude on the afterglow for g′, r′ and z′ bands using images of the X-Shooter

acquisition camera (de Ugarte Postigo et al. 2022a). It can also append that interesting events are monitored and observed quite longer after the initial trigger. It was the case of the ultra-long GRB 211024B. We performed a late time observation (153 days after the GRB) at the best GRB localization reported in order to detect potential emission lines from the host galaxy. A weak emission of [OII] 3727 and [OIII] 5008 was detected, and we inferred a redshift of $z = 1.11$ that we reported as GCN (de Ugarte Postigo et al. 2022b). Given the spatial coincidence between these emission lines and the afterglow, the redshift determined for this object is probably the redshift of the ultra-long GRB.

3.3 X-ray follow-up

Since the launch of *Swift* in 2004, thanks to its rapid observations performed of typically ~ 100 s after the BAT trigger, the early phases of GRB X-ray afterglows are routinely detected by XRT. Among the large *Swift* sample (> 1000 GRBs), no X-ray afterglow was detected for only a handful of cases with a prompt slew. For this reason, it is expected that long and short GRBs may all have an X-ray counterpart. In addition, the fading of the X-ray afterglow is used to confirm the nature of the detected source and classify it as a GRB. In this section, I discuss the typical X-ray spectra and light curves observed for GRBs (Sect. 3.3.1) and their relevance for studying their host galaxies in Sects. 3.3.3 and 3.3.2. Finally the Sect. 3.3.4 describes the expected MXT localization performance and the possible consequences to identify the host galaxy.

3.3.1 X-ray afterglows

The *Swift* GRB population showed that the majority of X-ray afterglow light curves are more complex than a single simple power law (Gehrels et al. 2009). It was also observed that the light curves can vary and evolve over more than 7 orders of magnitude in brightness and 6 orders of magnitude in time. It was found that a large fraction of GRBs have an X-ray light curve that can be decomposed into several components and a canonical form composed up to five components was proposed to describe them, see for example Zhang et al. (2006). In Fig. 3.13, the XRT light curves of GRB 220711B and GRB 211207A previously discussed in

Sect. 3.2.3.5 are shown. The light curves are processed by the UK Swift science data center[9] using the methods described in Evans et al. (2007, 2009). The method consists in the identification of the flares, fitting the underlying decay using power law functions and classifying the light curves. In case of failure, the fit might be improved by a human action.

The light curves are composed of two major types of data related to the possible XRT observation modes. The blue points are from the Windowed Timing (WT) mode, used for bright sources to avoid possible pile-up effects. This is achieved by reducing the time resolution down to 1.8 ms by compressing 10 rows into a single row and reading out only the central part of the field of view (200 columns) and thereby sacrificing one dimension of the collected data. The red points are data from the Photon-counting (PC) mode, with a full imaging and spectroscopic resolution, but with a larger integration time of 2.5 s. Finally, the cyan points are data collected in WT mode during the satellite slewing to the target source. This mode allows to start collecting data a few seconds earlier in the critical phase of the X-ray afterglow.

The XRT light curve of GRB 220711B (left panel) shows a canonical form with 2 breaks (green lines) separating the different decay phases. A temporal steep decay (Phase I) was observed with a slope of $-2.5^{+0.16}_{-0.12}$, then a shallow decay

[9] https://www.swift.ac.uk/xrt_products/index.php

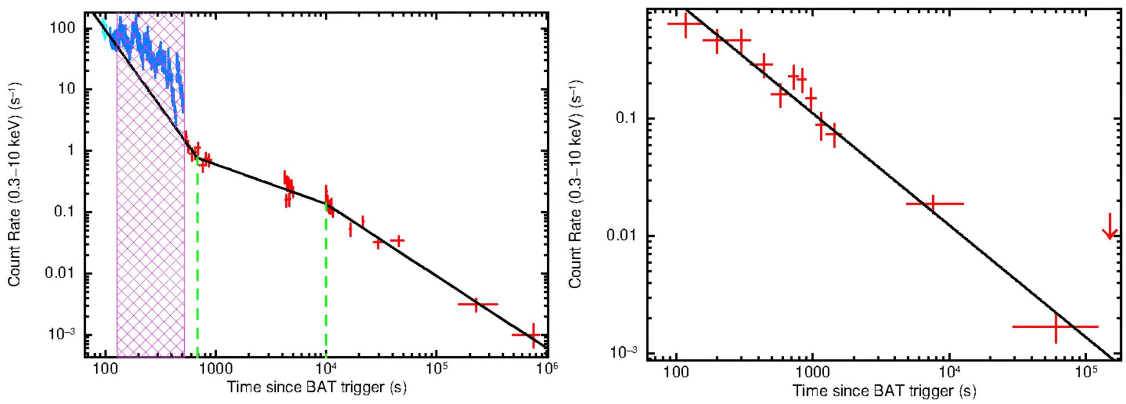

Figure 3.13: *Swift*/XRT light curves of GRB 220711B (left panel) and GRB 211207A (right panel). The color of the cross points are XRT data observed in different modes, WT settling (cyan), WT (blue) and PC (red). The best-fit model is shown as a black curve, the breaks used to improve the fit are marked by the dashed green lines and the purple area represents detected flare(s). (From UK Swift science data center)

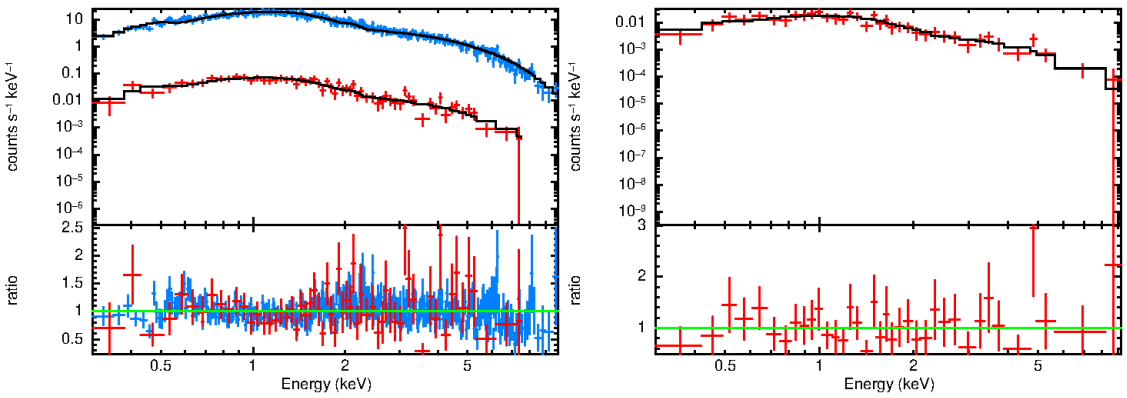

Figure 3.14: *Swift*/XRT time-averaged spectra of GRB 220711B (left panel) and GRB 211207A (right panel). The color of cross points are XRT data observed in different modes, WT (blue) and PC (red). The best-fit model is shown as a black curve. The bottom panels show the ratio between the data and the best-fit model. (From UK Swift science data center)

phase (Phase II), also called plateau, with a slope of $-0.64^{+0.09}_{-1.41}$, and finally, the "normal" decay phase had a slope of $-1.18^{+0.11}_{-0.09}$. X-ray flares were also observed at 127 to 519 s during the Phase I. The exact reasons of these flares are not clear but might be caused by energy injection, probably from the central engine. On the other hand, the XRT light curve of GRB 211207A is much simpler: no flares are observed and no breaks are needed to fit the light curve. These two examples highlight the significant diversity that a light curve can have from burst to burst.

The UK Swift science data center also provides a spectrum for each source and each XRT mode. The spectrum of the source is built from the events of the source extracted from the individual source snapshots. The spectrum is then automatically fit by `XSPEC` using an absorbed power-law model, considering the Galactic absorption at the source location and the extragalactic absorption over the line of sight, see Evans et al. (2009) for additional details.
The XRT spectra for GRB 220711B and GRB 211207A are shown in Fig. 3.14. For both GRBs, the spectra derived from the PC observations are similar and show an increase of the flux up to an energy of $\sim$ 1 keV and then a decay. The low energy ($<$ 1 keV) absorption is thought to be caused by all elements present over the line of sight, see Sect. 3.3.2 for more details on the contribution of the host galaxy. It is worth noting that the spectrum derived from WT observations using early data is often not used to perform such an analysis. This is mainly because early spectra may be subject to spectral evolution due to possible contamination

by the prompt emission, compared to late spectra.

3.3.2 Constraint on the host gas content

As already mentioned, the GRB afterglows are thought to be produced by synchrotron emission from external shock with their surrounding environment. The intrinsic afterglow spectrum is therefore expected to be well modeled by a simple power-law function. However, the soft X-ray afterglow of GRBs are found to have an excess of absorption compared to the Galactic value (Galama & Wijers 2001; Stratta et al. 2004; Campana et al. 2006b; Watson et al. 2007; Campana et al. 2010, 2012; Starling et al. 2013). The left panel of Fig. 3.15 shows an example of method used to derived the neutral hydrogen column density from an XRT spectrum. Below 1 keV, the excess of absorption is clearly visible and the Galactic absorption can only explain a small fraction of the observed total absorption. It is thought to be due to photoelectric absorption from metals and elements not fully ionized along the GRB LOS. This means that the quantity derived is not a direct tracer of the neutral hydrogen. An assumption about the metallicity of the environment is therefore made to derive the neutral hydrogen *equivalent* column density (hereafter $N_{\rm HX}$). In addition, since all the matter between the observer and the source contributes to the observed absorption (i.e., the local GRB environment, the host galaxy, the intergalactic medium (IGM) and the Galactic medium), their respective contributions are not easy to disentangle.
It is common to make the assumption that the observed excess is at the redshift of the GRB (i.e. internal host galaxy origin). Previous studies showed that the $N_{\rm HX}$ derived under this assumption increases with the redshift (e.g., Campana et al. 2010; Watson & Jakobsson 2012; Campana et al. 2015), even when considering large or unbiased GRB samples (Campana et al. 2012; Rahin & Behar 2019). Moreover, it was observed that the neutral intrinsic hydrogen columns ($N_{\rm HI}$) derived from the Lyman-α absorption of UV/optical afterglows differ from the $N_{\rm HX}$ values (Watson et al. 2007; Watson 2011; Rahin & Behar 2019), as can be seen in the right panel of Fig. 3.15. In addition, no particular evolution with z was observed for the $N_{\rm HI}$ (e.g., Tanvir et al. 2019). It is also worth noting that the $N_{\rm HX}$ is often based on the assumption of a solar metallicity. Given that GRBs are generally observed in a subsolar environment, using a lower metallicity increases the value of the $N_{\rm HX}$ and thus the discrepancy between $N_{\rm HI}$ and $N_{\rm HX}$ (Dalton &

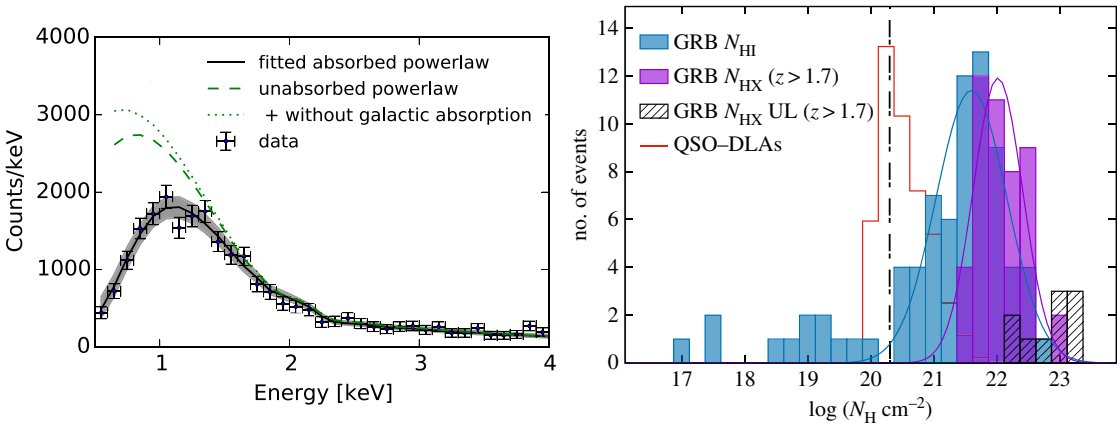

Figure 3.15: *Left panel: Swift*/XRT spectrum of GRB 081221 in PC mode. The best-fit model is shown with a black solid curve. The intrinsic power-law emission (before absorption) is represented as a green dotted line, while the green dashed line only accounts for the Galactic extinction (Buchner et al. 2017) *Right panel:* Distribution of host galaxy hydrogen column densities measured from Lyman-α absorption ($N_{\rm HI}$) in blue color and equivalent column densities measured from X-ray spectra ($N_{\rm HX}$) in purple color. Both are measured using the GRB afterglow. (Schady 2017)

Morris 2020).

The cause of the $N_{\rm HX}-z$ relation and $N_{\rm HX}$ excess over $N_{\rm HI}$ is still a source of debate. The two main explanations reported in the literature are an internal host origin or an IGM origin. The GRB host cause is supported by many evidence such as, the possible presence of ultra-ionized gas in the GRB vicinity (Schady et al. 2011), a dust extinction bias at low redshift (Watson & Jakobsson 2012) or the possible relation between $N_{\rm HX}$ and the stellar mass of the host galaxy (Buchner et al. 2017). On the other hand, the diffuse IGM and intervening systems may be responsible of the observed excess and the redshift dependence of $N_{\rm HX}$ (Behar et al. 2011; Starling et al. 2013; Campana et al. 2015; Tanga et al. 2016; Rahin & Behar 2019; Dalton et al. 2021). It is also possible that the actual explanation is due to a combination of the two causes mentioned above. The limited spectral resolution of current X-ray instruments prevents deriving an unambiguous interpretation of this excess of absorption. The exact origin may not be solved until the launch of a very sensitive and high resolution instrument able to detect absorption features coming from this gas, such as the X-IFU instrument on board ATHENA (Barret et al. 2016, 2018).

In the forthcoming SVOM era, MXT will collect the GRB X-ray afterglows be-

tween 0.2 to 5 keV and will continue to measure the $N_{\rm HX}$ of GRBs in the majority of cases. The optimized pointing law and follow-up strategy will provide a better controlled and more homogeneous GRB sample, where high-z GRBs will be quickly identified. The $N_{\rm HX}$ distribution of the SVOM sample will contribute to provide a new perspective of the discrepancy between $N_{\rm HX}$ and $N_{\rm HI}$, and the $N_{\rm HX}$ correlation with z.

3.3.3 Dust extinction curves

The association of the X-ray and NIR afterglow can be used to study the dust content of typical star-forming regions up to very high redshift. From NIR to X-ray wavelengths, the intrinsic afterglow spectrum is expected to be modeled by a power law or a broken power law. The break in the spectrum is produced by the cooling of electrons. It can appear between the X-ray and optical/NIR wavelengths depending of the GRB synchrotron spectrum and observational time. On the optical/UV side, the extinction is caused by the dust reddening while for X-rays it is due to gas below 3 keV. The lack of absorption above 3 keV (Sect. 3.3.2) and the simple power law model allow to constrain and measure the absolute extinction curves of the sources along their LOS (Fig. 3.16). The analysis is usually performed by fitting the emissions obtained at a similar post-burst time, within 3 hours after the trigger to ensure a large variety of extinction curves (Corre et al. 2018b). Previous studies using this method enabled the determination of GRB afterglow visual extinctions (A_V) and extinction curves for sources up to $z \sim 9$ (Zafar et al. 2012; Bolmer et al. 2018; Zafar et al. 2018).
In the SVOM era, the synergy between MXT and ground-based telescopes such as Colibri, with its wide coverage (400-1800 nm), will offer the possibility to further investigate and constrain the dust extinction curves of star-forming regions across z.

3.3.4 GRB localization

Within the few minutes following the detection of the GRB prompt emission (T_0), the afterglow X-ray emission appears bright and not strongly absorbed by dust and metals along the LOS of the GRB (Sect. 3.3.2). The localization error provided by ECLAIRs (< 12 arcmin) will be improved by MXT to be better than 2 arcmin in

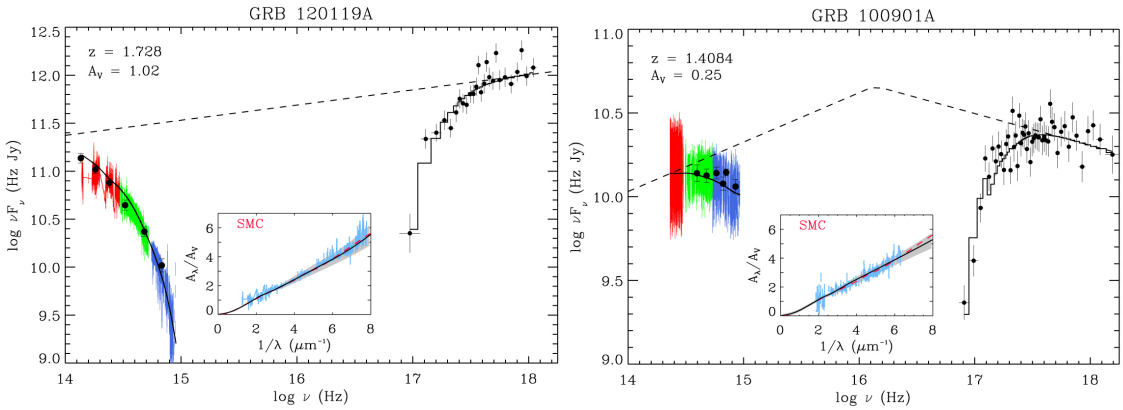

Figure 3.16: Example of GRB afterglow SEDs and their best-fitting using power law (left) and broken power law (right) models. Black points are optical-NIR photometry data (left) and *Swift*/XRT (right) observations. The spectra of the VLT/X-shooter are visible in blue for the UVB arm, in green for the VIS arm and red for the NIR arm. The dashed black lines are the best-fit models. Each inset panel shows the canonical SMC extinction curve (red) compared to those derived from the best-fit of the afterglow SED (black) or the X-Shooter spectra (blue). (Zafar et al. 2018)

the majority (80-90%) of the sources. The MXT position will then help to further localize the GRB with the VT and optical ground telescopes.

The MXT localization ability is therefore a critical element of the instrument. It depends on the PSF shape, the instrument effective area, the expected background ($\sim$ 1 counts/s) and the duration of the SVOM slew. To perform the most realistic possible simulations and determine the expected localization capabilities of MXT, the performance of the flight model instrument are essential. These performance were obtained during the end-to-end test of MXT at the Panter facility and are further described in Sect. 4.3.2 of Chapter 4. An important result of the Panter campaign was that the PSF size of the integrated instrument is slightly larger (about 10% at 1.5 keV, passing from 10 to 11 arcmin) than previously observed by considering independently the flight model (FM) optics. This is probably due to distortion introduced during the integration into the MXT structure and optics defects resulting from the manufacturing process.

The localization capability of MXT is expressed by the R_{90}. For a given signal-to-noise ratio (S/N), this parameter defines the radius within which 90% of the sources are found (for additional details, see Gotz et al. (2022)). The R_{90} was evaluated using an MC simulation, which consists in injecting randomly a thousand of sources in the MXT FOV and finding back their position considering the

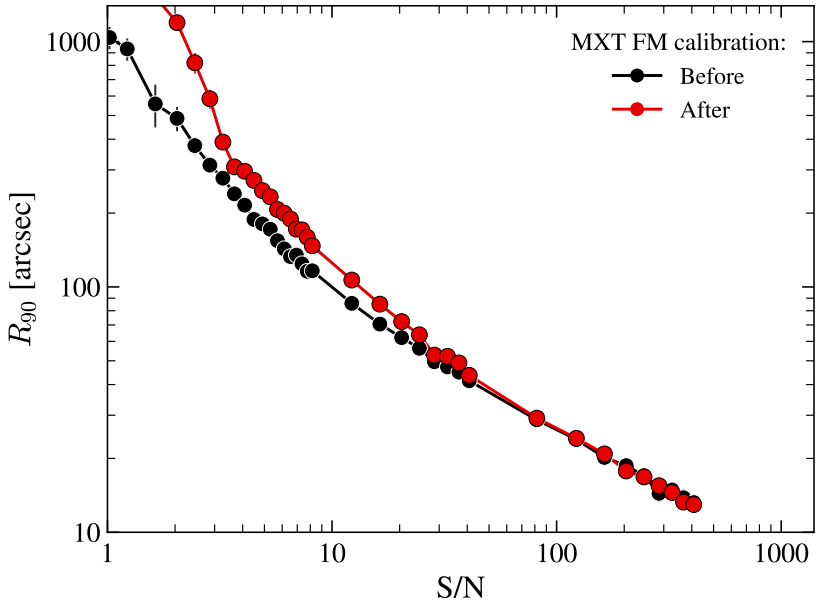

Figure 3.17: MXT localization error as a function of signal-to-noise ratio of the observed source. The black and red curves show the expected performance before and after the MXT flight model end-to-end test at the Panter facility. (Courtesy of D. Götz)

instrument response. The expected localization ability as a function of S/N before and after the MXT end-to-end test is shown on Fig. 3.17. The observed larger PSF size induces an increase in R_{90} as the S/N decreases. This means that the localization accuracy of MXT is slightly inferior than previously estimated. At high S/N, both simulations exhibit a similar trend, which indicates that the 10% PSF size difference is no longer the limiting factor for the localization capacity.

To assess the fraction of GRBs that MXT will be able to localize at a given R_{90}, $\sim$ 1000 GRBs detected and localized by *Swift*/XRT were used. Among them, only those with an ECLAIRs detection probability higher than 50% were considered, given the lower sensitivity of ECLAIRs compared to BAT. Then, given that the MXT effective area is smaller than XRT, for each GRB, the parameters of the time-averaged spectrum measured by XRT were extracted and used to determine the *count rate conversion factor* between the two instruments. This factor was applied on each XRT GRB light curve to simulate a MXT-like light curve. Using the simulated light curve, the number of counts detected after the end of the slew over a duration of 10 min of observing time was integrated to get the simulated S/N of the GRB. Finally, the R_{90} of each GRB was obtained using the relation

Table 3.3: Expected fraction of localized sources for different R_{90} localization errors. The values are obtained by considering *Swift* GRBs detected by ECLAIRs with a probability higher than 50% and observed by MXT during 0.6 ks (10 min).

Fraction of GRBs	Localization error (R_{90})
34%	30 arcsec
46%	60 arcsec
75%	110 arcsec

determined in Fig. 3.17. In table. 3.3, the fractions of GRBs located better than 30, 60, and 110 arcsec are provided. The results indicate that MXT will be able to localize $\sim 50\%$ of the GRBs with an accuracy of less than 60 arcsec.
As mentioned in Sect. 2.2.3.4, approximately $25-40\%$ of *Swift* GRBs are sources with faint or no optical afterglow (dark GRBs). Although the VT has a redder optical spectral band than *Swift*/UVOT (400-1000 nm vs 170-650 nm), it is likely that a non-negligible fraction of GRBs will only be located by MXT. As highlighted in Chap. 2, it is fundamental for many GRB studies to consider a sample that is not biased against a certain population. Therefore, it will be important to characterize these MXT-localized GRBs and identify their host galaxy, to limit the possible bias towards optically-bright GRBs within the SVOM sample. In Sect. 2.2.3.2, the HUDF was used to determine the number of possible host galaxies with an H-band magnitude lower than 24 within a given radius (Rafelski et al. 2015). The same analysis can be done to find the potential density of sources given the expected R_{90} of MXT. The density of sources observed in the HUDF for an aperture of 30 and 60 arcsec as a function of H-band magnitude is shown in Fig. 3.18. For a $F160W$ magnitude of 24, the expected number of sources within 30 and 60 arcsec is about 30 and 120, respectively. This demonstrates the challenge of identifying the host galaxy among the possible sources within the MXT error location box for this peculiar GRB population. However, this has to be contrasted with the possibility of triggering ToO with other X-ray space telescopes, in particular *Swift* or *Einstein Probe* which could give an X-ray localization of a few arcsec. In addition, the GRBs (including the one with dark afterglow) could be observed in the NIR wavelength range, for example with the CAGIRE (CApturing Grbs InfraRed Emission) camera of the Colibri (Sect. 1.3.2.2) telescope. In this case, the typical localization errors returned by MXT will be sufficient to detect and improve the GRB localization.

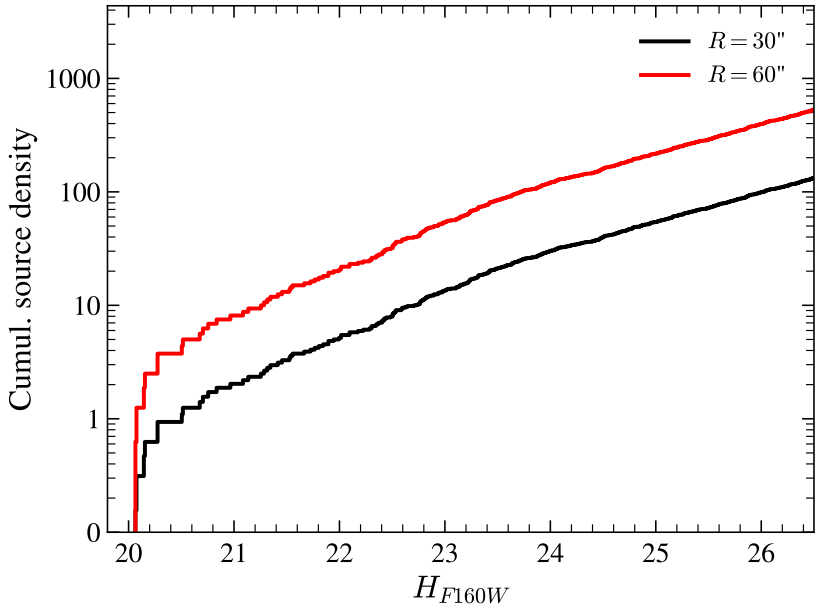

Figure 3.18: Cumulative distribution of sources observed in the HUDF as a function of $F160W$ AB magnitude. The source density is shown for two apertures defined with a radius of 30 and 60 arcsec.

3.4 Conclusions

This chapter has demonstrated the key aspect of GRB follow-up observations and the rich amount of information that can be obtained from the broad-band wavelengths of the afterglow emission. These observations need to be performed as fast as possible after the trigger received from the satellite in order to maximize the probability of detecting the emission. In the perspective of the SVOM mission, an optical follow-up training is currently performed with ground-based telescopes on the basis of Swift alerts. It aims at preparing the SVOM community to react quickly and efficiently to future alerts. Two instruments were presented (MISTRAL and X-Shooter) that could support the community to build a complete and well-characterized SVOM GRB sample. The upcoming SVOM mission thus promises to provide new insights into GRBs through its optimized follow-up strategy.

Chapter 4

Performance of the MXT flight model instrument

Contents

The raw observational data measured by a telescope are not directly usable for scientific purposes. For this reason, a data reduction is performed to improve the quality of the observations and provide enhanced data products. These products are then used to extract the maximum of scientific information from the observations. An essential point when analyzing and interpreting the data is to track the different assumptions made during the reduction process. This ensures to know the limit of your data and provides an additional asset for the interpretation and the conclusions drawn from the observations.
In 2021, the X-ray telescope on board SVOM was fully integrated in its flight configuration and characterized in a dedicated facility. This chapter describes my work on the data analysis of the end-to-end tests and my contribution to the development and implementation of the data reduction procedure that will be used by the ground segment to calibrate in energy the data collected in-flight by MXT. Moreover, it presents my work on the MXT focal plane flight spare model to better characterize the detector and its electronic readout chain at the low energy range (< 2 keV) of the instrument. This chapter aims to better understand and structure the spectral calibration method that will be applied to the raw MXT data to produce enhanced data products and is part of the preparation of the scientific analysis of MXT observations.
After a more detailed overview of the MXT instrument and its subsystems (Sect. 4.1), Sect. 4.2 discusses the principle of the data analysis and in particular the energy calibration method of the MXT camera. Then, Sect. 4.3 describes the data analysis and the results of the end-to-end test of the MXT flight model (FM) instrument, as well as the calibration campaign of the MXT flight spare camera. Finally, the preparation of the MXT flight operations is presented in Sect. 4.4.

4.1 The Microchannel X-ray Telescope

As introduced in Sect. 1.3.2.1, the Microchannel X-ray Telescope (MXT) is a spectro-imager focusing the soft X-ray photons on board the SVOM mission. In this section, I will further introduce and describe the MXT specifications, the micropore optics, the camera design and detector used to explore the soft X-ray

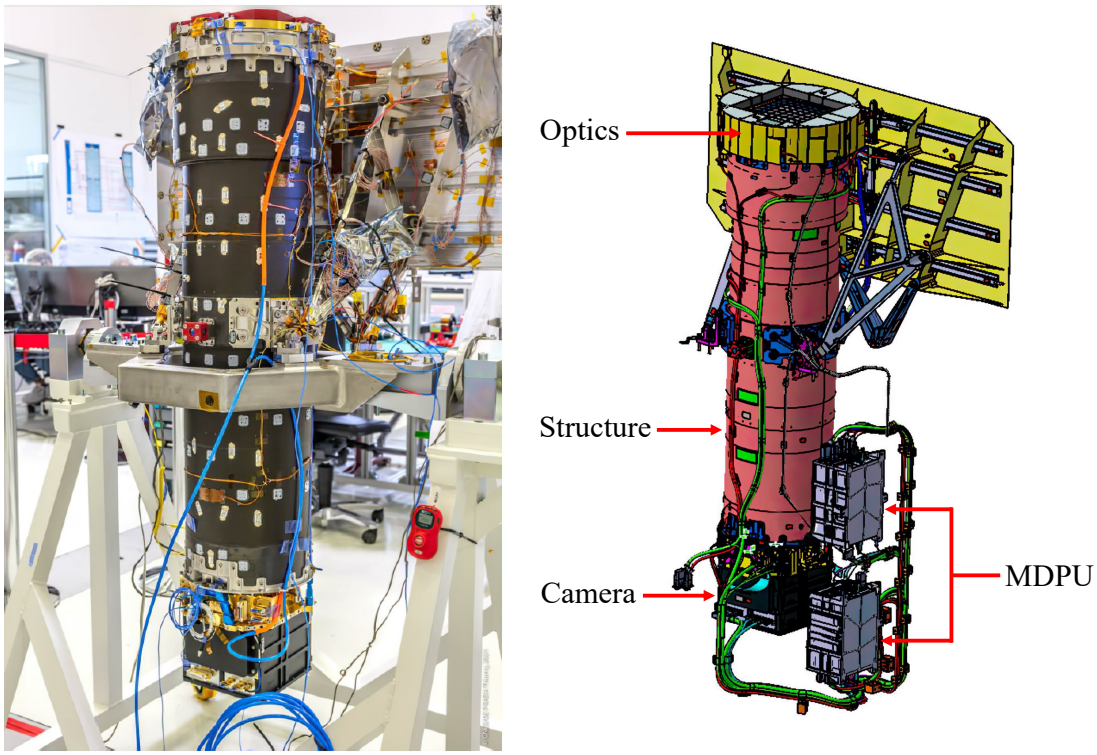

Figure 4.1: The Microchannel X-ray Telescope. Picture of the fully integrated MXT FM instrument (left panel) and a partial expanded view of the instrument (right panel) where the optics, the telescope structure, the camera and the two MDPUs are indicated. (Credit: CNES)

counterpart of transient phenomena.

4.1.1 Specifications and design overview

The MXT is an innovative compact (focal length of ~ 1.15 m) and light (42 kg) X-ray telescope focusing photons in the $0.2 - 10$ keV energy band (Fig. 4.1). It has a narrow field of view (FOV) of 58×58 arcmin and a sensitivity below the mCrab. The MXT instrument characteristics derived from data collected during the Panter campaign before its integration to the SVOM payload (see Sect. 4.3.2) and the expected scientific performance obtained from simulations (Sect. 3.3.4) are summarized in Table 4.1.

The primary objective of MXT is to improve the ECLAIRs localization and reduce the error box at a few tens of arc seconds for the majority of GRBs and including dark ones. In the case of optically-bright GRBs, the MXT localization will help the VT and other ground follow-up telescopes to easily identify the optical GRB

Table 4.1: MXT instrument characteristics.

Energy range	$0.2 - 10$ keV
Field of View	58×58 arcmin
Angular resolution	10 arcmin at 1.5 keV
Source location accuracy	< 120 arcsec for 80% GRBs
Effective area	~ 35 cm^2 at 1.5 keV
Sensitivity (5σ)	10 mCrab in 10 s
	150 μCrab in 10 ks
Energy resolution	< 80 eV at 1.5 keV
Time resolution	100 ms

afterglow. The instrument is the result of a large European collaboration, between the Centre National D'Etudes Spatiales (CNES), CEA, IJClab, the University of Leicester and the Max Planck Institute for Extraterrestrial Physics (MPE) and was developed under the responsibility of CNES.
MXT is composed of the MXT OPtical assembly (MOP) based on square Micro-Pore Optics (MPO), the MXT CAMera (MCAM) hosting the detector, a telescope tube in carbon fiber (MST), two MXT Data Processing Units (MDPUs) in cold redundancy and a radiator for cooling the system. The MDPU is the brain of MXT. It is the computer responsible for the management and the configuration of the camera, the thermal control of the optics and the detector, the generation of telemetry packets as well as the prompt scientific analysis of MXT data for the location of GRB afterglow candidates. The development of the MXT camera was a real challenge due to several reasons such as the low Earth orbit of SVOM subject to high proton flux and strong thermal variations, the small volume, mass and power allocations for this instrument in the SVOM payload, and the export rules to China limiting the choice of available materials. The technical challenges, the design solutions of the MCAM and its validation are further described by Meuris, et al., (2022).

4.1.2 The MXT optics

Although both X-ray and visible light are electromagnetic waves moving in a similar manner in space, due to the higher energy and frequency of X-ray photons,

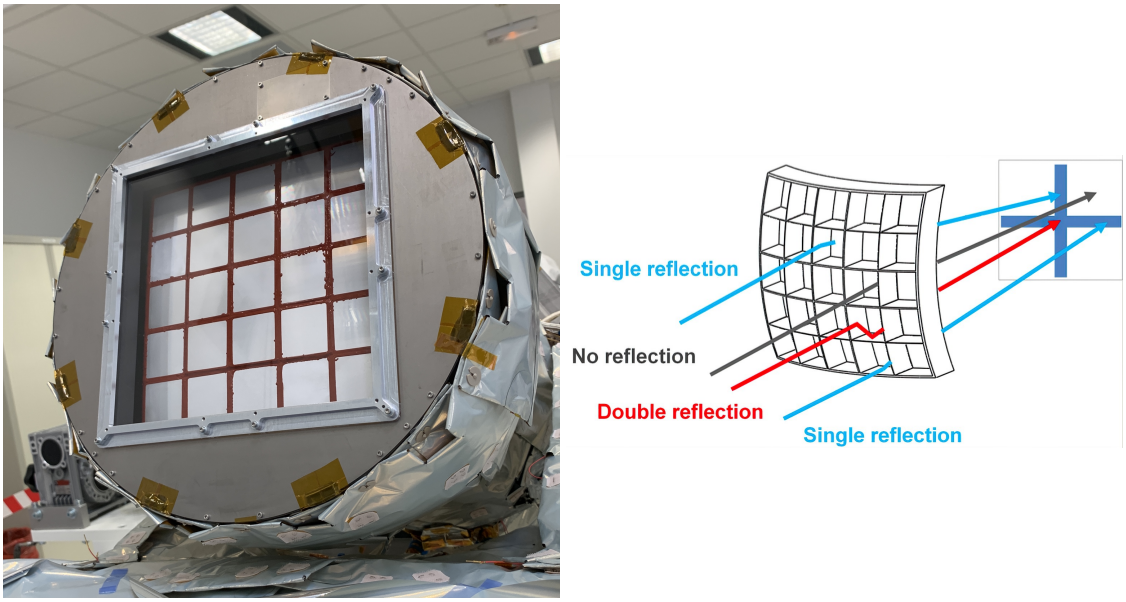

Figure 4.2: The MXT optics. *Left panel:* Picture of the MXT FM micro-pore optics once integrated in the telescope (Credit: University of Leicester/CNES). *Right panel:* Principle of lobster-eye optics used by MXT. X-ray photons with two, one and no reflection are focused on the central sport, the cross-arms and in the diffuse background, respectively. (Credit: NAOC)

their interaction with matter is radically different. Traditional methods of focusing visible light (lenses and mirrors) cannot be used for X-rays since the majority of photons penetrate and are scattered or absorbed by the matter without being reflected. While this property can be useful for producing fluorescence energy lines or characterizing elements of a material (e.g., the X-ray photoelectron spectroscopy technique), different methods have to be adopted to focus the X-ray photons on a focal plane. In astronomy, the most common technique uses the principle of grazing incidence reflection, in which the reflecting surface is placed at a very small angle from the incident beam. Wolter (1952) introduced the design of three grazing reflection optics to focus X-rays via two reflections, for instance type I Wolter optics consists in a parabolic mirror followed by a hyperbolic mirror. To increase the flux in the focal point, a set of nested mirrors is concentrically disposed around the optical axis. This optic design was largely used for space X-ray missions such as for the XMM-Newton telescope, the Chandra X-ray Observatory, the *Swift*/XRT instrument or the future Athena mission. Wolter optics have a very sharp PSF and XRT has demonstrated the possibility to locate GRBs at a few arc seconds. However, they have the disadvantage of a high mass budget due to the set of nested

mirrors. The size and mass constraints imposed by the SVOM payload do not allow a similarly designed optics to be carried by MXT. For this reason another design using grazing incidence reflection and based on the lobster vision was adopted to focus X-rays on the MXT focal plane. The design was first proposed by Angel (1979) and consists in a grid of square pores (MPO) with a size of a few tens of micrometers. The MXT optics is composed of 25 MPO plates of 40 mm side arranged in a 5×5 configuration, as shown in the left panel of Fig. 4.2. Each MPO is composed of silicon square pores with a side of 40 μm and where the inner walls are coated with a 25 nm Iridium (Ir) layer to improve the reflectivity of the optics. The thickness of MPOs was optimized for the small MXT FOV and varies from 2.4 mm in the central part to 1.2 mm at the edges. MPOs are arranged and glued on an aluminum frame with a target spherical surface of 2300 mm-radius. The plates are also coated with a 70 nm Al layer to limit the optical light hitting the detector. In the inner part of the frame, 36 magnets are disposed to deviate electrons from the focal plane direction and reduce the background signal. Optics arranged in a so-called lobster-eye configuration produce a peculiar PSF with a form of cross (for an example, see Fig. 4.43). The central part of the cross is produced by double reflections, the cross-arms by single reflection and the remaining fraction of photons not interacting with the optics produces a diffuse background (right panel of Fig. 4.2). The MPOs were produced by the French Photonis company and the MOP was designed and assembled by the University of Leicester. The resulting focal length of MXT is about 1.15 m for a mass budget of $\sim$ 2 kg and therefore well adapted to compact and small X-ray telescopes. In addition, the effective area of the MOP is maximum below 2 keV where the GRB afterglow emission is most intense (power law dependence with E). Experimentally, the FWHM of the PSF at 1.5 keV (Al-K) was measured to be 10% larger than the requirement of 10 arcmin (Gotz et al. 2022, see) affecting slightly the localization performance of MXT. This is likely due to intrinsic and manufacturing defects in the MPOs, misalignment of the MPOs and mechanical mismatch of the frame.

4.1.3 The MXT detection chain

The design and integration of the MXT camera (MCAM) was in charge of the CEA. The system is composed by a focal plane assembly (FPA), a front-end electronics assembly (FEE), a wheel assembly and a mechanical support structure.

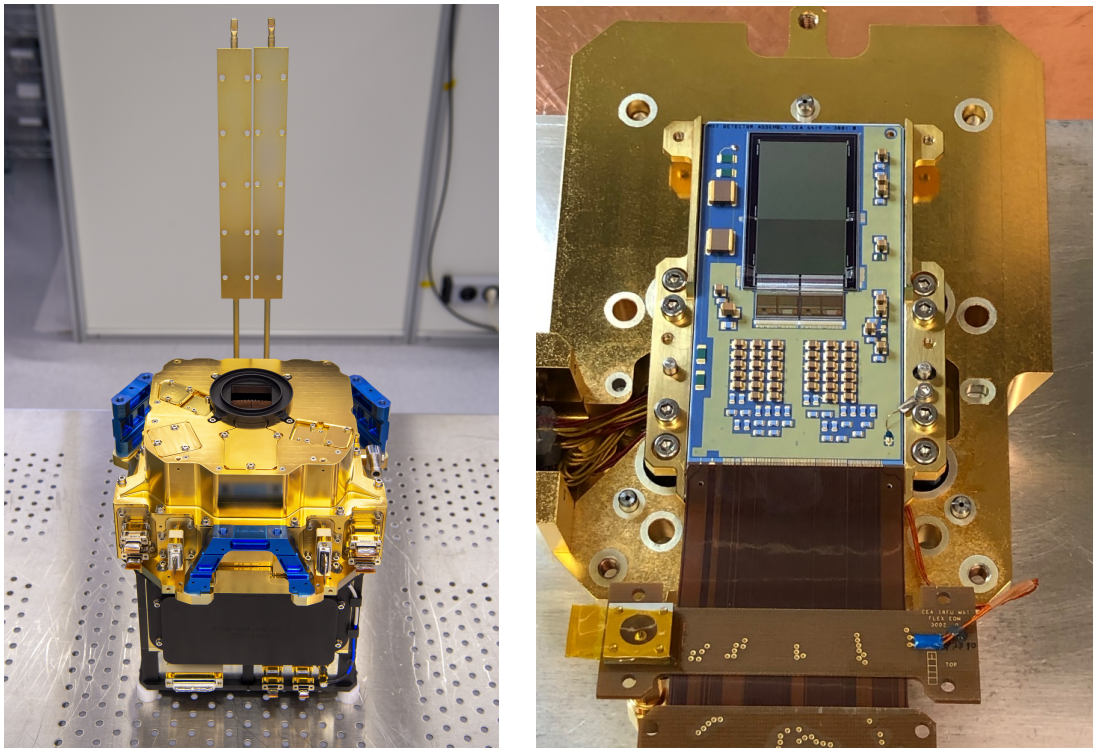

Figure 4.3: The MXT camera (left panel) and the MXT focal plane assembly (right panel). The detector and the ceramic board are located at the center of the FPA. The proton shield (gold-coated aluminum) is visible in gold color at the top of the MXT camera and in the background of the FPA. The front-end electronics is identifiable in black color at the bottom of the camera. (Credit: L. Godart/CEA)

The MCAM and FPA are visible on the left and right panels of Fig. 4.3, respectively. The primary objective of the MCAM is to ensure the correct operation of the detector (thermally and electrically) and a pre-processing of the data to save only relevant information of X-ray events. The enclosure and the shielding (30 mm of aluminum with a thin coating made of copper, nickel and gold) protect the detector from space radiation and limit the background signal (non-X-ray photons) during observations. The system is a square box of about 20 cm side with a height of 27 cm, for a total mass of 9 kg and a nominal power of 7 W. At the center, the focal plane is based on a back-illuminated pnCCD fully-depleted (450 μm depth) and read out by two Application-Specific Integrated Circuits (ASICs) of 128-channels, named CMOS Amplifier and MultiplEXer (CAMEX), both provided by the MPE (see left panel of Fig. 4.4).

The design of the pnCCD is an upgraded version of the European Photon Imaging pn-Camera (EPIC-pn) on board ESA's X-ray Multi Mirror (XMM) mission

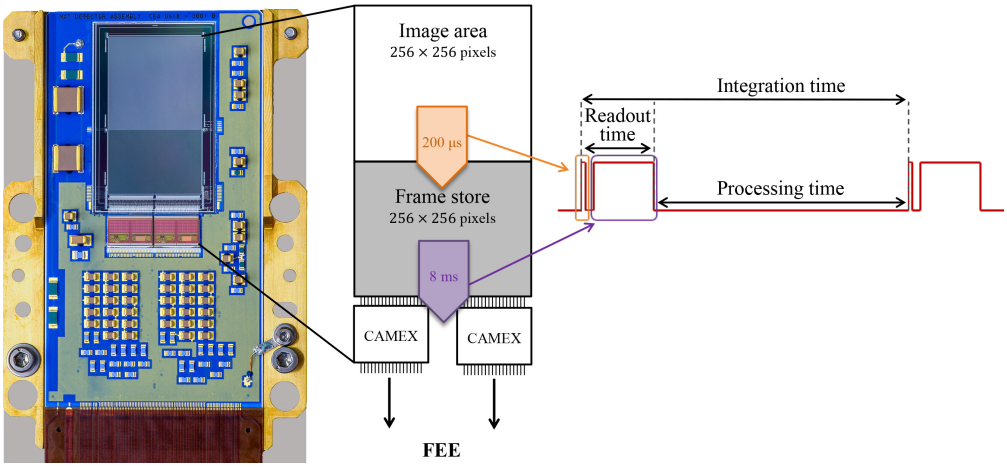

Figure 4.4: Front side picture of the MXT detector assembly. The pnCCD is composed of two areas, image and frame-store, which differ by their color shade in the picture. The two CAMEX ASICs are visible in the bottom part of the frame-store area. On the right, a schematic view of the detector is shown, along with the typical sequence to collect a frame and process it in the FEE. (Credit: L. Godart/CEA)

(Strüder et al. 2001) and a direct heritage of the pnCCD of the DUO mission project (Griffiths et al. 2004; Meidinger et al. 2004). It is composed of an image area with 256×256 pixels of 75 μm side and an unexposed frame store area of 75×51 μm shielded to X-ray light to reduce out-of-time events. The CAMEX ASICs are identical to the one used for the eROSITA instrument on board the Spektrum Roetgen Gamma mission (Meidinger et al. 2006, 2010). The detector and the ASICs are mounted on a ceramic board composed of alumina (Al_2O_3) where all bias voltages and connections are routed. The board is glued to a copper-molybdenum (MoCu) substrate providing a mechanical interface for the detector. The front-end electronics (FEE) provides all bias voltages for the ASIC and the pnCCD as well as the readout control signals. The FEE also ensures the amplification and digitization of the analog channels, and performs a mode-dependent processing of the pixel data before transmission to the MDPU (further described in Sect. 4.2.1.2).

The image area integrates photon events during 100 ms. Then, charges generated by the events are rapidly transferred into the frame store area in 200 μs (right panel of Fig. 4.4). The frame store is read out row by row by transferring the charges to the anodes of the pnCCD columns. The signals of each column are converted into voltages by the on-chip JFETs and then amplified and filtered by

the CAMEX analog channels; they are then timely multiplexed at the CAMEX analog outputs during the processing of the next row. This allows a readout of the frame store in 10 ms. The frame rate of 10 images per second was chosen as a good compromise to sample the GRB afterglow and the photon incident rate to limit the pile-up[1] effect. The main (analog) stages of the CAMEX are switched-off during integration and turned on just for the read-out phase to reduce heating power in the focal plane. The detector is cooled and maintained at an operational temperature of $-65°C$ using an active cooling system based on three thermoelectric coolers (TEC) connected through propylene heat pipes to the MXT radiator. Finally, the wheel assembly has three main positions: (i) a calibration position with a radioactive ^{55}Fe source fully illuminating the detector, (ii) an open position for sky observations, and (iii) a closed position with a 10 mm thick copper shutter to ensure the protection of the detector against radiation damage during the regular passages through the South-Atlantic Anomaly.

4.2 Principles of data processing

This section briefly describes the principles of data reduction and calibration used for MXT to analyze on-ground calibration tests and proposed as a basis for on-ground analysis during in-flight operations. The algorithms and processing steps were initially developed for the eROSITA mission (Andritschke et al. 2008). The improved and optimized methods used during on-ground laboratory tests were presented in Ceraudo et al. (2020) and were also used to validate the performance of the on-board processing performed by the MDPU.

4.2.1 Image data reduction

When an X-ray photon interacts with the detector, it induces via photoelectric effect an amount of charge at its interaction position that is proportional to its energy. Depending on the photon hit position, the collected charges at the electrodes can be spread over several pixels and generate a *pattern*. Before extracting the patterns and the relevant signal of X-ray photons, a specific treatment on frames

[1] This phenomenon may occur during the integration time when several photons hit the same pixels and create an amount of charge equal to the sum of the photons.

has to be applied. To perform the image reduction, several algorithms were developed depending on the approach or technical constraints (e.g., CPU power, buffer size).

4.2.1.1 Frame reduction

The main ingredient used for frame reduction is the *dark frames*, which are images collected without illuminating or exposing the detector to X-ray photons, i.e. without source and with closed shutter. The corrections applied during the data reduction are determined from a few hundred of dark frames (e.g., 200 frames) to increase the statistics and limit the possible contamination by ionized particles (i.e., cosmic rays) that might hit the detector during the integration time. The treatment applied on each frame illuminated with X-ray photons (photon frames) consists in subtracting an *offset* and *common mode* values.

Offset correction It is performed by subtracting a pixel-dependent value to each pixel of the matrix. This offset represents the minimal value over which photons deposit their energy. It is the sum of the leakage current accumulated in pixels during the integration time and the baseline value of every analog channel of the front-end electronics (ASICs). The offset values can be computed from the average of several dark frames. It is worth noting that the offset map is temperature and time -dependent and needs to be frequently calculated and measured at the same temperature as the collected photon frames.

Common mode correction The common mode noise is a row-dependent noise induced by the parallel readout, row by row, of the Charge Coupled Device (CCD). It is induced by temporal variations in the electronics, for instance by fluctuations in the power supply during the switch-on time of CAMEXs. This noise has by definition a short-period nature and affects all channels of a CAMEX in common. For these reasons, it is calculated by averaging the values row-by-row for the left and right CAMEX ASICs separately and for each offset-subtracted frame.

Noise map The dark frames corrected from the offset and common noise are then used to quantify the pixel-dependent noise level. This noise is generated by the statistical fluctuation of leakage currents of each pixel, and the amplification

and discretization of the signals by the electronics readout chain. The noise map is defined by the standard deviation measured from the dark frames subtracted from the offset and the common noise. The standard deviation can be computed with different techniques to be more robust to arbitrary asymmetric distributions and manage the flight scenario of a few cosmic rays detection during dark measurements.

Event extraction After subtracting the offset and the common noise from photon frames, the hit pixels produced by an X-ray source have to be distinguished from the noise level. This is achieved by comparing the pixel values to k times the noise level determined from offset and common noise subtracted dark frames. A low value of k minimizes the risk of losing part of the incident photon energy but increases the probability to consider a noise pixel has an X-ray event. On the opposite, a too high value of k minimizes the risk to consider noise as a real event but increases the fraction of the charge lost during the charge splitting. In any case, this thresholding step induces a loss of information in the collected data and the best compromise has to be found to minimize the two effects mentioned earlier.

4.2.1.2 Onboard MXT data reduction

A frame collected by MXT represents about 1 Mbits of data. Due to the telemetry limitation, a real-time processing is implemented on the frames to extract and transmit only the "events", defined as the pixels containing a significant signal. This "event mode" is the nominal readout mode and is performed at a speed of 10 frames per second. This data reduction discussed above is done by the FEE at the pixel level and consists in: (i) subtracting a pixel dependent offset value to its raw amplitude, (ii) subtracting a frame dependent common-mode noise value (calculated for each CAMEX row of each frame), and (iii) comparing the resulting amplitude to a pixel dependent low-level threshold (LLT) set to k times the noise level value of the pixel, with k being programmable. If the pixel signal is above the threshold, the pixel is considered as a true signal, produced by an X-ray or an ionizing particle, and not as a noise fluctuation. Practically, $k = 4$ was determined to be a good compromise to ensure the extraction of X-ray events and obtain the sharpest energy lines.

The transmission of all data collected by the exposed area (image area) to the MDPU is also possible in a "full frame mode" with a decimation factor of two (5 images per second but maintaining the integration time of 100 ms in the detector). This mode is used on board to collect dark frames with the wheel in close position and from which the MDPU calculates the offsets and LLT values for each pixel. The two resulting tables are then uploaded to the FEE for the "event mode" processing discussed above.

Onboard MXT, the CPU power of the MDPU is limited by the existing components for space applications. To compute the offset and noise maps, it is therefore not possible to use the on-ground analysis based on unbiased estimators (see, Ceraudo et al. 2020) which requires expensive sorting operations and buffering a large number of frames. An alternative approach was developed to reject outliers in dark images. The method consists in using N_r frames of the dark sequence and compute for each pixel the mean (μ_r) and the variance (σ_r^2) of raw amplitudes. Then, for each frame, outliers are rejected if $A_{i,j} - \mu_{r_{i,j}} > n_r \sigma^2_{r_{i,j}}$ where $A_{i,j}$ is the pixel(i, j) raw amplitude and n_r a parameter specified in the configuration table. Then, the offset map is determined by computing pixel-by-pixel the mean value of N_o frames cleaned from outliers. Similarly, the noise map is derived by computing pixel-by-pixel the standard deviation value of N_t frames cleaned from outliers and subtracted from the offset and common mode noise. Due to the truncation applied during outlier rejection, the standard deviation is corrected (e.g., by a factor 1.00222 for a 3σ truncated distribution) to recover the full Gaussian distribution. The offset and noise maps returned by the onboard and on-ground methods were carefully compared for a same dark data set and showed very similar results.

4.2.1.3 Additional on-ground processing: event clustering

The X-band packets returned by the MDPU consists in a list of hit pixels with a deposited energy above the defined threshold (i.e., LLT). The design of the MXT detector (pixel size, detector thickness, voltage) implies that collected electrons can be shared from 1 to 4 adjacent pixels[2], leading to a number of 13 unique valid patterns (X-ray event). To determine the pattern, the neighboring pixels are firstly grouped from the event list by using an improved and optimized `Python` routine

[2]Considering the electrons drift and the electrostatic repulsion, one finds that the diameter of the charge cloud is $D \lesssim 40$ μm, smaller than an MXT pixel of $75\mu\text{m} \times 75\mu\text{m}$.

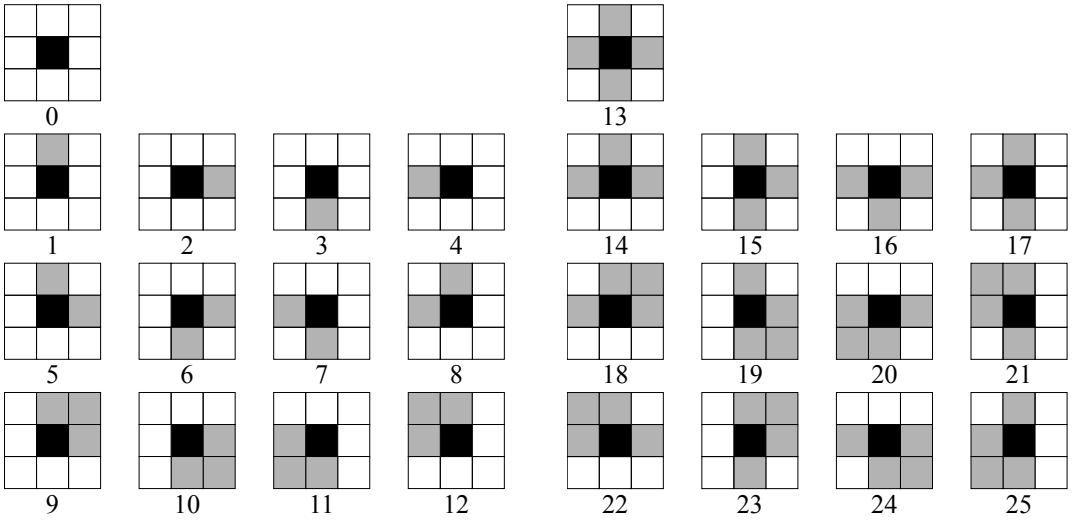

Figure 4.5: Patterns identified by the clustering algorithm. Allowed patterns are visible on the left-hand side of the figure, while "not allowed" patterns are shown on the right. For a given pattern, the black pixel indicates the impact position with the highest deposit energy and gray pixels show the clustered pixels above the LLT value.

based on the *scipy.ndimage* package. Group of pixels are then classified with a pattern code following the standard convention previously used by the XMM/EPIC and other X-ray space instruments (Fig. 4.5). It may happen that the energy of the incoming photon is not fully contained in the hit pixels returned by the FEE. This occurs if the charge sharing between pixels leads to a signal below the FEE low-level threshold for the pixel(s) adjacent to the main charge distribution peak. This problem and its implications on the spectral performances are further discussed in Sect. 4.3.2.6. Note that the pattern identification is performed on the ground at the FSC. Although a clustering is also performed on board MXT by the MDPU to locate the X-ray source, only the resulting source positions are sent to the ground through VHF packets.

4.2.2 Spectral data reduction

After the data frame reduction discussed in Sect. 4.2.1, additional steps are needed to determine an accurate energy estimate of the reconstructed photons. In this section, the energy calibration, charge transfer inefficiency and charge sharing effect are discussed. During the MXT flight operations, these steps will be performed on ground by the FSC using the MXT pipeline developed by the Strasbourg Ob-

servatory (ObAs) using the calibration and correction files provided by the MIC.

4.2.2.1 Energy calibration methods

The energy calibration is a critical step in the data analysis. The pulse height amplitude (PHA) returned by the readout electronics has no direct physical signification and makes the data interpretation typically impossible. The calibration process consists of finding a relation between the digitized signal returned by the analog-to-digital converter (ADC) in analog-to-digital units (ADU) and the energy of the incoming photons. Considering an N-bit ADC, the procedure lies in finding the energies corresponding to the 2^N possible pulse height values. This process requires prior knowledge of the X-ray source energy (e.g., a radioactive isotope, an X-ray tube, or a well-studied astrophysical source) irradiating the detector. To get the most accurate PHA-to-Energy conversion of the entire matrix, the X-ray source needs to (1) illuminate the detector as uniformly as possible, (2) have a sufficient number of photons to avoid statistical fluctuation and (3) have a sufficient number of energy lines spread over the whole detector energy range.
At first order, the relation is often assumed to be linear even if non-linearity effect might be introduced by the detector response or the readout electronics, for instance by the ASIC or ADC. Finally, the ADU-keV relation varies with operating configurations (e.g., bias voltage or temperature) and can drastically degrade the resulting calibrated spectrum, especially the spectral resolution and line positions. For this reason, the procedure is performed frequently to maintain an accurate calibration of the whole matrix and thus a high-quality of the reduced data products.

To perform an energy calibration, several methods exist. The *peak fitting* approach consists in finding on the uncalibrated spectrum the center of the reference lines emitted by the known X-ray source. To fit the peak, it is common to assume a Gaussian function but more complex functions can also be used such as an asymmetric Gaussian function in order to be more robust, e.g., to charge-loss. A linear fit is then performed between the values determined for the Gaussian center (in ADU) and the theoretical values (in keV). The fitted parameters give the gain and the offset of the system under consideration (e.g., pixel, channel or detector). This approach presents different disadvantages. It requires a sufficient

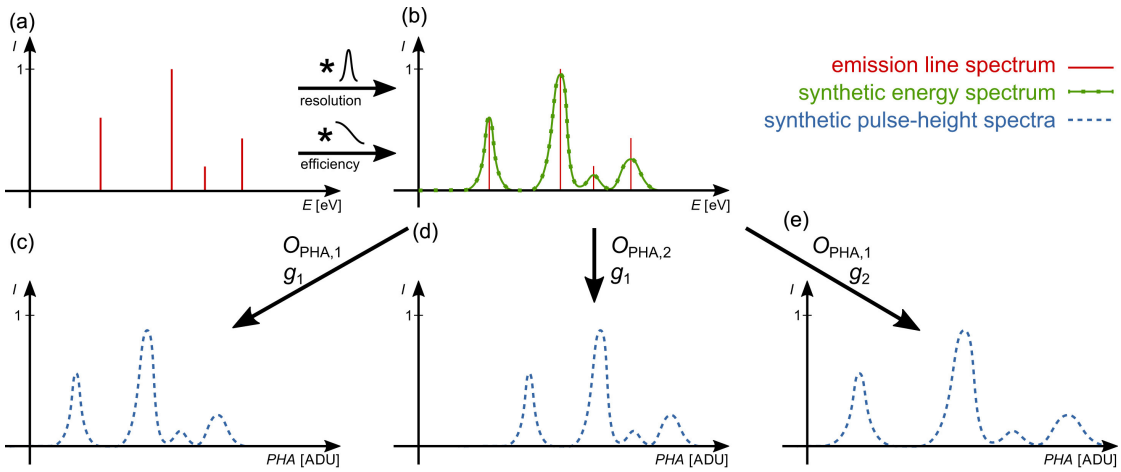

Figure 4.6: *Top panels:* Principle of a synthetic spectrum creation used by ECC. (*a*) Emission lines radiated by the reference X-ray source. (*b*) Convolution of the emission lines spectrum by the expected energy resolution and quantum efficiency of the detector to produce the most realistic possible synthetic spectrum. *Bottom panels:* Synthetic spectrum converted to ADU space using different gain and offset values. (Maier & Limousin 2016)

statistics on the raw spectrum, e.g., Majewski et al. (2014) reported a minimum of 500 photons to have a reliable calibration. Furthermore, the accuracy of the calibration is limited by the quality of the Gaussian fitting and the number of peaks provided by the calibration source. These two limitations are often not a problem for ground experimentation, but become critical during in-flight operations where constraints are stronger. To address these issues, a new method was introduced by Maier & Limousin (2016) named *Energy calibration via correlation* (ECC). The method consists in finding the maximum of correlation between a synthetic spectrum of the reference source and the uncalibrated observed spectrum. The strength of this method is its ability to use for each energy line the shape of the peak (Gaussian profile) instead of a single point (Gaussian center) as in the peak fitting method. The synthetic spectrum is created from the prior on the emission lines of the calibration source, convolved with the expected response and performance of the detector (i.e., energy resolution and QE). These steps are described in Fig 4.6 where the bottom panels show an example of three synthetic spectra used to perform the correlation. For each spectrum, a different set of parameters (gain, offset) is applied to convert the original synthetic spectrum in keV to ADU. It is worth mentioning that only the offset differs between panels (c) and (d), highlighting the shift produced by this parameter between the two spectra, while only

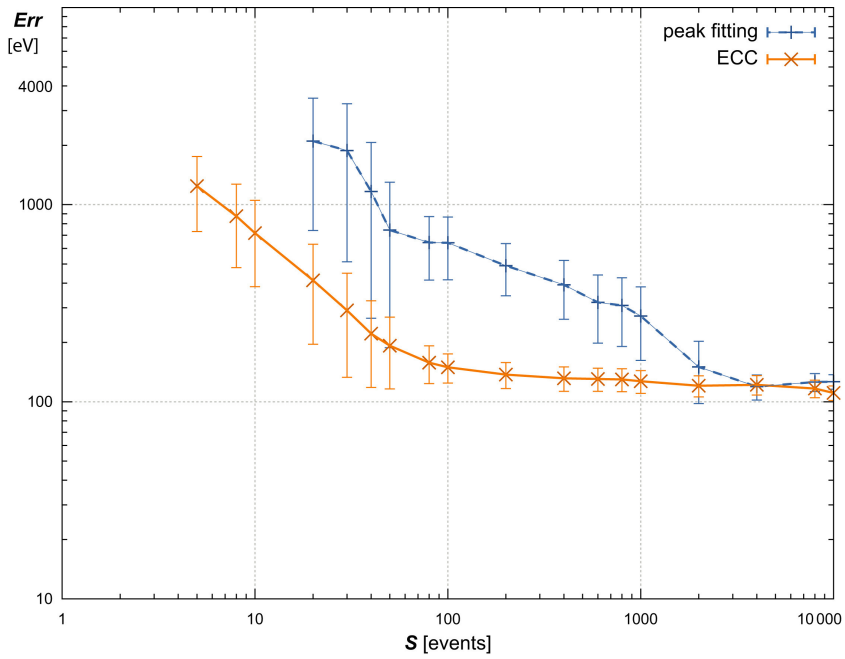

Figure 4.7: Line position errors as a function of the spectrum sample size at an energy of 26.35 keV (^{241}Am) for the peak fitting and ECC methods. (Maier & Limousin 2016)

the gain changes between panels (d) and (e), causing a stretching or a squeezing of the spectra. ECC works with linear models as well as more complex models with a multi-dimensional space. The best calibration parameters are searched by equally discretizing the parameter space and calculating for each combination the correlation between the observed spectrum and the synthetic spectrum converted to ADU. Then, the highest correlation found corresponds to the best calibration parameters determined with respect to the data and the used ECC configurations. Depending on the expected precision, the computation time can become very high. To reduce the running time, an upgraded version of ECC using an adaptive mesh refinement (AMR) to discretize the parameter space has been released by Maier et al. (2020). AMR is a numerical analysis method that consists in increasing the resolution only for regions of interest. This method is also often used in astrophysics, e.g., in cosmological simulation codes to improve spatial resolution in areas of interest (dense regions) while limiting the computation time.

The benefits of ECC on the conventional peak fitting method is its fast processing and robustness regarding the low counting statistic as shown by Fig. 4.7. In a high statistical regime, both methods reach similar performance, while in a low statistical regime, the ECC outperforms the peak fitting approach with an order

of magnitude smaller sample size. The limitations of the ECC are its sensitivity to the resolution of the reference spectrum and its tendency to favor the correct calibration of high intensity peaks of the synthetic spectrum, although the latter can also be an asset to favor a calibration on a part of the detector energy range.

For MXT, the pnCCD uses two CAMEX ASICs with 128 channels each to read out the detector column-by-column. This implies that each detector channel has a unique and different readout chain, i.e., column-dependent set of calibration parameters. This effect is highlighted in the left panel of the Fig. 4.8 where three uncalibrated spectra returned by three different channels of the same CAMEX are shown. A shift between the three spectra is clearly visible. Without considering this effect and by stacking the spectra individually, the global spectrum (sum spectrum) would have a degraded resolution compared to the "true" performance. Thus, in addition to finding the conversion between ADU and keV, the energy calibration process also realigns these spectra to obtain the sharpest possible lines once stacked on a single spectrum. Furthermore, the channel-dependent readout design of MXT implies that the calibration has to be performed using only the single events (with the possibility to increase the statistic using the double events along columns) to avoid mixing data with different gains.
For a pixel in row i and column j, the equation for a linear calibration in energy may be expressed as

$$E_{i,j} = G_j \times \mathrm{PHA}_{i,j} + O_j, \tag{4.1}$$

where, $E_{i,j}$ is the energy in keV of the pixel, G_j the gain in keV/ADU, $\mathrm{PHA}_{i,j}$ the pulse height value in ADU and O_j the offset in keV.

4.2.2.2 Charge transfer (in-)efficiency correction

When the electrons collected in the image area are progressively moved and transferred row-by-row to the anode, a fraction of the charge packets might be captured by traps caused by crystal defects. This phenomenon named charge transfer efficiency (CTE) or equivalently charge transfer inefficiency (CTI = 1 − CTE) is cumulative at each transfer and therefore the most distant row from the anode is the most affected. The energy of the reconstructed photons is thus slightly underestimated and the center of the lines is shifted to a lower energy (see right panel

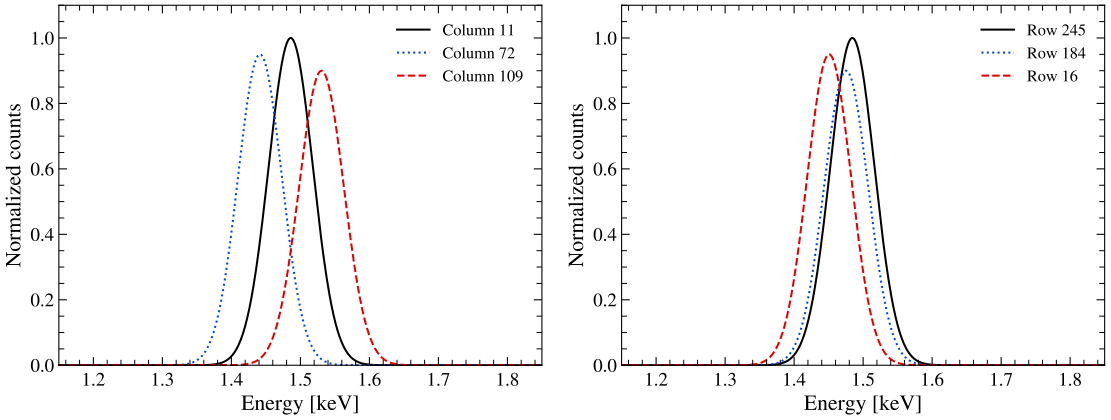

Figure 4.8: Simulated MXT spectrum of Al-K after an energy calibration. *Left panel:* Calibrated using the same gain for all columns. Each color shows the spectrum read out by a different channel of the CAMEX ASIC. *Right panel:* Without charge transfer inefficiency correction. Each spectrum corresponds to a different detector row. The number of transfers is given by $256 - N$, with N the row number.

of Fig. 4.8). In addition, the spectral performance (e.g., the energy resolution) might be degraded. Even if this effect is negligible at first order, it is expected to increase with time due to the radiation in space increasing the trap concentration in the detector. Theoretical calculation of the CTE is complex and challenging because it depends on many parameters, such as operating conditions (temperature, operating voltage), detector defects (material, radiation damage) or X-ray source properties (energy, photon flux), which makes the empirical approach more appropriate. The CTE of the detector at a given energy (E) can be estimated by using data sets with similar prescriptions to the ones described in Sect. 4.2.2.1. Because this effect is line-dependent and the data sets need to be calibrated in energy to mitigate the row-dependent gain effect discussed in Sect. 4.2.2.1. For the same reason, only single events from the calibrated data sets are considered, with the possibility to increase the statistic using the double events along the rows. For the 256-row spectra constructed with single events, the line position centers are determined by a Gaussian fit. The CTE is then derived by fitting the line centroids as a function of the number of transfers using the following model:

$$E_n = E_0 \mathrm{CTE}^n, \tag{4.2}$$

where E_n is the energy after n transfers and E_0 a free parameter supposed to be lower than the incident photon energy.
The number of electrons captured by crystal defects is expected to be a constant number. Given that an incident X-ray photon produces a number of electrons proportional to its energy, the CTE is therefore expected to be a function of E. To determine the CTE-E relation, several lines over the energy range are required. The CTE for different energies can be then successively derived by applying the same method and eq. 4.2.
It is worth noting that for MXT the CTE determined by this approach is a composition of several CTEs, from the fast transfer between the image area to the frame store, and from the slow transfer between the frame store to the readout electronics. As the CTE of the frame store is not measurable (X-ray shield above it), it is not possible to disentangle the different CTE values of the system.
Finally, the energy calibration and CTE correction are interdependent. During the "first" data calibration, the data might attenuate the CTE effect and thus its estimate obtained on the calibrated data. For this reason, only an iterative process, where relative CTEs and gains are successively estimated, can approximate the absolute values of these parameters.

4.2.2.3 Charge sharing effect

If charges produced by an X-ray photon extend over several pixels, the photon energy is reconstructed during the post- data processing by summing the individual energy in pixels. When one or several pixels have a lower energy than the LLT value (i.e., the threshold for suppressing noise events), a fraction of the photon energy gets lost and the recombined photon energy is thus slightly underestimated (see Fig. 4.9). This produces a charge sharing (CS) energy effect, which on one side induces a shift of the line position to lower energy, and on the other side degrades the spectral performance of the instrument. For a given energy, the fraction of energy loss depends on the event multiplicity and affects therefore particularly the spectral performance of the spectrum combining all event types. The allocation of the incident photon energy to each pixel involved in a multiple event was introduced by Dennerl et al. (2012) to improve the spatial resolution of the eROSITA instrument. The fraction of energy loss by charge splitting is estimated by performing a Monte Carlo (MC) simulation based on a formalism

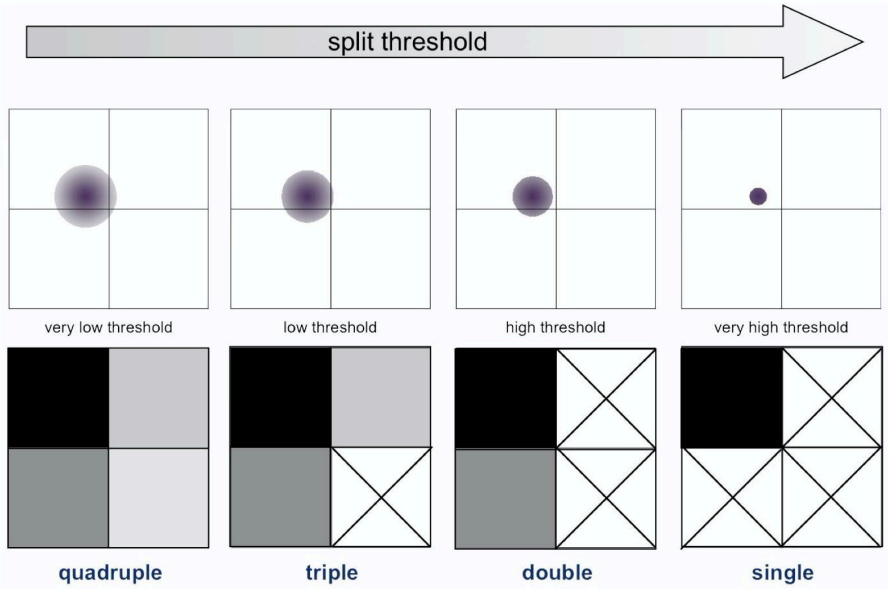

Figure 4.9: Charge distribution and the measured event multiplicity depending on the low-energy threshold (split threshold) applied during the event extraction. As the threshold increases, the resulting events have a lower multiplicity and therefore a larger fraction of the energy is lost. (Dennerl et al. 2012)

similar to Dennerl et al. (2012). For symmetry reasons, only a matrix of 2×2 pixels is considered and the simulation is restricted to the square region defined by the four pixel centers (see Fig. 4.10). Given an energy between 0.1 to 10 keV, 100 000 photons are randomly drawn in the restricted region. At each interaction position, the following Gaussian-like function $f(r) = \exp\left(-(r/a)^2\right)$ is assumed to model the radial charge distribution and determine the deposited energy in surrounding pixels. Note that for the MXT pnCCD detector design, the size of the charge cloud distribution evolves by only $\sim 10\%$ for a photon energy of 1 to 10 keV. For this reason, the pattern statistics and the CS loss depends mainly on the ratio between the photon energy and the fixed LLT value considered for all energies.

Given the simulated charge distributions in the pixels, the threshold value (LLT) is applied to the distributions and the pixels passing the threshold are summed. At this stage, the expected pattern statistics is obtained given the incident photon energy, a and LLT values considered. In addition, for each multiplicity of E, the energy distribution of the line is then convolved with the MXT spectral response (RMF) to determine the simulated reconstructed spectrum. The average energy loss is finally derived by comparing the line center of the reconstructed spectrum

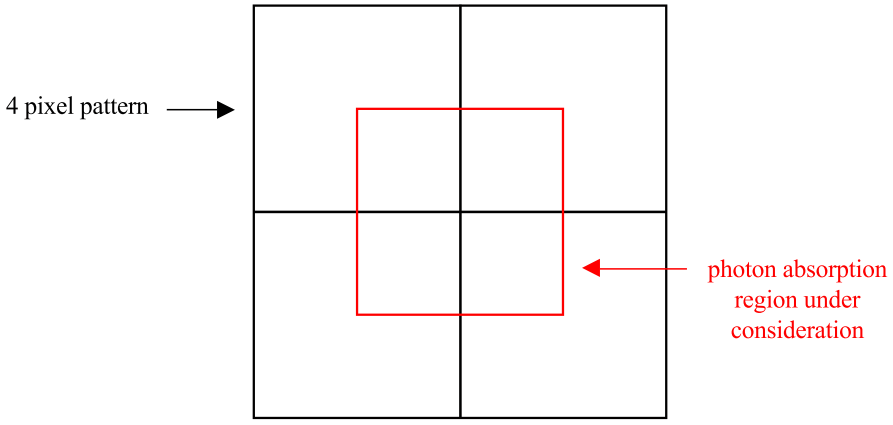

Figure 4.10: Geometry of the model considered to determine the charge sharing loss. The black squares represent the pixels. For symmetry reasons, the red square shows the restricted region considered for the MC simulation. (Adapted from Dennerl et al. 2012)

(determined by a Gaussian fit) with the expected value of the incident energy. For the considered settings, the output of the MC simulation provides the expected pattern statistics and the charge sharing loss fraction as a function of energy for the four multiplicities (Fig. 4.31 for an example). Given the geometry of the MXT detector, the charge distribution can be spread over a maximum number of four adjacent pixels. For this reason, when a quadruple is detected, it means that all pixels pass the threshold and no charge is lost during the event extraction step. It is therefore expected that no correction needs to be applied for this multiplicity. For the other multiplicities, one or more pixels may be below the low-energy threshold and produce the loss of a part of the photon energy. Consequently, the multiplicity of events has to be included to correct this loss and accurately reconstruct the "true" photon energy. The method for applying this charge loss effect to the data is described in more detail in the Sect. 4.3.2.6.

4.3 Calibration campaigns

The development of the MXT requires intensive tests to determine and anticipate the performance of the instrument at the beginning of life and its evolution with time. I have actively participated and contributed to two calibration campaigns, at the SOLEIL facility and at the Panter facility. In Sect. 4.3.1 and Sect. 4.3.2, I describe the main results regarding the spectral performance of the MXT camera

obtained from these campaigns and the consequence on the expected scientific performance of MXT.

4.3.1 MXT camera calibration in SOLEIL facility

In November 2021, the MXT flight spare detector model was installed and irradiated at the X-ray metrology line of the SOLEIL synchrotron. Before the campaign, I was involved in the development of a quicklook software to get a fast visualization of the beam line energy spectrum and MXT performance. Then, during the one-week campaign (24/7), I participated in data collection at the facility. Finally, I reduced and analyzed the entire data sets collected in order to determine the spectral performance in the low energy range of MXT, between 300 to 1 800 eV. This section is adapted from Meuris, Schneider et al., (2022) and presents the results, conclusions and issues encountered during the campaign.

4.3.1.1 The X-ray metrology line

The SOLEIL (Source Optimisée de Lumière d'Energie Intermédiaire du LURE[3]) facility is a particle accelerator producing synchrotron radiation located on the Plateau de Saclay in France and mainly financed by the CEA and the CNRS. The facility is used for fundamental research (e.g., crystallography of biological macromolecules), applied research (e.g., chemistry) and industrial applications (e.g., cosmetics). The project started in 2000 and the first light was obtained in 2006. To remain competitive at the European level, SOLEIL has started an upgrade project named "SOLEIL II" (see `https://www.synchrotron-soleil.fr` for more details).
The synchrotron radiation is an emission of light produced by relativistic charged particles and emitted tangentially to the particle trajectories. To produce this radiation, SOLEIL uses electrons firstly accelerated in a linear accelerator (LINAC) and then in a circular accelerator (Booster) up to 2.75 GeV. The electron packets are finally stored in a 354 m circumference storage ring. Around the ring, a total of 29 experimental stations (beamlines) are distributed (see top panel of Fig. 4.11) and cover a wide energy range, from far infrared to hard X-rays (100 keV). Each beamline is composed of (i) an optical room to select the wavelength and focus

[3]Laboratoire d'Utilisation du Rayonnement Électromagnétique

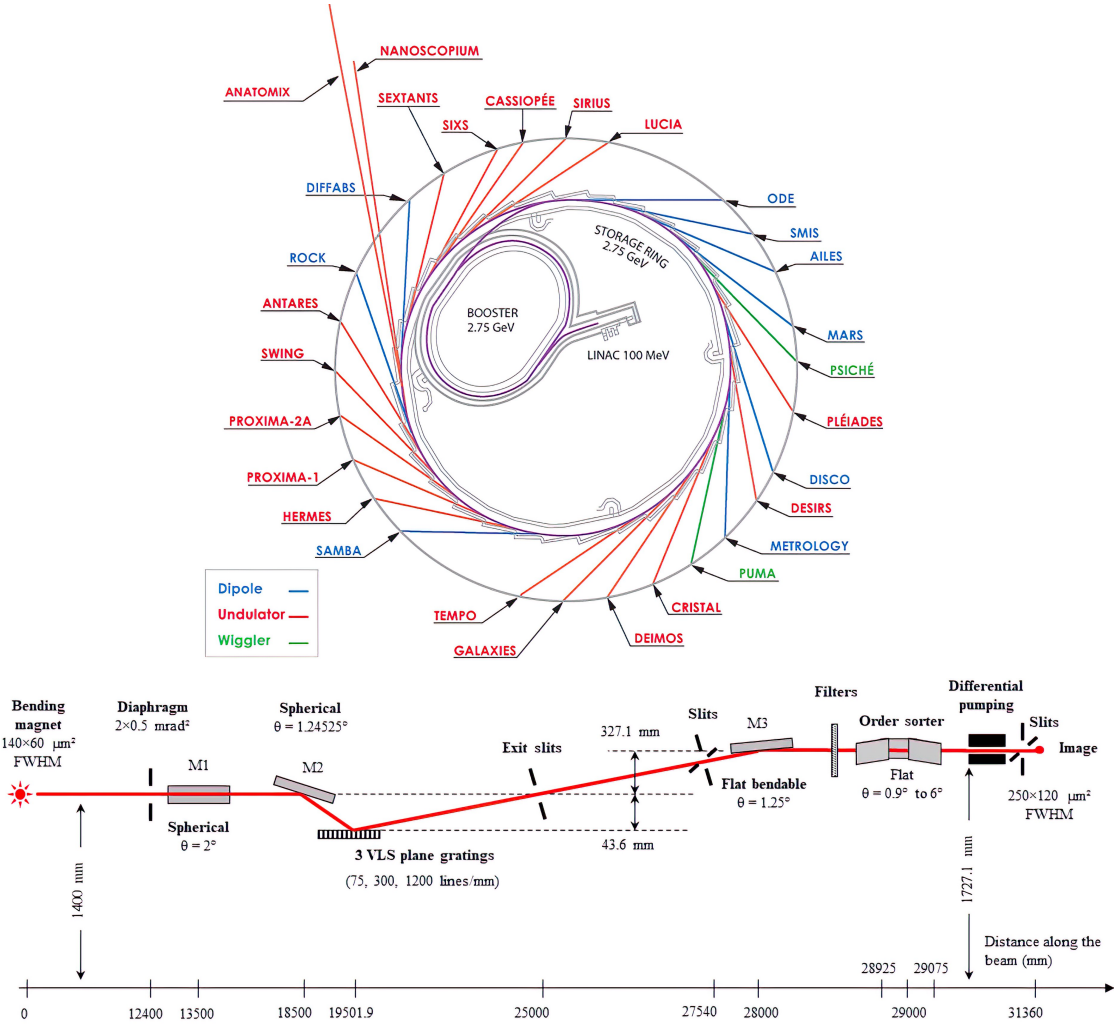

Figure 4.11: The SOLEIL synchrotron facility. *Top panel:* Scheme of the facility showing the Linac, Booster and Storage ring to accelerate the electrons as well as the 29 experimental stations available. *Bottom panel:* Optical scheme of the soft X-ray Metrology beamline. (Credit: Synchrotron SOLEIL)

the incident beam, (ii) an experimental room to install the samples being studied, and (iii) a workstation to control the beam.

Among the 29 experimental stations, the MXT cryostat was installed on the soft X-ray branch of the Metrology Beamline (Idir et al. 2006, 2010) as shown in Fig. 4.12. This beamline was designed to characterize and calibrate X-ray optical components and detectors. It is composed of two branches, a Soft X-ray branch from 30 to 1800 eV and a hard X-ray branch from 100 eV to 40 keV. In the storage ring, the radiations for the Metrology beamline are produced using bending magnets (dipole). The beam of the Soft X-ray branch follows the optical scheme visible in

the bottom panel of Fig. 4.11. It passes through a filter line and a low pass filter (order sorter) to attenuate higher order harmonics produced by the monochromator (gratings) and get a spectral purity better than 99% for the selected energy. The beam obtained this way is a spot of 250×120 μm^2 FWHM with a typical flux between 10^9 to 10^{12} photons/s.

4.3.1.2 Campaign objectives

The FM of the FPA was integrated in the flight instrument in 2021 by the CNES and fully characterized in November 2021 at the Panter facility (see Sect. 4.3.2). The flight spare model of the FPA is used for complementary tests and characterization. The results obtained on the flight spare are expected to be valid for the FM since the detector (pnCCD) was manufactured from the same CCD wafer and the front-end electronics (CAMEXs) with the same electronic components. Both FPAs were firstly calibrated and characterized at CEA using a custom cryostat and X-ray source. The X-ray source is based on an X-ray tube irradiating a composite target to produce fluorescence X-ray lines from 1.5 keV to 9 keV (see Fig. 4 of Ceraudo et al. 2020).

The X-ray source has the advantage to provide a rapid energy calibration and an estimate of the energy resolution over the whole MXT energy range. However, it has several limitations. First, in addition to fluorescence energy lines a *Bremsstrahlung* continuum is produced by the X-ray tube and limits the accuracy of the energy calibration and the spectral performance. Then, the source illuminates uniformly the detector and might affect the CTI measurements by filling the crystal defects (traps) before the transfer of charge packets. Moreover, multiple spectral lines are produced at the same time by the X-ray source and might affect the CTE measurements at the different energies. Finally, the X-ray source has only one line below 2 keV (Al-K at 1.5 keV) to study the electronics response in the most sensitive part of the MOP.

On the other hand, the MXT camera is similar to the eROSITA camera but differs from its conception design in two major aspects. The on-chip optical filter on the pnCCD has a different composition. Therefore, the quantum efficiency (QE) measured by the eROSITA team is expected to be different for MXT. In addition, the warm front-end electronics (FEE) uses a US-free design and might have different performance and linearity than eROSITA.

The SOLEIL campaign was designed to address these questions and improve our understanding of the MXT performance in its low energy range (< 2 keV). The spectral purity, the monoenergetic lines and the energy resolution of a few eV between 30 to 1800 eV delivered by the SOLEIL metrology line make it an appropriate facility to achieve these objectives. Furthermore, the focused beam and the calibrated flux of the beamline offer the possibility to measure the detector QE over multiple areas of the detector and test the uniformity of the on-chip filter.

4.3.1.3 Tuning of the beam

The nominal flux of the Metrology beamline is about 10^9 photon/s in a spot of 250×120 μm^2 which corresponds to a flux of 10^8 photon/s/pixel considering the MXT pixel size (75×75 μm^2). To avoid the pile-up effect (several photons hitting the same pixel), a flux lower than 0.1 photon/s/pixel ($< 1\%$) is required. Therefore, one of the challenges of this campaign was to reduce the incident flux by 9 orders of magnitude while maintaining the spectral purity of the beam.
First, the MXT cryostat was installed 5 m away from the default position to increase the beam size. The divergence of the beam is about 1 mrad and 0.3 mrad in each direction. This corresponds to increasing the beam size by 1 mm and 0.3 mm every meter. Moving the focal plane 5 meters away from its initial position allowed to illuminate about $\times 300$ more pixels and thus reduce the incident flux per pixel. Then, by reducing the size of the exit slit (from 100 to 2 μm), the flux

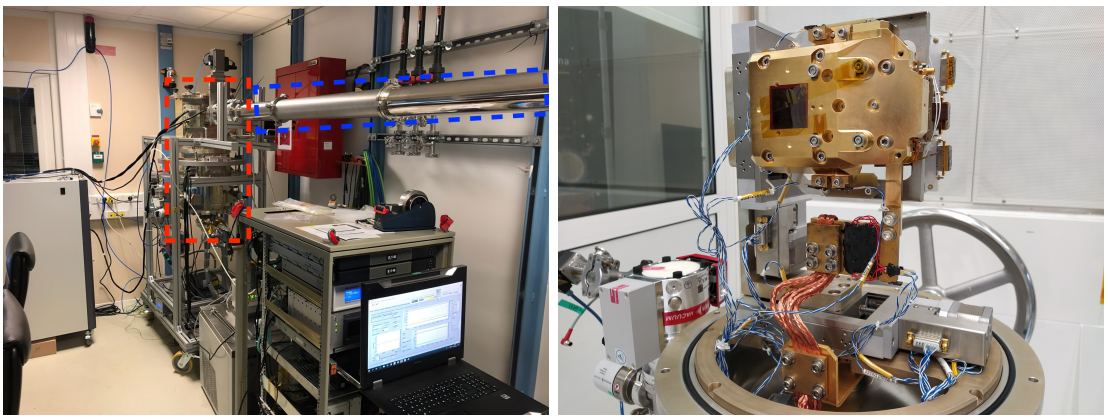

Figure 4.12: MXT setup at the Metrology beamline of SOLEIL. *Left panel:* MXT cryostat (red dashed line) installed and connected to the beamline (blue dashed line). *Right panel:* Inner part of the MXT cryostat showing the focal place assembly (gold color) where the detector is installed.

on the focal plane can be further reduced by about 10^2. Finally, X-ray filters (e.g., Al, Cu or Co) of different thickness can be introduced to reduce the incident flux of the fundamental energy by 10^2 to 10^6. However, this has the disadvantage of not filtering the harmonic lines produced by the diffraction grating. The consequence is that the spectral purity might be affected, resulting in a spectrum with energy lines at k times the beam energy[4]. The solution adopted to reduce the harmonic lines was to increase the grazing angle of the low-pass filter. The configurations leading to a photon flux of about 200 photons/s for the MXT detector and the one used for the reference silicon diode are provided in Appendix 4.3.1.A.

4.3.1.4 MXT setup

During the campaign, the flight spare FPA was installed in the custom MXT cryostat designed by the CEA team and specially adapted for the metrology beamline. The cryostat was rotated from its initial configuration to be interfaced with the beamline (left panel of Fig. 4.12). In addition, the previous cooling system using liquid nitrogen was replaced by a baseplate filled with coolant fluid. The FPA was mounted on two displacement tables (right panel of Fig. 4.12) to move the detector perpendicular to the beam spot and scan the entire detector surface. Finally, the FEE FS was used to control the detector and pre-process the collected signal to save only X-ray events (event mode).

4.3.1.5 Background perturbations

During the first measurements at SOLEIL, in addition to the beam spot an important background signal was measured over the entire detector, visible on the left panel of Fig. 4.13. This noise generated several hundred of events per frame above the LLT values and significantly increased the amount of data to be processed by the pipeline. Even when the shutter of the beamline was closed, these events were observed, supporting the hypothesis of an origin differing from photons.
A security valve (Vatlock system, hereafter VAT) was installed on the MXT cryostat to protect and isolate the detector in case of vacuum failure of the system. This noise was only visible on dark frames when the VAT valve was opened. The

[4]The harmonics and the pile-up effect produce similar spectral lines, making them difficult to distinguish.

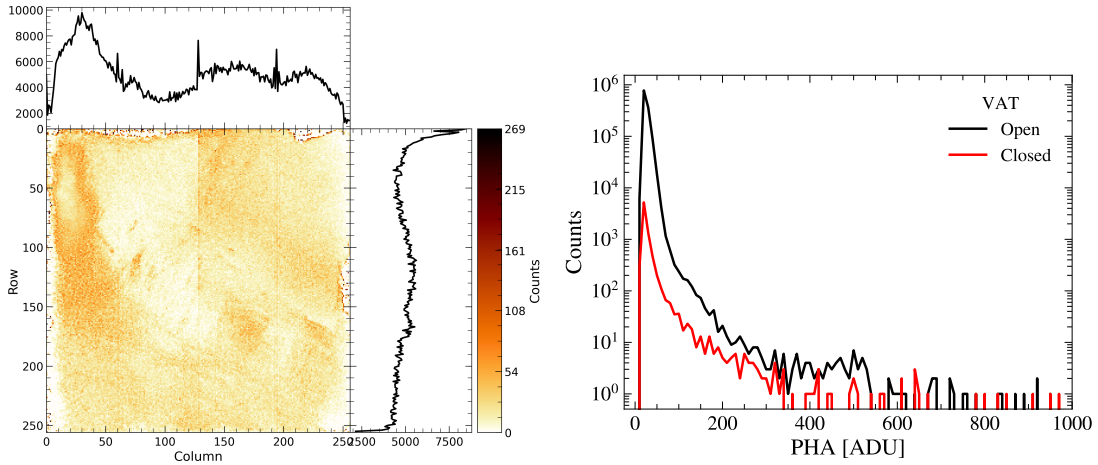

Figure 4.13: Perturbative effects observed during the SOLEIL campaign. *Left panel:* Count maps of the background signal above the LLT threshold produced by the security valve. *Right panel:* Spectrum of the events with the security valve open and closed.

right panel of Fig. 4.13 shows the spectrum of dark frame measurements with the VAT valve closed and opened. We can clearly see that the low-energy events are two orders of magnitude larger when the VAT is opened. This confirmed that these events are not electronic noise produced by the detection chain but parasitic events likely caused by currents induced in the VAT valve of our cryostat to maintain the valve open.

Unfortunately, this problem could not be solved during the campaign and all data were contaminated by the parasitic noise. Prior to the SOLEIL campaign, I was responsible for developing a quicklook version of the full MXT data reduction pipeline. The quicklook allows a "quick" reduction of MXT data using single events while maintaining a reasonable quality of the products. However, the larger number of events produced by the VAT valve significantly increased the processing time, as well as the time to obtain the detector status and tune the beamline configuration. I therefore quickly updated the software during the campaign, to handle this noise and reduce the data in a reasonable period of time. The full offline data reduction and analysis is further discussed in Sect. 4.3.1.7 and 4.3.1.8.

4.3.1.6 Event statistics

The collected data from 300 to 1800 eV were used to characterize the pattern statistics of MXT close to the low energy threshold (0.2 keV) of the detection

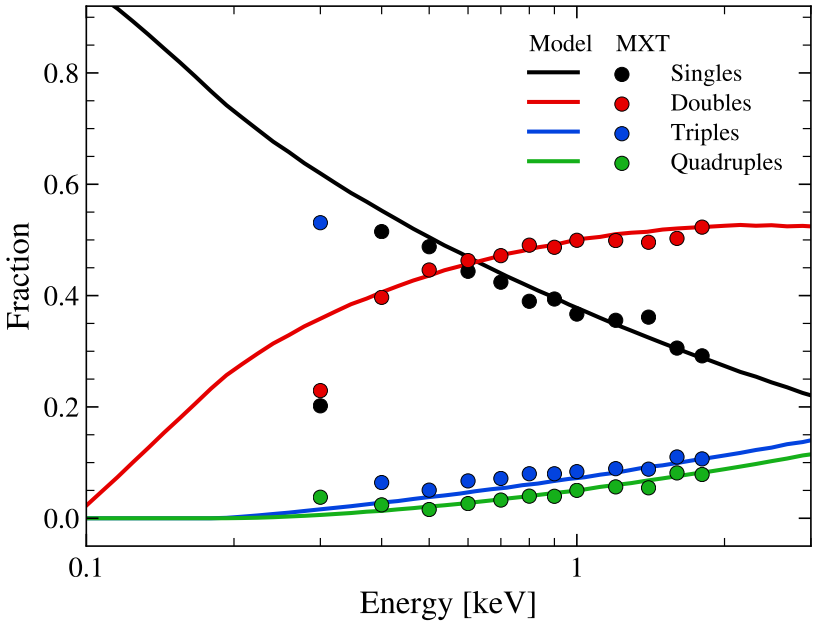

Figure 4.14: Pattern statistics for single (black), double (red), triple (blue) and quadruple (green) events measured at SOLEIL (circles) and from a tailored charge sharing model (lines).

chain. It also provides a sanity check to verify the possible impact of the parasitic events from the VAT on the reduced data. The theoretical framework to determine the expected pattern statics as a function of energy was introduced in Sect. 4.2.2.3 (see also Sect. 4.3.2.6). The expected pattern statistics were obtained by running the CS model with a configuration adapted to that of SOLEIL (-60°C, 44 eV LLT, 75 μm pixel size) and considering a radial distribution of the electron packet of $a = 0.355$. On the other hand, the observed pattern statistics from SOLEIL data were determined by measuring the fraction of events for each multiplicity within a radius of $\pm 3\sigma$ of the energy line. The spectral lines close to the low-energy threshold were optimized by hand.

The comparison is shown in Fig. 4.14. The measured fractions are in good agreement and consistent with the fractions returned by the CS model for $E_{\mathrm{beam}} \gtrsim$ 400 eV. Below 400 eV, the pattern statistics tends to differ from the model. This is likely a consequence of a large amount of residual parasitic events not property filtered during the data reduction. The possible contamination is also suggested by the spectrum of parasitic events shown in Fig. 4.13 where a significant amount of events is observed for PHA $\sim$ 200 ADU (i.e., $\sim$ 400 eV).

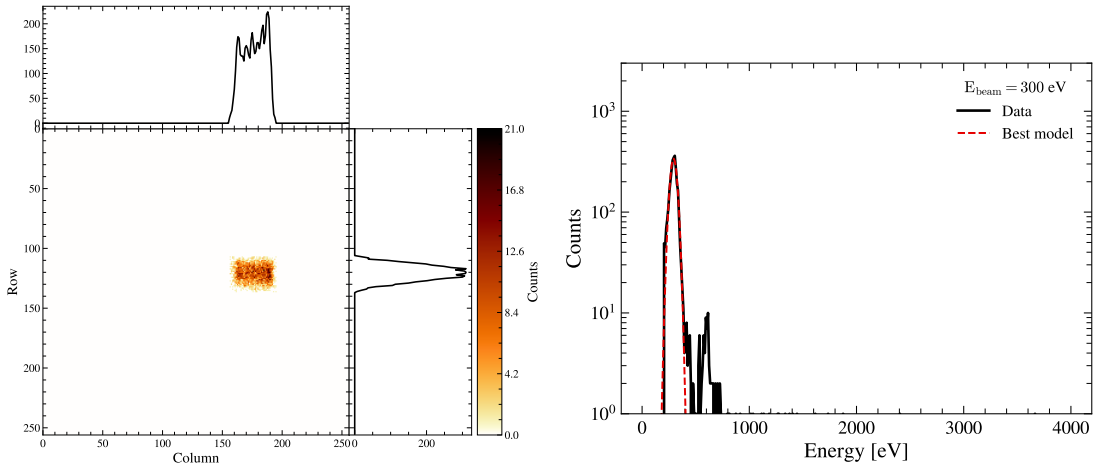

Figure 4.15: Example of data set collected at an energy beam of 300 eV. *Left panel:* Count maps showing the beam spot position. *Right panel:* Spectrum calibrated in energy of the spot visible on the left panel. The red dashed line shows the best-fit model used to measure the spectral resolution.

4.3.1.7 Energy resolution

The energy resolution of the system was derived from 300 to 1800 eV using an optimized Gaussian fit method (see Sect. 4.3.2.8 for more details). The measurement was performed down to 300 eV and 400 eV for single and all events, respectively. An example, for a 300 eV energy beam, of the (filtered) count map showing the beam spot and its associated spectrum is visible in Fig. 4.15. We can see small energy lines ($< 3\%$) at $E_{\text{beam}} = 2 \times 300$ eV likely caused by either pile-up or harmonic photons. An additional set of selected spectra from 400 to 1800 eV are provided in Appendix 4.3.1.B (Fig. 4.18 for singles and Fig. 4.19 for all events). The single events spectra demonstrated the excellent purity of the energy line for the obtained beamline configuration. It is worth noting that at $E_{\text{beam}} > 600$ eV, the spectra for single events indicate small residual parasitic events around 300 eV that might slightly affect and distort the shape of energy lines around 300 eV. These parasitic events are even more prominent in the spectra of all events.

For single events, the energy resolution as a function of energy was compared to the one derived from the same setup but using the laboratory composite X-ray source (left panel of Fig. 4.16). At 1.5 keV, we obtained comparable values, 88 eV for SOLEIL versus 84 eV for the X-ray source. The difference might be explained by less favorable experimental conditions during the SOLEIL campaign (e.g., with thermal (-60°C vs -65°C in lab), vibrational and electromagnetic (VAT noise),

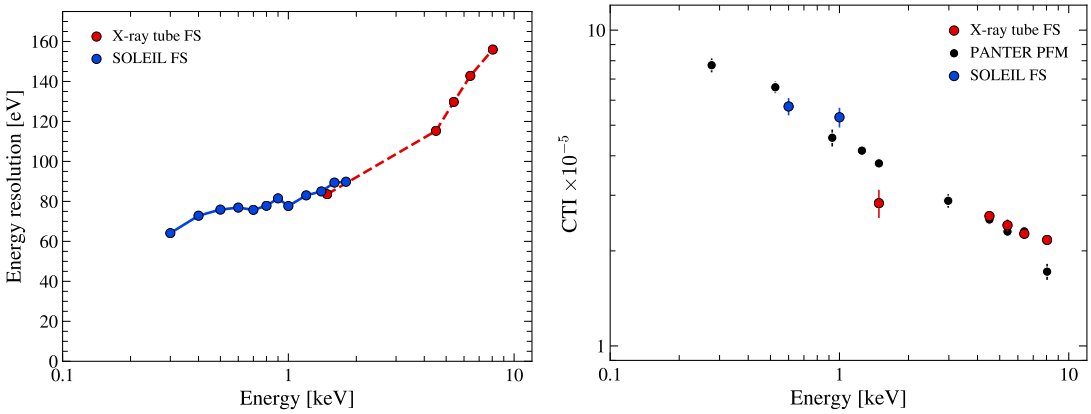

Figure 4.16: Spectral performance of the flight spare model. *Left panel:* Energy resolution as a function of energy. The blue circles show the values obtained at SOLEIL and red circles the values determined in the lab using the X-ray tube. *Right panel:* Charge transfer inefficiency as a function of energy. The blue and red circles show the value measured at SOLEIL and in the lab for the FS model. The black circles present the value determined at Panter on the FM camera.

as well as the new cryostat configuration. For the next SOLEIL campaign with the MXT FS model, some modifications on the setup will be made to improve this aspect, for instance the shielding of the external harness or the grounding scheme inside the cryostat.

4.3.1.8 Charge transfer (in-)efficiency

To determine the CTI of a CCD detector, the method consists in fitting the line center positions of row spectra as a function of the number of charge transfer using eq. 4.2 (see Sect. 4.2.2.2). One of the objectives of this campaign was to measure the CTI by illuminating a small area of the detector in order to avoid any possible bias with the usual method where the whole matrix is uniformly illuminated.
The spot of the SOLEIL beam illuminates only a small area of the detector (typically 25 rows) as shown in the left panel of Fig. 4.15. Given the expected small deviation of adjacent rows for the current state of the detector, a robust CTI estimate was measured by stacking three spot positions along the same columns. The beam configuration remained unchanged between each position to limit possible beam influences on the measurement. The right side of the detector was chosen instead of the left because of the apparently lower VAT noise susceptible of contaminating the data. (Fig. 4.13). After identifying the best beam configurations,

the time remaining at the end of the campaign only permitted to collect data for three energies, at 360, 600 and 1000 eV.

For each energy, the data sets were independently reduced and then stacked to determine the CTI. An additional filtering step was developed and added to the process to limit the effect of parasitic events. The problem of extracting the spot positions from the VAT noise is analogous to the problem of extracting a galaxy from the sky background signal. For this reason, `SExtractor` appeared to be well adapted to this problem and was used to extract the spots. The raw count map, the segmentation map of `SExtractor` (mask) and the filtered count map are visible in Figs. 4.20-4.22 of Appendix 4.3.1.C. Once the data were reduced, filtered and stacked, the CTI was determined by considering 2 or 3 spots. The method using 2 spots was motivated by the deviation observed for one of the spots (at 360 eV). The best-fit obtained for both methods and the comparison of the derived CTI values are shown in Figs. 4.23 and 4.24 of Appendix 4.3.1.C. The results are consistent for 600 and 1000 eV for both methods, but differ significantly for 360 eV. Given the likely contamination of the data by VAT noise at this energy, this estimate was discarded in the rest of the analysis.

On the right panel of Fig. 4.16, the CTI estimates for 3 spots at SOLEIL are compared to previous estimates with a similar pixel flux (0.1 count/pixel/s). The red circles show the CTI estimates using the same configuration but under uniform illumination of the matrix by the composite X-ray source. The black circles are measurements obtained from the MXT FM instrument (see Sect. 4.3.2.7), and it is expected that the CTI values are similar (or at least comparable) since both pnCCDs are produced from the same CCD wafer. The results show a very good agreement with a similar trend for the three independent CTI estimates. This gives an important result which confirms that the method using full and spot illumination gives similar CTI estimates. Given the current state of the detector and the fast transfer of charges into the frame store (200 μs), it suggests that charges are mainly captured by crystal defects in the frame store area where they spend a larger amount of time before being read out (10 ms). This might not be the case after radiation damages that the detector will undergo during flight operations. The next SOLEIL campaign with an improved configuration and without VAT noise will allow to consolidate the extracted CTI values, to increase the number of points and to confirm the results of this first campaign.

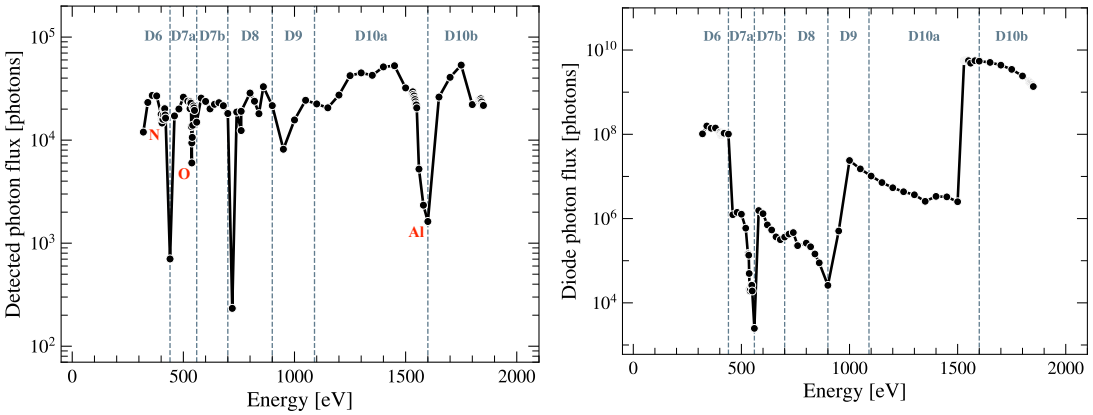

Figure 4.17: Photon flux detected by MXT (left panel) and measured by the diode (right panel) as a function of energy. The dashed blue lines show the beam line configuration used to reduce the incident flux. K-edges are indicated in red color.

4.3.1.9 Quantum efficiency

The QE was inferred using an indirect method exploiting the reference silicon diode of the beamline. Given the excellent reproducibility of the beamline settings (e.g., $E_{\text{beam}} \pm 0.2$ eV and $\theta_{\text{LPF}} \pm 0.001°$), an indirect measurement of the QE is theoretically possible. The flux measured by the diode was converted to a number of events and then to the incoming photon flux into the MXT detector. The equations used for the conversion are provided in Meuris, Schneider et al., (2022). The QE was finally determined by computing the ratio between the photon flux detected by MXT and the converted flux measured by the diode.
However, the measured QE was far from expectations and gave unrealistic values. Figure. 4.17 shows the photon flux detected by MXT (left panel) and the photon flux detected by the diode for the different beam configurations used in the process (see Appendix 4.3.1.A). A part of the breaks observed in the MXT photon flux are produced by X-ray absorption of K-edges of the chemical elements on the on-chip filter[5] (N at 410 eV, O at 544 eV and Al at 1560 eV). The right panel highlights that the diode flux is subject to large variations of several orders of magnitude and might be the source of significant uncertainties. To reduce the uncertainties from the diode current conversion and the applied filter correction, the diode and filters were calibrated (Appendix. 4.3.1.D). In addition, the uncertainties on the detected MXT photon flux were reduced by excluding the possible photons created by the

[5]The theoretical composition of the on-chip filter is 100 nm Al, 40 nm Si3N4, 30 nm SiO2.

VAT noise. Despite the redefined analysis, no realistic QE value was determined. The exact reasons are not clear at this stage, but are likely due to wrong offset values in the diode current measurement or in the slot opening. The next SOLEIL campaign will focus on determining possible "relative" variations of the QE (caused by variations of the on-chip filter thickness) by scanning the whole detector array.

4.3.1.10 Conclusion

This section presents the results of the first calibration campaign performed at the soft X-ray Metrology Beamline of SOLEIL with the flight spare detection chain of the MXT instrument. For the first time at the Metrology Beamline, a set of configurations was found to have monoenergetic lines from 300 to 1800 eV with a flux down to 1 photon/s/pixel on the focal plane. In a more general context, this demonstrates the ability of the soft X-ray Metrology Beamline of SOLEIL to test and characterize X-ray detectors at $E < 2$ keV with monoenergetic lines.
During the campaign, the energy resolution of the MXT flight spare model was determined down to 300 eV and showed very good agreement with previous measurements at higher energy in the laboratory. The charge transfer efficiency was also robustly determined for two energies (600 and 1000 eV) using spot illumination. Interestingly, the results support the trend previously observed using a full illumination of the matrix and in particular support the values determined on the MXT FM. The objective of the QE measurement was not achieved due to inherent uncertainties caused by the indirect measurement of the incident flux.
For the next campaign, the configuration will be improved and the VAT noise removed to obtain better quality data. This campaign could investigate the response of the detection chain between 100 and 300 eV and consolidate the trend of the charge transfer efficiency for different energies. In addition, a full scan of the matrix could reveal possible uniformity of the on-chip detector filter and relative variations in the detector QE. Finally, the charge transfer efficiency will be quantified after a proton irradiation of the flight spare model to predict the performance of the focal plane assembly and the expected science performance of MXT over the mission lifetime.

Appendices

4.3.1.A Beamline configurations

Table 4.2: Configuration of the beamline found for the MXT detector and the reference silicon diode. For each energy range, the low-pass filter (LPF) and its incident angle, the slit opening and the line filter are provided.

Band reference	Energy (eV)	LPF angle	Slit (μm)	Filter (μm)
MXT detector				
D6	300-440	Cr 5.5°	15-100	Co 0.5
D7a	460-560	Si 3.2°	8-100	Co 0.5
D7b	560-700	Si 2.2°	2-3	Co 0.5
D8	760-900	Si 2.1°	2-2.5	Cu 0.9
D9	910-1090	Si 1.2°	4-40	Cu 0.9
D10a	1100-1550	Si 1.1°	2-2.5	Al 25
D10b	1600-1800	∅	2-7	Co 5
Reference silicon diode				
D6	300-440	Cr 2.5°	100	∅
D7a	460-560	Si 3.2°	100	∅
D7b	560-700	Si 2.2°	100	∅
D8	760-900	Si 2.1°	100	∅
D9	910-1090	Si 1.8°	100	∅
D10a	1100-1550	Si 1.1°	100	∅
D10b	1600-1800	∅	100	∅

4.3.1.B Spectra of single and all events

Figure 4.18: Spectrum of single events calibrated in energy. The red curve is the best-fit model found and used to determine the energy resolution.

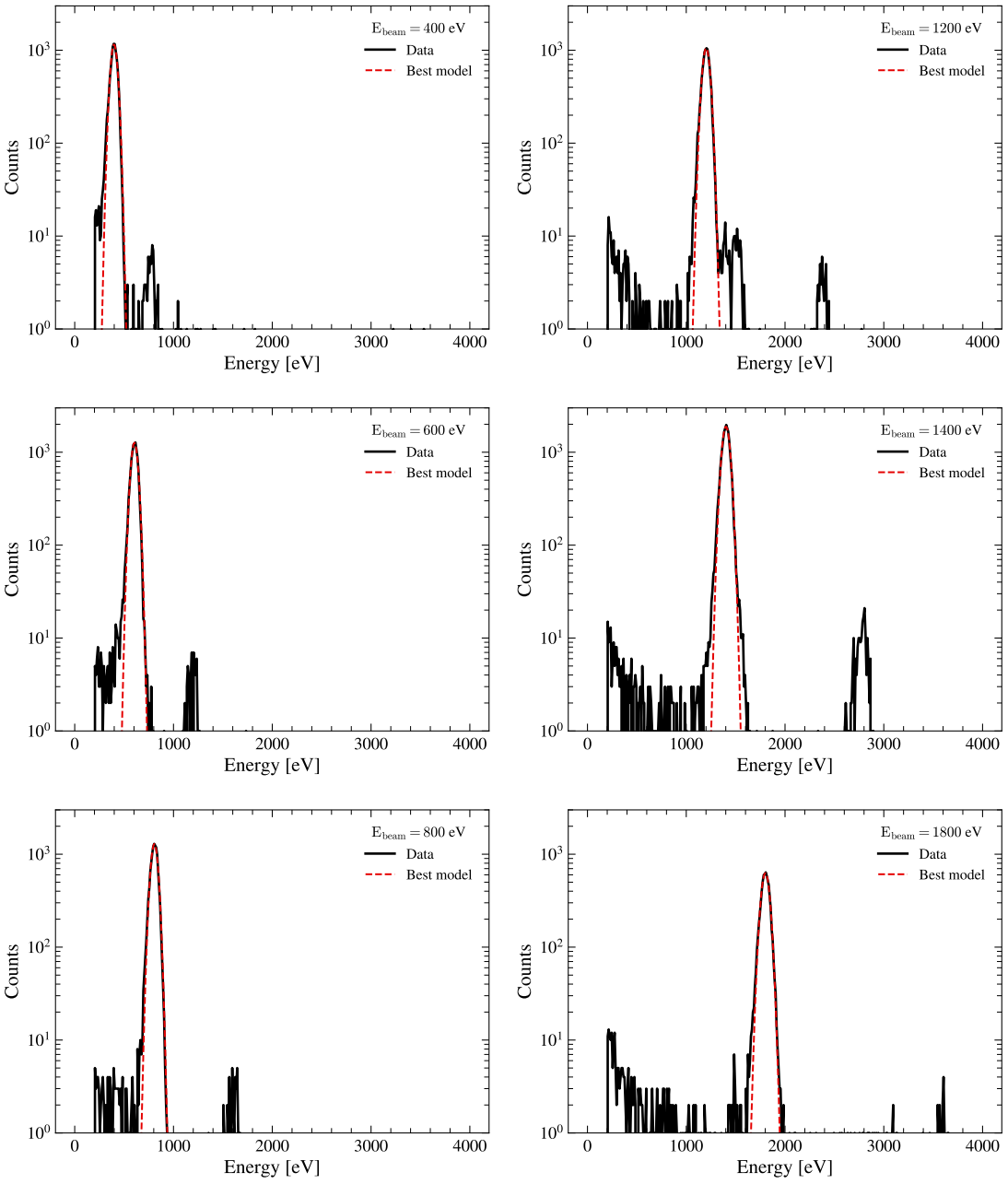

Figure 4.19: Spectrum of all events calibrated in energy. The red curve is the best-fit model found and used to determine the energy resolution.

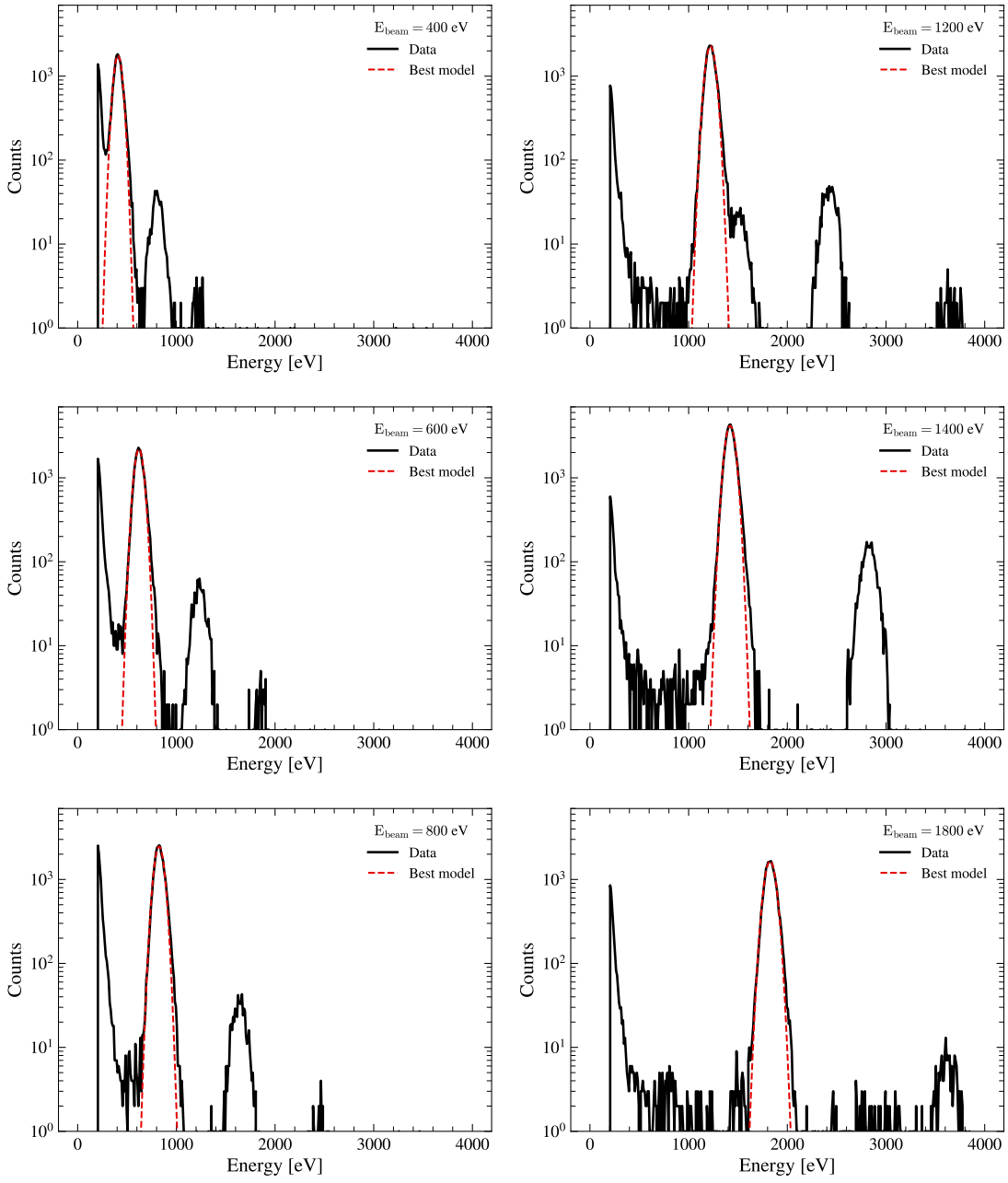

4.3.1.C Charge transfer inefficiency estimates

Figure 4.20: Count map of data sets combining 3 positions to determine the CTE at 360 eV. The raw data (bottom panel), mask (middle panel) and filtered data (bottom panel) are visible.

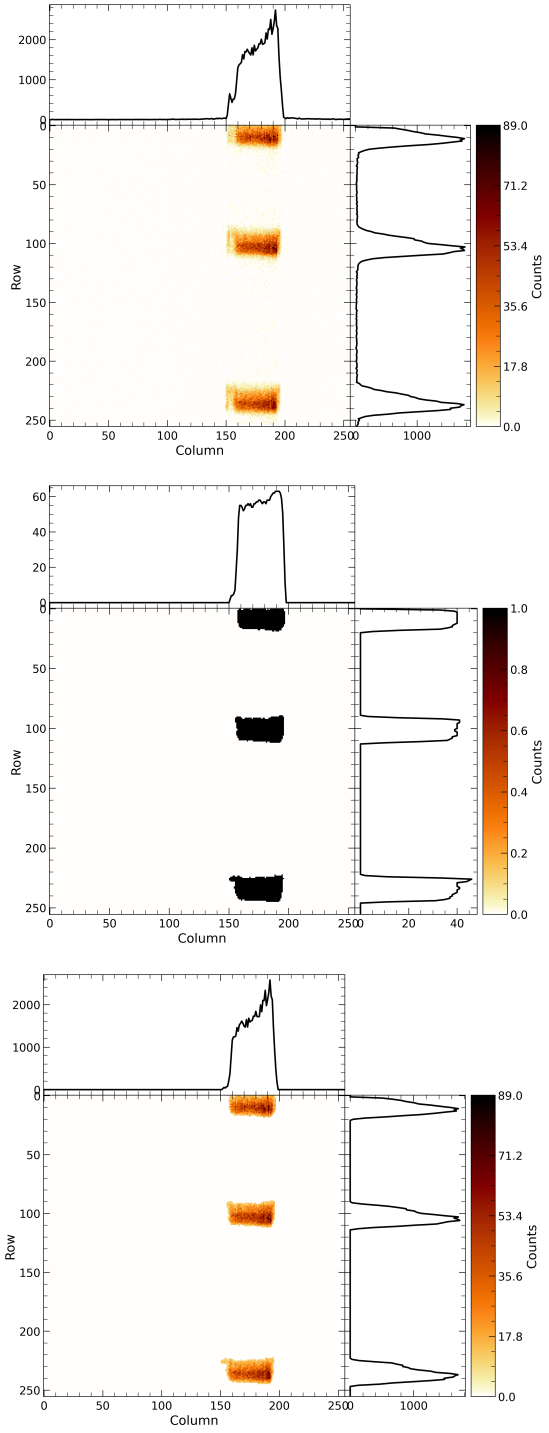

Figure 4.21: Count map of data sets combining 3 positions to determine the CTE at 600 eV. The raw data (bottom panel), mask (middle panel) and filtered data (bottom panel) are visible.

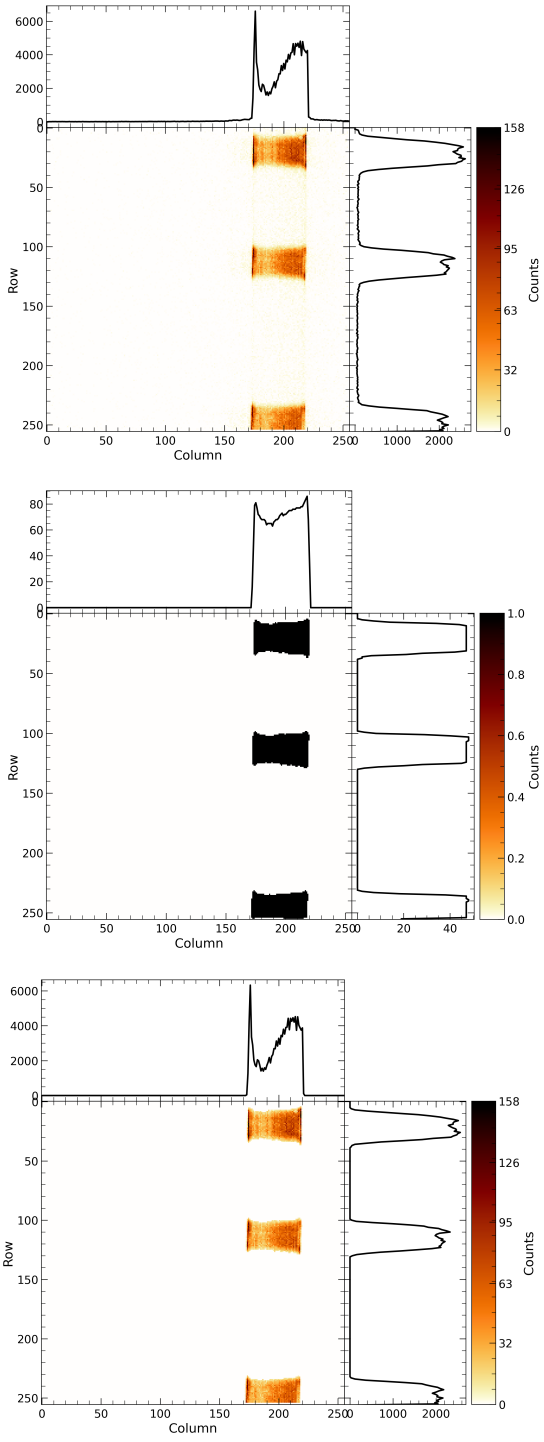

Figure 4.22: Count map of data sets combining 3 positions to determine the CTE at 1000 eV. The raw data (bottom panel), mask (middle panel) and filtered data (bottom panel) are visible.

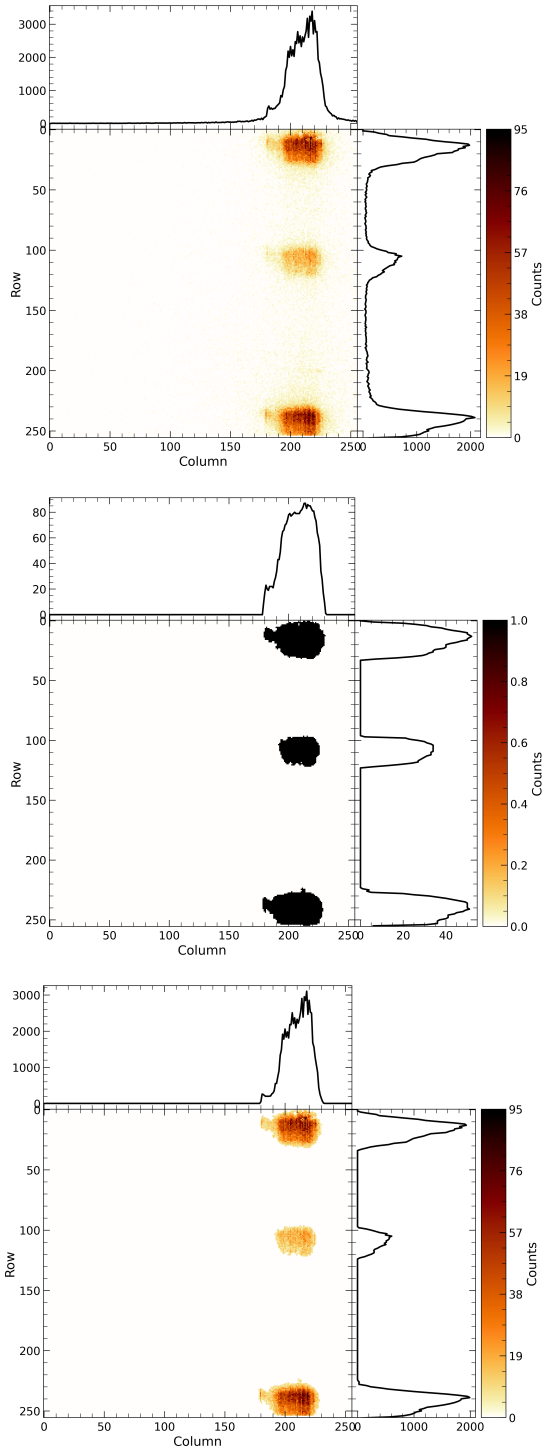

Figure 4.23: Line center position as a function of transfer number using two or three positions visible on Figs. 4.20 to 4.22. Circles represent peak positions determined by a Gaussian fit on row spectra. The best-fit model obtained to derive the CTI is shown as a red line.

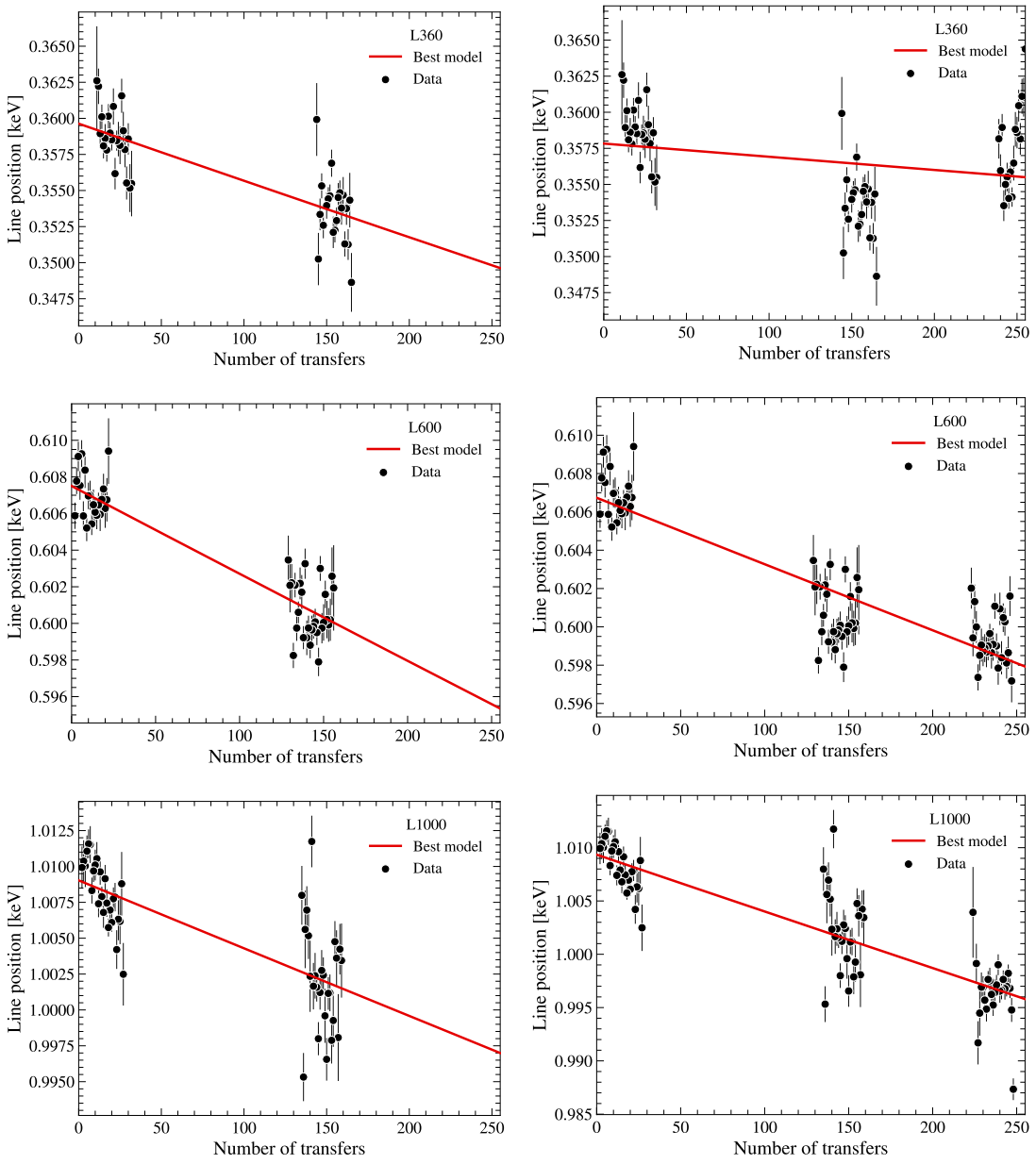

Figure 4.24: Charge transfer inefficiency as a function of energy derived from Fig. 4.23. Values derived using two and three spots are visible in black and blue, respectively.

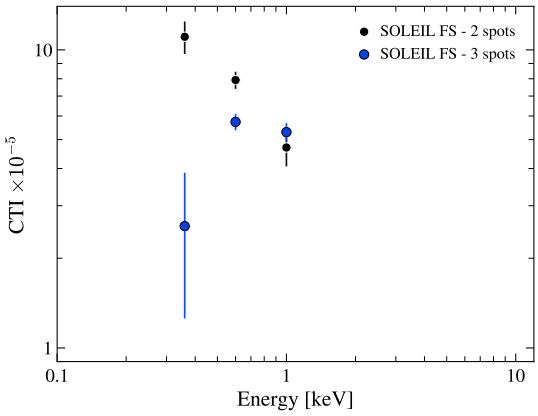

4.3.1.D Filters and diode calibration

Figure 4.25: Comparison between theoretical (black) and measured (red) values for the most commonly-used metrology beam filter (top panels and bottom left panel). Only measurements every 10 eV are shown. The bottom right panel shows the comparison between the diode calibration values (red) and a simple model (black) considering a filter of Al of 150 nm on the diode.

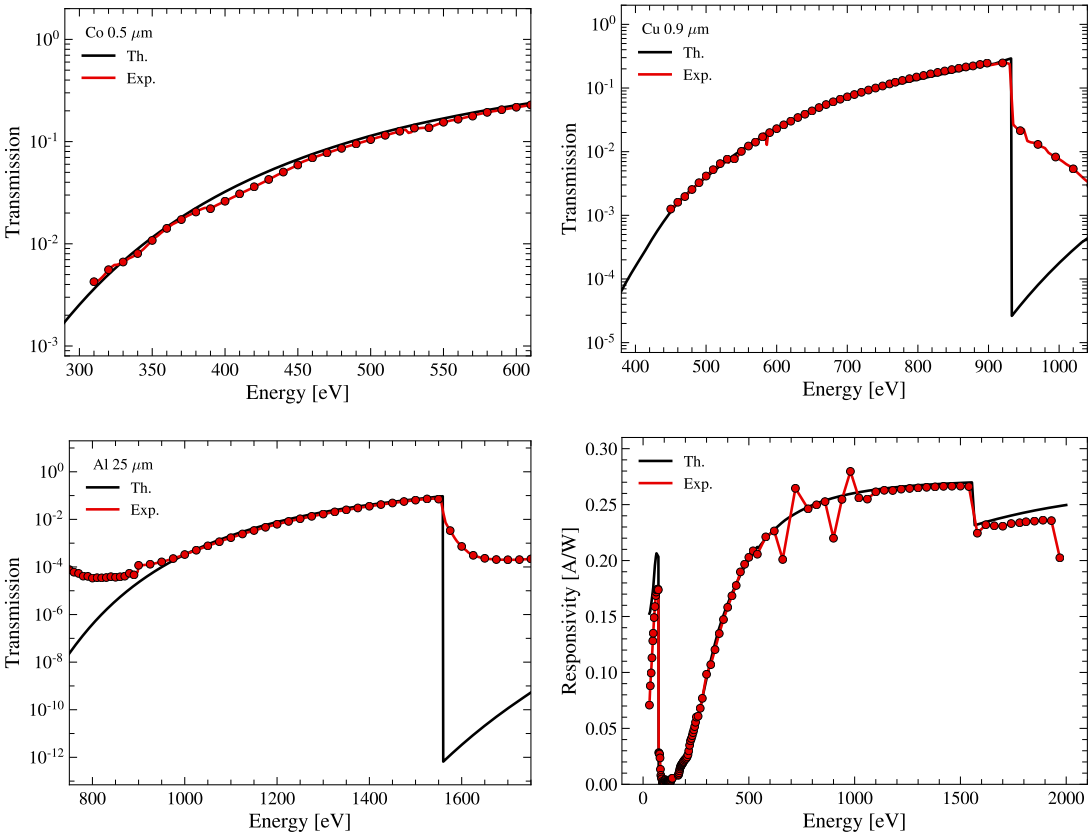

4.3.2 MXT instrument calibration in PANTER facility

After years of development and prototype models, the MXT project has reached its final stage with the complete integration of the flight model. To evaluate and validate the imaging and spectral performance of the FM instrument prior to launch and in-orbit operations, we performed an end-to-end test campaign at the Panter X-ray test facility. During the campaign, we fully characterized and evaluated the performance of the instrument for multiple camera and optics temperatures, beam energies and point spread function (PSF) positions.
This section describes the main results regarding the spectral performance of the MXT measured at Panter and is adapted from Schneider et al. (2022) accepted for publication in Experimental Astronomy.

4.3.2.1 The PANTER X-ray test facility

From October 20th to November 5th 2021, the MXT FM instrument has been intensively tested and characterized at the Panter X-ray test facility[6] (Burwitz et al. 2013; Bradshaw et al. 2019) of the MPE, located in Neuried on the southwest part of Munich. It consists of an X-ray tube producing energy lines from 0.28 to 10 keV and a thermal vacuum chamber (TVAC) for the focal plane instrumentation, separated from each other by a 130-m-long and 1-m-diameter vacuum beamline (Fig. 4.26). The TVAC chamber has a size of 12-m-long and 3.5-m-diameter, which allows to test and characterize a huge variety of X-ray systems and subsystems, e.g., focal plane instruments, optics systems or complete telescopes. This configuration allows to produce an almost point-like source (i.e., a quasi-parallel beam), and the chamber provides the environmental space conditions of pressure

[6] https://www.mpe.mpg.de/heg/panter

Figure 4.26: Aerial picture of the PANTER X-ray test facility. (Credit: MPE)

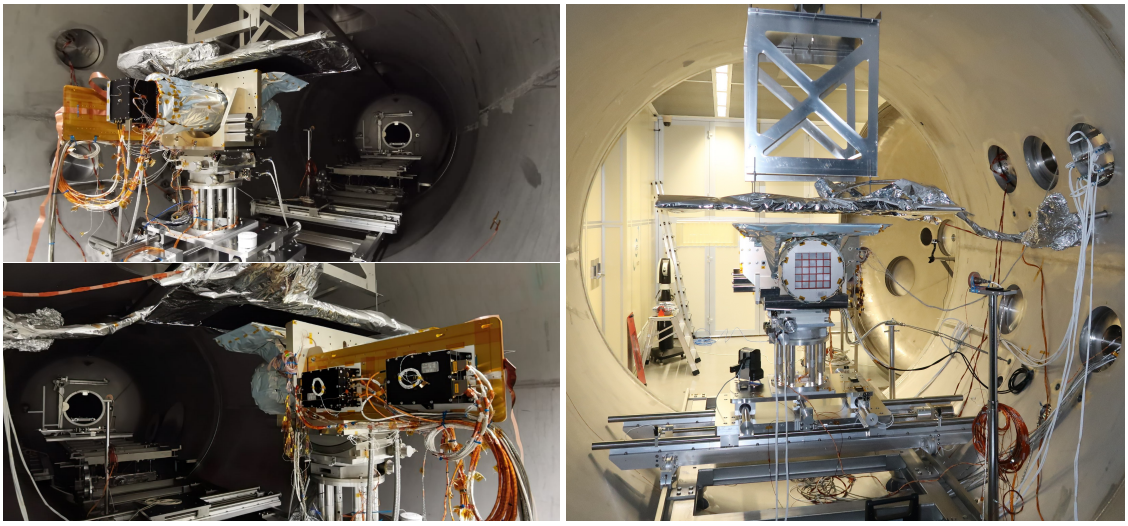

Figure 4.27: MXT FM instrument integrated in the thermal vacuum chamber of the PANTER X-ray facility. Each picture corresponds to a different viewing angle of the MXT FM instrument. (Credit: MPE/CNES)

and temperature at which X-ray telescopes are operated in-flight.

PANTER was involved and used for many projects including *XMM-Newton*, *Suzaku*, *BeppoSAX*, *Swift* or *eROSITA* missions. Currently in addition to *SVOM*, it is involved in the development of the future *ATHENA* and *Einstein Probe* missions. The optics can be mounted on a mobile table (telescope manipulator) to illuminate it from different viewing angles. A detector is placed behind the optics to detect and measure its response to a point-like source at different energies. Several detectors are available at Panter depending on the tests that are performed, for instance TRoPIC (Third Roentgen Photon Imaging Counter), a pnCCD similar to MXT based on the eROSITA design, or a counting Silicon Drift Detector (SDD).

During the end-to-end tests of MXT at Panter, the instrument was in its final flight configuration, including the FM Optics, the FM Camera and the nominal and redundant MDPUs. MXT was integrated in the PANTER TVAC chamber (Fig. 4.27) and placed on a moving table to adjust the alignment of the telescope with the beamline. Throughout the campaign, I was in charge of the online (and quick) data reduction as well as the preliminary offline data analysis. The online analysis consisted in providing a rapid status of the detector such as the on-going count rates or the spectral resolutions. This ensured that the data for the full offline analysis was fully exploitable by the entire scientific team. Then, at the end of each day, a preliminary offline data analysis was performed and permitted

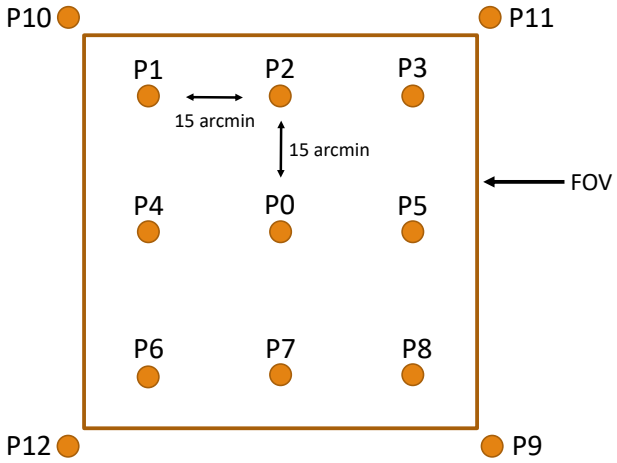

Figure 4.28: Layout of the twelve PSF positions measured at Panter. The detector FOV is represented by the thick orange square. The positions P0-P8 are in-FOV positions and P9-P12 out-of-FOV positions used for the spectral calibration.

to deeply evaluate the good health of the detector and to provide temporary data calibrated in energy for the whole science team. In addition to the initial spectral calibration, this offline analysis was used to estimate PSF positions and compare these values with those of the on-board algorithms to validate the scientific software. In total, we acquired more than 300 runs to fully characterize the optics and the camera response to a point-like source between 0.2-10 keV.

4.3.2.2 Data acquisition

We acquired data for nine source positions (P0-P8) inside the detector FOV, separated by 15 to 50 arcmin from the center, and four source positions (P9-P12) with the PSF center outside the detector FOV (i.e., with the X-ray flux passing through the MPOs without being reflected) to obtain a more uniform illumination of the detector. The out-of-FOV positions exploited the special properties of the micropore optics (Fig. 4.28). A diffuse background (straight flux) is produced when the photons do not interact (no reflection) with the optics (black arrow on the right panel of Fig. 4.2). By positioning the PSF outside the FOV, it is possible to only illuminate the detector this diffuse background. This was particularly appropriate for the spectral calibration purposes, which required to illuminate the maximum of pixels as evenly as possible. The left panel of the Fig. 4.29 shows the count maps of the four corner positions outside the FOV for an energy of 1.49 keV (Al-K), see Appendix 4.3.2.B for positions in-FOV (Fig. 4.42). The count maps show a good

uniform illumination overall, except in some areas where we can clearly see the shadow of the mechanical structure holding the MPOs, which absorbs a significant fraction of the X-ray flux.

CCD detectors such as the one used in MXT, accumulate photons in the image area during a fixed "integration time" (100 ms in the MXT "event mode" configuration, see Sect. 4.2.1.2). Then, the charges created by X-ray photons are quickly transferred to the frame store (200 μs) and read out by the electronics (10 ms). During the integration time, several photons can hit the same pixels and produce a quantity of charge equal to the sum of the photons, a phenomenon called pile-up. The X-ray spectra generated by the Panter facility are not purely monochromatic, and *Bremsstrahlung* emission and by-products created by the X-ray tube may be present in addition to the selected energy. In a pile-up regime with multiple energy lines, it becomes complex and difficult to disentangle the contributions of each photon and thus to reconstruct the individual photon energy. We minimized this phenomenon by tuning the flux of the X-ray source before taking our calibration data. Because the MXT effective area is energy-dependent, the flux optimization was performed for each selected energy (Table 4.3). We tuned the photon counting rate to have less than 0.01 count/pixel/frame in the central PSF core for positions inside the FOV and in the entire frame for positions outside the FOV. This ensures to minimize the pile-up effect ($< 1\%$, see Ballet 1999) and preserves a reasonable acquisition time (a few minutes) to reach a statistic of approximately 20 000 and 64 000 photons for $\mathrm{P} < \mathrm{P9}$ and $\mathrm{P} \geq \mathrm{P9}$, respectively.

We derived and characterized the detector response over the entire MXT energy range by stacking the data from positions P9 to P12 (as shown in the right panel of Fig. 4.29 for Al-K). The resulting data sets allow us to have a sufficient uniform coverage of the detector. We collected between 1 500 and 3 000 counts per column (i.e., more than 284 000 photons over the entire detector), exceeding the minimum of 1 000 counts per column required for the energy calibration. At the Cu-K line energy, the instrument effective area becomes too small for keeping a reasonable acquisition time with the out-of-FOV positions, and we thus used the sum of the in-FOV positions from P0-P8. The resulting count map is not as uniform as for the lower energies, due to the presence of the PSF core inside the FOV of the detector, but the minimum of 1 000 counts per column criterion is satisfied.

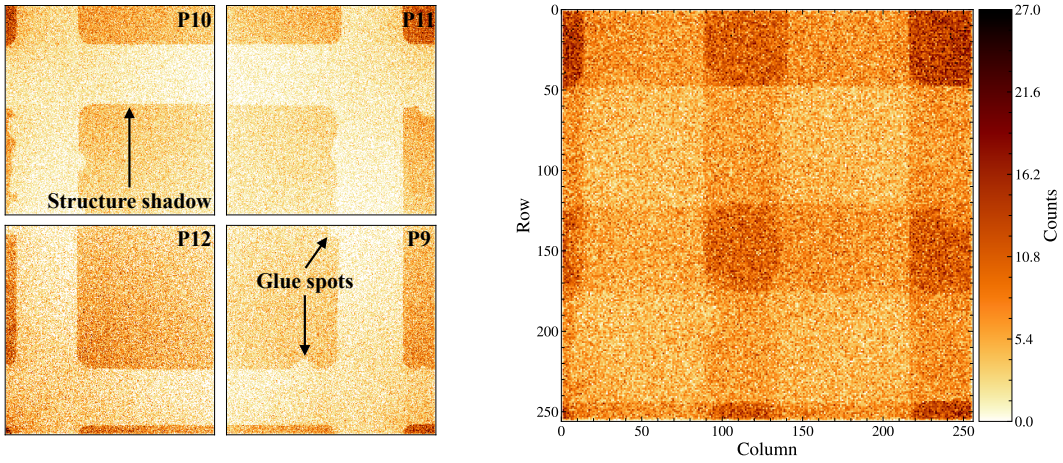

Figure 4.29: *Left panel*: Count maps of the four PSF positions (P9-P12) outside the FOV detector at 1.49 keV (Al-K) and at a detector temperature of −65°C. The lighter vertical and horizontal area (lower counts number) represents the shadow of the mechanical structure holding the MPO. Along the shadows, we can moreover identify small spots produced by the glue used during the optics manufacturing process. *Right panel*: Count map resulting from the stacking of the count maps P9, P10, P11 and P12 visible on the left panel.

4.3.2.3 Dark noise and low-level threshold

As discussed in Sect. 4.2.1.2 for the "event mode", the extraction of events is performed in real-time by the FEE. Only pixels with a value above four times the pixel noise level (i.e., LLT value) are considered as valid X-ray events and sent to the ground. As the offset and LLT might evolve with environmental conditions and in-flight aging, the offset and LLT tables will be regularly calculated (in the MDPU) and updated (in the FEE) on-board. Throughout the Panter campaign, about 40 offsets and LLT tables were calculated between −75°C and −65°C and showed a very good stability over time. An example of the LLT value histogram at −65°C is shown on Fig. 4.30. The histogram shows the 256 × 256 LLT values assigned to each pixel. It reveals the good uniformity for all pixels with a mean LLT value of 46.61 eV, and it demonstrates for dark frames the very low noise performance with an equivalent noise charge (ENC) of 3.22 e^-_{rms} in the MXT detection chain. We can also see that the mean LLT values are slightly different by $\sim$ 1 eV for the two CAMEXs. We also note that for each CAMEX, the LLT values are not strictly constant over the channels, but decrease by about 1 eV from the left to the right CAMEX column. Finally, we measured the dependence of the LLT

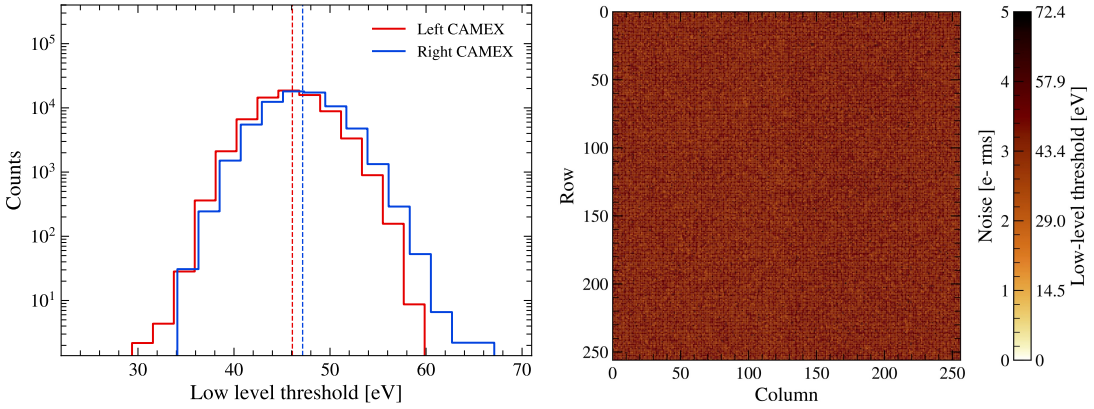

Figure 4.30: Histogram (left panel) and count map (right panel) of LLT values at −65°C for the 256 × 256 pixels of the MXT FM. Red (blue) color shows the distribution for the left (right) CAMEX. The dashed line indicates the mean value of each histogram. The mean LLT value of the 65536 pixels is ∼ 46.5 eV and corresponds to an average equivalent noise charge of ∼ 3.2 e^-_{rms}.

table with temperature, and found that the mean LLT value evolves from 45.8 eV at −75°C to 46.6 eV at −65°C, which is likely due to the higher thermal leakage current.

4.3.2.4 Pattern statistic and CS effect

We ran the CS model described in Sect. 4.2.2.3 using parameters tailored to the MXT configuration and adapted to the Panter campaign. We used for the split threshold the mean value derived from LLT tables (i.e., 46 eV). We determined the pattern ratios obtained at Panter by considering all events within $\pm 3\sigma$ of the energy line, except for peaks with a close second line transition (e.g., Cu-K) where we optimized the value by hand. For the a parameter, which defines the radial distribution of the electron packet in the CS model, we found that $a = 0.357$ provides good agreement with the observed pattern ratios (left panel of Fig. 4.31). We noted that the fraction of pattern is slightly underestimated (overestimated) for triples (quadruples) at $E > 5$ keV.

The results of the CS model for the ratio of the reconstructed photon energy to the incident photon energy is shown in the right panel of Fig. 4.31. We found that the reconstructed energy for single, double and triple events is lower than the incoming photon energy. At 0.3 keV, the CS loss corresponds to 14 eV, 8 eV and 26 eV for single, double and triple events, respectively. Then, the ratios increase with E to

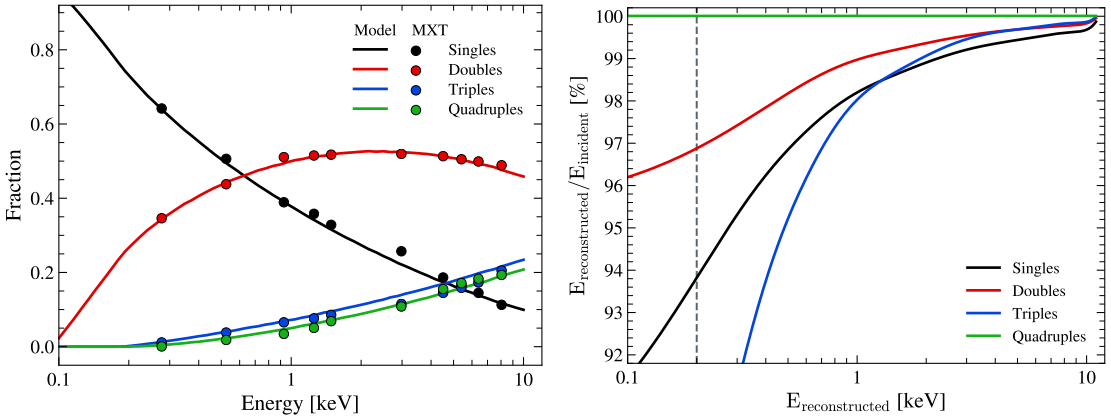

Figure 4.31: *Left panel*: Pattern fractions of single (black), double (red), triple (blue) and quadruple (green) events as a function of energy. The circles are ratios determined from the datasets collected at Panter with the MXT FM. The curves are simulated fractions using the Dennerl et al. (2012) formalism and simulated for the MXT configuration (−65°C, 46 eV LLT, 75 μm pixel size). *Right panel*: Fraction of charge sharing loss as a function of energy for the four pattern multiplicities produced by an X-ray photon. The dashed gray line represents the 0.2 keV minimum energy threshold of MXT.

reach almost one at 10 keV. At 8 keV, we found that the CS loss is about 31 eV for singles, 18 eV for doubles and 14 eV for triples. Only for quadruple events the ratio remains equal to one over the entire energy range, meaning that no energy is lost for these events. As mentioned earlier, considering the MXT detector geometry, the charge cloud can only be split on a maximum of four pixels. If a quadruple event is detected, it means that the four pixel values are above the LLT value and that no energy from the incident photon was lost during the FEE thresholding step.

4.3.2.5 Initial energy calibration

The initial energy calibration follows the standard approach described in Sect. 4.2.2.1 (see also Andritschke et al. 2008; Ceraudo et al. 2020) where no specific corrections are applied to the raw data (ADU) before running the first calibration process. We extracted only single events and created one spectrum by column with all the lines listed in Table 4.3 and with the stacked data from positions 9 to 12. The observed combined spectrum and the synthetic spectrum provided to ECC are visible on Fig. 4.32. We then fed ECC with the 256-column spectra to

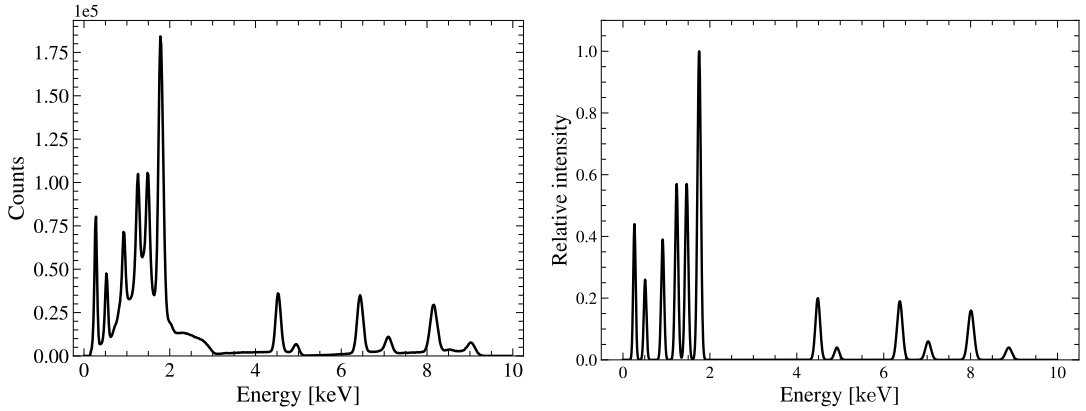

Figure 4.32: Combined spectrum used to derive the energy calibration. Only well-resolved fluorescence lines produced by the Panter X-ray source (Table 4.3) are considered. The left panel shows the observed spectrum and the right panel the synthetic spectrum used to run ECC.

determine the set of parameters (i.e., gain and offset) per column. The gain and offset distributions are shown in Fig. 4.33. We found a very good uniformity with a low dispersion of the gain and offset values over the columns. We determined a median gain and offset of about 2.2 eV/ADU and 26 eV, respectively. The dispersion is less than $\sim 1\%$ for the gains and about 10% for the offsets. We observed a discontinuity in the gain estimates between the two CAMEXs (separated by the gray dashed line in Fig. 4.33), which is caused by mismatch variations during the manufacturing processes. We also noticed that the gains gradually increase in the multiplexing sequence direction, from column 0 to 127 for left CAMEX and from 128 to 255 for right CAMEX. We interpreted that as a possible effect of the bandwidth limitations in the FEE analog channels.

To test the accuracy of our energy calibration, we computed the energy scale (i.e., $E_{\text{reconstructed}} - E_{\text{incident}}$) as a function of the energy for single and all events (singles, doubles, triples and quadruples). Figure 4.34 shows that the energy scale is within the $\pm\,20$ eV instrument requirement up to $\sim$ 7 keV and $\sim$ 3 keV for single and all events, respectively. The calibration error for singles is more uniformly spread around zero while the calibration error for all events is systematically positive. For the Cu-K line ($\sim$ 8 keV), we noted in both cases that the value is shifted regarding the trends at $E < 6$ keV, suggesting a possible small non-linearity of the electronic chain in the high-energy range of MXT.

We investigated how the Cu-K line could affect the calibration law by running a calibration with a data set excluding this line. The results revealed a good over-

Element	Energy [eV]
C-K	277
O-K	525
Cu-L	930
Mg-K	1253
Al-K	1486
W-M	1774
Ti-Kα	4508
Ti-Kβ	4950
Fe-Kα	6398
Fe-Kβ	7053
Cu-Kα	8047
Cu-Kβ	8910

Table 4.3: Fluorescence lines produced by the Panter X-ray source and used for the spectral calibration. Energies are extracted from the X-Ray Data Booklet (Thompson et al. 2009).

all agreement, with a small tendency to degrade the energy scale at $E > 5$ keV. This confirmed that Cu-K has only a small contribution to the calibration process, which is explained by its limited weight in the correlation compared to the multiple lines existing at $E < 3$ keV. Moreover, ECC performed a correlation with a synthetic spectrum without any background signal while our data sets present a non-negligible background, especially at $E < 3$ keV (Fig. 4.32). As the calibration could also be affected by this problem, we created a data set by selecting only lines with low background signal and performed a new calibration. The results showed that the background has no significant impact on the calibration law and that the measured spectral resolutions are consistent with the one using all energy lines plus a background. We concluded that the set of calibration parameters remains of good quality and consistent even when considering different energy line configurations.

4.3.2.6 Correction of the multiple events

To integrate the correction of the CS effect into the calibration process (Sect. 4.3.2.4), the order of the steps applied to the raw data has to be considered

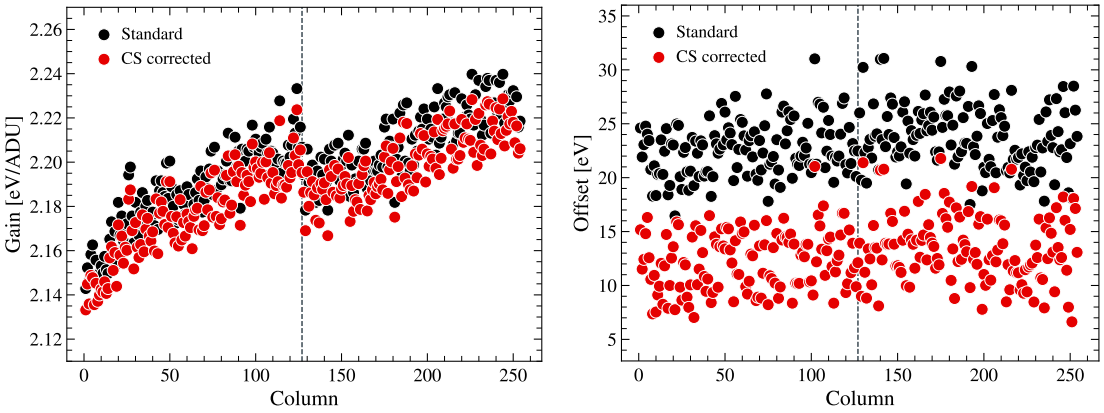

Figure 4.33: Detector gains (*left panel*) and offsets (*right panel*) as a function of columns (CAMEX channels). Black circles are obtained by the standard calibration method and red circles after considering the charge sharing loss correction in the calibration process. The gray dashed line shows the separation between the left and right CAMEXs.

carefully. As with CTI, CS loss can be mitigated during the calibration process. Because single raw events are affected by the CS loss, we started by creating a synthetic spectrum for ECC that suffers from a CS loss. It was done by using the relation for singles found in the right panel of Fig. 4.31. This allows us to disentangle the possible effect of the CS on the calibration parameters and anticipate the CS correction applied later. The gains and offsets obtained using this approach are shown in red color in Fig. 4.33. We found that gains and offsets have similar trend to the one without CS correction (Sect. 4.3.2.5) but with lower overall values. This is a direct consequence of the spectral shift towards the lower energies of the synthetic spectrum caused by the preliminary CS correction. We then applied the set of parameters derived from single events on raw ADU data (without any CS correction) to obtain calibrated data in keV. Once calibrated, we corrected the reconstructed events from the CS loss by applying the relation derived for each multiplicity visible in the right panel of Fig. 4.31. Again, we tested the accuracy of the calibration by measuring the energy scale on single and all events spectra (Fig. 4.34). For singles, we found that the CS correction slightly improves the position of the lines at $E < 5$ keV and more significantly at $E > 5$ keV. For all events, this additional correction significantly improves the line positions over the entire energy range. The positions fall within the requirement up to ~ 6.5 keV compared to ~ 3 keV with the standard approach. In addition, the CS correction contributed to reduce the supposed non-linearity previously observed in the high

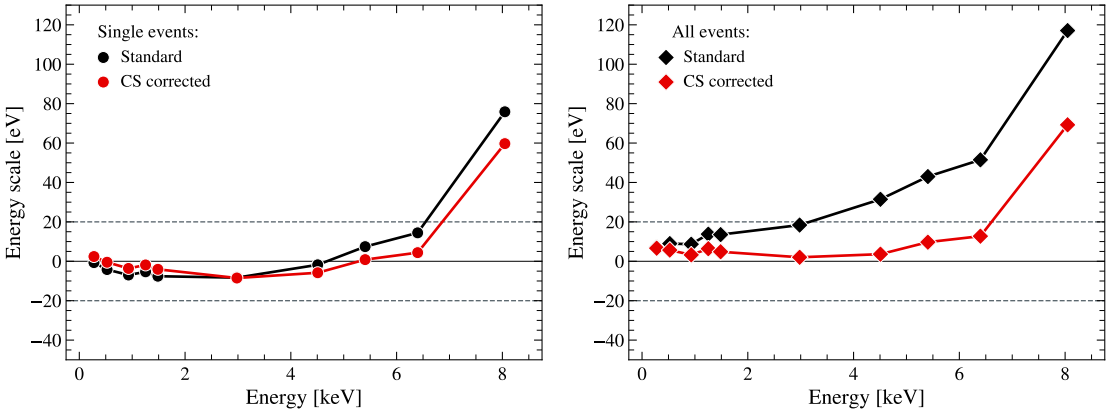

Figure 4.34: Energy scale ($E_{\text{reconstructed}} - E_{\text{incident}}$) as a function of energy. Circles (*left panel*) are for singles and diamonds (*right panel*) for all events (singles, doubles, triples and quadruples). Black and red colors represent the performance without and with the CS correction. The dashed gray line shows the instrument requirement.

energy domain of MXT. However, despite the CS correction, we noted that the position of Cu-K is still off the instrument instrument requirement, suggesting that a non-linear calibration would be necessary to improve the positions at the end of the MXT energy band. The effect of the CS correction on the energy resolution is further discussed in Sect. 4.3.2.8.

4.3.2.7 Charge transfer (in-)efficiency

The left panel of Fig. 4.35 clearly shows the effect of the CTI on the measured line position of Al-K, see Appendix 4.3.2.D for other energy lines (Fig. 4.45). For the rows closest to the CAMEX (i.e., $\lesssim 5$ transfers), only a slightly fraction of the incident photon energy is captured by crystal defects (probably in the frame-store area) leading to a measured position close to the theoretical value of 1.486 keV. Then, as the number of transfers increases, the position is gradually shifted to a lower energy and reaches its minimum at the farthest row from the anode. The visible dispersion of the positions might be explained by the statistical fluctuations of the process that traps and re-emits electrons. To determine the CTI of the MXT detector at the beginning of its life and evaluate its trend as a function of energy, we consider the ten most intense lines obtained at Panter and that probe the entire MXT energy range. We then derived the CTI on each line individually as shown in the left panel of Fig. 4.35 and previously described in Sect. 4.2.2.2.

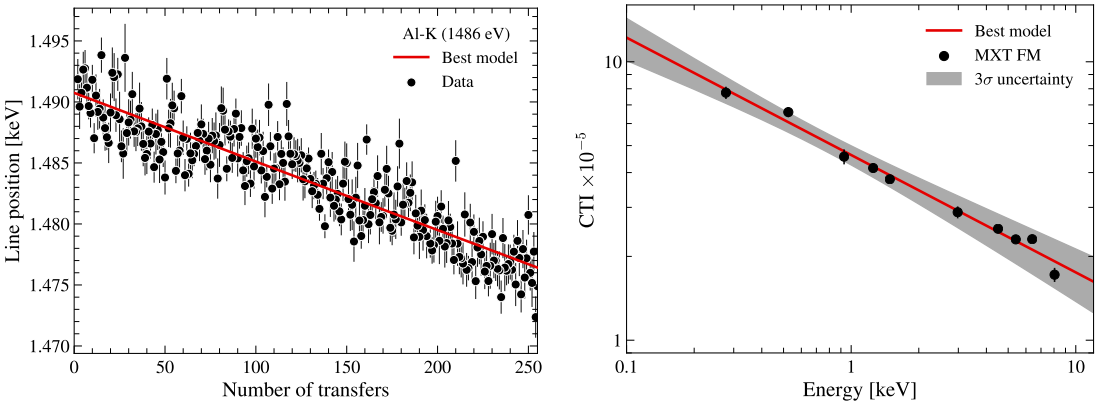

Figure 4.35: *Left panel*: Line center position for Al-K as a function of transfer number. Circles represent peak positions determined by a Gaussian fit on row spectra. The best-fit model obtained to derive the CTI is shown as a red line. *Right panel*: Charge transfer inefficiency (CTI) as a function of energy. The best-fit model is shown in red. The gray area represents the 3σ uncertainty associated to the model.

The right panel of Fig. 4.35 shows the resulting estimates as a function of the energy. The CTI is in the range of $10^{-5} - 10^{-4}$ and we found that it decreases as the incoming energy photons increases. We expect this trend because the number of charges generated by an X-ray photon is proportional to its incoming energy and the electrons captured by crystal defects is a constant number related to the number of traps. It is therefore consistent with having low energy photons with a higher CTI value. We modeled the CTI with E using a power law function and the best-fit model was found for:

$$\mathrm{CTI}(\mathrm{E}_i) = 4.63 \pm 0.09 \cdot 10^{-5} \times \mathrm{E}_i^{-0.42\pm0.02}, \text{ with } \mathrm{E_i} \text{ in keV}. \tag{4.3}$$

We noted that only an iterative process can determine the absolute CTI due to the interdependence of the gain (column-wise) and CTI (row-wise) corrections (see Sect. 4.3.2.7). We observed that after one iteration loop, the CTI estimates are even smaller ($10^{-7} - 10^{-6}$) and constant over the entire energy range. This confirmed that our first estimates were already close to the absolute CTI. We also investigated the possible effect of the CS loss correction on the CTI estimates. We determined the CTI for both data sets, with and without CS correction. We found very good agreement for the two resulting CTI trends. However, it is worth noting that the CTI should be derived before any CS correction on the data, given that the correction would tend to reduce the dispersion between the line positions of

the low and high row spectra. Considering the current CTI, the CS correction has only a negligible effect on the deviation of line positions observed in the left panel of Fig. 4.35, resulting in a similar CTI trend between the two data sets.
These CTI estimates represent the current level of the detector defects and impurities before the first radiation damage that MXT will suffer during in-orbit operations. The evolution of the CTI and how space radiation will affect MXT performance have been theoretically investigated using `Geant4` simulations (Ceraudo 2019) and will be experimentally investigated on the flight spare model produced from the same CCD wafer.

4.3.2.8 Energy resolution

The energy resolution (ΔE) of the MXT camera was measured on ten intense X-ray lines from 0.28 keV to 8.05 keV produced by the Panter X-ray source. For each line, we determined the full width at half maximum (FWHM) with an optimized `Python` routine based on the *lmfit* package (Newville et al. 2014). The routine fits a function composed of 3 to 6 parameters that correspond to a combination of a Gaussian function with constant, linear or quadratic functions expressed as

$$f(x) = A_1 e^{-\frac{1}{2}\left(\frac{x-A_2}{A_3}\right)^2} + A_4 + A_5 x + A_6 x^2, \tag{4.4}$$

where A_1 is the amplitude, A_2 the mean value and A_3 the variance of the Gaussian function, and A_4, A_5 and A_6 are the coefficients of the quadratic polynomial function.
The resulting best-fit models for single events are visible in Fig. 4.36, see Appendix 4.3.2.C for best-fit models for all events (Fig. 4.44). All fluorescence lines produced by the X-ray tube lie on a background signal (*Bremsstrahlung* radiations) with an intensity depending on the source configuration (e.g., anode type, intensity or voltage, ...). To mitigate its influence on the spectral performance, we found that a model composed of 5 or 6 terms (i.e., a Gaussian plus a linear or quadratic function) minimized the χ^2 statistic and provided the best results. The Fig. 4.37 shows for single and all events the MXT energy resolution as a function of the energy. For the single events, we found no significant effect of the CS correction on the spectral resolution compared to the standard calibration method. However, the benefit of this correction is more significant for the spectral performance of all

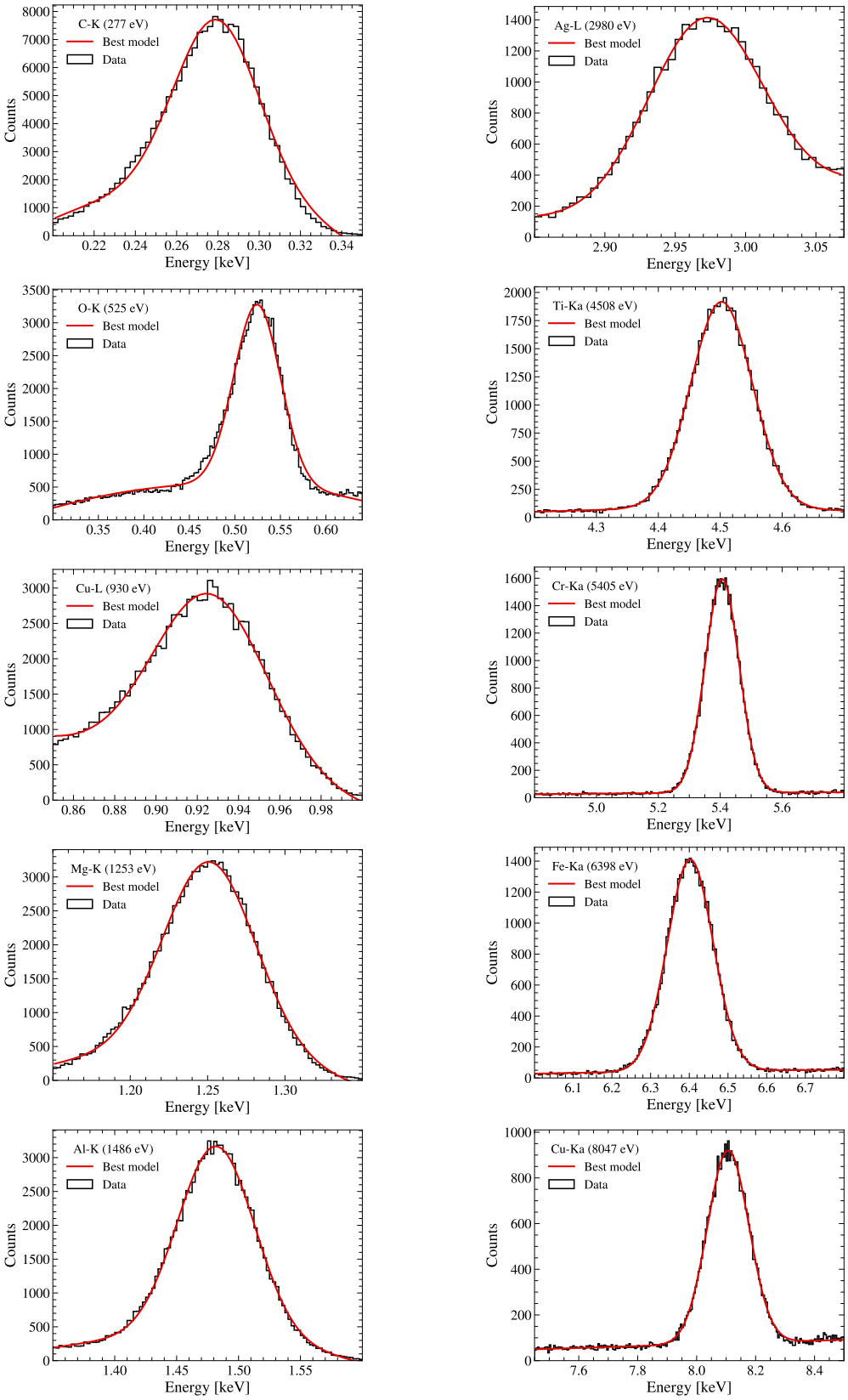

Figure 4.36: Spectrum of single events calibrated in energy and corrected from charge sharing effect. The red curve is the best-fit model found and used to determine the MXT energy resolution.

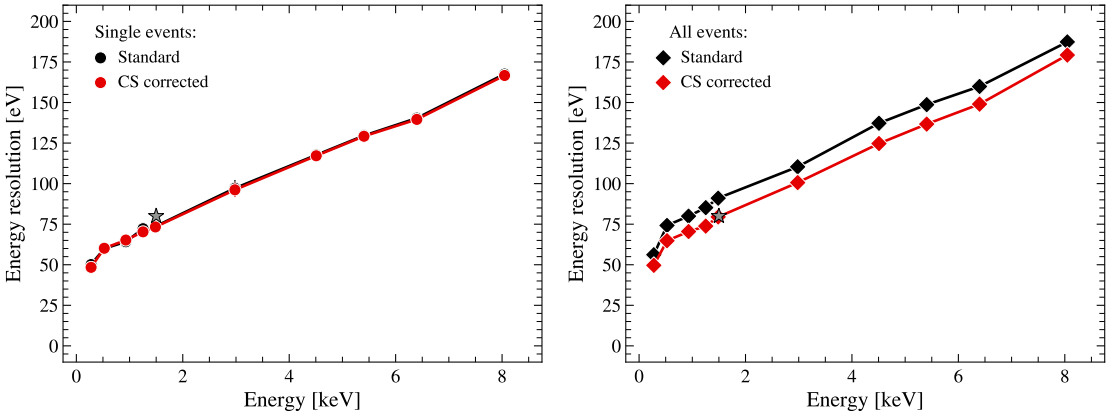

Figure 4.37: Energy resolution (ΔE in eV) as a function of energy. Circles (*left panel*) are for singles and diamonds (*right panel*) for all events (singles, doubles, triples and quadruples). Black and red colors represent the energy resolution without and with the CS correction. The gray star shows the instrument requirement of 80 eV at 1.5 keV.

events where, for all energy lines, the spectral resolution is considerably improved compared to the standard approach and closer to the performance of single events. The reason is that at first order, the CS correction shifts the energy line position of each multiplicity to its expected (theoretical) position, thus resulting in a combined spectrum with sharper lines and a better energy resolution. We determined an energy resolution of ~ 73 eV and ~ 79 eV for Al-K (1.49 keV) for single and all events, respectively. These performances are fully compliant with the instrument requirement of 80 eV at 1.5 keV and demonstrate the excellent spectral performance of MXT at beginning-of-life. It is worth noting that Meidinger et al. (2006) reported the state-of-the-art in spectral performance for this generation (DUO) of pnCCD. They achieved a ΔE of 66 eV for single events and 74 eV for all events on the Al-K line at a similar temperature (-70°C) to MXT but under more favorable conditions, i.e., not fully integrated in a space designed instrument free from US components.

Using all data sets (except the Cu-K) calibrated in energy and corrected from CS and CTI, we modeled the ΔE relation by considering the Fano noise[7] (Fano 1947) and readout noise, i.e., with 2 free parameters (F, ENC) and a given pair creation energy (ϵ_w) of 3.62 eV in silicon.

[7]The Fano noise is a stochastic noise induced by the statistical fluctuation of electron-hole pairs from the absorption of a photon of energy E in a semiconductor detector.

For single events, we fit the following equation ($N_{\text{split}} = 1$):

$$\Delta E_i = 2.35\sqrt{\epsilon_w E_i F + N_{\text{split}}(\epsilon_w \text{ENC})^2}, \text{ with } E_i \text{ in eV.} \tag{4.5}$$

The best-fit model returned a Fano factor F of 0.131 ± 0.003, which is consistent with estimates reported in the literature (Kotov et al. 2018) and an ENC of 4.9 ± 0.2 e^-_{rms}. This electronics noise includes the contribution of the detector leakage current (measurable with dark frames, Sect. 4.3.2.3) and the calibration errors inherent to the methods and the considered assumptions (e.g., linear calibration). Throughout the campaign, we also investigated the energy resolution as a function of detector temperature (T_{det}). We acquired a series of measurements for three fluorescence lines (O-K, Cu-L and Al-K) and $T_{\text{det}} = -75°\text{C}$. We found very similar performance with no significant difference in the spectral performance between $-65°\text{C}$ and $-75°\text{C}$, which indicates that the electronics noise was minimal at the nominal temperature of the MXT ($-65°\text{C}$) and was not the limiting factor of performances. However, this may not be the case at the end of the mission if the dark noise becomes more important due to radiation damage.
Finally, the measurement on the C-K line confirmed the ability of MXT to detect photons down to 200 eV and the Cu-Kβ line up to ~ 9 keV. Both results demonstrate at the instrument level the low and high energy threshold of MXT and the compliance with the instrument requirements.

4.3.2.9 Iteration process

The gain and offset parameters depend at first order on the detector column due to the parallel readout of the pnCCD by the CAMEX, while the CTI effect depends on the detector row due to the row-by-row charge transfers. The two corrections are therefore interdependent and one correction can counterbalance the other. A possible solution is to consider an energy calibration at the pixel level. This approach requires to illuminate the detector uniformly with multiple energy lines and to have a large statistics of photons by pixel. This would be in principle possible using the fast ECC calibration method but practically impossible with the limited time dedicated for calibration during in-flight operation. The alternative method considered for MXT is to perform an iterative process and to progressively get the absolute set of calibration parameters. I investigated this approach to determine the performance benefits and to evaluate the number of

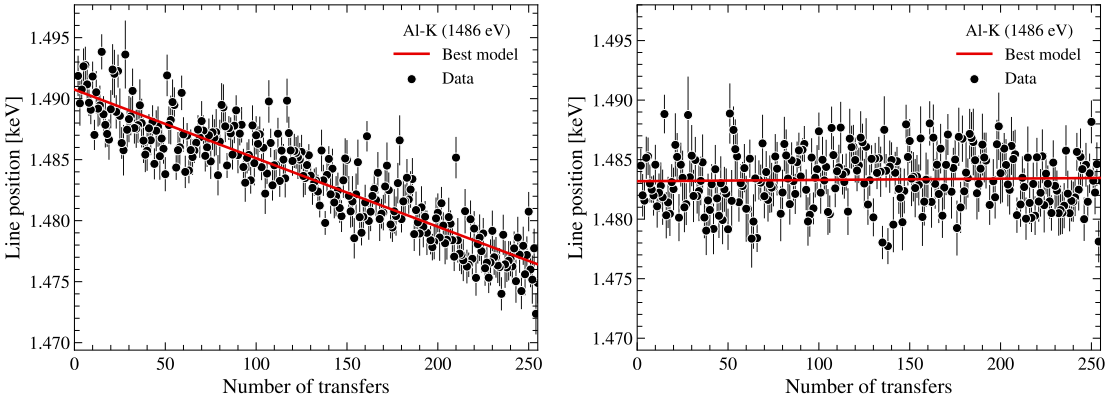

Figure 4.38: CTI determination for the Al-K lines during the iteration process. The left and right panels show the line center position as a function of transfer number for iteration 0 and 1, respectively. The symbols are identical to those of the left panel of Fig. 4.35.

iterations needed to achieve the best possible reduced data products. This work is part of the effort to improve the calibration process that will be applied to MXT observational data.

For the initial iteration (iter0), the CTI_0 is assumed to be null or equal to the values from older calibrations. The raw ADU data are corrected from the CTI_0 and then an energy calibration is performed on the CTI-corrected raw ADU data. The CTI_1 is finally determined on the already CTI-corrected and calibrated data. Note that the CTI_1 obtained here is a relative CTI that depends on the CTI_0 assumed for the initial iteration. For each iteration, the "total" CTI_{total} of the system is therefore the product of previously determined CTIs.

For the next iteration (iter1), the raw ADU are corrected by the product of $CTI_0 \times CTI_1$ and the same steps are performed as for iter0.

The iteration loop is ended when the difference of the set of parameters (CTI, gains, offsets) between two iterations is less than the expected accuracy.

We performed on Panter data an iterative energy calibration of the MXT FM instrument. We found that after one iteration the variation in the set of parameters was very small, with a CTE value of about $10^{-7} - 10^{-6}$ and constant over the energy range. The evolution of the relation (line center as a function of E) used to determine the CTI is shown in Figure 4.38 for iter0 (left panel) and iter1 (right panel). We can clearly see that the relation evolves between the two iterations and that for iter1 the line center positions are identical for all detector

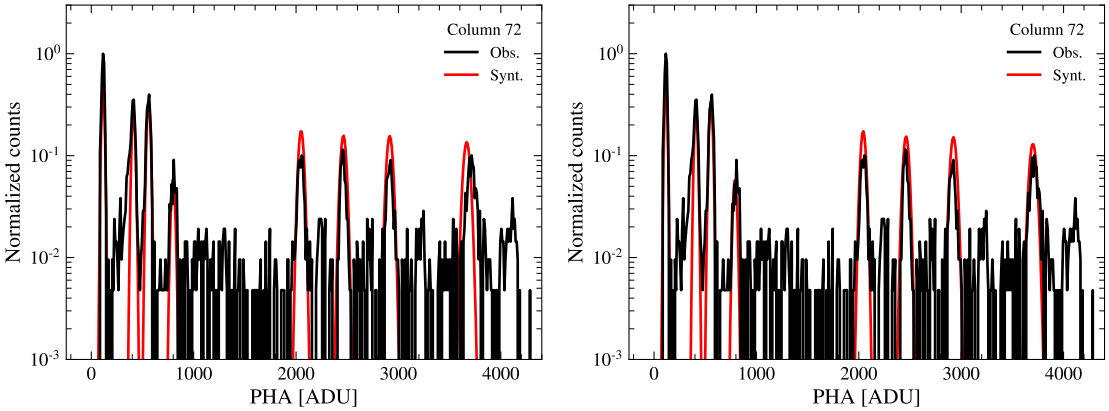

Figure 4.39: Example of an ECC calibration using a linear (left panel) and a non-linear (right panel) model. The observed spectrum (black) is correlated with the synthetic spectrum (red) and the maximum of correlation after the optimization gives the set of parameters used for the energy calibration.

rows. This confirms the efficiency of the CTE correction and its estimation method, and demonstrates that the CTI_0 determined at iter0 is already close to the "absolute" value of the system.

4.3.2.10 Non-linear calibration

The calibrations described so far were all based on the assumption of a linear response of the MXT detection chain. In Sect. 4.3.2.5 and 4.3.2.6, a possible small non-linearity of the detection chain in the high energy range of MXT ($E > 5$ keV) was discussed. Given the effective area of MXT (see Fig. 4.48) and the fact that the afterglow emission is the most intense for $E < 2$ keV, it appears that a non-linearity of the detection chain at $E > 5$ keV would not have a strong impact on the scientific performances of MXT. However, because the energy calibration during in-flight operation will use a ^{55}Fe radioactive source emitting two spectral lines at 5.9 keV and 6.5 keV (Sect. 4.4.1), it is interesting to quantify the non-linearity and its possible impact on the calibration.

The version of ECC (v7.3) used to perform the linear calibration also includes the possibility to run a non-linear (NL) calibration. It is defined as follows

$$E_{i,j} = \frac{(\mathrm{PHA}_{i,j} - O_j)}{G_j} + \mathrm{nonl}(\mathrm{PHA}_{i,j} - O_j)^2, \tag{4.6}$$

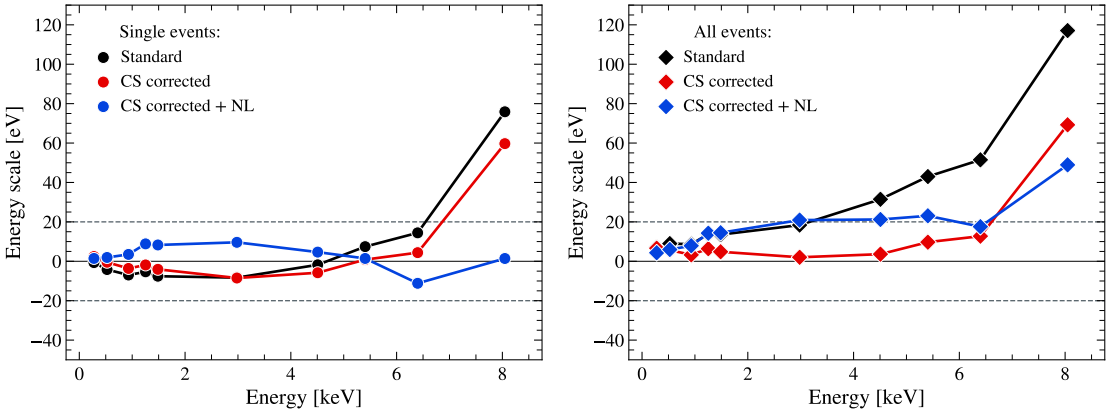

Figure 4.40: Energy scale as a function of energy. Circles (*left panel*) are for singles and diamonds (*right panel*) for all events (singles, doubles, triples and quadruples). Black, red and blue colors represent the performance without the CS correction, with the CS correction, and for a non-linear calibration, respectively. The dashed gray line shows the instrument requirement.

where $E_{i,j}$ is the energy in keV of the pixel, G_j the gain in ADU/keV, $\mathrm{PHA}_{i,j}$ the pulse height value in ADU, O_j the offset in ADU, and nonl the non-linearity in keV/ADU^2.

Using a model with additional free parameters (i.e., 2 to 3) substantially increases the number of combinations to be tested for finding the best-fit parameters. To help ECC return a calibration in a reasonable time and avoid possible local solutions, I investigated the non-linearity using the calibrated data sets with a linear calibration. ECC was then ran with initial conditions around the determined NL value and the previous gains/offset estimates returned by the linear calibration. A direct comparison between the linear and NL calibration for a given column of the pnCCD is shown in Fig. 4.39. The benefit of using an NL model is clearly observed on the Cu-K lines (PHA $\sim$ 3 600 ADU) where the NL model fits better the observed line position (right panel) compared to the linear model (left panel). We found a non-linear term of about -10^{-8} keV/ADU^2. In addition, the linear (i.e., gains) and constant (i.e., offsets) coefficients are slightly increased and decreased, respectively.

The NL calibration was then applied to the raw ADU data sets using eq. 4.6. The energy scale and energy resolution as a function of E were finally calculated in a similar way to the linear calibration (Sect. 4.3.2.5 and 4.3.2.8). The energy scale between the standard, linear and NL calibration for the single and all events spectra is visible on Fig. 4.40. The results for single events shows that the energy scale

is significantly improved for the Cu-K and becomes compliant with the ±20 eV requirement of the mission. However, for all events, the benefit on the energy scale is more limited for the Cu-K line. Furthermore, in the low energy range, the positions of the lines tend to be moved away from their expected positions. This is probably due to the higher gain values found for this calibration compared to the standard and CS corrected calibration, and the fact that NL factor did not sufficiently compensate for these higher gains in the intermediate energy range. A piecewise solution, linear at low energy range and quadratic at high energy range, would possibly be more adapted to these data but more complex to implement. Finally, the energy resolution is mostly improved for the Cu-K line with single events (−10 eV) but is marginal for the other lines independently of the event type.
In any case, since the GRB afterglow emission is low above 2 keV (e.g., Fig. 3.14) and the MXT effective area is very small at $\gtrsim 2$ keV (< 8 cm^2, see Fig. 4.48), this non-linearity should have only a minor impact on data reduction and scientific exploitation.
The numerical values derived for all calibrations are provided in Appendix 4.3.2.E for the energy resolution and in Appendix 4.3.2.F for the place scale.

4.3.2.11 Conclusion

During three weeks, we performed end-to-end tests to fully characterize the MXT instrument in its flight configuration and under space-like temperature and vacuum conditions at the MPE Panter facility. In this section, we investigated the spectral performance of the MXT instrument with a series of measurements collected from 0.28 keV up to ~ 9 keV for focused and defocused sources. First, we found that the pattern fractions for all multiplicities are in good agreement with the theoretical expectations obtained from MC simulations, confirming the high-quality of the collected data. We demonstrated the very good homogeneity and stability over time of the detector and its electronic chain regarding the dark noise and the calibration parameters. Then, we evaluated the spectral performance of MXT by optimizing the energy calibration process, especially by reducing the charge sharing effect induced by the LLT used to extract X-ray events. We verified the accuracy of our energy calibration process by measuring the positions of the calibrated lines with respect to their theoretical positions, and showed that the line positions are

within the ± 20 eV instrument requirement up to ~ 6 keV for single and all events. Above this energy, the trend of the line positions suggests a small non-linearity in the electronic readout chain. Moreover, we found an energy resolution at 1.5 keV better than the MXT requirement of 80 eV for single and all events, and determined a CTI between $10^{-5} - 10^{-4}$ for the current detector state. Finally, we confirmed the ability of MXT to detect photons down to 200 eV and up to 10 keV. The end-to-end campaign has demonstrated the excellent spectral performance of MXT and its compliance with the instrument requirements, offering promising prospects for future science with MXT on GRBs and the time-domain astrophysics.

Appendices

4.3.2.A Panter X-ray fluorescence lines

Figure 4.41: Individual X-ray fluorescence lines collected at Panter facility between 0.2-10 keV. Each color represents a different energy line(s) produced by the X-ray tube. The C-K and O-K energy lines show a strong background signal due to the *Bremsstrahlung* emission produced by the X-ray tube. The energy line at 1.8 keV is the characteristic radiation emitted by the ionization of the X-ray tube anode (tungsten, W-M), visible in particular for the C-K and Cu-L spectral lines.

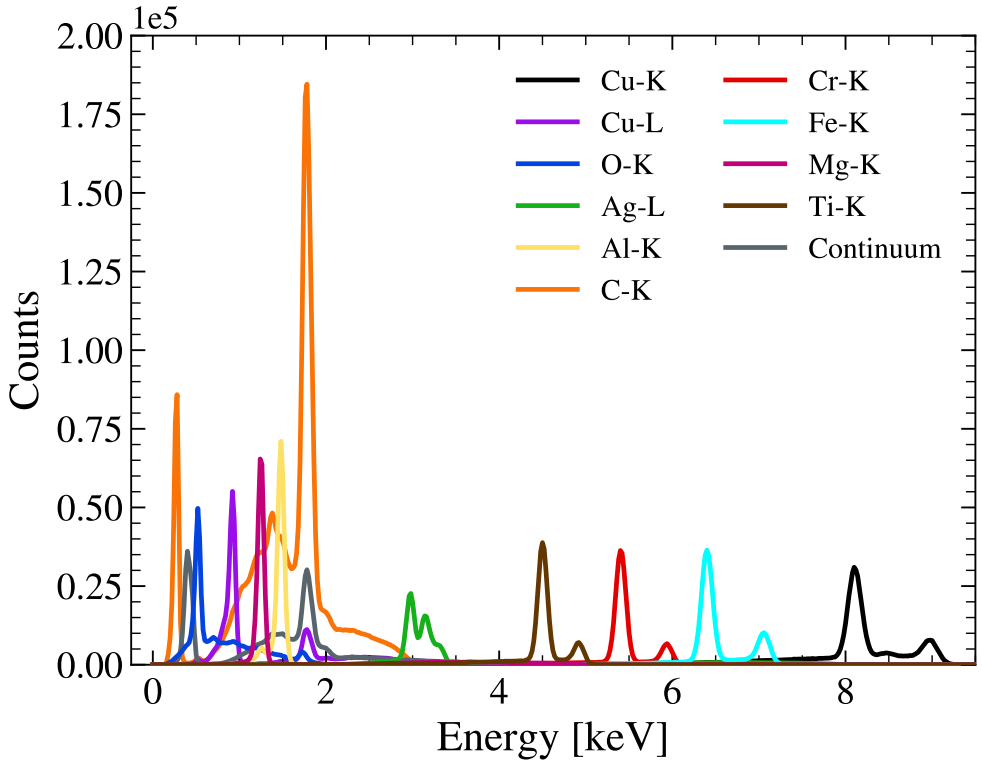

4.3.2.B Count maps of in-FOV PSF positions

Figure 4.42: Count map obtained from the sum of the nine positions inside the detector FOV separated by 15 arcmin introduced in Fig. 4.28 and visible individually in Fig. 4.43.

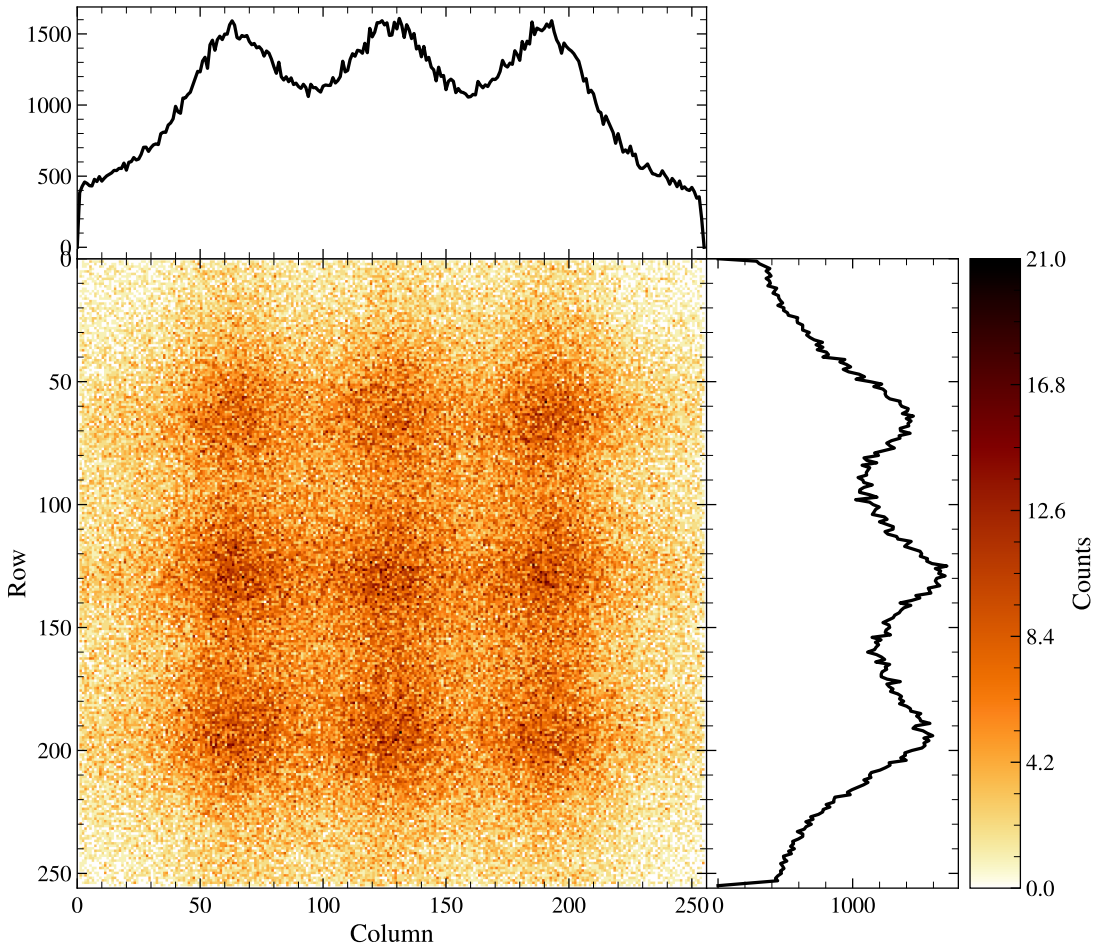

Figure 4.43: Count map of the nine positions inside the detector FOV presented in Fig. 4.28. The central panel shows the position P0 with the typical MXT PSF produced by the lobster-eye configuration optics of MXT. The number of photons per pixel in the central core of the PSF is about 10 and the PSF FWHM is about 11 arcmin.

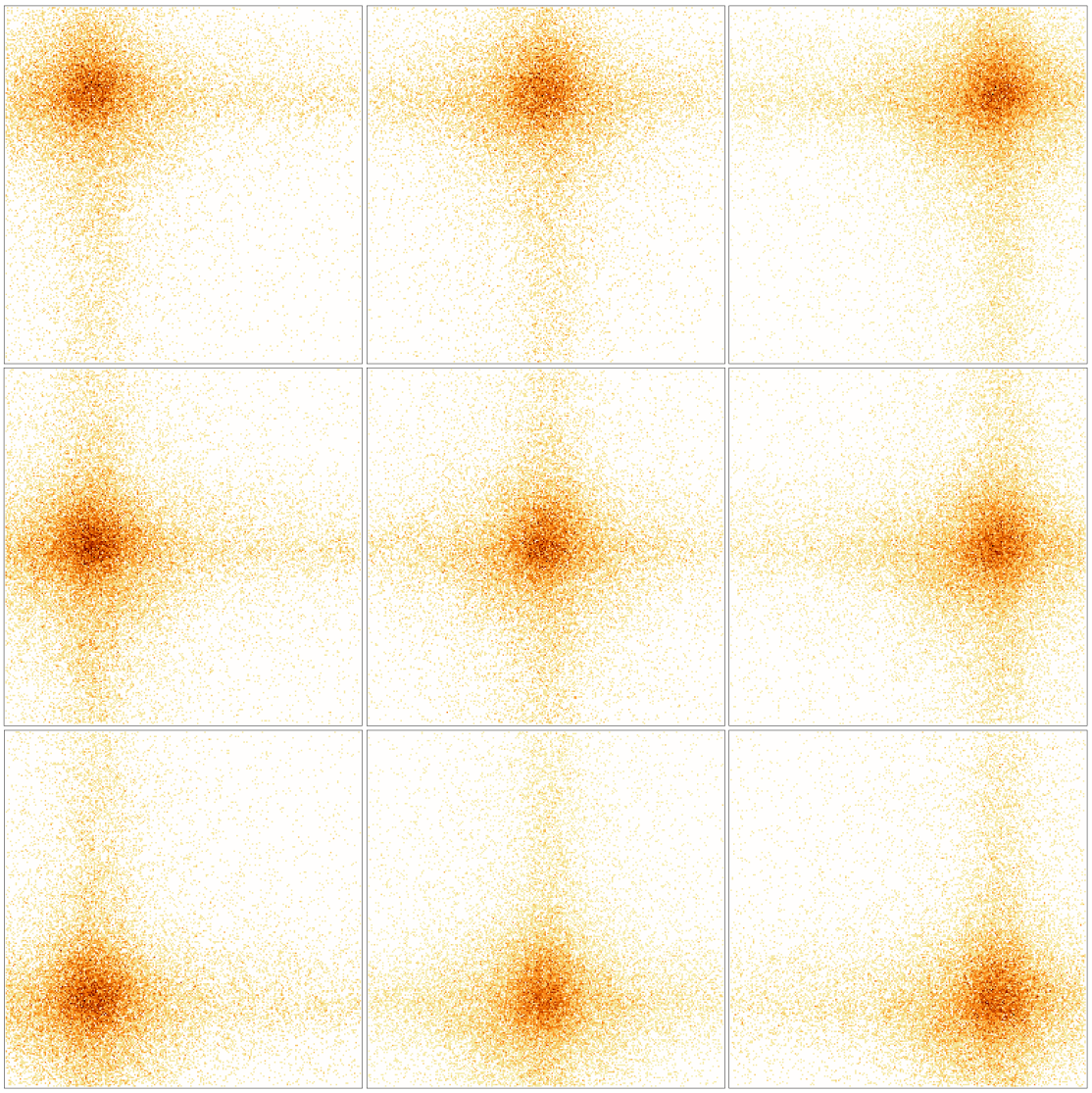

4.3.2.C Spectrum of all events

Figure 4.44: Spectrum of all events calibrated in energy and corrected from charge sharing effect. The red curve is the best-fit model found and used to determine the MXT energy resolution.

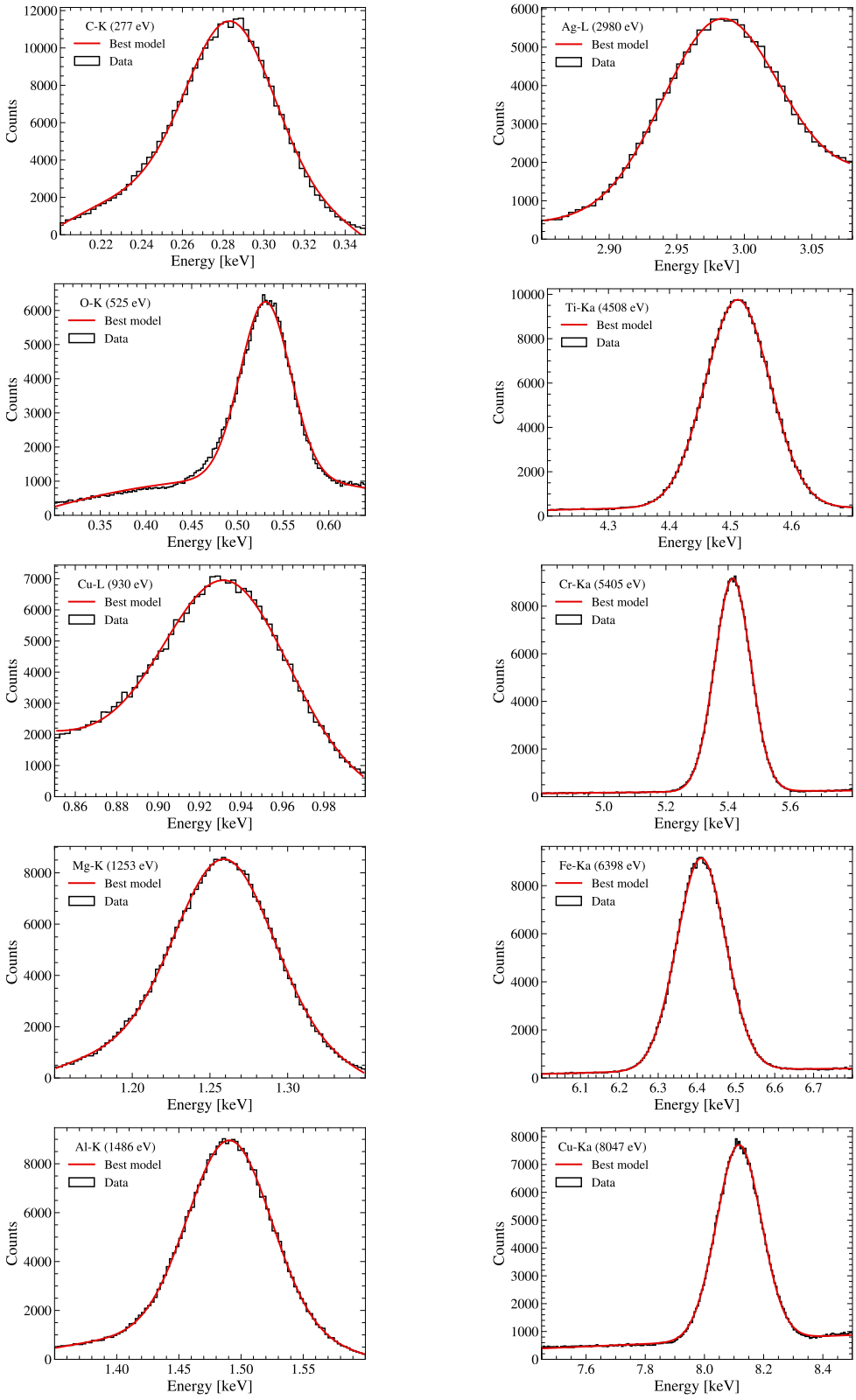

4.3.2.D Charge transfer inefficiency estimates

Figure 4.45: Line center position as a function of transfer number for all energy lines. Circles represent peak positions determined by a Gaussian fit on row spectra. The best-fit model obtained to derive the CTI is shown as a red line.

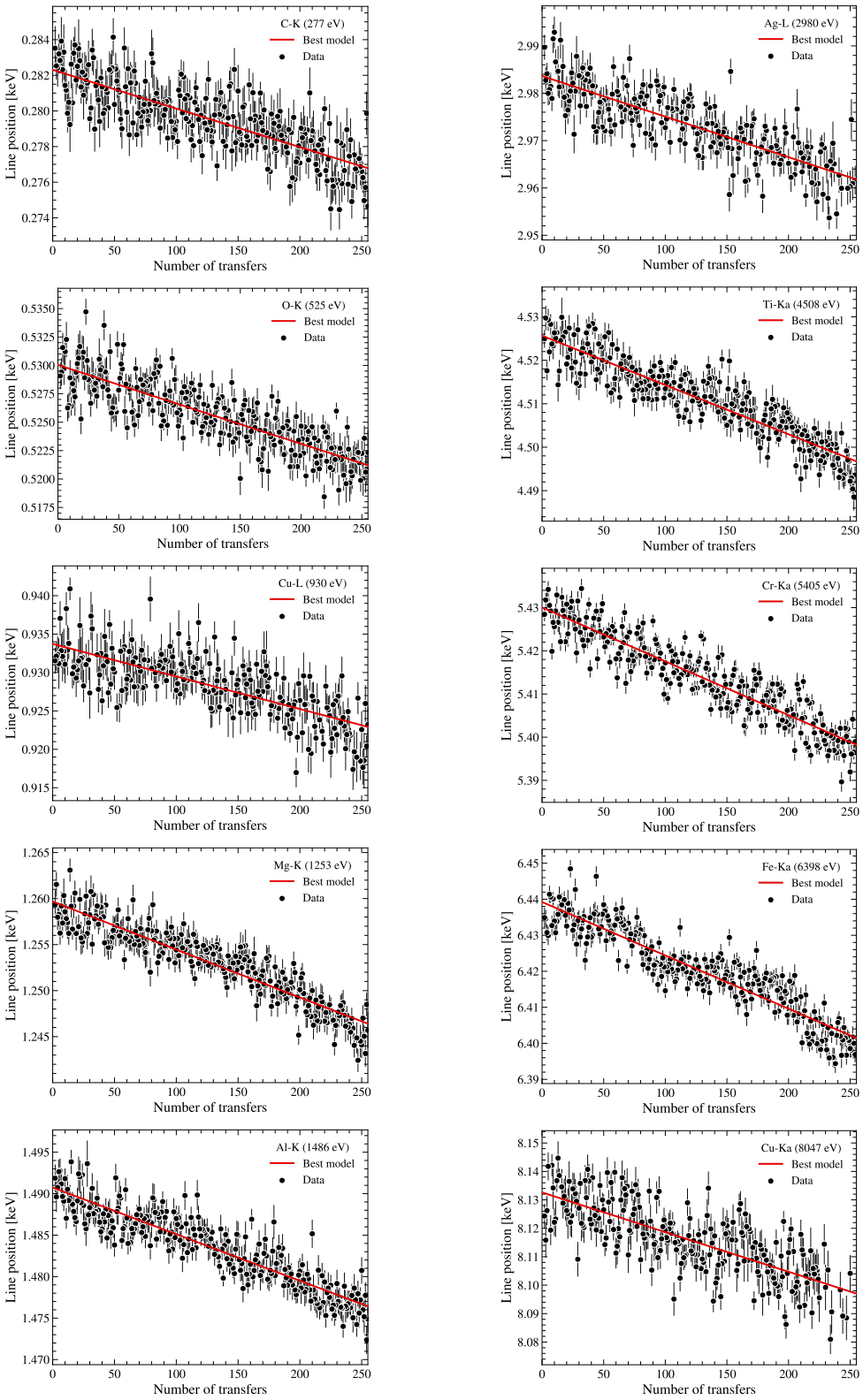

4.3.2.E Energy resolution estimates

Table 4.4: Energy resolution (ΔE) for Panter spectral lines and using different energy calibrations: standard (STD), CS corrected (iter0), CTE and CS corrected (iter1), and non-linear (NL). The FWHM errors are given at 1σ.

Energy (keV)	ΔE (eV) STD	ΔE (eV) iter0	ΔE (eV) iter1	ΔE (eV) NL
0.277	50.1 ± 2.1	48.4 ± 1.8	48.1 ± 1.6	49.5 ± 2.5
0.525	60.0 ± 0.8	60.2 ± 0.8	60.0 ± 0.8	61.0 ± 0.8
0.930	64.2 ± 1.2	65.2 ± 1.2	65.3 ± 0.9	68.1 ± 1.5
1.253	72.2 ± 1.8	70.3 ± 1.6	69.2 ± 1.4	68.8 ± 1.2
1.486	73.6 ± 0.9	73.3 ± 0.9	72.7 ± 0.6	74.1 ± 0.8
2.980	97.2 ± 5.0	96.2 ± 4.5	96.5 ± 4.6	95.4 ± 3.2
4.508	117.6 ± 0.8	117.2 ± 0.8	115.5 ± 0.7	115.4 ± 0.7
5.405	129.6 ± 0.5	129.2 ± 0.5	127.3 ± 0.5	126.6 ± 0.5
6.398	140.4 ± 1.0	139.6 ± 0.8	136.9 ± 0.8	136.0 ± 0.9
8.047	167.5 ± 0.9	166.7 ± 0.9	164.5 ± 1.0	155.6 ± 0.7
0.277	56.2 ± 1.3	49.6 ± 1.0	49.5 ± 0.9	49.8 ± 1.7
0.525	74.2 ± 0.5	64.8 ± 0.6	64.5 ± 0.6	64.2 ± 0.6
0.930	79.9 ± 1.1	70.5 ± 1.0	70.4 ± 0.8	71.2 ± 1.1
1.253	85.2 ± 1.2	73.8 ± 0.8	73.4 ± 0.8	74.0 ± 0.8
1.486	91.0 ± 0.7	79.5 ± 0.5	79.3 ± 0.4	79.1 ± 0.4
2.980	110.4 ± 2.4	100.6 ± 2.3	99.7 ± 2.0	102.2 ± 1.6
4.508	137.2 ± 0.5	124.7 ± 0.3	123.0 ± 0.4	124.2 ± 0.4
5.405	148.7 ± 0.3	136.7 ± 0.2	134.8 ± 0.2	135.7 ± 0.2
6.398	159.9 ± 0.4	149.0 ± 0.4	146.6 ± 0.3	147.4 ± 0.3
8.047	187.4 ± 0.5	179.3 ± 0.5	176.9 ± 0.4	174.7 ± 0.4

4.3.2.F Energy line position estimates

Table 4.5: Reconstructed line positions for Panter spectral lines and using different energy calibrations: standard (STD), CS corrected (iter0), CTE and CS corrected (iter1), and non-linear (NL). The energy scale in eV unit is provided in parenthesis ($E_{\text{reconstructed}} - E_{\text{incident}}$).

E_{incident} (keV)	$E_{\text{rec.}}$ (keV) STD	$E_{\text{rec.}}$ (keV) iter0	$E_{\text{rec.}}$ (keV) iter1	$E_{\text{rec.}}$ (keV) NL
0.277	0.276 (-1)	0.279 (2)	0.280 (3)	0.278 (1)
0.525	0.521 (-4)	0.525 (0)	0.525 (0)	0.527 (2)
0.930	0.923 (-7)	0.926 (-4)	0.928 (-2)	0.933 (3)
1.253	1.248 (-5)	1.251 (-2)	1.252 (-1)	1.262 (9)
1.486	1.478 (-8)	1.482 (-4)	1.483 (-3)	1.494 (8)
2.980	2.972 (-8)	2.972 (-8)	2.972 (-8)	2.990 (10)
4.508	4.506 (-2)	4.502 (-6)	4.502 (-6)	4.513 (5)
5.405	5.412 (7)	5.406 (1)	5.404 (-1)	5.406 (1)
6.398	6.412 (14)	6.402 (4)	6.400 (2)	6.387 (-11)
8.047	8.123 (76)	8.107 (60)	8.099 (52)	8.048 (1)
0.277	0.284 (7)	0.284 (7)	0.284 (7)	0.281 (4)
0.525	0.534 (9)	0.531 (6)	0.531 (6)	0.531 (6)
0.930	0.939 (9)	0.933 (3)	0.934 (4)	0.938 (8)
1.253	1.267 (14)	1.259 (6)	1.261 (8)	1.267 (14)
1.486	1.500 (14)	1.491 (5)	1.492 (6)	1.500 (14)
2.980	2.998 (18)	2.982 (2)	2.984 (4)	3.001 (21)
4.508	4.539 (31)	4.512 (4)	4.513 (5)	4.529 (21)
5.405	5.448 (43)	5.415 (10)	5.416 (11)	5.428 (23)
6.398	6.449 (51)	6.411 (13)	6.411 (13)	6.416 (18)
8.047	8.164 (117)	8.116 (69)	8.112 (65)	8.096 (49)

4.4 Preparation of MXT observations

In this section, I report my preliminary analysis regarding the preparation for MXT data reduction after launch. In particular, the section discusses the energy and flux calibration, and CTI modeling that will be essential to reduce and obtain high quality data over time. Optimized data reduction will ensure that the science performance of MXT, including the localization of GRBs and the ability to measure $N_{H,X}$ remains robust during the mission.

4.4.1 In-flight energy calibration

As introduced in Sect. 4.1.3, the Calibration Wheel Assembly disposes of one position to fully illuminate the detector with a ^{55}Fe source. The source will be placed in front of the detector for calibration purposes at each Earth occultation during the time outside the South Atlantic Anomaly. This corresponds to about 40 min per orbit.

The radioactive source is encapsulated in a package of Al behind a beryllium window. The source produces two major spectral lines at 5898 eV (Mn-Kα) and 6490 eV (Mn-Kβ). The main disadvantage is that the source has a 2.7 yr half-life which is quite short compared to the expected 5 yr lifetime of SVOM and the additional delays before launch. Moreover, the source activity was limited to 1 MBq due to exportation rules to China. The option of direct rather than indirect illumination was chosen to maximize the count rate given its rapidly decreasing activity with time but with the disadvantage of having only two closed spectral lines.

During the end-to-end test at Panter, four data sets were collected at the nominal temperature with the radioactive source illuminating the detector. The four data sets were stacked to increase the statistic and obtain a single file of about 2.1 ks of illumination. The spectrum produced by the radioactive source is visible on the left panel of Fig. 4.46. In addition to the two expected radioactive lines (Mn-Kα, Mn-Kβ), three significant spectral lines were also detected. The line at 1.5 keV was identified as a byproduct of the source produced by the fluorescence of the aluminum housing (Al-K). The doublet at $\sim$ 3 keV was spotted as the spectral lines of Ag-Lα (3 keV) and Ag-Lβ (3.2 keV) but given that the FPA design does not

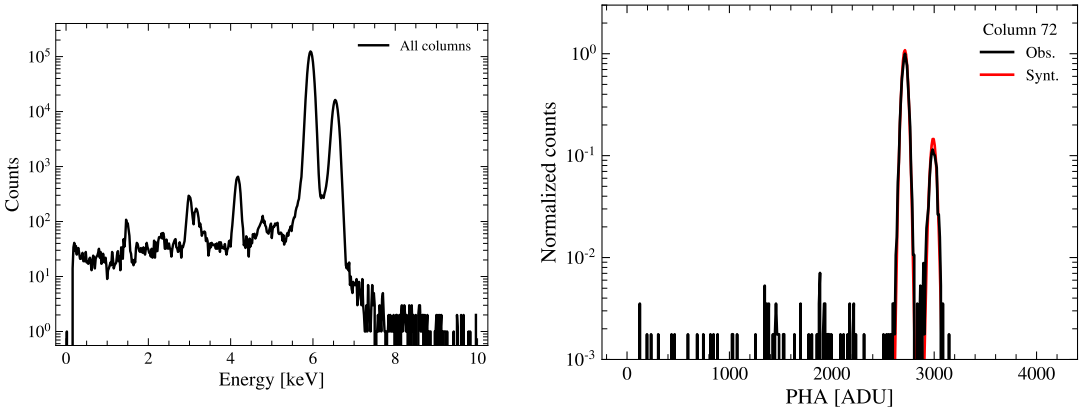

Figure 4.46: Spectrum of the ^{55}Fe radioactive source on board MXT. *Left panel:* Example of the source spectrum calibrated in energy. *Right panel:* ECC calibration of column 72 using the radioactive source and a synthetic spectrum with two lines. The observed spectrum is in black and the synthetic model convolved by ECC in red.

contain silver, this was surprising. It was later confirmed by the manufacturer of the source (Eckers&Ziegler) that the brazing solder contains a significant fraction of silver. Therefore, the doublet is the Ag-L fluorescence line generated in the brazing solder of the ^{55}Fe housing. Finally the spectral line at 4.7 keV corresponds to the Si-escape peak of Mn-Kα ($5890 - 1750$ eV).

To study the performance of the in-flight calibration using the ^{55}Fe source, ECC was run considering two models. One is based on the two main lines (Mn-Kα, Mn-Kβ) of the source, and the other considering the two main lines plus the Si-escape peak to potentially benefit from the low count regime capacity of ECC. At this moment, both configurations have failed and do not provide a realistic set of calibration parameters. Although it appeared that the intensity of the Si-escape fraction was significant (left panel of Fig. 4.46), ECC was not capable of constraining the model using this peak. This is because the number of counts is less than the minimum requirement of ECC once a given column is considered (e.g., right panel of Fig. 4.46). A simulated data set with a larger statistics might help to understand if this line can constrain the ECC calibration. An alternative approach was tested by forcing the offset to be constant at the average value of the Panter calibration offsets, i.e., 12 eV. (Sect. 4.3.2.6). In this case, ECC was able to determine a set of gains with a similar trend to the one observed in Fig. 4.33 for the Panter calibration. To test the energy calibration, all the data sets of Panter were calibrated with the calibration parameters derived from the

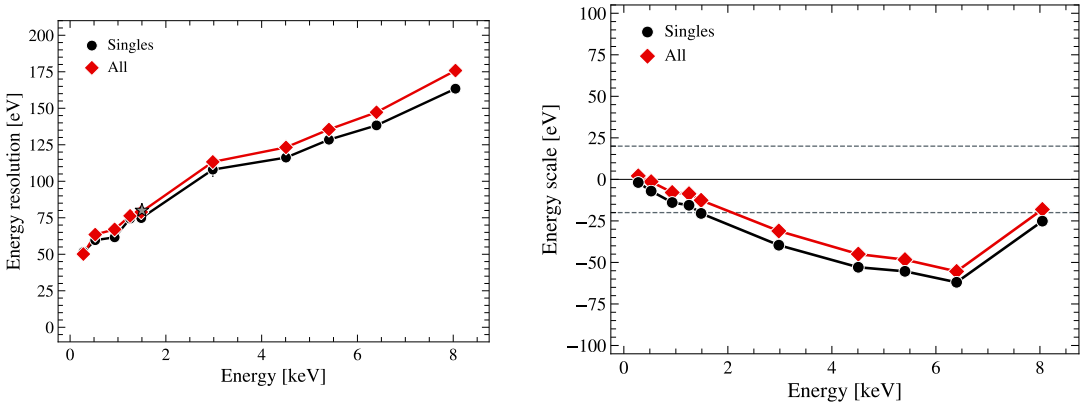

Figure 4.47: Energy resolution (left panel) and energy scale (right panel) as a function of energy for Panter spectral lines calibrated with the on board ^{55}Fe source. The black circles are single events and red diamonds show all events performance. The gray dashed line and the star are the MXT instrument requirements.

^{55}Fe source. The energy resolution and the energy scale as a function of energy is shown in Fig. 4.47. The energy resolution was slightly degraded but consistent with the ones using the Panter calibration. Interestingly, the energy scale showed a similar trend to Fig. 4.34, where a linear trend is observed up to 6 keV but with an increasing offset from $y = 0$. This is likely due to the underestimation of the mean value of the gain ($\sim$ 0.02 eV/ADU), producing an increasing shift of the peak position with E. In other words, ECC was able to find the dispersion of the gain between columns but not its absolute value. If no prior was known on the offset, the results were similar by constraining the offset to 0.

This offers the possibility of performing a calibration with a two-step algorithm where (i) ECC is run to find the relative gains assuming an average offset (zero or from a previous calibration) on the raw ADU calibration data sets, and (ii) ECC is rerun on the combined ADU spectrum of the 256 columns corrected for column gain dispersion to find the average gain and offset. Since the combined spectrum has a larger Si-escape line (Fig. 4.46), a 3-line model could better constrain the average gain and offset values. In this approach, only the dispersion of the gains can be recovered and not the dispersion of offsets. The latter should only have a limited impact on the calibration. This is because the main contribution of the offsets and their dispersion is corrected during the image data reduction using the dark frames (Sect. 4.2.1.1). The residual offsets and their dispersion are thought to be caused by variations (e.g., temperature) during the data acquisition compared to the dark measurements. In contrast, the dispersion of the gains is corrected

for the first time and depends on each column. Therefore, it is expected that at first order, the gains have the strongest impact on the calibration performance. This is further supported by the results with the ^{55}Fe calibration presented above (Fig. 4.47). Since ECC is faster than most calibration methods, even a two-step calibration should be very fast. This method has not yet been implemented and represents a possible prospect for this work. Other more traditional methods, such as the peak fitting method, should be tested to determine the strengths and weaknesses of each method and get the best possible set of calibration parameters. Complementary to the on board radioactive source, MXT will observe every six months during 10 ks a well-known high-energy astronomical source. The source needs to be constant in time with resolvable lines to be able to track the instrument evolution with time. For this purpose Supernova Remnants (SNRs) are ideal sources in the 0.3-2.0 keV bandpass. The most commonly used sources are the Galactic SNR Cas-A, the Large Magellanic Cloud remnant N132D and the Small Magellanic Cloud remnant 1E 0102.2-7219 (E0102). The E0102 SNR seems the most suitable source to calibrate MXT in its low bandbass (0.5 to 1.5 keV) due to the uniform morphology, small size ($r \sim 24$ arcsec) and simple X-ray spectrum of this source. ECC seems particularly well adapted to calibrate X-ray detectors based on SNR spectra since it is able to take into account the complete spectrum shape (energy lines and the thermal emission). Finally, it is worth noting that the International Astronomical Consortium for High Energy Calibration (IACHEC)[8] is a working group trying to develop a (flux and energy) calibration standard for X-ray astronomy using a cross-calibration study involving the instruments on board Chandra, Suzaku, *Swift* and XMM-Newton (e.g., Plucinsky et al. 2012, 2017). Their standard spectral model of E0102, combined with the final MXT performance obtained at Panter, could provide an interesting starting point to better predict and improve the MXT in-flight calibration method.

4.4.2 Effective area modeling

The MXT effective area is the product of the MOP effective area and the QE of the pnCCD. The effective area of the MOP FM was primarily determined independently at Panter in January 2021. Due to experimental difficulties during the Soleil test campaign discussed in Sect. 4.3.1, the FM detector QE was not

[8] https://iachec.org

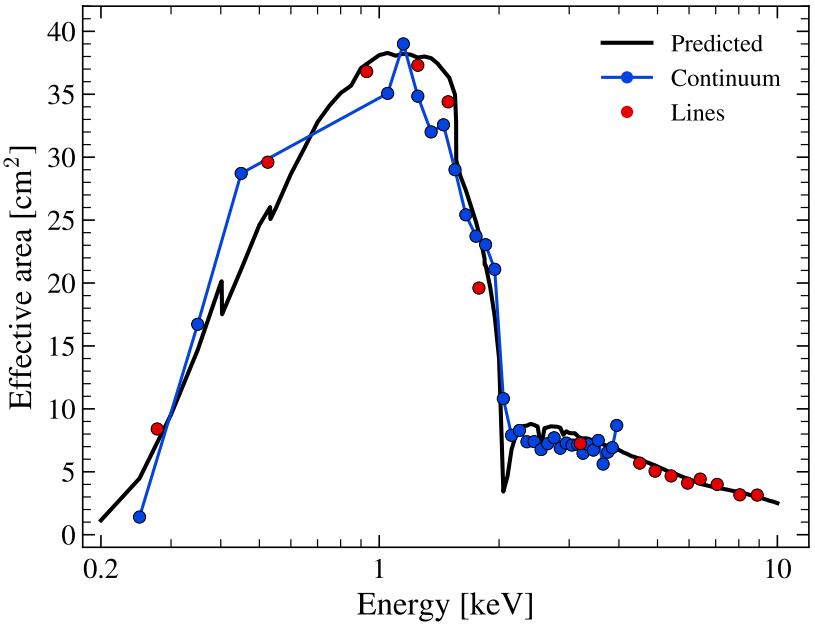

Figure 4.48: Effective area as a function of energy for the MXT FM instrument. The red circles are values obtained from fluorescence energy lines and blue circles from a continuum spectrum, all measured at Panter during the end-to-end test of MXT. (Courtesy of D. Willingale/University of Leicester)

measured and the model prediction of the MXT effective area is based on measurements performed by Meidinger et al. (2006). The effective area of the MXT FM was determined during the Panter campaign. Figure 4.48 shows the comparison between the predicted area and two measurement methods (spectral lines and a *Bremsstrahlung* continuum) with the Panter data sets. The (direct) measurement of the incident flux was performed using a monitor counter (silicon drift detector, SDD) available in the Panter beamline.

The method with spectral lines consists in measuring the number of photons detected by MXT in each energy line and comparing this value to the incident flux obtained from the monitor counter. The incident flux is determined using the number of photons detected by the SDD, the quantum efficiency of the SDD and a geometric conversion factor. The QE of the SDD has not yet been calibrated and a theoretical model was used instead. This increases the uncertainties of the effective area, especially at $E < 0.3$ keV where the theoretical QE is lower than 10% and could be subject to large uncertainties. The second method consists in comparing a continuum spectrum (e.g., gray line of Fig. 4.41 in Appendix 4.3.2.A) observed with MXT and the monitor counter. Both methods provided similar re-

sults and in good agreement with the predicted effective area (Fig. 4.48).
The column density along the GRB line of sight could be measured by MXT as discussed in Sect. 3.3. To obtain reliable measurements an accurate flux calibration is required, especially in the low-energy range of MXT, where the X-ray afterglow is the most intense. The uncertainties associated with the QE of the SDD and MXT used to derive the effective surface at Panter should have been improved by using the soft X-ray Metrology Beamline of SOLEIL. However, given the unrealistic values obtained during the SOLEIL campaign with the flight spare model (Sect. 4.3.1.9), the possibility of improving the QE before launch is less and less probable. For this reason, MXT will perform an additional flux calibration after launch. This could be achieved using the well-known previous sources mentioned in Sect. 4.4.1 (Plucinsky et al. 2017) or with the Crab Nebula. The Crab Nebula is a strong X-ray emitter and can be well modeled by an absorbed power law. Finally, although this source is known to have time-variable emissions, many multi-mission cross-calibration studies provide up-to-date information on its flux. For these reasons, the Crab Nebula is an excellent source for testing and calibrating the effective area of MXT.

4.4.3 CTI modeling

The excellent quality of the data collected at Panter allowed to derive a CTI model with E for the current state of the detector (see Sect. 4.3.2.7 and Fig. 4.35). During in-flight operation and in spite of the camera shielding, the detector will undergo space radiations (e.g, galactic cosmic rays or solar particles) that will degrade the performance of the detector and its electronic detection chain over time. The evolution of the spectral performance will be carefully tracked by spectral calibration measurements during the mission. The 10 MeV-equivalent proton dose is expected to be $1 \cdot 10^{10}$ protons/cm^2 after 5 years of mission. This will create displacement damage in the silicon detector causing dark current increase and charge trapping during the transfer. Both will increase the effective LLT which is essential for a fast source localization. Theoretical studies currently predict that the low-energy threshold of 200 eV can be maintained during the mission lifetime.
To verify and confirm the theoretical model of CTI and possible temporary effects of space radiations on the electronics, a proton test campaign was initiated. The flight spare model and its cold front-end electronics were firstly irradiated at the

ARRONAX facility[9] in June 2022. Half of the detector and both CAMEXs were illuminated by a proton beam to produce an equivalent dose of 3 years in-flight (i.e., $6 \cdot 10^9$ protons/cm^2). The MXT flight spare FPA was then characterized by the laboratory's composite X-ray source and data analyses are in progress. Later, for the second campaign, the detector will be irradiated again to produce 3 different damaged regions to simulate 3, 5, and 10 years of operation and preserve one region from radiations.
The laboratory X-ray tube produces a cocktail of fluorescence lines from 1.5 to 9 keV. Radiation damage is expected to increase the CTI of the detector and thus degrade the spectral performance (larger spectral resolution). In addition to the *Bremsstrahlung* emission, the X-ray source generates many spectral lines close to each other in energy. Close and broad spectral lines imply that they are probably mixed together, producing even broader spectral lines than those produced by the CTI itself. This X-ray source is therefore not well-designed to quantify the CTI as a function of energy. Given the characteristics of the soft X-ray Metrology Beamline of SOLEIL (small spot, monoenergetic lines) and the success of the first campaign, this facility represents an excellent candidate to evaluate the CTI of the 4 detector regions. Acquisition of data from 300 to 1800 eV of the control and the three irradiated regions will help improve the CTI modeling of the detector as a function of time. Finally, the possible low energy (100 to 300 eV) generated by SOLEIL could allow to better characterize the low-energy threshold of the detection chain at the end of the SVOM mission.

4.4.4 Conclusion

This section described the preliminary analysis to prepare for the on-board energy calibration of MXT. I investigated the spectral performance of MXT using data from the on-board ^{55}Fe radioactive source measured at Panter under nominal conditions. The results showed that the energy resolution was close to that derived using a more accurate calibration with multiple lines. However, the energy scale was more affected by an energy calibration using the two emission line of the radioactive source. To improve this, I proposed an alternative ECC-based method. In addition, I discussed the effective area modeling and CTI modeling. The expected CTI evolution will be explored in details during the second SOLEIL

[9] https://www.arronax-nantes.fr/

campaign and will provide key information to anticipate the spectral degradation of MXT with space radiation.

4.5 Summary and conclusion

In this chapter, I presented my work on the energy calibration of the X-ray telescope on board SVOM. As part of this study, I participated in two calibration campaigns, one with the MXT FM instrument at the Panter facility and a second with the MXT spare camera model at the SOLEIL synchrotron facility. The excellent data collected at Panter allowed us to study and evaluate in detail the spectral calibration of MXT. In this context, I significantly contributed to the development of the offline data reduction method that will be used during the in-flight operation. This treatment corrects the charge transfer inefficiency (CTI) and energy loss due to the charge sharing effect, both affecting the spectral performance. In particular, the latter is a correction based on a physical model of the phenomenon. This means that this correction could be adapted to the MXT configuration and to the evolution of the detector state. These analyses have provided a better understanding of the MXT data reduction process. A summary of the MXT data acquisition and specifically the spectral calibration procedure proposed in this chapter is presented in Figs. 4.49 and 4.50.
These analyses also demonstrated that a meticulous processing of the data can significantly improve the final products, and to be close to the intrinsic performance of the instrument. From an astrophysical perspective, it highlighted the interest of developing specific and accurate methods of data reduction in order to extract the maximum information from the raw data for scientific exploitation. MXT is now ready to be launched with detailed knowledge of the instrument and its performance. We have reached a good level of maturity regarding the data reduction and this experience will be a key aspect during flight operations.

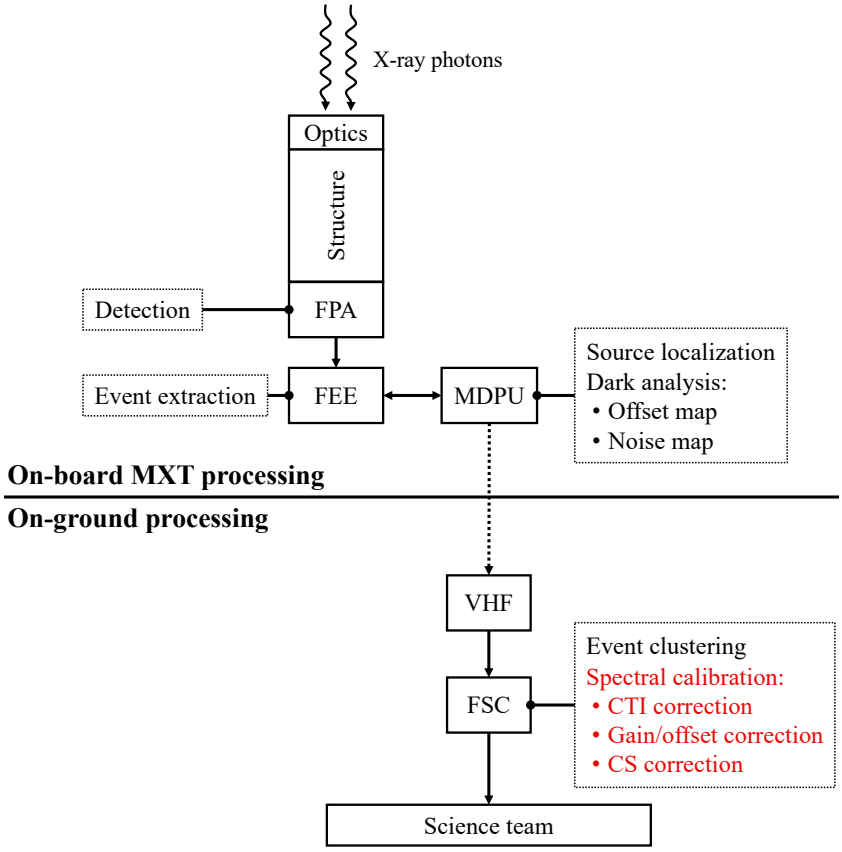

Figure 4.49: Summary of the complete MXT data acquisition chain, from X-ray photon detection (top) to reduced data delivery to the science team (bottom). The ground-based data calibration processing (red text) is described in more detail in Fig. 4.50.

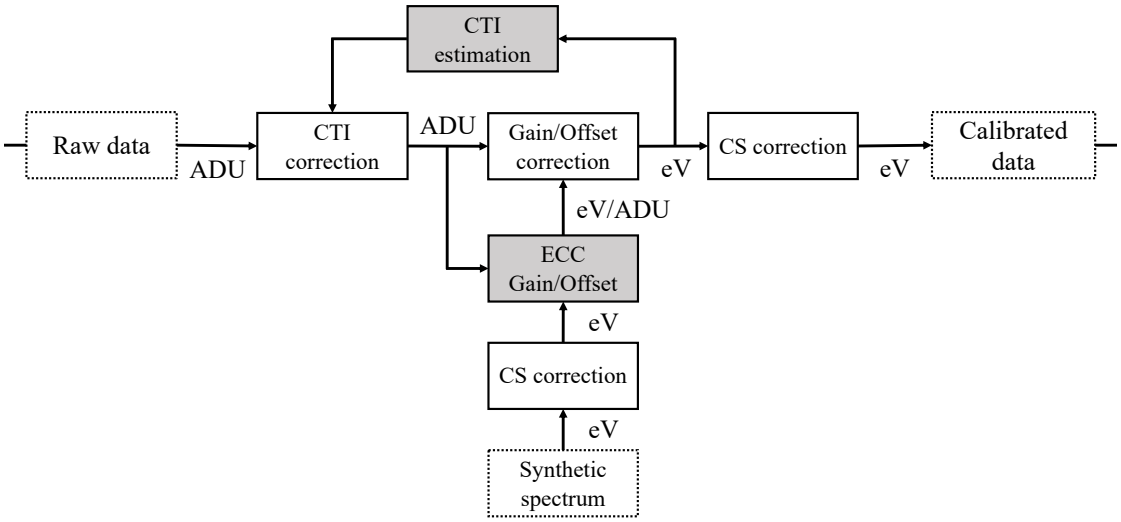

Figure 4.50: Proposed procedure for the energy calibration of MXT data by the MXT instrument center. The process starts with the raw data from the event clustering (left) and ends with the calibrated data (right). The boxes show the correction applied on the data, except the grey boxes which indicate the external process used to determine the coefficient to be applied. This process will be done offline after accumulating calibration data for typically one month.

Chapter 5

General conclusions and perspectives

Contents

This thesis was part of the scientific preparation of the upcoming SVOM mission, from the energy calibration of the onboard X-ray telescope, the development of follow-up observations of the future SVOM alerts, up to the study of the stellar density of a GRB host galaxy sample. In a more general context, this work was part of the on-going effort to better understand the progenitor and the formation mechanism of GRBs. In this chapter, I summarize the main results reported in the manuscript and the possible perspectives of this work for the coming years.

5.1 Stellar density of GRB hosts

To understand possible factors that could affect the efficiency of long GRB formation, I studied a sample of GRB hosts observed by HST with the WFC3 camera in the infrared band. This sample of host galaxies was composed mainly of *Swift*

GRBs with a redshift measurement and a location better than 5 arcsec to ensure the association between the burst and the host galaxy. The investigated property was the stellar density of GRB host galaxies at $1 < z < 3.1$. To derive this quantity, the size of each object was determined by modeling the 2D luminosity profile of the galaxy and then combined with the most robust star formation rate and stellar mass estimates of the galaxy available in the literature. After carefully controlling and quantifying the bias that selection effects and the methods might introduce, the GRB host samples were compared to a typical star formation sample observed under similar conditions. This comparison was performed by fixing the redshift and stellar mass of the objects to mitigate any possible effects of cosmic evolution or from the metallicity bias previously found for the GRB host population.
The main findings of the study are the following:

- The sample of GRB hosts at $1 < z < 2$ clearly shows a deviation towards compact and dense environments from the median value of star-forming galaxies in the field and weighted by their SFR, as previously observed for a population of GRB hosts at $z < 1$.
- The preference for a dense environment was similarly observed for host galaxies of dark and optically bright GRBs, suggesting that these properties are common to both populations.
- At $2 < z < 3.1$, the GRB hosts were observed to be more consistent with the field galaxies, suggesting a possible evolution of the bias with redshift, although in this redshift range the sample size and the prevalence of dark GRB host galaxies prevent a firm conclusion.

The main limitation of this analysis was the size of the considered GRB host sample. First, the study would benefit from a larger and more complete sample to confirm the observed trend. Since all current HST WFC3/IR archive observations were used, this would only be possible by performing new observations with for example the HST.
Then, a natural extension of this study would be to perform a similar study at $z > 3$. This could be achieved with the JWST or the ELT, which can/will provide a considerable improvement in resolution and probe the optical rest frame of galaxies at $z > 3$.
Furthermore, my queries in the HST archive database revealed that many observations with the WFC3/IR camera of GRB hosts at $z < 1$ are available.

These data could be used to further investigate the stellar density at $z < 1$ with a larger sample of GRB hosts and more resolved images than previous work. However, closer and better resolved galaxies may often require more than one Sérsic function to be correctly modeled, which further complicates the concept of galaxy size.
Finally, the study of molecular gas compactness in GRB hosts using ALMA could provide a complementary approach to study the density of the GRB environment. A similar analysis on the size and stellar density of the short GRB hosts could also be worthwhile. Given their presumed association with the merger of compact objects and the diversity of observed host galaxies, a different trend might be expected compared to the long GRB population. Improving the typical properties of the host galaxies would optimize the strategy for targeting galaxies in the large error box of gravitational wave events returned by LIGO/VIRGO and thus increase the probability of finding an electromagnetic counterpart to the event.

5.2 Follow-up of SVOM GRBs

The follow-up observations are a crucial aspect of the SVOM mission and will provide essential information on the transient sources detected by SVOM. In this manuscript, two facilities that could be used to observe the upcoming SVOM alerts were presented. Both facilities are subject to a *call for proposals* and the currently allocated observing time was granted to a large collaboration with a strong interest in the transient sky. Since SVOM is not currently in operation, these observations were performed using *Swift* alerts that provide similar well-located GRBs.
First, I presented my contribution to the development and the first results of follow-up observations using the low resolution spectro-imager MISTRAL mounted on the T193 at OHP. This telescope was proposed for the first time in ToO mode. A proposal under the leadership of SVOM was accepted with an allocated observing time suitable for 10-12 alerts. Between March and July 2022, we triggered MISTRAL for a total of 3 alerts. This allowed to improve the ToO protocol and to train the entire sequence, from operators to scientists on duty.
Then, I presented the follow-up observations obtained with the X-Shooter instrument in the framework of the *Stargate* consortium. This observing time is not under SVOM leadership but will offer a precious help to build-up the well-

characterized and complete GRB sample of SVOM.
The natural extension of this work would be to continue the effort to develop the SVOM follow-up network in order to ensure efficient and rapid observations of the future SVOM alerts.

5.3 Spectral performance of MXT

The X-ray telescope on board the SVOM satellite will systematically observe the X-ray counterpart of GRBs to improve the localization of the source, monitor its light curve, and obtain its spectrum. Prior to launch, the flight model was extensively tested and characterized to evaluate the performance of the fully assembled instrument and refine the predictions on the expected localization performance.
First, I presented my work on the energy calibration of the flight model instrument following the end-to-end test at the Panter facility. The data were calibrated and analyzed using an optimized and improved process. In particular, the charge sharing effect was corrected using a physical model of the phenomenon, which will allow us to adapt this correction during MXT operations. The results of the Panter campaign demonstrated that the spectral performance of MXT is compliant with the mission requirements.
I also participated and analyzed the results of the first campaign performed at the metrology beamline of the SOLEIL synchrotron with the MXT flight spare camera. This campaign offered the unique opportunity to characterize in details the low energy (< 2 keV) instrumental response of the camera. The results confirmed the trend of the resolution energy previously observed at higher energy and demonstrated for the first time the capability of the X-ray metrology line to test X-ray detectors between 300 to 2000 eV. In addition, the CTE determined in both campaigns allowed to build an empirical model as a function of energy for the current detector state.
The evolution of the CTE due to space radiations will be investigated during the next campaign at SOLEIL after a proton irradiation of the flight spare model. The results of this second campaign will allow to model and predict the evolution of the CTE during in-orbit operations and thus to improve the performance of MXT over time. Finally, a key aspect will be to monitor the evolution of the set of calibration parameters. This will be done with the on-board ^{55}Fe radioactive source and the observations of well-known X-ray sources. In the manuscript, a

calibration method based on the ^{55}Fe source was proposed but not yet fully implemented. Prior to launch, it would be important to validate our ability to use the on-board radioactive source to find realistic and accurate gain/offset values in order to ensure our ability to track the calibration evolution.
Through these analyses, I contributed to the development of the on-ground spectral calibration. This will allow to produce enhanced reduced data products of the future MXT observations and to optimize the scientific exploitation of the observations.

This thesis overviewed various aspects of the SVOM mission in the context of preparing the scientific exploitation of the mission. In the coming year, time-domain and multi-messenger astrophysics will enter a new era not only with the advent of the Vera C. Rubin Observatory, which promises millions of alerts per night, but also with the upgrade of the LIGO/VIRGO interferometers. The synergy of these facilities with SVOM promises significant discoveries and advances in transient sky astronomy.

Published papers

Publications

(1) *Are the host galaxies of Long Gamma-Ray Bursts more compact than star-forming galaxies of the field?*
B. Schneider, E. Le Floc'h, M. Arabsalmani, S. D. Vergani, and J. T. Palmerio 2022, A&A, 666, A14.

(2) *Spectral performance of the Microchannel X-ray Telescope on board the SVOM mission*
B. Schneider, N. Renault-Tinacci, D. Götz, A. Meuris, et al. 2022, accepted for publication in Experimental Astronomy.

(3) *Characterization of the focal plane of the Microchannel X-ray Telescope at the X-ray metrology line of the SOLEIL synchrotron for the space astronomy mission SVOM*
A. Meuris, **B. Schneider**, H. Allaire, D. Baudin, et al. 2022, accepted for publication in Nucl. Instrum. Methods Phys. Res. A.

(4) *The Scientific Performance of the Microchannel X-ray Telescope on board the SVOM Mission*
D. Götz, M. Boutelier, V. Burwitz, [...], **B. Schneider**, et al. 2022, arXiv, accepted for publication in Experimental Astronomy.

(5) *Design and performance of the camera of the SVOM Micro-channel X-ray Telescope*
A. Meuris, A. Arhancet, D. Bachet, [...], **B. Schneider**, et al. 2022, accepted for publication in Nucl. Instrum. Methods Phys. Res. A.

(6) *Metal enrichment of ionised and neutral gas of galaxies in the EAGLE simulations*
M. Arabsalmani, L. Garratt-Smithson, N. Wijers, [...], **B. Schneider**, et al. 2022, submitted to ApJ.

(7) *Analysis methods to localize and characterize X-ray sources with the Micro-channel X-ray Telescope on board the SVOM satellite*
S. Hussein, F. Robinet, M. Boutelier, [...], **B. Schneider**, et al. 2022, submitted to ApJL.

(8) *IDeF-X HDBD: Low-Noise ASIC for Imaging Spectroscopy With Semiconductor Detectors in Space Science Applications*
D. Baudin, O. Limousin, O. Gevin, [...], **B. Schneider**, et al. 2022, IEEE Trans Nucl Sci, 69, 3, 620-626.

(9) *The Infra-Red Telescope (IRT) on board the THESEUS mission*
D. Götz, S. Basa, F. Pinsard, [...], **B. Schneider**, et al. 2021, Proc. SPIE, Space Telescopes and Instrumentation 2020: Ultraviolet to Gamma Ray, 114442M.

(10) *Low star formation efficiency due to turbulent adiabatic compression in the Taffy bridge*
B. Vollmer, J. Braine, B. Mazzilli-Ciraulo, and **B. Schneider** 2021, A&A, 647, A138.

(11) *Characterization of the detection chain of the Micro-channel X-ray Telescope*
C. Francesco, A. Meuris, E. Doumayrou, [...], **B. Schneider** et al. 2020, Nucl. Instrum. Methods Phys. Res. A, 973, 164164.

GCN Circulars

(12) *GRB 221009A: OHP optical observations*
B. Schneider, C. Adami, E. Le Floc'h, et al. 2022, GRB Coordinates Network, Circular Service, No. 32753.

(13) *GRB 220611A: Host galaxy redshift from VLT/X-shooter*
B. Schneider, D. B. Malesani, J. P. U. Fynbo, et al. 2022, GRB Coordinates Network, Circular Service, No. 32595.

(14) *GRB 220623A: T193-OHP optical upper limit*
B. Schneider, D. Turpin, E. Le Floc'h, et al. 2022, GRB Coordinates Network, Circular Service, No. 32271.

(15) *GRB 211207A: VLT/X-shooter redshift*
B. Schneider, L. Izzo, D. B. Malesani, et al. 2021, GRB Coordinates Network, Circular Service, No. 31188.

(16) *GRB 211024B: Host galaxy redshift from X-shooter/VLT*
A. Ugarte Postigo, **B. Schneider**, D. B. Malesani, et al. 2022, GRB Coordinates Network, Circular Service, No. 31800.

(17) *GRB 221009A: Redshift from X-shooter/VLT*
A. Ugarte Postigo, L. Izzo, G. Pugliese, D. Xu, **B. Schneider**, et al. 2022, GRB Coordinates Network, Circular Service, No. 32648.

(18) *GRB 220427A: VLT/X-shooter photometry*
A. Ugarte Postigo, H. Fausey, D. A. Kann, [...], **B. Schneider**, et al. 2022, GRB Coordinates Network, Circular Service, No. 31967.

(19) *GRB 220708B: T193-OHP optical upper limit*
D. Turpin, C. Adami, **B. Schneider** et al. 2022, GRB Coordinates Network, Circular Service, No. 32360.

Poster

(20) *9^{th} international conference on new developments in photodetection (NDIP), Troyes, 2022* (see below)

Characterization of the focal plane of the Microchannel X-ray Telescope on the Metrology beamline of the SOLEIL synchrotron for the space astronomy mission SVOM

B. Schneider[1], A. Meuris[1], H. Allaire[1], D. Baudin[2], I. Cojocari[1], P. Da Silva[4], E. Doumayrou[1], P. Ferrando[1], D. Götz[1], P. Laurent[1], M. Lortholary[1], N. Meidinger[3], P. Mercère[4], T. Pichon[1], F. Pinsard[1], M. Prieur[1], L. Provost[1], D. Renaud[1], N. Renault-Tinacci[1], T. Tollet[1], F. Visticot[1].

[1]DAP-AIM, IRFU, CEA, Université Paris-Saclay, CEA Saclay; [2]DEDIP, IRFU, CEA, Université Paris-Saclay, CEA Saclay, 91191 Gif-sur-Yvette, France;
[3]Max-Planck-Institut für Extraterrestrische Physik, 85748 Garching, Germany;
[4]SOLEIL synchrotron, L'Orme des Merisiers – Saint-Aubin, BP48, 91192 Gif-sur-Yvette cedex, France.

INTRODUCTION

The SVOM mission

The Chinese-French *Space Variable Object Monitor* (SVOM) mission to be launched in 2023 includes four space instruments and three ground based robotic telescopes for the study of the gamma-ray bursts and more generally to play a key role in the era of the time domain astrophysics and multi-messenger astrophysics.

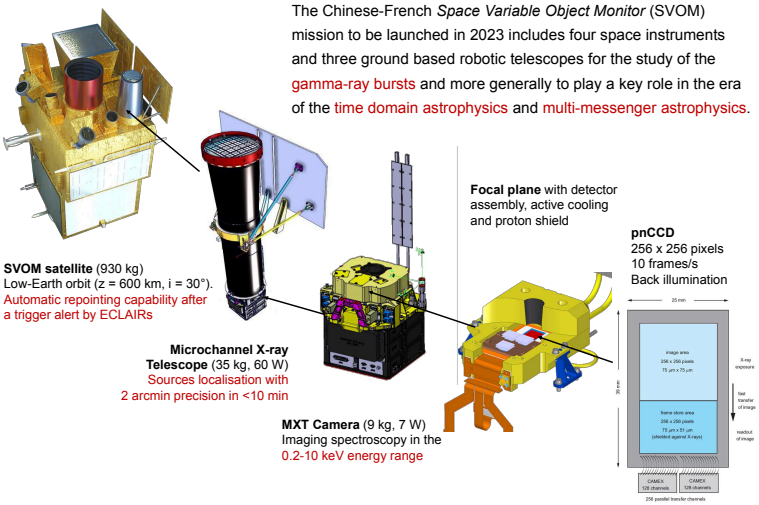

Fig. 1: Implementation of the MXT focal plane based on 256 × 256 pixel pnCCD on-board the SVOM mission [1].

METHOD

The soft X-ray metrology beamline of the SOLEIL synchrotron

This test facility was identified as suitable for the characterization of the MXT focal plane:

- Monoenergetic beam, tunable from 40 to 1800 eV → spectral response where MXT is the most sensitive;
- Flux calibrated beam → quantum efficiency of the detector with its on-chip filter;
- Beam spot → charge transfer efficiency (CTE) and uniformity of the Al layer of the on-chip filter.

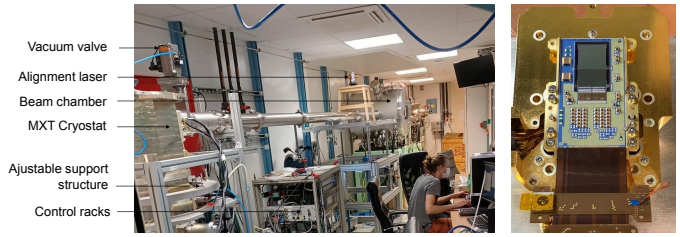

Fig. 2: Test configuration in the experience room. The MXT cryostat is placed 5 meters away from the beam chamber and contains the flight spare model of the focal plane mounted on displacement tables.

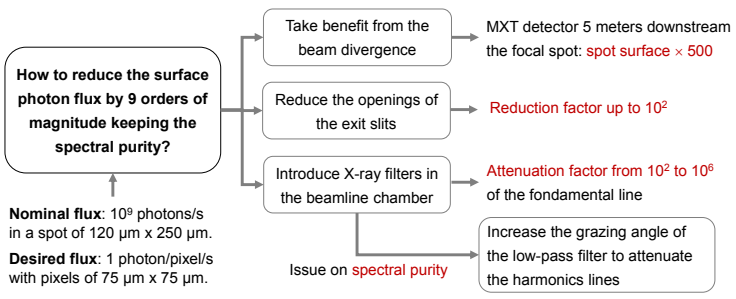

Fig. 3: Method to address the issue of the nominal photon flux causing photon pile-up in the pnCCD pixels.

RESULTS

Energy resolution

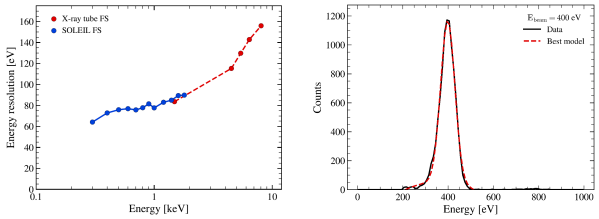

Fig. 4: Energy resolution obtained with single events, with an example of spectrum at 400 eV.

Charge transfer efficiency

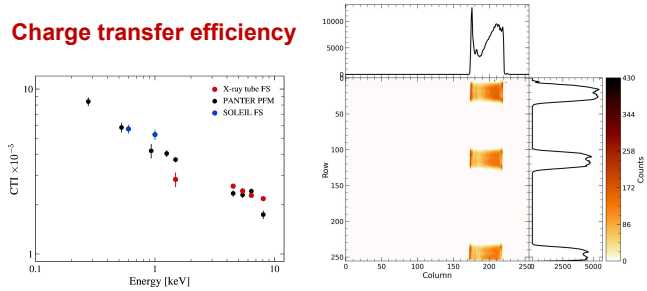

Fig. 5: Charge transfer inefficiency (1 – CTE) computed from 3 runs per energy and comparison with data obtained with the X-ray source in the lab (comparable pixel flux but full illumination).

Photon event multiplicity

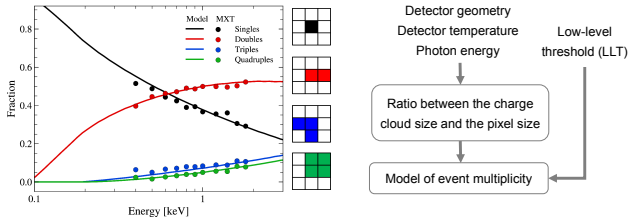

Fig. 6: Event multiplicity statistics adjusted with a model of charge sharing adapted from [2] to the MXT configuration (-60°C, 44 eV LLT, 75 µm pixel size).

CONCLUSIONS

Scientific goals	Results of the first campaign	To prepare for the next campaign
Spectral response below 1.5 keV	Beam parameters successfully found from 300 to 1800 eV to get low flux mono-energetic source. Results in good agreement with other test facilities.	Find other filters for the 200-300 eV band. Upgrade the MXT cryostat to eliminate low energy perturbations (vacuum valve).
Charge transfer efficiency	Method demonstrated with 2 energies and 3 positions.	Repeat with more positions and more energies.
Quantum efficiency below 2 keV	Not achieved despite reduction in the uncertainties. Indirect incident flux measurement and output flux impacted by low energy perturbations.	Find another reference detector for very low flux metrology or remove this goal.
Uniformity of the aluminium layer of the on-chip filter	Not achieved due to an anomaly in the displacement tables of the MXT cryostat.	Upgrade the MXT cryostat to allow continuous scan of the matrix with the beam and measure relative QE.

The next campaign will focus on the CTE and energy resolution after proton irradiation to investigate the evolution of the MXT spectral performance during in-flight operations.

[1] J. Wei, B. Cordier et al., "The deep and transient Universe: New Challenges and Opportunities – Scientific Prospects of the SVOM Mission," arXiv: 1610.06892, 2016.

[2] K. Dennerl et al., "Determination of the eROSITA mirror half energy width (HEW) with subpixel resolution," SPIE Proc., Vol. 8443 (2012), 844350.

Résumé en Français

Cette thèse porte sur l'étude des phénomènes transitoires les plus enigmatiques de l'Univers, capables de libérer une quantité d'énergie colossale en un temps extrêmement court. Plus particulièrement dans cette thèse, je me suis intéressé à la préparation et à l'exploitation scientifique de la mission SVOM qui aura pour but d'étudier et de caractériser ces phénomènes très lumineux et éphémères.

Contexte scientifique et la mission SVOM

Les sursauts gamma (Gamma-Ray Bursts ou GRBs en anglais) sont de brefs flashs de rayons gamma et représentent les phénomènes les plus énergétiques connus dans l'Univers. Ils sont provoqués par des jets ultra-relativistes après la formation d'un trou noir stellaire. Leur émission caractéristique est composée par deux phases, une première émission brève de quelques secondes principalement dans les rayons gamma, appelée émission prompte, et d'une seconde émission avec un spectre plus large, des rayons X aux ondes radio, qui peut durer plusieurs heures à plusieurs jours, appelée émission rémanente. On distingue deux grandes familles de GRBs par rapport à leur durée caractéristique, les sursauts gamma courts (short-duration GRBs or SGRBs en anglais) qui durent dans la majorité des cas moins de deux secondes et les sursauts gamma longs (long-duration GRBs or LGRBs en anglais) qui durent de quelques secondes à plusieurs minutes. Bien que leurs émissions caractéristiques soient globalement similaires, ces deux populations de GRBs sont très différentes compte tenu de leur progéniteur. Les SGRBs sont produits par la coalescence de deux objets compacts (un système binaire d'étoiles à neutron ou un système composé d'une étoile à neutrons et d'un trou noir) alors que le LGRBs sont issus de la fin de vie d'étoiles très massives (> 40 $M_{\odot}$).

La future mission franco-chinoise SVOM prévue pour un lancement fin 2023, sera dédiée à l'observation des GRBs. Cette mission ouvrira une nouvelle ère dans le domaine du ciel transitoire et multi-messager. Elle se distingue des précédents missions par deux aspects. Premièrement, elle embarque à bord un télescope capable d'observer la lumière visible jusqu'au proche infrarouge et deuxièmement elle propose une meilleure synergie entre la détection des GRBs par les instruments à bord du satellite et leur suivi par les télescopes au sol. Grâce à cela, SVOM promet d'apporter un nouveau regard sur ces phénomènes extrêmes.

Densité stellaire des galaxies hôtes de sursaut gamma

La sous-population constituée des LGRB s'est révélée être associée à la fin de vie des étoiles massives, ce qui en fait des traceurs prometteurs de la formation stellaire cosmique jusqu'à de très grands décalages spectraux (z > 8). Cependant, des études ont suggéré que certaines conditions semblent être requises pour former un LGRB, liées par exemple à la faible métallicité du progéniteur ou à son environnement proche. À travers mon travail, j'ai étudié l'influence de la densité stellaire sur l'efficacité de formation des LGRBs. Puisque ces phénomènes sont extragalactiques, ce type d'étude ne peut se faire qu'à travers les propriétés globales de la galaxie hôte. Pour cela, j'ai utilisé des observations disponibles dans les archives de galaxies hôtes de LGRBs observées par le HST avec sa camera WFC3 dans l'infrarouge proche. Ces images ont permis d'estimer la taille de ces galaxies avec un logiciel appelé `GALFIT` pour un ensemble de galaxies hôtes à $1 < z < 3$. En combinant la taille de ces galaxies avec des estimations de la masse stellaire et du taux de formation d'étoiles, la densité surfacique de masse stellaire et de formation d'étoiles de chaque galaxie a été déterminée. Les valeurs de ces paramètres pour les galaxies hôtes de LGRBs ont ensuite été comparées à celles d'un échantillon représentatif de galaxies à formation d'étoiles obtenu à partir d'un sondage profond de l'Univers. Comme précédemment rapporté dans une étude à $z < 1$, j'ai montré pour la première fois qu'à $z < 2$ les LGRBs ont tendance à être observés plus fréquemment dans des galaxies compactes ayant une densité de formation d'étoiles et de masse stellaire plus élevées que la normale. Cette étude suggère ainsi que d'autres paramètres comme la densité stellaire de l'environnent du LGRB peuvent

impacter et jouer un rôle dans la formation de ces phénomènes.

Suivi des rémanences de sursauts gamma

La constitution du nouvel échantillon de GRBs proprement caractérisés et identifiés par la mission SVOM nécessitera un suivi efficace des alertes par la communauté scientifique de SVOM. La stratégie de pointage de SVOM (anti-solaire) fera que chaque GRB détecté sera observable depuis la face cachée de la Terre. Il est donc nécessaire d'avoir une couverture géographique importante pour avoir systématiquement l'accès à un télescope au sol afin d'observer les GRBs détectés par SVOM. De plus, en amont de la mission, il est primordial d'accumuler de l'expérience sur le suivi des alertes pour savoir comment réagir et déclencher des observations efficaces et les plus appropriées aux phénomènes détectés.
Dans ce but, j'ai pris part de manière active au programme mené par le consortium Stargate à l'aide du Very Large Telescope (VLT) au Chili pour conduire le suivi des GRBs actuellement détectés par la mission *Swift*. J'ai eu l'occasion de déclencher à plusieurs reprises des observations avec l'instrument X-Shooter du VLT et déterminer notamment le redshift d'un GRB. J'ai également joué un rôle important dans la récente mise en place du suivi de ces alertes avec le spectro-imageur MISTRAL installé sur le T193 de l'Observatoire de Haute-Provence. Depuis le début du programme MISTRAL, nous avons également pu déclencher plusieurs observations suite à des alertes *Swift* et nous exercer à répondre aux futures alertes SVOM avec cet instrument.

Performance du modèle de vol de l'instrument MXT

SVOM effectuera un suivi systématique des GRBs dans le domaine des rayons X en utilisant un télescope X à bord du satellite (MXT). La réduction des données d'un télescope est une étape clef dans l'utilisation de ces données pour leur exploitation scientifique afin d'en extraire le plus d'informations scientifiques. En 2021, MXT a été assemblée dans sa configuration de vol et testée avant son intégration sur le satellite SVOM.
Dans ce contexte, j'ai participé activement à deux campagnes de calibration, une

avec l'instrument de vol dans l'installation Panter à Munich et une autre avec le modèle de réserve de MXT au Synchrotron SOLEIL proche du CEA. Les données récoltées ont notamment permis de calibrer en énergie le modèle de vol de MXT et démontrer l'excellente performance spectrale de l'instrument avant son lancement. De plus, j'ai également contribué à la mise en place de traitements optimisés des données de MXT. Ces traitements permettent notamment de prendre en compte l'inefficacité du transfert de charge ainsi que la perte de charge qui est provoquée lors de l'extraction du signal (seuillage). Une fois en vol, ces traitements seront utilisés par le segment sol pour réduire les données et permettront de tirer le meilleur parti des données pour leur exploitation scientifique.

Bibliography

Abbott, B. P., Abbott, R., Abbott, T. D., et al. 2017a, ApJ, 848, L13 12

Abbott, B. P., Abbott, R., Abbott, T. D., et al. 2017b, ApJ, 848, L12 12, 15

Abdalla, H., Adam, R., Aharonian, F., et al. 2019, Nature, 575, 464 126

Abraham, R. G. & Merrifield, M. R. 2000, AJ, 120, 2835 53

Abraham, R. G. & van den Bergh, S. 2001, Science, 293, 1273 46

Abraham, R. G., van den Bergh, S., & Nair, P. 2003, ApJ, 588, 218 54

Adamo, A., Kruijssen, J. M. D., Bastian, N., Silva-Villa, E., & Ryon, J. 2015, MNRAS, 452, 246 99

Adamo, A., Östlin, G., & Zackrisson, E. 2011, MNRAS, 417, 1904 99

Aggarwal, K., Budavári, T., Deller, A. T., et al. 2021, ApJ, 911, 95 68, 69

Ahumada, T., Singer, L. P., Anand, S., et al. 2021, Nature Astronomy, 5, 917 10

Amati, L., O'Brien, P. T., Götz, D., Bozzo, E., & Santangelo, A. 2021a, arXiv e-prints, arXiv:2102.08702 9

Amati, L., O'Brien, P. T., Götz, D., et al. 2021b, Experimental Astronomy, 52, 183 9

Andrae, R., Jahnke, K., & Melchior, P. 2011, MNRAS, 411, 385 54

Andritschke, R., Hartner, G., Hartmann, R., Meidinger, N., & Struder, L. 2008, IEEE Nucl Sci Symp Conf Rec, 2166 169, 208

Angel, J. R. P. 1979, in Society of Photo-Optical Instrumentation Engineers (SPIE) Conference Series, Vol. 184, Space optics: Imaging X-ray optics workshop, ed. M. Weisskopf, 84-85 166

Arabsalmani, M., Garratt-Smithson, L., Wijers, N., et al. 2022, submitted to ApJ 127

Arabsalmani, M., Le Floc'h, E., Dannerbauer, H., et al. 2018a, MNRAS, 476, 2332 23

Arabsalmani, M., Møller, P., Perley, D. A., et al. 2018b, MNRAS, 473, 3312 96, 97, 126

Arabsalmani, M., Renaud, F., Roychowdhury, S., et al. 2020, ApJ, 899, 165 65

Arabsalmani, M., Roychowdhury, S., Starkenburg, T. K., et al. 2019, MNRAS, 485, 5411 65, 98

Arabsalmani, M., Roychowdhury, S., Zwaan, M. A., Kanekar, N., & Michałowski, M. J. 2015, MNRAS, 454, L51 65

Atteia, J. L., Cordier, B., & Wei, J. 2022, International Journal of Modern Physics D, 31, 2230008 9, 24, 100

Ballet, J. 1999, A&AS, 135, 371 205

Band, D., Matteson, J., Ford, L., et al. 1993, ApJ, 413, 281 5

Barden, M., Häußler, B., Peng, C. Y., McIntosh, D. H., & Guo, Y. 2012, MNRAS, 422, 449 59, 70

Barret, D., Lam Trong, T., den Herder, J.-W., et al. 2016, in Society of Photo-Optical Instrumentation Engineers (SPIE) Conference Series, Vol. 9905, Space Telescopes and Instrumentation 2016: Ultraviolet to Gamma Ray, ed. J.-W. A. den Herder, T. Takahashi, & M. Bautz, 99052F 154

Barret, D., Lam Trong, T., den Herder, J.-W., et al. 2018, in Society of Photo-Optical Instrumentation Engineers (SPIE) Conference Series, Vol. 10699, Space Telescopes and Instrumentation 2018: Ultraviolet to Gamma Ray, ed. J.-W. A. den Herder, S. Nikzad, & K. Nakazawa, 106991G 154

Barthelmy, S. D., Barbier, L. M., Cummings, J. R., et al. 2005, Space Sci. Rev., 120, 143 7

Basa, S., Lee, W. H., Dolon, F., et al. 2022, in Society of Photo-Optical Instrumentation Engineers (SPIE) Conference Series, Vol. 12182, Ground-based and Airborne Telescopes IX, ed. H. K. Marshall, J. Spyromilio, & T. Usuda, 121821S 33

Behar, E., Dado, S., Dar, A., & Laor, A. 2011, ApJ, 734, 26 154

Bell, E. F. & de Jong, R. S. 2001, ApJ, 550, 212 80

Berger, E. 2010, ApJ, 722, 1946 15

Berger, E. 2014, ARA&A, 52, 43 13, 15

Berger, E., Price, P. A., Cenko, S. B., et al. 2005, Nature, 438, 988 14

Bershady, M. A., Jangren, A., & Conselice, C. J. 2000, AJ, 119, 2645 53

Bertin, E. 2011, in Astronomical Society of the Pacific Conference Series, Vol. 442, Astronomical Data Analysis Software and Systems XX, ed. I. N. Evans, A. Accomazzi, D. J. Mink, & A. H. Rots, 435 75

Bertin, E. & Arnouts, S. 1996, A&AS, 117, 393 54, 68, 74

Blanchard, P. K., Berger, E., & Fong, W.-f. 2016, ApJ, 817, 144 8, 22, 64, 68, 69, 79, 91, 92, 93, 100, 116, 117, 118, 128

Blandford, R. D. & Znajek, R. L. 1977, MNRAS, 179, 433 16

Blanton, M. R., Hogg, D. W., Bahcall, N. A., et al. 2003, ApJ, 592, 819 44

Bloom, J. S., Djorgovski, S. G., Kulkarni, S. R., & Frail, D. A. 1998, ApJ, 507, L25 5, 8

Bloom, J. S., Kulkarni, S. R., & Djorgovski, S. G. 2002, AJ, 123, 1111 63, 68, 69

Boella, G., Butler, R. C., Perola, G. C., et al. 1997, A&AS, 122, 299 5

Boissier, S., Salvaterra, R., Le Floc'h, E., et al. 2013, A&A, 557, A34 22

Bolmer, J., Greiner, J., Krühler, T., et al. 2018, A&A, 609, A62 20, 126, 155

Bolmer, J., Ledoux, C., Wiseman, P., et al. 2019, A&A, 623, A43 126

Bonfini, P. 2014, PASP, 126, 935 57

Boquien, M., Burgarella, D., Roehlly, Y., et al. 2019, A&A, 622, A103 79

Bradshaw, M., Burwitz, V., Hartner, G., et al. 2019, in Society of Photo-Optical Instrumentation Engineers (SPIE) Conference Series, Vol. 11119, Optics for EUV, X-Ray, and Gamma-Ray Astronomy IX, ed. S. L. O'Dell & G. Pareschi, 1111916 202

Brammer, G. B., van Dokkum, P. G., Franx, M., et al. 2012, ApJS, 200, 13 45, 70

Breda, I., Papaderos, P., Gomes, J. M., & Amarantidis, S. 2019, A&A, 632, A128 57

Briggs, M. S., Paciesas, W. S., Pendleton, G. N., et al. 1996, ApJ, 459, 40 5

Briggs, M. S., Pendleton, G. N., Kippen, R. M., et al. 1999, ApJS, 122, 503 4

Brisbin, D. & Harwit, M. 2012, ApJ, 750, 142 96

Bromm, V. & Yoshida, N. 2011, ARA&A, 49, 373 18

Brown, G. E. & Lee, C.-H. 2004, New A, 9, 225 14

Buchner, J., Schulze, S., & Bauer, F. E. 2017, MNRAS, 464, 4545 154

Burrows, D. N., Hill, J. E., Nousek, J. A., et al. 2005, Space Sci. Rev., 120, 165 7, 133

Burwitz, V., Bavdaz, M., Pareschi, G., et al. 2013, in Society of Photo-Optical Instrumentation Engineers (SPIE) Conference Series, Vol. 8861, Optics for EUV, X-Ray, and Gamma-Ray Astronomy VI, ed. S. L. O'Dell & G. Pareschi, 88611J 202

Campana, S., Lodato, G., D'Avanzo, P., et al. 2011, Nature, 480, 69 10

Campana, S., Mangano, V., Blustin, A. J., et al. 2006a, Nature, 442, 1008 12

Campana, S., Romano, P., Covino, S., et al. 2006b, A&A, 449, 61 153

Campana, S., Salvaterra, R., Ferrara, A., & Pallottini, A. 2015, A&A, 575, A43 153, 154

Campana, S., Salvaterra, R., Melandri, A., et al. 2012, MNRAS, 421, 1697 153

Campana, S., Thöne, C. C., de Ugarte Postigo, A., et al. 2010, MNRAS, 402, 2429 153

Cano, Z., Wang, S.-Q., Dai, Z.-G., & Wu, X.-F. 2017, Advances in Astronomy, 2017, 8929054 13

Cantiello, M., Yoon, S. C., Langer, N., & Livio, M. 2007, A&A, 465, L29 63

Capaccioli, M. 1989, in World of Galaxies (Le Monde des Galaxies), ed. J. Corwin, Harold G. & L. Bottinelli, 208-227 55

Carnall, A. C., Leja, J., Johnson, B. D., et al. 2019, ApJ, 873, 44 101

Ceraudo, F. 2019, 214

Characterization and Performance Optimization of the Focal Plane of the Micro-channel X-ray Telescope on-Board the Space Astronomy Mission SVOM, PhD thesis, Université Paris-Saclay

Ceraudo, F., Meuris, A., Doumayrou, E., et al. 2020, Nuclear Instruments and Methods in Physics Research A, 973, 164164 169, 172, 184, 208

Chabrier, G. 2003, PASP, 115, 763 66

Chandar, R., Fall, S. M., & Whitmore, B. C. 2015, ApJ, 810, 1 99

Chandar, R., Fall, S. M., Whitmore, B. C., & Mulia, A. J. 2017, ApJ, 849, 128 99

Chen, W. J., Urata, Y., Huang, K., et al. 2020, ApJ, 891, L15 124

Chrimes, A. A., Levan, A. J., Stanway, E. R., et al. 2019, MNRAS, 486, 3105 73, 79, 89, 149

Chrimes, A. A., Stanway, E. R., & Eldridge, J. J. 2020, MNRAS, 491, 3479 63, 64, 95

Chrimes, A. A., Stanway, E. R., Levan, A. J., et al. 2018, MNRAS, 478, 2 78

Christensen, L., Hjorth, J., & Gorosabel, J. 2004, A&A, 425, 913 21

Cirasuolo, M., Afonso, J., Carollo, M., et al. 2014, in Society of Photo-Optical Instrumentation Engineers (SPIE) Conference Series, Vol. 9147, Ground-based and Airborne Instrumentation for Astronomy V, ed. S. K. Ramsay, I. S. McLean, & H. Takami, 91470N 141

Conselice, C. J. 2003, ApJS, 147, 1 53

Conselice, C. J. 2014, ARA&A, 52, 291 46, 50

Conselice, C. J., Bluck, A. F. L., Ravindranath, S., et al. 2011, MNRAS, 417, 2770 49

Conselice, C. J., Vreeswijk, P. M., Fruchter, A. S., et al. 2005, ApJ, 633, 29 24, 65

Cordier, B., Desclaux, F., Foliard, J., & Schanne, S. 2008, in American Institute of Physics Conference Series, Vol. 1000, Gamma-ray Bursts 2007, ed. M. Galassi, D. Palmer, & E. Fenimore, 585-588 27

Corre, D., Basa, S., Klotz, A., et al. 2018a, in Society of Photo-Optical Instrumentation Engineers (SPIE) Conference Series, Vol. 10705, Modeling, Systems Engineering, and Project Management for Astronomy VIII, ed. G. Z. Angeli & P. Dierickx, 107051R 34

Corre, D., Buat, V., Basa, S., et al. 2018b, A&A, 617, A141 78, 81, 89, 118, 155

Costa, E., Frontera, F., Heise, J., et al. 1997, Nature, 387, 783 7

Cucchiara, A., Levan, A. J., Fox, D. B., et al. 2011, ApJ, 736, 7 18, 141

Dagoneau, N., Schanne, S., Atteia, J.-L., Götz, D., & Cordier, B. 2020, Experimental Astronomy, 50, 91 11

Dalton, T. & Morris, S. L. 2020, MNRAS, 495, 2342 154

Dalton, T., Morris, S. L., & Fumagalli, M. 2021, MNRAS, 502, 5981 154

De Rossi, M. E., Bower, R. G., Font, A. S., Schaye, J., & Theuns, T. 2017, MNRAS, 472, 3354 97

de Ugarte Postigo, A., Blazek, M., Janout, P., et al. 2014, in Society of Photo-Optical Instrumentation Engineers (SPIE) Conference Series, Vol. 9152, Software and Cyberinfrastructure for Astronomy III, ed. G. Chiozzi & N. M. Radziwill, 91520B 146

de Ugarte Postigo, A., Fausey, H., Kann, D. A., et al. 2022a, GRB Coordinates Network, 31967, 1 150

de Ugarte Postigo, A., Schneider, B., Malesani, D. B., Kann, D. A., & Stargate Collaboration. 2022b, GRB Coordinates Network, 31800, 1 150

de Vaucouleurs, G. 1948, Annales d'Astrophysique, 11, 247 55

de Vaucouleurs, G. 1959, Handbuch der Physik, 53, 275 46, 52

D'Elia, V., Fiore, F., Perna, R., et al. 2009, ApJ, 694, 332 145

Della Valle, M., Chincarini, G., Panagia, N., et al. 2006, Nature, 444, 1050 13

Dennerl, K., Burkert, W., Burwitz, V., et al. 2012, in Society of Photo-Optical Instrumentation Engineers (SPIE) Conference Series, Vol. 8443, Space Telescopes and Instrumentation 2012: Ultraviolet to Gamma Ray, ed. T. Takahashi, S. S. Murray, & J.-W. A. den Herder, 844350 179, 180, 181, 208

Dieleman, S., Willett, K. W., & Dambre, J. 2015, MNRAS, 450, 1441 60

Ding, X., Birrer, S., Treu, T., & Silverman, J. D. 2021, arXiv e-prints, arXiv:2111.08721 57

Dong, Y., Wu, B., Li, Y., Zhang, Y., & Zhang, S. 2010, Science China Physics, Mechanics, and Astronomy, 53, 40 30

Eddington, A. S. 1913, MNRAS, 73, 359 44

Eichler, D., Livio, M., Piran, T., & Schramm, D. N. 1989, Nature, 340, 126 15

Ellison, S. L., Patton, D. R., Simard, L., & McConnachie, A. W. 2008a, ApJ, 672, L107 96

Ellison, S. L., Patton, D. R., Simard, L., & McConnachie, A. W. 2008b, AJ, 135, 1877 97

Evangelista, Y., Fiore, F., Fuschino, F., et al. 2020, in Society of Photo-Optical Instrumentation Engineers (SPIE) Conference Series, Vol. 11444, Society of Photo-Optical Instrumentation Engineers (SPIE) Conference Series, 114441T 9

Evans, P. A., Beardmore, A. P., Page, K. L., et al. 2009, MNRAS, 397, 1177 151, 152

Evans, P. A., Beardmore, A. P., Page, K. L., et al. 2007, A&A, 469, 379 151

Faber, J. A., Baumgarte, T. W., Shapiro, S. L., & Taniguchi, K. 2006, ApJ, 641, L93 15

Fan, X., Zou, G., Wei, J., et al. 2020, in Society of Photo-Optical Instrumentation Engineers (SPIE) Conference Series, Vol. 11443, Society of Photo-Optical Instrumentation Engineers (SPIE) Conference Series, 114430Q 31

Fano, U. 1947, Physical Review, 72, 26 216

Ferrari, F., de Carvalho, R. R., & Trevisan, M. 2015, ApJ, 814, 55 57

Ferreira, L., Adams, N., Conselice, C. J., et al. 2022, ApJ, 938, L2 47

Fong, W. & Berger, E. 2013, ApJ, 776, 18 14

Fong, W.-f., Nugent, A. E., Dong, Y., et al. 2022, ApJ, 940, 56 15

Förster Schreiber, N. M. & Wuyts, S. 2020, ARA&A, 58, 661 68

Frail, D. A., Kulkarni, S. R., Nicastro, L., Feroci, M., & Taylor, G. B. 1997, Nature, 389, 261 5

Friis, M., De Cia, A., Krühler, T., et al. 2015, MNRAS, 451, 167 147

Fruchter, A. S. & Hook, R. N. 2002, PASP, 114, 144 51

Fruchter, A. S., Levan, A. J., Strolger, L., et al. 2006, Nature, 441, 463 21, 22, 24, 64, 65, 68, 86, 128

Fryer, C. L. & Heger, A. 2005, ApJ, 623, 302 63

Fryer, C. L., Woosley, S. E., & Hartmann, D. H. 1999, ApJ, 526, 152 15

Fukugita, M., Hogan, C. J., & Peebles, P. J. E. 1998, ApJ, 503, 518 46

Fynbo, J. P. U., Jakobsson, P., Prochaska, J. X., et al. 2009, ApJS, 185, 526 73, 136

Fynbo, J. P. U., Watson, D., Thöne, C. C., et al. 2006, Nature, 444, 1047 13

Gal-Yam, A., Fox, D. B., Price, P. A., et al. 2006, Nature, 444, 1053 13

Galama, T. J., Vreeswijk, P. M., van Paradijs, J., et al. 1998, Nature, 395, 670 12

Galama, T. J. & Wijers, R. A. M. J. 2001, ApJ, 549, L209 153

Gardner, J. P., Mather, J. C., Clampin, M., et al. 2006, Space Sci. Rev., 123, 485 101

Gehrels, N., Chincarini, G., Giommi, P., et al. 2004, ApJ, 611, 1005 5

Gehrels, N., Norris, J. P., Barthelmy, S. D., et al. 2006, Nature, 444, 1044 13

Gehrels, N., Ramirez-Ruiz, E., & Fox, D. B. 2009, ARA&A, 47, 567 8, 150

Gehrels, N., Sarazin, C. L., O'Brien, P. T., et al. 2005, Nature, 437, 851 14

Gendre, B., Stratta, G., Atteia, J. L., et al. 2013, ApJ, 766, 30 10, 11

Ghirlanda, G. & Salvaterra, R. 2022, ApJ, 932, 10 20, 64

Goddard, Q. E., Bastian, N., & Kennicutt, R. C. 2010, MNRAS, 405, 857 99

Godet, O., Nasser, G., Atteia, J. ., et al. 2014, in Society of Photo-Optical Instrumentation Engineers (SPIE) Conference Series, Vol. 9144, Space Telescopes and Instrumentation 2014: Ultraviolet to Gamma Ray, ed. T. Takahashi, J.-W. A. den Herder, & M. Bautz, 914424 29

Goldstein, A., Veres, P., Burns, E., et al. 2017, ApJ, 848, L14 15

Gotz, D., Boutelier, M., Burwitz, V., et al. 2022, arXiv e-prints, arXiv:2211.13489 156, 166

Götz, D., Osborne, J., Cordier, B., et al. 2014, in Society of Photo-Optical Instrumentation Engineers (SPIE) Conference Series, Vol. 9144, Space Telescopes and Instrumentation 2014: Ultraviolet to Gamma Ray, ed. T. Takahashi, J.-W. A. den Herder, & M. Bautz, 914423 30

Graham, A. W. & Driver, S. P. 2005, PASA, 22, 118 55

Graham, A. W. & Worley, C. C. 2008, MNRAS, 388, 1708 57

Graham, J. F. & Fruchter, A. S. 2013, ApJ, 774, 119 22, 96

Graham, J. F. & Fruchter, A. S. 2017, ApJ, 834, 170 22

Greiner, J., Fox, D. B., Schady, P., et al. 2015, ApJ, 809, 76 64

Greiner, J., Krühler, T., Klose, S., et al. 2011, A&A, 526, A30 73, 120

Griffiths, R., Petre, R., Hasinger, G., et al. 2004, in Society of Photo-Optical Instrumentation Engineers (SPIE) Conference Series, Vol. 5488, UV and Gamma-Ray Space Telescope Systems, ed. G. Hasinger & M. J. L. Turner, 209-221 168

Grogin, N. A., Kocevski, D. D., Faber, S. M., et al. 2011, ApJS, 197, 35 45, 48, 70

Haghi, H., Safaei, G., Zonoozi, A. H., & Kroupa, P. 2020, ApJ, 904, 43 99

Harwit, M. & Brisbin, D. 2015, ApJ, 800, 91 96

Hashimoto, T., Chaudhary, R., Ohta, K., et al. 2018, ApJ, 863, 95 23

Hashimoto, T., Hatsukade, B., Goto, T., et al. 2019, MNRAS, 488, 5029 24, 78

Hashimoto, T., Perley, D. A., Ohta, K., et al. 2015, ApJ, 806, 250 78, 97

Hatsukade, B., Hashimoto, T., Kohno, K., et al. 2019, ApJ, 876, 91 23

Hatsukade, B., Ohta, K., Endo, A., et al. 2014, Nature, 510, 247 23

Hatsukade, B., Ohta, K., Hashimoto, T., et al. 2020, ApJ, 892, 42 23

Häussler, B., McIntosh, D. H., Barden, M., et al. 2007, ApJS, 172, 615 74, 76, 114

Heintz, K. E., Malesani, D., Wiersema, K., et al. 2018, MNRAS, 474, 2738 23, 65

Hjorth, J., Malesani, D., Jakobsson, P., et al. 2012, ApJ, 756, 187 22, 82

Hjorth, J., Sollerman, J., Møller, P., et al. 2003, Nature, 423, 847 12, 63, 68, 128

Holmberg, E. 1958, Meddelanden fran Lunds Astronomiska Observatorium Serie II, 136, 1 46

Hsiao, T. Y.-Y., Hashimoto, T., Chang, J.-Y., et al. 2020, MNRAS, 496, 4405 78, 82

Hubble, E. P. 1926, ApJ, 64, 321 46, 52

Hubble, E. P. 1936, Realm of the Nebulae 46, 52

Huertas-Company, M., Gravet, R., Cabrera-Vives, G., et al. 2015, ApJS, 221, 8 60

Hunt, L. K., Palazzi, E., Michałowski, M. J., et al. 2014, A&A, 565, A112 64, 78, 89

Ichikawa, T., Kajisawa, M., & Akhlaghi, M. 2012, MNRAS, 422, 1014 57

Idir, M., Mercere, P., Moreno, T., & Delmotte, A. 2006, Synchrotron Radiation News, 19, 18 183

Idir, M., Mercere, P., Moreno, T., et al. 2010, in American Institute of Physics Conference Series, Vol. 1234, Sri 2009, 10th International Conference on Synchrotron Radiation Instrumentation, ed. R. Garrett, I. Gentle, K. Nugent, & S. Wilkins, 485-488 183

Izzo, L., de Ugarte Postigo, A., Maeda, K., et al. 2019, Nature, 565, 324 124

Izzo, L., Thöne, C. C., Schulze, S., et al. 2017, MNRAS, 472, 4480 21

Jakobsson, P., Hjorth, J., Fynbo, J. P. U., et al. 2004, ApJ, 617, L21 73

Japelj, J., Vergani, S. D., Salvaterra, R., et al. 2016, A&A, 590, A129 23

Jiang, L., Wang, S., Zhang, B., et al. 2021a, Nature Astronomy, 5, 262 18

Jiang, L., Wang, S., Zhang, B., et al. 2021b, Nature Astronomy, 5, 998 18

Kangas, T., Fruchter, A. S., Cenko, S. B., et al. 2020, ApJ, 894, 43 67

Kann, D. A., Blazek, M., de Ugarte Postigo, A., & Thöne, C. C. 2020, Research Notes of the American Astronomical Society, 4, 247 18

Kann, D. A., Klose, S., Zhang, B., et al. 2011, ApJ, 734, 96 127, 128

Kann, D. A., Klose, S., Zhang, B., et al. 2010, ApJ, 720, 1513 127, 128, 133, 134

Kelly, P. L., Filippenko, A. V., Modjaz, M., & Kocevski, D. 2014, ApJ, 789, 23 24, 65, 91, 92, 93, 95, 100, 116, 117, 118

Kelvin, L. S., Driver, S. P., Robotham, A. S. G., et al. 2012, MNRAS, 421, 1007 56

Kennicutt, Robert C., J. 1998, ARA&A, 36, 189 83, 101

Kewley, L. J. & Ellison, S. L. 2008, ApJ, 681, 1183 147

Kistler, M. D., Yüksel, H., Beacom, J. F., Hopkins, A. M., & Wyithe, J. S. B. 2009, ApJ, 705, L104 20

Kistler, M. D., Yüksel, H., Beacom, J. F., & Stanek, K. Z. 2008, ApJ, 673, L119 64

Kistler, M. D., Yuksel, H., & Hopkins, A. M. 2013, arXiv e-prints, arXiv:1305.1630 20

Klebesadel, R. W., Strong, I. B., & Olson, R. A. 1973, ApJ, 182, L85 3

Koekemoer, A. M., Faber, S. M., Ferguson, H. C., et al. 2011, ApJS, 197, 36 45, 70

Kotov, I. V., Neal, H., & O'Connor, P. 2018, Nuclear Instruments and Methods in Physics Research A, 901, 126 217

Kouveliotou, C., Granot, J., Racusin, J. L., et al. 2013, ApJ, 779, L1 126

Kouveliotou, C., Meegan, C. A., Fishman, G. J., et al. 1993, ApJ, 413, L101 5, 10

Kouveliotou, C., Wijers, R. A. M. J., & Woosley, S. 2012, Gamma-ray Bursts 2

Kriek, M., Shapley, A. E., Reddy, N. A., et al. 2015, ApJS, 218, 15 23

Kriek, M., van Dokkum, P. G., Labbé, I., et al. 2009, ApJ, 700, 221 101

Krist, J. E., Hook, R. N., & Stoehr, F. 2011, in Society of Photo-Optical Instrumentation Engineers (SPIE) Conference Series, Vol. 8127, Optical Modeling and Performance Predictions V, ed. M. A. Kahan, 81270J 75

Krühler, T., Greiner, J., Schady, P., et al. 2011, A&A, 534, A108 73, 89

Krühler, T., Kuncarayakti, H., Schady, P., et al. 2017, A&A, 602, A85 21, 64

Krühler, T., Malesani, D., Fynbo, J. P. U., et al. 2015, A&A, 581, A125 69, 78, 82, 96, 97, 118

Krühler, T. & Schady, P. 2017, Photometry and Stellar Masses for GRB Host Galaxies with Emission-line Spectra 78, 118

Kruijssen, J. M. D. 2012, MNRAS, 426, 3008 99

Kruijssen, J. M. D. & Bastian, N. 2016, MNRAS, 457, L24 99

Kumar, P. & Zhang, B. 2015, Phys. Rep., 561, 1 17

Laigle, C., McCracken, H. J., Ilbert, O., et al. 2016, ApJS, 224, 24 80

Lam, M. C., Smith, R. J., Arcavi, I., et al. 2021, arXiv e-prints, arXiv:2111.02127 137

Lange, R., Driver, S. P., Robotham, A. S. G., et al. 2015, MNRAS, 447, 2603 56

Langer, N. & Norman, C. A. 2006, ApJ, 638, L63 14

Laskar, T., Berger, E., & Chary, R.-R. 2011, ApJ, 739, 1 126

Laskar, T., Berger, E., Zauderer, B. A., et al. 2013, ApJ, 776, 119 125, 126

Le Floc'h, E., Duc, P. A., Mirabel, I. F., et al. 2003, A&A, 400, 499 21, 64

Levan, A., Crowther, P., de Grijs, R., et al. 2016, Space Sci. Rev., 202, 33 14

Levan, A. J., Tanvir, N. R., Starling, R. L. C., et al. 2014, ApJ, 781, 13 8, 11

Levesque, E. M., Berger, E., Soderberg, A. M., & Chornock, R. 2011, ApJ, 739, 23 64

Levesque, E. M., Bloom, J. S., Butler, N. R., et al. 2010a, MNRAS, 401, 963 67, 78

Levesque, E. M., Kewley, L. J., Graham, J. F., & Fruchter, A. S. 2010b, ApJ, 712, L26 23, 65

Levesque, E. M., Soderberg, A. M., Kewley, L. J., & Berger, E. 2010c, ApJ, 725, 1337 23

Li, G., Guo, S., Lv, J., Zhao, K., & He, Z. 2021, Advances in Space Research, 67, 1701 34

Li, L., Liang, E.-W., Tang, Q.-W., et al. 2012, ApJ, 758, 27 128

Li, P., Qian-Qing, Y., Li, Z., et al. 2022, submitted to Experimental Astronomy 9

Lintott, C., Schawinski, K., Bamford, S., et al. 2011, MNRAS, 410, 166 52

Lintott, C. J., Schawinski, K., Slosar, A., et al. 2008, MNRAS, 389, 1179 52

Lisker, T. 2008, ApJS, 179, 319 54

Lotz, J. M., Primack, J., & Madau, P. 2004, AJ, 128, 163 54

Lucatelli, G. & Ferrari, F. 2019, MNRAS, 489, 1161 57

Lyman, J. D., Levan, A. J., Tanvir, N. R., et al. 2017, MNRAS, 467, 1795 22, 64, 68, 69, 77, 79, 128

Madau, P. & Dickinson, M. 2014, ARA&A, 52, 415 46, 68

MAGIC Collaboration, Acciari, V. A., Ansoldi, S., et al. 2019a, Nature, 575, 455 126

MAGIC Collaboration, Acciari, V. A., Ansoldi, S., et al. 2019b, Nature, 575, 459 126

Maier, D. & Limousin, O. 2016, Nuclear Instruments and Methods in Physics Research A, 812, 43 175, 176

Maier, D., Limousin, O., & Daniel, G. 2020, in European Physical Journal Web of Conferences, Vol. 225, European Physical Journal Web of Conferences, 01003 176

Majewski, P., Aschauer, F., Aschauer, S., et al. 2014, Experimental Astronomy, 37, 525 175

Malesani, D. B., Kann, D. A., Vergani, S. D., et al. 2022a, GRB Coordinates Network, 32368, 1 147

Malesani, D. B., Zhu, Z. P., Keniger, M. A., & Durfeldt Pedros, O. 2022b, GRB Coordinates Network, 32377, 1 149

Malmquist, K. G. 1922, Meddelanden fran Lunds Astronomiska Observatorium Serie I, 100, 1 44

Mannucci, F., Cresci, G., Maiolino, R., Marconi, A., & Gnerucci, A. 2010, MNRAS, 408, 2115 96

Marks, M., Kroupa, P., Dabringhausen, J., & Pawlowski, M. S. 2012, MNRAS, 422, 2246 99

Maselli, A., Melandri, A., Nava, L., et al. 2014, Science, 343, 48 126

Mayor, M. & Queloz, D. 1995, Nature, 378, 355 129

McConnell, M. L., Baring, M., Bloser, P., et al. 2021, in Society of Photo-Optical Instrumentation Engineers (SPIE) Conference Series, Vol. 11821, UV, X-Ray, and Gamma-Ray Space Instrumentation for Astronomy XXII, ed. O. H. Siegmund, 118210P 9

McDermid, R. M., Cresci, G., Rigaut, F., et al. 2020, arXiv e-prints, arXiv:2009.09242 141

Meidinger, N., Andritschke, R., Ebermayer, S., et al. 2010, Nuclear Instruments and Methods in Physics Research A, 624, 321 168

Meidinger, N., Andritschke, R., Hälker, O., et al. 2006, Nuclear Instruments and Methods in Physics Research A, 568, 141 168, 216, 234

Meidinger, N., Bonerz, S., Englhauser, J., et al. 2004, in Society of Photo-Optical Instrumentation Engineers (SPIE) Conference Series, Vol. 5501, High-Energy Detectors in Astronomy, ed. A. D. Holland, 66-77 168

Mészáros, P. 2001, Progress of Theoretical Physics Supplement, 143, 33 15

Meszaros, P. & Rees, M. J. 1993, ApJ, 405, 278 16

Mészáros, P. & Rees, M. J. 1997, ApJ, 476, 232 5, 17, 124

Mészáros, P. & Rees, M. J. 2010, ApJ, 715, 967 18

Metha, B., Cameron, A. J., & Trenti, M. 2021, MNRAS, 504, 5992 97, 127

Metha, B. & Trenti, M. 2020, MNRAS, 495, 266 97, 126

Metzger, B. D., Martínez-Pinedo, G., Darbha, S., et al. 2010, MNRAS, 406, 2650 145

Metzger, M. R., Djorgovski, S. G., Kulkarni, S. R., et al. 1997, Nature, 387, 878 5, 8

Meurer, G. R., Heckman, T. M., & Calzetti, D. 1999, ApJ, 521, 64 101

Meuris, A., Arhancet, A., Bachet, D., et al. 2022a, accepted for publication in Nucl. Instrum. Methods Phys. Res. A, 18 164

Meuris, A., Schneider, B., Allaire, H., et al. 2022b, accepted for publication in Nucl. Instrum. Methods Phys. Res. A, 12 182, 192

Michałowski, M. J., Castro Cerón, J. M., Wardlow, J. L., et al. 2016, A&A, 595, A72 65

Michałowski, M. J., Kamiński, K., Kamińska, M. K., & Wnuk, E. 2021, Nature Astronomy, 5, 995 18

Michałowski, M. J., Karska, A., Rizzo, J. R., et al. 2018, A&A, 617, A143 23

Miller, T. B., van Dokkum, P., Mowla, L., & van der Wel, A. 2019, ApJ, 872, L14 55

Mobasher, B., Dahlen, T., Ferguson, H. C., et al. 2015, ApJ, 808, 101 101

Modjaz, M., Kewley, L., Kirshner, R. P., et al. 2008, AJ, 135, 1136 22, 96

Momcheva, I. G., Brammer, G. B., van Dokkum, P. G., et al. 2016, ApJS, 225, 27 45, 70, 71

Mortlock, A., Conselice, C. J., Hartley, W. G., et al. 2013, MNRAS, 433, 1185 47

Mowla, L. A., Nelson, E. J., van Dokkum, P., & Tadaki, K.-i. 2019, ApJ, 886, L28 47

Nair, P. B. & Abraham, R. G. 2010, ApJS, 186, 427 52

Narayan, R., Paczynski, B., & Piran, T. 1992, ApJ, 395, L83 15, 16

Narayana Bhat, P., Meegan, C. A., von Kienlin, A., et al. 2016, ApJS, 223, 28 11

Nardini, M., Greiner, J., Krühler, T., et al. 2011, A&A, 531, A39 128

Newville, M., Stensitzki, T., Allen, D. B., & Ingargiola, A. 2014, LMFIT: Non-Linear Least-Square Minimization and Curve-Fitting for Python, Zenodo 214

Niino, Y. 2011, MNRAS, 417, 567 23

Nir, G., Ofek, E. O., & Gal-Yam, A. 2021, Research Notes of the American Astronomical Society, 5, 27 18

Noll, S., Burgarella, D., Giovannoli, E., et al. 2009, A&A, 507, 1793 79

Nugent, A. E., Fong, W.-F., Dong, Y., et al. 2022, ApJ, 940, 57 14

O'Connor, B., Troja, E., Dichiara, S., et al. 2022, MNRAS, 515, 4890 15

Ørum, S. V., Ivens, D. L., Strandberg, P., et al. 2020, A&A, 643, A47 98

Paciesas, W. S., Meegan, C. A., Pendleton, G. N., et al. 1999, ApJS, 122, 465 5, 6

Pacifici, C., da Cunha, E., Charlot, S., et al. 2015, MNRAS, 447, 786 101

Paczynski, B. & Rhoads, J. E. 1993, ApJ, 418, L5 16

Padmanabhan, H. & Loeb, A. 2022, General Relativity and Gravitation, 54, 24 18

Palmerio, J. T., Vergani, S. D., Salvaterra, R., et al. 2019, A&A, 623, A26 22, 23, 64, 72, 73, 78, 81, 84, 96

Peng, C. Y., Ho, L. C., Impey, C. D., & Rix, H.-W. 2002, AJ, 124, 266 57, 69, 70, 74

Peng, C. Y., Ho, L. C., Impey, C. D., & Rix, H.-W. 2010, AJ, 139, 2097 57, 69, 70, 74

Perley, D. A., Cenko, S. B., Bloom, J. S., et al. 2009, AJ, 138, 1690 77

Perley, D. A., Cenko, S. B., Corsi, A., et al. 2014, ApJ, 781, 37 125, 126

Perley, D. A., Krühler, T., Schulze, S., et al. 2016a, ApJ, 817, 7 22, 72, 73, 120

Perley, D. A., Levan, A. J., Tanvir, N. R., et al. 2013, ApJ, 778, 128 73, 89, 95, 118

Perley, D. A. & Perley, R. A. 2013, ApJ, 778, 172 64

Perley, D. A., Perley, R. A., Hjorth, J., et al. 2015, ApJ, 801, 102 65

Perley, D. A., Tanvir, N. R., Hjorth, J., et al. 2016b, ApJ, 817, 8 23, 64, 68, 72, 73, 78, 79, 89, 96, 118

Petrosian, V. 1976, ApJ, 210, L53 57

Petrovic, J., Langer, N., & van der Hucht, K. A. 2005, A&A, 435, 1013 64

Pforr, J., Maraston, C., & Tonini, C. 2012, MNRAS, 422, 3285 101

Pian, E., Mazzali, P. A., Masetti, N., et al. 2006, Nature, 442, 1011 12

Piran, T. 1999, Phys. Rep., 314, 575 15

Planck Collaboration, Aghanim, N., Akrami, Y., et al. 2020, A&A, 641, A6 66

Plucinsky, P. P., Beardmore, A. P., DePasquale, J. M., et al. 2012, in Society of Photo-Optical Instrumentation Engineers (SPIE) Conference Series, Vol. 8443, Space Telescopes and Instrumentation 2012: Ultraviolet to Gamma Ray, ed. T. Takahashi, S. S. Murray, & J.-W. A. den Herder, 844312 233

Plucinsky, P. P., Beardmore, A. P., Foster, A., et al. 2017, A&A, 597, A35 233, 235

Prochaska, J. X., Chen, H.-W., & Bloom, J. S. 2006, ApJ, 648, 95 21

Qin, Y., Liang, E.-W., Liang, Y.-F., et al. 2013, ApJ, 763, 15 10

Qin, Y.-J., Zabludoff, A., Kisley, M., et al. 2022, ApJS, 259, 13 10

Rafelski, M., Teplitz, H. I., Gardner, J. P., et al. 2015, AJ, 150, 31 69, 158

Rahin, R. & Behar, E. 2019, ApJ, 885, 47 153, 154

Rees, M. J. & Meszaros, P. 1994, ApJ, 430, L93 16

Rees, M. J. & Mészáros, P. 2005, ApJ, 628, 847 16

Reichherzer, P., Schüssler, F., Lefranc, V., et al. 2021, ApJS, 256, 5 134

Robertson, B. E. & Ellis, R. S. 2012, ApJ, 744, 95 19, 20, 64

Robotham, A. S. G., Taranu, D. S., Tobar, R., Moffett, A., & Driver, S. P. 2017, MNRAS, 466, 1513 57

Roming, P. W. A., Kennedy, T. E., Mason, K. O., et al. 2005, Space Sci. Rev., 120, 95 7

Rossi, A., Frederiks, D. D., Kann, D. A., et al. 2022, A&A, 665, A125 143

Rossi, A., Klose, S., Ferrero, P., et al. 2012, A&A, 545, A77 89

Rosswog, S., Ramirez-Ruiz, E., & Davies, M. B. 2003, MNRAS, 345, 1077 15

Ruffert, M. & Janka, H. T. 1999, A&A, 344, 573 15

Salvaterra, R., Campana, S., Vergani, S. D., et al. 2012, ApJ, 749, 68 22, 72

Salvaterra, R., Della Valle, M., Campana, S., et al. 2009, Nature, 461, 1258 18, 64, 65, 126

Sana, H., de Mink, S. E., de Koter, A., et al. 2012, Science, 337, 444 14

Sánchez Almeida, J. & Dalla Vecchia, C. 2018, ApJ, 859, 109 96

Sari, R. & Piran, T. 1999, ApJ, 520, 641 17

Sari, R., Piran, T., & Narayan, R. 1998, ApJ, 497, L17 17, 124

Savaglio, S., Glazebrook, K., & Le Borgne, D. 2009, ApJ, 691, 182 21, 118

Savaglio, S., Rau, A., Greiner, J., et al. 2012, MNRAS, 420, 627 65

Schady, P. 2017, Royal Society Open Science, 4, 170304 20, 154

Schady, P., Krühler, T., Greiner, J., et al. 2015, A&A, 579, A126 23

Schady, P., Savaglio, S., Krühler, T., Greiner, J., & Rau, A. 2011, A&A, 525, A113 154

Schady, P., Tanvir, N. R., Arabsalmani, M., et al. 2021, Mapping emission and absorption line metallicities onto the same univeral scale, JWST Proposal. Cycle 1, ID. #2344 147

Schlafly, E. F. & Finkbeiner, D. P. 2011, ApJ, 737, 103 80, 83

Schneider, B., Izzo, L., Malesani, D. B., et al. 2021, GRB Coordinates Network, 31188, 1 146, 148

Schneider, B., Renault-Tinacci, N., Götz, D., et al. 2022, submitted to Experimental Astronomy, 20 202

Schneider, B., Turpin, D., Le Floc'h, E., et al. 2022, GRB Coordinates Network, 32271, 1 139

Schulze, S., Krühler, T., Leloudas, G., et al. 2018, MNRAS, 473, 1258 65

Schüssler, F., Alkan, A. K., Lefranc, V., & Reichherzer, P. 2022, in 37th International Cosmic Ray Conference, 935 134

Sérsic, J. L. 1963, Boletin de la Asociacion Argentina de Astronomia La Plata Argentina, 6, 41 55, 70

Sersic, J. L. 1968, Atlas de Galaxias Australes 55, 70

Sharan Salafia, O. & Ghirlanda, G. 2022, arXiv e-prints, arXiv:2206.11088 124

Shibata, M. & Taniguchi, K. 2011, Living Reviews in Relativity, 14, 6 15

Silva-Villa, E., Adamo, A., & Bastian, N. 2013, MNRAS, 436, L69 99

Simard, L., Willmer, C. N. A., Vogt, N. P., et al. 2002, ApJS, 142, 1 57

Skelton, R. E., Whitaker, K. E., Momcheva, I. G., et al. 2014, ApJS, 214, 24 43, 45, 70, 72, 80

Sokolov, V. V., Fatkhullin, T. A., Castro-Tirado, A. J., et al. 2001, A&A, 372, 438 21, 63

Spruit, H. C., Daigne, F., & Drenkhahn, G. 2001, Astronomy and Astrophysics, v.369, p.694-705 (2001), 369, 694 16

Stanek, K. Z., Matheson, T., Garnavich, P. M., et al. 2003, ApJ, 591, L17 12, 63

Stanway, E. R., Levan, A. J., Tanvir, N. R., Wiersema, K., & van der Laan, T. P. R. 2015, ApJ, 798, L7 23

Starling, R. L. C., Willingale, R., Tanvir, N. R., et al. 2013, MNRAS, 431, 3159 153, 154

Steinhardt, C. L., Andersen, M. I., Brammer, G. B., et al. 2021, Nature Astronomy, 5, 993 18

Stratta, G., Fiore, F., Antonelli, L. A., Piro, L., & De Pasquale, M. 2004, ApJ, 608, 846 153

Stratta, G., Gendre, B., Atteia, J. L., et al. 2013, ApJ, 779, 66 11

Strüder, L., Briel, U., Dennerl, K., et al. 2001, A&A, 365, L18 168

Svensson, K. M., Levan, A. J., Tanvir, N. R., Fruchter, A. S., & Strolger, L. G. 2010, MNRAS, 405, 57 22

Svensson, K. M., Levan, A. J., Tanvir, N. R., et al. 2012, MNRAS, 421, 25 73, 89

Swenson, C. A., Roming, P. W. A., De Pasquale, M., & Oates, S. R. 2013, ApJ, 774, 2 128

Tal, T., Dekel, A., Oesch, P., et al. 2014, ApJ, 789, 164 71

Tanga, M., Krühler, T., Schady, P., et al. 2018, A&A, 615, A136 21

Tanga, M., Schady, P., Gatto, A., et al. 2016, A&A, 595, A24 154

Tanvir, N., Rossi, A., Xu, D., et al. 2021a, GRB Coordinates Network, 30771, 1 143

Tanvir, N. R., Barnard, V. E., Blain, A. W., et al. 2004, MNRAS, 352, 1073 21

Tanvir, N. R., Fox, D. B., Levan, A. J., et al. 2009, Nature, 461, 1254 18, 64, 126, 141

Tanvir, N. R., Fynbo, J. P. U., de Ugarte Postigo, A., et al. 2019, MNRAS, 483, 5380 19, 147, 153

Tanvir, N. R., Le Floc'h, E., Christensen, L., et al. 2021b, Experimental Astronomy, 52, 219 17

Thompson, A. C., Attwood, D. T., Gullikson, E. M., et al. 2009, X-Ray Data Booklet, 3rd edn. (Lawrence Berkeley National Laboratory, University of California) 210

Thöne, C. C., Campana, S., Lazzati, D., et al. 2011a, MNRAS, 414, 479 67, 98

Thöne, C. C., de Ugarte Postigo, A., Fryer, C. L., et al. 2011b, Nature, 480, 72 10

Tinney, C., Stathakis, R., Cannon, R., et al. 1998, IAU Circ., 6896, 3 18

Tolman, R. C. 1930, Proceedings of the National Academy of Science, 16, 511 49

Tolman, R. C. 1934, Proceedings of the National Academy of Science, 20, 169 49

Toma, K., Sakamoto, T., & Mészáros, P. 2011, ApJ, 731, 127 18

Tremonti, C. A., Heckman, T. M., Kauffmann, G., et al. 2004, ApJ, 613, 898 96

Tuccillo, D., Huertas-Company, M., Decencière, E., et al. 2018, MNRAS, 475, 894 60

Turpin, D., Adami, C., Schneider, B., Le Floch, E., & Basa, S. 2022, GRB Coordinates Network, 32360, 1 139

Turpin, D., Wu, C., Han, X.-H., et al. 2020, Research in Astronomy and Astrophysics, 20, 013 33

van der Horst, A. J., Levan, A. J., Pooley, G. G., et al. 2015, MNRAS, 446, 4116 78

van der Wel, A., Bell, E. F., Häussler, B., et al. 2012, ApJS, 203, 24 70, 71, 74, 104, 114

van der Wel, A., Franx, M., van Dokkum, P. G., et al. 2014, ApJ, 788, 28 70, 71, 72, 74, 76, 90, 102, 103, 104, 115, 116

van Paradijs, J., Groot, P. J., Galama, T., et al. 1997, Nature, 386, 686 5, 7

Vedrenne, G. & Atteia, J.-L. 2009, Gamma-Ray Bursts 2

Vergani, S. D., Palmerio, J., Salvaterra, R., et al. 2017, A&A, 599, A120 78

Vergani, S. D., Salvaterra, R., Japelj, J., et al. 2015, A&A, 581, A102 23, 64, 96, 118

Vernet, J., Dekker, H., D'Odorico, S., et al. 2011, A&A, 536, A105 142, 143

Vielfaure, J. B., Vergani, S. D., Gronke, M., et al. 2021, A&A, 653, A83 126

Vielfaure, J. B., Vergani, S. D., Japelj, J., et al. 2020, A&A, 641, A30 20, 126

Vikram, V., Wadadekar, Y., Kembhavi, A. K., & Vijayagovindan, G. V. 2010, MNRAS, 409, 1379 57, 74

Vink, J. S., de Koter, A., & Lamers, H. J. G. L. M. 2001, A&A, 369, 574 14

Virgili, F. J., Mundell, C. G., Pal'shin, V., et al. 2013, ApJ, 778, 54 11

Vreeswijk, P. M., Ledoux, C., Smette, A., et al. 2007, A&A, 468, 83 21

Vreeswijk, P. M., Ledoux, C., Smette, A., et al. 2011, Corrigendum: Rapid-response mode VLT/UVES spectroscopy of GRB 060418. Conclusive evidence for UV pumping from the time evolution of Fe II and Ni II excited- and metastable-level populations, Astronomy & Astrophysics, Volume 532, id.C3, 1 pp. 21

Wainwright, C., Berger, E., & Penprase, B. E. 2007, ApJ, 657, 367 24, 65, 91, 98

Wang, F. Y. 2013, A&A, 556, A90 20

Wang, J., Li, H. L., Xin, L. P., et al. 2020, AJ, 159, 35 32, 33

Wang, T., Schreiber, C., Elbaz, D., et al. 2019, Nature, 572, 211 64

Watson, D. 2011, A&A, 533, A16 153

Watson, D., Hjorth, J., Fynbo, J. P. U., et al. 2007, ApJ, 660, L101 153

Watson, D. & Jakobsson, P. 2012, ApJ, 754, 89 153, 154

Wei, J., Cordier, B., Antier, S., et al. 2016, arXiv e-prints, arXiv:1610.06892 9, 24, 25, 100, 136

Weinzirl, T., Jogee, S., Khochfar, S., Burkert, A., & Kormendy, J. 2009, ApJ, 696, 411 57

Whitaker, K. E., Franx, M., Leja, J., et al. 2014, ApJ, 795, 104 70, 71, 101, 102

White, N. E., Bauer, F. E., Baumgartner, W., et al. 2021, in Society of Photo-Optical Instrumentation Engineers (SPIE) Conference Series, Vol. 11821, UV, X-Ray, and Gamma-Ray Space Instrumentation for Astronomy XXII, ed. O. H. Siegmund, 1182109 9

Williams, R. J., Quadri, R. F., Franx, M., van Dokkum, P., & Labbé, I. 2009, ApJ, 691, 1879 70

Wolter, H. 1952, Annalen der Physik, 445, 94 165

Woosley, S. E. 1993, ApJ, 405, 273 13, 63

Woosley, S. E. & Heger, A. 2006, ApJ, 637, 914 23, 63

Wuyts, E., Kurk, J., Förster Schreiber, N. M., et al. 2014, ApJ, 789, L40 96

Wuyts, S., Labbé, I., Franx, M., et al. 2007, ApJ, 655, 51 70

Xin, L. P., Li, H. L., Wang, J., et al. 2021, ApJ, 909, 106 33

Xu, D., de Ugarte Postigo, A., Leloudas, G., et al. 2013, ApJ, 776, 98 63

Xu, Y., Xin, L. P., Wang, J., et al. 2020, PASP, 132, 054502 32

Yabe, K., Ohta, K., Iwamuro, F., et al. 2014, MNRAS, 437, 3647 96

Yabe, K., Ohta, K., Iwamuro, F., et al. 2012, PASJ, 64, 60 96

Yonetoku, D., Mihara, T., Sawano, T., et al. 2014, in Society of Photo-Optical Instrumentation Engineers (SPIE) Conference Series, Vol. 9144, Space Telescopes and Instrumentation 2014: Ultraviolet to Gamma Ray, ed. T. Takahashi, J.-W. A. den Herder, & M. Bautz, 91442S 9

Yoon, S.-C., Kang, J., & Kozyreva, A. 2015, ApJ, 802, 16 18

Yoon, S. C. & Langer, N. 2005, A&A, 443, 643 14

Yoon, S. C., Langer, N., & Norman, C. 2006, A&A, 460, 199 23, 63, 64

Yuan, W., Zhang, C., Feng, H., et al. 2015, arXiv e-prints, arXiv:1506.07735 9

Zafar, T., Heintz, K. E., Karakas, A., Lattanzio, J., & Ahmad, A. 2019, MNRAS, 490, 2599 126

Zafar, T., Watson, D., Elíasdóttir, Á., et al. 2012, ApJ, 753, 82 155

Zafar, T., Watson, D., Møller, P., et al. 2018, MNRAS, 479, 1542 126, 155, 156

Zahid, H. J., Kashino, D., Silverman, J. D., et al. 2014, ApJ, 792, 75 96

Zhang, B. 2018, The Physics of Gamma-Ray Bursts 2

Zhang, B., Fan, Y. Z., Dyks, J., et al. 2006, ApJ, 642, 354 124, 150

Zhang, B., Zhang, B.-B., Virgili, F. J., et al. 2009, ApJ, 703, 1696 10

Zhang, B. B., Liu, Z. K., Peng, Z. K., et al. 2021, Nature Astronomy, 5, 911 10

Zhang, B.-B., Zhang, B., Murase, K., Connaughton, V., & Briggs, M. S. 2014, ApJ, 787, 66 11

université PARIS-SACLAY

ÉCOLE DOCTORALE
Astronomie
et Astrophysique
d'Île-de-France (AAIF)

Titre: Les environnements à l'origine des sursauts gamma longs : préparation à la mission SVOM

Mots clés: Sursauts gamma, Structure des galaxies, Formation stellaire, Suivi des alertes, SVOM, MXT

Résumé: Les sursauts gamma (GRBs) sont de brefs flashs de rayons gamma causés par des jets ultra-relativistes après la formation d'un trou noir stellaire et représentent les phénomènes les plus énergétiques connus dans l'Univers. La future mission franco-chinoise SVOM sera dédiée à l'observation des GRBs et ouvrira une nouvelle ère dans le domaine du ciel transitoire et multi-messager. Grâce à une meilleure synergie entre la détection des GRBs par les instruments à bord du satellite et leur suivi par les télescopes au sol, SVOM promet d'apporter un nouveau regard sur ces phénomènes extrêmes. Dans cette thèse, je me suis intéressé à la préparation et à l'exploitation scientifique de la mission à long, moyen et court terme.
À long terme : parmi la population des GRBs, une sous-population constituée des sursauts gamma longs (LGRB) s'est révélée être associée à la fin de vie des étoiles massives, ce qui en fait des traceurs prometteurs de la formation stellaire cosmique jusqu'à de très grands décalages spectraux ($z > 8$). Cependant, des études ont suggéré que certaines conditions semblent être requises pour former un LGRB, liées par exemple à la faible métallicité du progéniteur ou de son environnement proche. À travers mon travail, j'ai étudié l'influence de la densité stellaire sur l'efficacité de formation des LGRBs. Puisque ces phénomènes sont extragalactiques, ce type d'étude ne peut se faire qu'à travers les propriétés globales de la galaxie hôte. En comparant un échantillon de galaxies hôtes de LGRBs à un échantillon de galaxies à formation d'étoiles obtenu à partir d'un sondage profond de l'Univers, j'ai montré que les LGRBs ont tendance à être observés plus fréquemment dans des galaxies compactes ayant une densité de formation d'étoiles et de masse stellaire plus élevées que la normale.
À moyen terme : la constitution du nouvel échantillon de GRBs proprement caractérisés et identifiés par la mission SVOM nécessitera un suivi efficace des alertes par la communauté scientifique de SVOM. Dans ce but, j'ai pris part de manière active au programme mené par le consortium Stargate à l'aide du Very Large Telescope pour conduire le suivi des GRBs actuellement détectés par la mission Swift. J'ai également joué un rôle important dans la récente mise en place du suivi de ces alertes avec le spectro-imageur MISTRAL installé sur le T193 de l'Observatoire de Haute-Provence.
À court terme : SVOM effectuera un suivi systématique des GRBs dans le domaine des rayons X en utilisant un télescope X à bord du satellite (MXT). Dans ce contexte, j'ai participé activement à la calibration en énergie du modèle de vol de MXT et à la mise en place d'un traitement optimisé des données. Ceci a permis de démontrer l'excellente performance spectrale de MXT avant son lancement. Une fois en vol, ces traitements permettront de tirer le meilleur parti des données pour leur exploitation scientifique.

Title: The environments giving birth to Long Gamma-Ray Bursts: preparing the SVOM science

Keywords: Gamma-ray bursts, Galaxies structure, Star formation, Follow-up, SVOM, MXT

Abstract: Gamma-Ray Bursts (GRBs) are brief flashes of gamma-ray photons produced by ultra-relativistic jets after a newly born stellar black hole, and represent the most energetic phenomena known in the Universe. The forthcoming Sino-French mission SVOM will be dedicated to the observation of GRBs and will open a new era in the time-domain and multi-messenger astrophysics. With a better synergy between the detection of GRBs by instruments on board the satellite and their follow-up with ground telescopes, SVOM will offer a new insight on these extreme phenomena. In this thesis, I focused on the preparation and the scientific exploitation of the mission on long, medium and short term.
Long-term: among the GRB population, a subpopulation known as Long Gamma-Ray Bursts (LGRBs) is believed to be associated with the death of massive stars, which makes them promising tracers of the cosmic star formation history up to very high redshift ($z > 8$). However, previous work suggested that some conditions seem to be required to form an LGRB, related for instance to the low metallicity of the progenitor or its surrounding environment. Through my work, I studied the influence of the stellar density on the efficiency of LGRB formation. Given that these phenomena are extragalactic, the analysis can only be performed through the global properties of the host galaxy. By comparing a sample of LGRB host galaxies to a sample of star-forming galaxies obtained from a deep survey, I showed that LGRBs tend to be observed more frequently in compact galaxies with a density of star formation and stellar mass higher than found in galaxies of the field.
Mid-term: the build-up of the new sample of well-characterized GRBs identified with SVOM will require an efficient follow-up by the SVOM science community. In this goal, I actively contributed to the program led with the Very Large Telescope by the Stargate consortium to follow-up the GRBs currently detected by the Swift satellite. I also played a key role in setting up the recent follow-up of these alerts with the MISTRAL spectro-imager mounted on the T193 at the Observatoire de Haute-Provence.
Short-term: SVOM will perform a systematic X-ray follow-up of GRBs using the X-ray telescope on board the satellite (MXT). In this context, I actively participated in the energy calibration of the MXT flight model and in the development of an optimized data processing. This demonstrated the excellent spectral performance of MXT before its launch. Once in flight, this processing will ensure high quality reduced products for scientific analysis.